



**This electronic thesis or dissertation has been
downloaded from Explore Bristol Research,
<http://research-information.bristol.ac.uk>**

Author:

Keyen, Ukrit

Title:

Understanding Reactions and Processes in Solid-State Materials at the Atomic Level

General rights

Access to the thesis is subject to the Creative Commons Attribution - NonCommercial-No Derivatives 4.0 International Public License. A copy of this may be found at <https://creativecommons.org/licenses/by-nc-nd/4.0/legalcode>. This license sets out your rights and the restrictions that apply to your access to the thesis so it is important you read this before proceeding.

Take down policy

Some pages of this thesis may have been removed for copyright restrictions prior to having it been deposited in Explore Bristol Research. However, if you have discovered material within the thesis that you consider to be unlawful e.g. breaches of copyright (either yours or that of a third party) or any other law, including but not limited to those relating to patent, trademark, confidentiality, data protection, obscenity, defamation, libel, then please contact collections-metadata@bristol.ac.uk and include the following information in your message:

- Your contact details
- Bibliographic details for the item, including a URL
- An outline nature of the complaint

Your claim will be investigated and, where appropriate, the item in question will be removed from public view as soon as possible.

Understanding Reactions and Processes in Solid-State Materials at the Atomic Level

By

UKRIT KEYEN



School of Chemistry
UNIVERSITY OF BRISTOL

A dissertation submitted to the University of Bristol
in accordance with the requirements of the degree of
DOCTOR OF PHILOSOPHY in the Faculty of Science.

AUGUST 2022

Word count: 50000 (Approx.)

ABSTRACT

This work uses modern computer simulation methods to investigate the thermodynamics and kinetics of processes and reactions in solid-state materials. First, the thermodynamics of the Ba^{2+} substitutional defect in MgO and the Ag substitutional defect in Cu metal are studied using classical and density functional theory lattice statics and lattice dynamics within the quasi-harmonic approximation. The computed defect energies show that the temperature variation of the defect energies is significant and not negligible as often assumed. We compare the defects in finite-size clusters with those in the bulk. While defect energies of larger clusters are closer to those in the bulk, the interfaces present in finite-size clusters give rise to differences in the degree of structural relaxation. Secondly, we emphasise the geochemical importance of such defect modelling for explaining the partitioning behaviour of trace elements between minerals and melts and explore the factors which are crucial in controlling partitioning. Lattice statics calculations were used to compute energies for the incorporation of various trace elements in CaO and in diopside. The defect modelling was also used to uncover the serious limitations of simple lattice strain models, *e.g.*, the poor description of lattice strains, the use of the invariant cation radii, the oversimplified assumption of the incorporation mechanisms and the disregard for the role of melt species when describing trace-element partitioning.

Finally, we turn to examine the kinetics of some zeolite-catalysed reactions in the context of macromolecular rate theory. Many zeolite-catalysed reactions exhibit non-Arrhenius behaviour in which the rate of reaction is lower than expected at higher temperatures. Based on similarities with enzyme catalysis, we suggest a negative change in the heat capacity of activation is a possible explanation of the negative curvature of the Arrhenius plots for these zeolitic reaction rates. The classical and *ab initio* calculations based on quasi-harmonic lattice dynamics, molecular dynamics and metadynamics have been employed to investigate the temperature dependence of the free-energy barriers and rates of several diffusion processes in MgO and zeolitic frameworks. The rates of the Mg^{2+} vacancy migration in MgO, the diffusion of an ethene molecule through an LTA zeolite pore and the diffusion of ethene molecules in the LTA framework are predicted to show deviations from the classical Arrhenius law, in line with macromolecular rate theory. Since macromolecular rate theory proves useful for understanding enzyme thermoadaptation and designing new enzymes with desirable temperature-dependent properties, we hope our findings will help in the design and synthesis of novel materials for special purposes.

DEDICATION AND ACKNOWLEDGEMENTS

I want to thank Mom and Dad for always encouraging me to go on every adventure, especially this one. I am thankful for my kind, supportive and brilliant supervisor, Professor Neil L. Allan, and every member of the Allan group. I wish to thank the Development and Promotion of the Gifted in Science and Technology Project (DPST) and the Centre for Doctoral Training in Theory and Modelling in Chemical Sciences (TMCS CDT) for the funding and great opportunities. I am also grateful to my most beloved family and dearest friends for helping me through many difficult times.

COVID-19 STATEMENT

When I was in the third year of my PhD study in March 2020, I decided to fly back home to Thailand while the UK was about to enter a state of national lockdown. I have remotely been working from home in Chiang Mai, Thailand, since then. During the lockdown, all the on-site work in the University by all students and teaching staff stopped completely. Many students who could not work in the lab migrated to computational projects; therefore, the University's high-performance computing facilities were overwhelmed by the surging demand. This extra load on the resources made the hardware less reliable and much more prone to malfunction, and the throughput of my long simulations was an order of magnitude slower than it had been under normal circumstances. Furthermore, the lack of access to the libraries also delayed the thesis writing-up process to a considerable extent. Discussing the work with my supervisor online during the pandemic was much more difficult than that in our regular face-to-face meetings due to the time difference. Apart from the obvious negative impact it had on my research and thesis writing, the severe restraints of COVID-19 in Thailand also put a huge toll on my mental health. As a result, I requested three short extensions of my PhD study and writing up from September 2021 until May 2022.

AUTHOR'S DECLARATION

I declare that the work in this dissertation was carried out in accordance with the requirements of the University's Regulations and Code of Practice for Research Degree Programmes and that it has not been submitted for any other academic award. Except where indicated by specific reference in the text, the work is the candidate's own work. Work done in collaboration with, or with the assistance of, others, is indicated as such. Any views expressed in the dissertation are those of the author.

SIGNED: DATE:

TABLE OF CONTENTS

	Page
List of Tables	xiii
List of Figures	xv
1 Introduction	1
1.1 Overview	1
1.1.1 Defects in Crystals	2
1.1.2 Trace-Element Partitioning between Minerals and Melts	4
1.1.3 Temperature Variation of Activated Processes in Solid-State Materials	5
1.2 Thesis Outline	6
2 Theory and Methods	9
2.1 Computational Methods for Solid-State Modelling	9
2.1.1 Periodic Boundary Conditions	11
2.1.2 Classical Interatomic Potentials	12
2.1.3 Energy Minimisation	14
2.1.4 Molecular Dynamics	17
2.1.5 Metadynamics	19
2.1.6 Quantum Mechanical Methods	20
2.1.7 Transition-State Optimisation	25
2.2 Computer Modelling of Point Defects	25
2.2.1 Defect Thermodynamics	28
2.2.2 Kröger-Vink Notation for Point Defects	29
2.3 List of Software Packages	29
2.3.1 GULP	29
2.3.2 DL_POLY4 and DL_Software	29

TABLE OF CONTENTS

2.3.3	CRYSTAL17	30
2.3.4	Quantum ESPRESSO	30
2.3.5	CP2K	30
2.3.6	PLUMED	30
2.3.7	VASP	31
2.3.8	Structure Visualisers	31
3	Defect Thermodynamics in Solids and Clusters	33
3.1	Introduction	34
3.2	Models and Computational Details	35
3.2.1	Classical Simulation	35
3.2.2	First-Principles Simulation	37
3.3	Results and Discussion	38
3.3.1	Variation of Defect Quantities with System Size	38
3.3.2	Effects of Temperature on Defect Properties	40
3.3.3	Finite-Size Effects	48
3.3.4	<i>Ab Initio</i> Calculations for Ba-Substitutional Defect in MgO	65
3.3.5	Defects in Metals	83
3.3.6	Effects of Defect Clustering	88
3.3.7	Applications	96
3.4	Conclusions	97
4	Trace-Element Partitioning in Minerals and Melts	101
4.1	Partitioning Controlling Factors	101
4.2	Onuma Diagrams	102
4.3	Thermodynamics of Trace-Element Partitioning	105
4.3.1	Fusion Equilibria for Mineral-Melt Partitioning	105
4.3.2	Exchange Equilibria for Mineral-Mineral Partitioning	107
4.4	Lattice Strain Models	109
4.5	Limitations of Lattice Strain Models	114
4.6	Energies of Trace-Element Incorporation in Minerals	117
4.6.1	Definitions of Energy Terms	117
4.6.2	Models and Computational Details	118
4.6.3	Homovalent Trace Elements in CaO and Diopside	125
4.6.4	Heterovalent Trace Elements in CaO and Diopside	135
4.6.5	Implications for Trace-Element Partitioning	151

4.6.6	Brief Comments on Solid Solutions and Direct Simulation Technique	152
4.7	Conclusions	154
5	Non-Arrhenius Reaction Rates in Solids	157
5.1	Chemical Catalysis	158
5.2	Non-Arrhenius Behaviour of Enzyme Rates	159
5.3	Similarities between Enzymes and Heterogeneous Catalysts	166
5.4	Exploring Non-Arrhenius Zeolite-Catalysed Reaction Rates	168
5.5	Simulation of Activated Processes in Solid-State Materials	180
5.5.1	Defect Migration in MgO	181
5.5.2	Ethene and Propene Diffusion through an LTA Zeolitic Micropore	184
5.5.3	Diffusion Rates of Ethene and Propene in LTA Zeolite	193
5.5.4	Hydrogen Hopping in the H-LTA Zeolite	197
5.5.5	<i>Ab initio</i> Simulation of Zeolitic Reactions	201
5.6	Conclusions	204
6	Conclusions and Future Work	207
6.1	Summaries	207
6.1.1	Defect Thermodynamics in Solids and Clusters	208
6.1.2	Trace-Element Partitioning in Minerals and Melts	208
6.1.3	Non-Arrhenius Reaction Rates in Solids	209
6.2	General Conclusions	210
6.3	Future Work	211
	Bibliography	215

LIST OF TABLES

TABLE	Page
3.1 Buckingham pair-potential parameters for modelling a Ba^{2+} substitutional defect in MgO	35
3.2 Supercells of MgO used in this work	35
3.3 Lennard-Jones pair-potential parameters for modelling the Ag substitutional defect in Cu metal	36
3.4 Experimental and calculated lattice parameters of MgO and BaO	66
3.5 Observed interionic distances in bulk MgO and BaO from classical and DFT calculations in the static limit	66
3.6 Observed interionic distances in defective MgO supercells from classical and DFT calculations in the static limit	67
4.1 Lattice strain parameters for the experimental partition coefficients of cations entering the <i>M2</i> -site of diopside equilibrated with silicate melts	112
4.2 Classical interionic potential parameters used for modelling the incorporation of trace-element cations into CaO and diopside	120
4.3 Calculated and experimental lattice parameters of CaO and diopside	121
4.4 Calculated and experimental elastic properties of CaO and diopside	122
4.5 Six-fold and eight-fold coordinated cation radii, calculated lattice energies, and DFT ion energies for studying the incorporation of trace cations in CaO and diopside	124
4.6 The calculated final defect formation, relaxation and solution energies for the incorporation of divalent dopants into CaO	125
4.7 The calculated final defect formation, relaxation and solution energies for the incorporation of divalent dopants into diopside	126
4.8 Defect, relaxation and solution energies for heterovalent substitutions in CaO	138
4.9 Defect, relaxation and solution energies for heterovalent substitutions in diopside	141

LIST OF TABLES

5.1	MMRT parameters for reactions catalysed by MFI-type zeolites	173
5.2	MMRT parameters for zeolite-catalysed conversion reactions	176
5.3	MMRT parameters for Cu-zeolite-catalysed redox reactions of NO _x and NH ₃	177
5.4	MMRT parameters of other chemical reactions over various zeolitic materials	180
5.5	Buckingham potential parameters for zeolite frameworks	187
5.6	CVFF potential parameters for alkenes	188
5.7	Lennard-Jones potential parameters for host-guest interactions between alkenes and zeolite framework	188

LIST OF FIGURES

FIGURE	Page
2.1 Periodic boundary conditions	11
2.2 Two models for defect calculations	26
3.1 Defect volume and defect energies as a function of supercell size for a Ba^{2+} substitutional defect in MgO in the static limit	39
3.2 Temperature variation of the defect volume of a Ba_{Mg}^x substitutional defect in bulk MgO	41
3.3 Temperature variation of defect free-energies and entropies for Ba_{Mg}^x in MgO	42
3.4 Phonon density of states (DOS) plots of bulk MgO and Ba_{Mg}^x defective structures	44
3.5 Temperature dependence of the change in constant-volume heat capacity of the Ba_{Mg}^x defect formation in MgO	45
3.6 Temperature dependence of the change in constant-pressure heat capacity of the Ba_{Mg}^x defect formation in MgO	47
3.7 Finite-size effects on the Ag_{Cu}^x defect energy in Cu metal and clusters as a function of system size in the static limit	50
3.8 Variation of defect energies and entropy changes of Ba_{Mg}^x defect formation in bulk MgO and clusters with system size	53
3.9 Temperature variation of defect energies and entropy changes of Ba_{Mg}^x defect formation in bulk MgO and cluster at constant pressure	54
3.10 Temperature variation of defect energies and entropy change of Ba_{Mg}^x defect formation in bulk MgO and cluster at constant volume	55
3.11 Phonon density of states (DOS) plots of MgO cluster and Ba_{Mg}^x defective structure	57
3.12 Mass effects on the temperature variation of defect entropies for Ba_{Mg}^x in bulk MgO and MgO cluster	59
3.13 Phonon density of states (DOS) plots of $^{137}\text{Ba}_{\text{Mg}}^x$ and $^{24}\text{Ba}_{\text{Mg}}^x$ substitutional defects in bulk MgO at constant pressure	60

LIST OF FIGURES

3.14	Variation of heat capacity changes of Ba_{Mg}^x in MgO with system size and temperature	62
3.15	Vibrational heat capacity and vibrational entropy as a function of wavenumber and temperature	63
3.16	Schematic illustration of the optimised distances between the Ba^{2+} and its neighbouring ions in the first nearest-neighbouring shells in a defective supercell of bulk MgO, and the relative shell displacements after geometry relaxation	69
3.17	Atomic displacements of Mg^{2+} and O^{2-} in the first few nearest-neighbouring shells on the logarithm scale as a function of initial ionic distance from the Ba^{2+} defect in a 216-ion supercell of MgO from constant-pressure DFT and classical simulations	70
3.18	Atomic displacements around a Ba_{Mg}^x substitutional defect along the (001) plane of a 2744-ion supercell of MgO	73
3.19	Atomic displacements around a Ba_{Mg}^x substitutional defect in a 2744-ion supercell of MgO as a function of initial interionic distance from the Ba^{2+} defect	74
3.20	Defect volume and constant-pressure and constant-volume defect energies as a function of system size for a Ba^{2+} substitutional defect in MgO in the static limit	75
3.21	Electron density maps of bulk MgO	77
3.22	Electron density maps of defective bulk MgO with a Ba_{Mg}^x substitutional defect	78
3.23	Temperature variation of the experimental and calculated DFT-QHA properties of bulk MgO	80
3.24	Temperature variations of constant-volume defect energies and changes in entropy and heat capacity of Ba_{Mg}^x defect in MgO	82
3.25	Variation of defect energies and entropy changes of Ag_{Cu}^x defect in bulk Cu metal and cubic-shaped Cu clusters with system size	84
3.26	Temperature variation of defect energies and entropy changes of Ag_{Cu}^x in bulk Cu metal and cluster at constant pressure	86
3.27	Temperature variation of defect energies and entropy change of Ag_{Cu}^x in bulk Cu metal and cluster at constant volume	87
3.28	Variations of changes in heat capacity of Ag_{Cu}^x in Cu metal with system size and temperature	89
3.29	Schematic illustration of the initial defective supercells of bulk MgO with two Ba_{Mg}^x defects	91

3.30	Variation of defect volume and defect energies per defect with interatomic distance of two Ba^{2+} substitutional defects in bulk MgO in the static limit . .	92
3.31	Schematic illustration of the defective supercells of bulk MgO with multiple Ba_{Mg}^x defects	94
3.32	Variation of defect volume and defect energies per defect with mole fraction of Ba^{2+} defects in bulk MgO in the static limit	95
4.1	Schematic and experimental Onuma diagrams	103
4.2	Crystal structure of diopside	122
4.3	Variation of calculated final relaxed defect energies with ionic radius for homovalent substitutions in CaO	127
4.4	Variation of calculated final relaxed defect energies with ionic radius for homovalent substitutions in diopside	128
4.5	Variation of calculated relaxation energies with ionic radius for divalent substitutions in CaO	129
4.6	Variation of calculated relaxation energies with ionic radius for divalent substitutions in diopside	130
4.7	Variation of calculated solution energies with ionic radius for divalent substitutions in CaO	133
4.8	Variation of calculated solution energies with ionic radius for divalent substitutions in diopside	134
4.9	Variation of classical solution energies with ionic radius for divalent substitutions in diopside	135
4.10	Calculated defect, relaxation and solution energies for monovalent substitutions in CaO	139
4.11	Calculated defect, relaxation and solution energies for trivalent substitutions in CaO	140
4.12	Calculated defect, relaxation and solution energies for monovalent substitutions in diopside	142
4.13	Calculated defect, relaxation and solution energies for trivalent substitutions in diopside	143
4.14	DFT defect energies of homovalent and heterovalent substitutions in CaO . .	145
4.15	DFT defect energies of homovalent and heterovalent substitutions at the two lattice sites in diopside	146
4.16	DFT relaxation and solution energies of homovalent and heterovalent substitutions in CaO	147

LIST OF FIGURES

4.17	DFT relaxation energies of homovalent and heterovalent substitutions at the two lattice sites in diopside	148
4.18	DFT solution energies of homovalent and heterovalent substitutions at the two lattice sites in diopside	150
5.1	Schematic plot of the Arrhenius equation	158
5.2	Schematic plot of biologically catalysed reaction rates as a function of $1/T$. . .	160
5.3	Effect of the sign of ΔC_p^\ddagger on the temperature variation of chemical reaction rates modelled using MMRT	162
5.4	MMRT equation fitted to kinetic data of a reaction catalysed by acid phosphatase	163
5.5	Schematic diagram of the change in heat capacity as an enzymatically catalysed reaction proceeds	164
5.6	Dependence of the magnitude of the change in heat capacity of activation on the degree of isotopic substitutions in the substrate species in an enzyme reaction	165
5.7	Arrhenius plots of methylation reactions catalysed by H-ZSM-5 zeolite	169
5.8	Fitted kinetic data of alkene methylation reactions catalysed by H-ZSM-5 zeolites into MMRT equation	171
5.9	Arrhenius plots of conversion reactions catalysed by Pt-H-MOR zeolites . . .	174
5.10	Fitted kinetic data of <i>n</i> -pentane and neopentane conversion reactions catalysed by Pt-H-MOR zeolites into MMRT equation	175
5.11	Arrhenius plots of NO decomposition over Cu-zeolites	178
5.12	Arrhenius plots of NO decomposition over Cu-ZSM-5 zeolites	179
5.13	Schematic illustration of Mg^{2+} vacancy migration in MgO	182
5.14	Temperature dependence of ΔG^\ddagger of Mg^{2+} vacancy migration in MgO	184
5.15	Temperature dependence of ΔH^\ddagger and ΔS^\ddagger of Mg^{2+} vacancy migration in MgO	185
5.16	Temperature dependence of ΔC_p^\ddagger of Mg^{2+} vacancy migration in MgO	186
5.17	Crystal structure of the LTA zeolite	186
5.18	Temperature dependence of the crystal volume of the LTA zeolite	189
5.19	Schematic illustration of the collective variable for the metadynamics simulation of the alkene diffusion through an LTA zeolitic pore	190
5.20	Free energy profiles and energy barriers of the ethene diffusion through an LTA zeolitic pore	191
5.21	Free energy profiles and energy barriers of the propene diffusion through an LTA zeolitic pore	192

5.22	Mean-square displacement plots of the centres of mass of ethene molecules at different temperatures in the LTA zeolite	193
5.23	Arrhenius plot of the ethene diffusion rate in the LTA zeolite over 100-600 K	195
5.24	Arrhenius plot of the propene diffusion rate in the LTA zeolite over 100-600 K	196
5.25	Structure of H-LTA zeolite for modelling hydrogen hopping	197
5.26	NEB energy profile for hydrogen hopping in H-LTA zeolite	198
5.27	Temperature dependence of the lattice parameter (a) of the LTA zeolite	199
5.28	Free-energy profiles at different temperatures for hydrogen hopping in the H-LTA zeolite	200
5.29	Temperature variation of the free energy barrier for hydrogen hopping in the H-LTA zeolite	201
5.30	Structure of H-ZSM-5 zeolite for modelling ethene methylation reaction by methanol	202
5.31	Transition-state geometry for the ethene methylation by methanol over H-ZSM-5 zeolite	203
5.32	Energy diagram for the ethene methylation by methanol over H-ZSM-5 zeolite	203

INTRODUCTION

1.1 Overview

The increasing power of highly-parallel supercomputers and advances in software engineering enable us to simulate highly complex chemical systems to gain microscopic insights into chemical phenomena. In the research field of materials modelling, advanced theoretical frameworks and massively parallel computer codes have been used to study the properties and behaviours of various types of complex solid-state materials computationally, *e.g.*, for predicting unknown crystal structures,¹ investigating the chemical bonding and electronic properties in solids,² modelling defects in crystals,^{3,4} studying surfaces and interfaces,⁵ examining sorption processes,⁶ studying transport processes of atoms and molecules in solids,⁷ simulating nano-structures,^{8,9} and so forth.

Although a number of computational methods are available for simulating those complex solid-state systems, one must consider the inevitable trade-off between computational cost and accuracy when contemplating the methods. It is always crucial to validate the numerical results of simple systems obtained from the chosen method with the known reference results, *e.g.*, from experiments or higher-level calculations, before performing a vast series of computationally expensive calculations of the more complicated systems. Calculations based on classical force fields are much faster and computationally cheaper than those based on quantum-mechanical, *i.e.*, first-principles or *ab initio*, methods. However, the accuracy and reliability of the classical results depend greatly on the quality of the potential parameters used. Typically, the potential parameters are fitted

or optimised to reproduce the properties of the perfect lattice, *e.g.*, lattice energy, lattice parameters, elastic constants or phonon dispersion curves; therefore, the fitted potential parameters can solely provide information for interatomic (or interionic) distances close to the equilibrium values and in highly symmetric materials, and cannot adequately describe the interactions at distances far from those sampled in the model systems, for example, in crystals at high pressures and/or high temperatures or in defective crystals and at surfaces.^{10,11} Furthermore, the classical simulation cannot probe the properties related to the electronic structure or other quantum mechanical effects. More importantly, classical simulations cannot be used to model chemical reactions; hence, the much more expensive quantum-mechanical methods are the only choice for those cases.

In this thesis, we will present the applications of various advanced atomistic modelling techniques to investigate (i) the defect thermodynamics in crystalline solids and clusters, (ii) the trace-element partitioning in solid minerals and melts and (iii) the temperature variation of the rates of activated processes in solid-state materials. Beyond this point, we will introduce the necessary general ideas and emphasise the importance of the computational studies of (i)-(iii) in several modern scientific research areas.

1.1.1 Defects in Crystals

Defects or imperfections play a vital role in characterising the physical and chemical properties of crystalline solids. In terms of statistical thermodynamics, any synthesised solid-state crystal always has a certain amount of defects in its structure at equilibrium above absolute zero. Strictly speaking, there is no completely perfect crystal. A number of studies show that the bulk, electronic, optical, and thermoelectric properties of solids depend greatly on the existence of such defects even though they are present in small amounts.¹² In our modern world, a number of ground-breaking innovations such as solid-state batteries, computer hardware, and fuel cells are all involved with the well-developed theories and in-depth understanding of defects in inorganic solids.

Generally, a defect in a crystal can be identified as either intrinsic or extrinsic. As the names imply, an intrinsic defect occurs with no change of solid composition, while an extrinsic defect involves the insertion of foreign atoms (or dopants) into the crystal lattice. Defects can also be categorised into different classes based on their dimensional characteristics. In the present work, however, we focus solely on defects which occur only right at (or around) a single lattice point and are so-called point defects. More general discussion of defects in crystals can be found in the widely used textbooks by Stoneham¹³ and Tilly,¹² for instance.

The thermodynamic properties of defects are essential to understanding their behaviour. For instance, defect formation energy can be used to estimate the equilibrium defect population, and migration energy can be used to predict the diffusivity and ionic conductivity.¹² These thermodynamic quantities, unfortunately, are not easily obtained via experiments. However, such parameters can conveniently be calculated using modern parallel computer codes running on state-of-the-art supercomputers.

For a few decades now, point-defect energies in ionic crystals – the majority of inorganic solids, have been extensively and comprehensively studied, resulting in a substantial insight into sophisticated defect phenomena in various chemical systems.³ Historically, the pioneering computational work in this field was performed using classical interatomic potentials as computers were not so powerful and there was a lack of well-developed codes at that time. Recently, however, much more advanced supercomputers and software engineering have made first-principles calculations become cheaper as a reliable and predictive tool for studying defects in solids. There are several recent publications on the topic and code developments. These include textbooks^{14–16} and critical review articles^{17–23} focusing on theoretical aspects of the *ab initio* simulation of point defects in various crystalline solids. Furthermore, practical tools for modelling point defects, *e.g.*, via first-principles methods and machine learning, have also been developed.^{24–27}

In addition, most calculations of point-defect thermodynamics in the past were performed based on static-lattice approaches, and the computation was carried out at constant volume in the static limit, *i.e.*, zero temperature is assumed and in the absence of lattice vibrations, for simplicity. These numerical results are often not useful as most of the experimental data have been obtained at constant pressure and elevated temperatures.²⁸ Therefore, simulation methods for evaluating temperature- and pressure-dependent defect free energies are needed in order to explore the impact of temperature and/or pressure on the calculated defect properties.

The calculation of point-defect free energies can be done in various ways. Direct methods, including molecular dynamics (MD) and Monte Carlo (MC), can be used. However, these approaches are very computationally expensive, especially for complex disordered solids. On the other hand, quasi-harmonic lattice dynamics based on lattice statics and the quasi-harmonic approximation can be used as an alternative, *i.e.*, valid up to two-thirds of the melting point, which are computationally cheaper for calculating the point-defect free energies.

1.1.2 Trace-Element Partitioning between Minerals and Melts

One of the challenging tasks for mineralogists and igneous geochemists is the understanding of how trace elements, whose concentrations are lower than 0.1% by weight, partition or distribute between two co-existing phases such as minerals and melts.²⁹ Trace-element distribution between minerals and melts is vital to several geochemical and industrial processes and an insightful understanding of trace-element partitioning controlling factors has implications for several processes, *e.g.*, the differentiation of the Earth and the management of radioactive waste.^{30,31} According to fundamental thermodynamics, a given trace element will have an equilibrium distribution between a mineral (solid) and melt, attaining equal chemical potentials in the co-existing phases. The partitioning behaviour of a particular trace element i in a given solid-state material equilibrated with its liquid melt can be described by a Nernst partition coefficient, D_i . The partition coefficient D_i quantifies the ratio of the amount of element i in the solid to that in the melt. For instance, the partitioning of two arbitrary elements A and B are considered in a given solid-melt mixture at equilibrium with the partition coefficients D_A and D_B , respectively. With $D_A > D_B$, this indicates that A is present at a higher concentration in the solid compared to B.

The variation of experimental partition coefficients with dopant size for an isovalent cation series at a given lattice site of a crystal of interest shows an approximately parabolic curve with a maximum occurring at an ionic radius close to the host cation. Such a partitioning curve is called an Onuma diagram.³² Previously, Blundy and Wood³³ proposed a lattice strain model by employing the expression of Brice³⁴ to explain the variation of experimental partition coefficients with ionic radius, *i.e.*, an Onuma curve. Although the simple strain model of Blundy and Wood³³ appears to explain well the Onuma curve for an isovalent series, describing strains using the expression of the Brice³⁴ model is found to be inadequate and oversimplified in terms of, *e.g.*, the incomplete description of lattice strains, the use of the fixed cation radii, the oversimplified assumption of the substitution mechanisms and the neglect of the role of melt species when explaining trace-element partitioning. However, computer simulation based on lattice statics enables us to uncover these serious limitations of the simple lattice strain model of Blundy and Wood.³³

1.1.3 Temperature Variation of Activated Processes in Solid-State Materials

Catalysis is one of the overarching aspects of modern chemistry, which plays a vital role in chemical and materials sciences. Catalysis involves directly the process of enhancing the rate of a chemical reaction by adding only a small amount of another chemical substance – a catalyst.³⁵ In general, catalysts accelerate chemical reactions by providing alternative pathways or reaction mechanisms with lower energy barriers than the uncatalysed pathways. Additionally, a chemical catalyst is not consumed and remains unchanged at the end of the reaction. Catalysis can be categorised into two types based on their phase separation, *i.e.*, homogeneous and heterogeneous catalysis in single-phase and multiple-phases systems, respectively.³⁶ For instance, enzyme catalysis belongs to the former, while solid-state inorganic catalysis belongs to the latter. The rate of the catalysed processes depends on several parameters, such as temperature.

According to the classical Arrhenius model, the rate of any catalysed reaction or process increases as the temperature increases.³⁷ However, this is not always the case for various complex chemical reactions due to several possible causes, *e.g.*, the change in the magnitude and number of low-frequency vibrational modes as an enzymatically catalysed reaction proceeds, the aggregation and denaturation or unfolding of enzymes, and reaching the transport or diffusion limit in a highly nanoporous inorganic catalyst. At high temperatures, most enzyme-catalysed reactions show decreases in their rates which is universally believed to be due to enzyme unfolding, and they can no longer accelerate the reactions. However, reaction rates catalysed by some cold-adapted enzymes are found to decrease at higher temperatures in the absence of denaturation, and this contrasts with a traditional explanation of this non-Arrhenius behaviour.³⁸

Macromolecular rate theory (MMRT) has been proposed to account for the deviation of the classical Arrhenius behaviour of those enzyme-catalysed reaction rates at high temperatures in the absence of enzyme denaturation or unfolding.³⁹ MMRT suggests that a negative change in the heat capacity of activation is the cause of the decrease in enzyme rate at elevated temperatures. In principle, a large negative change in heat capacity of activation reflects a very tight binding mode of the transition-state complex and a decrease in the number of conformational states (and/or fewer low-frequency vibrational and rotational modes) compared to those in the ground-state structure.³⁹ Several computational studies have been carried out to investigate the negative changes in heat capacity of activation of some enzymatic reactions.^{40–42} Using the MMRT concept,

modern scientists can understand the thermoadaptation of a *de novo* enzyme more fully and be able to design better enzymes for their purposes.^{43,44}

Catalytic activities of a zeolite occur at active catalytic centres within the cavity of its micro-sized pores, similar to those occurring within the active site of an enzyme structure. Within micron-sized voids in a zeolite framework, as a chemical reaction proceeds, the transition-state complexes and reactive transient species are stabilised via van der Waals and electrostatic interactions to decrease the activation energy.⁴⁵ These stabilisation effects affect the catalytic performance of the zeolitic framework directly. Hence, zeolites could be viewed as rigid variants of enzymes used for industrial purposes involving physical and chemical processes at high temperatures.⁴⁶ Based on similarities with enzyme catalysis, novel functional zeolitic materials have successfully been designed and synthesised by mimicking enzyme structures.^{47,48} In this regard, there are strong parallels in materials and inorganic chemistry, *i.e.*, heterogeneous catalysis, which still need to be explored based on the MMRT approach, as is explored in this thesis.

For instance, many zeolite-catalysed reaction rates show deviations from the Arrhenius behaviour in which the reaction rates are lower than expected at high temperatures and these phenomena have traditionally been explained by either the diffusional controls,^{49–51} the structural deformation (or the deactivation of the catalytic centres)^{51–54} or kinetic effects in different temperature regions.^{55–57} However, several studies state clearly that there is no direct evidence of the decrease in zeolite-catalysed reaction rate at high temperatures;^{52,53,58,59} thus, the non-Arrhenius behaviour of those zeolitic rates might be the direct consequence of negative changes in heat capacity of activation, as MMRT suggests. Theoretically, state-of-the-art computational simulations should also be employed to reveal these interesting phenomena.

1.2 Thesis Outline

In Chapter 2, we outline all the general theories, computational methods, and software packages used in this thesis. Chapter 3 focuses particularly on the investigation of the temperature and finite-size effects on the defect free energies in crystalline solids via classical and *ab initio* computer simulation based on lattice statics and quasi-harmonic lattice dynamics. In Chapter 4, we first discuss simple geological models for explaining the experimental partitioning data. Then, we review fundamental thermodynamic approaches before discussing the use of simple lattice strain models for studying the incorporation of trace elements into minerals and melts. We then explore the limitations

of the simple lattice strain model of Blundy and Wood³³ theoretically through classical and *ab initio* simulations based on lattice statics. In Chapter 5, we explore the possible factors that can give rise to the deviation of Arrhenius-like behaviours in solid-state inorganic catalysis based on the concept of macromolecular rate theory. We will show the calculations of temperature-dependent free energies of activation and diffusivity for diffusion processes in MgO and zeolites using various computer simulation techniques based on both classical and *ab initio* density functional theory approaches, including quasi-harmonic lattice dynamics, molecular dynamics and metadynamics. Finally, Chapter 6 summarises the results of all the thesis chapters individually and draws general conclusions from those results before discussing future work.

THEORY AND METHODS

Both the extraordinary high performance of modern computers and the recent advances in software engineering enable us to study theoretically the properties of various chemical systems, ranging from small isolated molecules to highly-complex systems, *e.g.*, biological macromolecules and solids. This chapter focuses particularly on the computational techniques for modelling solid-state materials. Here, we list all the general theories, computational methods, and software packages used in this thesis.

2.1 Computational Methods for Solid-State Modelling

Up to date, state-of-the-art modelling methods have successfully been applied to study computationally the properties and behaviours of various types of solid-state materials. For instance, computer simulation can be used for predicting crystal structures,¹ investigating the nature of chemical bonding and electronic properties in solids,² modelling defects in crystals,^{3,4} modelling solid surfaces and interfaces,⁵ modelling sorption processes,⁶ studying transport processes of atoms and molecules in solids,⁷ simulating nano-structures,^{8,9} and so on. In this thesis, as we are particularly interested in the applications of computational methods for investigating the defect formation and diffusion processes in several types of crystalline solids, some key papers are important for designing the methodologies used in this study and are worth mentioning. For instance, the classical and first-principles theoretical frameworks and computational

techniques for studying the properties of point defects in crystalline solids have previously been reviewed by Catlow and Mackrodt,⁶⁰ Harding,³ Taylor *et al.*⁶¹ and Bredow and co-workers.⁴ Additionally, several previous studies including Catlow *et al.*,⁶² Jobic and Theodorou,⁶³ O'Malley and co-workers,^{7,64} outline comprehensively the atomistic modelling methods for simulating the diffusion processes of guest (adsorbed) molecules in highly-porous zeolitic materials. These critical studies have been selected as the reference and starting point for designing the computational methods used in our present work.

There are numerous computational methods available that cover several orders of magnitude of time- and length-scale. Computational techniques for solid-state modelling can be categorised into two categories: (i) classical or potential-based and (ii) quantum mechanical approaches. Potential-based methods use analytical expressions for the interaction potential energies between the particles, *e.g.*, atoms or ions, in the solid of interest. Empirical variables in those expressions, *i.e.*, classical force fields, can be parameterised by fitting to the results of either experimental observations or highly accurate quantum mechanical calculations. These empirical potentials can be used in simulation methods including classical energy minimisation (also known as molecular mechanics, MM), lattice dynamics, molecular dynamics (MD) and Monte Carlo (MC) techniques. In contrast, first-principles quantum mechanical (or *ab initio*) methods are more accurate which solve directly the Schrödinger equation to attain the energy of a particular molecular or periodic system without the use of empirical interatomic potentials. All chemical problems in atomic-level modelling should ideally be solved using quantum mechanical approaches to calculate the wavefunction and the energy of the system of interest. However, *ab initio* methods are much more computationally expensive than potential-based techniques and these methods are solely limited to systems involving smaller numbers of atoms. Therefore, there is an unavoidable trade-off between accuracy and speed when choosing the appropriate modelling methods.

There are several excellent general textbooks on the simulation techniques in computational chemistry available, *e.g.*, by Leach,⁶⁵ Cramer,⁶⁶ Jensen,⁶⁷ and Harvey.⁶⁸ Details on computational techniques for materials modelling can be found in Catlow,⁶⁹ Deák *et al.*,⁷⁰ Allan,¹¹ and Dronskowski and Hoffmann,⁷¹ for instance. In this section, we aim to provide a brief overview of computational methods and their applications in materials modelling. We first begin this section with potential-based methods, the computationally cheapest approach and most appropriate for modelling chemical systems involving large numbers of constituent atoms, and then discuss the first-principles quantum mechanical

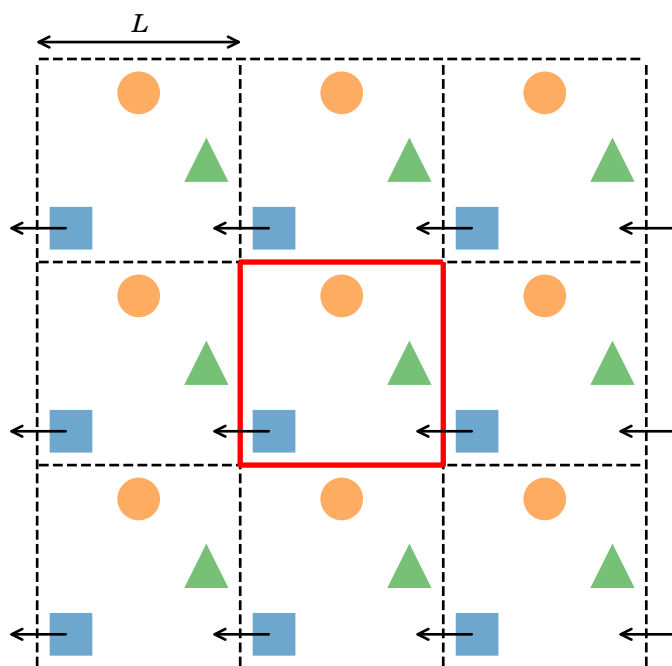


FIGURE 2.1. Schematic illustration of a cubic simulation box or a cubic unit cell (marked by the red square) with a cell length of L for a three-dimensional periodic system using periodic boundary conditions.

methods, the much more computationally expensive approach appropriate for systems consisting of smaller numbers of atoms.

2.1.1 Periodic Boundary Conditions

For modelling a bulk liquid or solid (large infinite system), *e.g.*, in molecular dynamics (MD) or lattice statics simulations, a simulation box can be constructed by making replicas of the smaller original simulation box containing the atoms or molecules of interest, *i.e.*, the unit cell, throughout three-dimensional space to avoid an unwanted interface at each side. This approximation uses periodic boundary conditions, which is schematically illustrated in Figure 2.1. When a particular particle exits the box through one of the faces, its image enters to the opposite face. With these periodic boundary conditions (PBC), the total number of constituent particles is conserved.

2.1.2 Classical Interatomic Potentials

In potential-based methods (also known as force-field methods), the electronic motion is not explicitly taken into account. The energy of a system is calculated as a function of the nuclear (atomic) positions only, *i.e.*, making the Born-Oppenheimer approximation. In this approach, a given system, *e.g.*, a molecule, liquid or solid, is comprised of a set of interacting spheres whose motions obey the laws of classical rather than quantum mechanics. The classical methods do not provide any information concerning chemical bonding, reaction pathways, charge transfer or other properties related to electronic properties. However, these details are not often required for calculating thermodynamic properties. Highly accurate potentials describing the interatomic interactions can thus provide much faster access to accurate results comparable with those of the higher-level first-principles methods.

For a given periodic system comprised of N atoms, *e.g.*, constructed by a unit cell with periodic boundary conditions, as illustrated in Figure 2.1 and discussed in Section 2.1.1, the classical potential energy, Φ , can be written as a sum of various many-body interaction potentials, ϕ 's, as follows:

$$\Phi = \sum_{i<j}^N \phi_{ij} + \sum_{i<j<k}^N \phi_{ijk} + \sum_{i<j<k<l}^N \phi_{ijkl} + \cdots, \quad (2.1)$$

where each of the subscript labels denotes a given atom. The three terms on the right-hand side of equation (2.1) are two-body, three-body and four-body potentials, respectively. The contribution from higher-order terms is expected to become progressively smaller for most systems; hence, those higher-order terms are negligible and the degree of empirical parameterisation is determined by only the first few terms remaining. For instance, the three-body and four-body interactions are often neglected for modelling polar solids, while omitting these terms leads to poor results for semiconductors and metals (see, *e.g.*, Sutton⁷² for further details).

One possible expression of the interaction potential for a given molecular solid consisting of discrete molecules can be written as

$$\begin{aligned} \Phi = & \sum_{\text{bonds}} \frac{k_r}{2} (r - r_0)^2 + \sum_{\text{angles}} \frac{k_\theta}{2} (\theta - \theta_0)^2 + \sum_{\text{torsion angles}} \frac{k_\omega}{2} (1 + \cos(n\omega - \xi)) \\ & + \sum_{i<j}^N \frac{q_i q_j}{4\pi\epsilon_0 r_{ij}} + \sum_{i<j}^N 4\epsilon_{ij} \left[\left(\frac{\sigma_{ij}}{r_{ij}} \right)^{12} - \left(\frac{\sigma_{ij}}{r_{ij}} \right)^6 \right]. \end{aligned} \quad (2.2)$$

The first three interaction potential terms on the right-hand side of equation (2.2) define the intramolecular interactions. The first two-body harmonic potential term involves

the summation over all pairs of directly bonded atoms within the molecules. k_r is the force (spring) constant of each bond and r_0 is the equilibrium bond length. Similarly, the second term is the three-body harmonic potential for all triplets of bonded atoms in the molecules with the spring constant k_θ and the equilibrium bond angle θ_0 . The third term, on the other hand, is the four-body potential describing the rotation about the bonds in the molecules, *i.e.*, torsion or dihedral angles. For a quartet of bonded atoms, ω is the torsion angle, k_ω is the force constant, n is a constant defining the periodicity of rotation, and ξ is a phase factor.

The last two terms on the right-hand side of equation (2.2) are the long-range electrostatic (Coulombic) and van der Waals potentials, respectively. q_i and q_j are the ionic charges and ϵ_0 is the vacuum permittivity in the long-range Coulombic term, while ϵ_{ij} and σ_{ij} are constants defining the van der Waals potential in the last term. In both terms, r_{ij} is the interatomic distance of atoms i and j . For periodic ionic solids, special numerical techniques, *e.g.*, the Ewald method, are required to compute the overall long-range electrostatic potential (see Leach,⁶⁵ Cramer,⁶⁶ and Jensen⁶⁷ for more details). The final term is the widely-used 12-6 Lennard-Jones function chosen for representing the van der Waals interactions between pairs of non-bonded atoms. As directional bonding is largely absent in many polar solids, only the two-body interactions are taken into account, whereas the three-body and four-body terms are often omitted. Hence, the two-body interactions U_{ij} in equation (2.1) between any ion pair i and j is the sum of the Coulombic and van der Waals terms:

$$\phi_{ij} = \frac{q_i q_j}{4\pi\epsilon_0 r_{ij}} + \phi_{\text{vdW}}(r_{ij}). \quad (2.3)$$

There are various functional forms for the van der Waals terms, *e.g.*, the 12-6 Lennard-Jones potential in equation (2.2). Another common alternative is the Buckingham potential form, where the r^{-12} term is replaced by an exponential:

$$\phi_{\text{Buck}} = A \exp\left(-\frac{r_{ij}}{\rho}\right) - \frac{C}{r_{ij}^6}, \quad (2.4)$$

where A , ρ and C are constants. Additional terms for the electronic polarisation effect of each atomic type can also be included, *e.g.*, using the shell model.⁷³ When evaluating the energy of very large systems, the pairwise energy for two atoms that are very far from each other vanishes. For that reason, cutoffs in potentials are needed in order to lessen the computation time.

The quality and accuracy of any set of interatomic potential or force field parameters depend essentially on the assignment of both atomic or ionic charges for individual

constituents and the values (*i.e.*, constants) chosen for the parameters in the various functional forms. There are two possible approaches to obtain these parameters: (i) by fitting to experimental quantities, *e.g.*, observed lattice constants, bond lengths, bond angles, vibrational spectra, and heat of formation, and (ii) by fitting to potential energy landscapes generated by high-level *ab initio* methods. A key requirement of any set of potential parameters is its transferability when modelling more complex systems outside the range of structural properties, *e.g.*, interatomic distances, used in the fitting procedure, especially in defect calculations, surfaces or interfaces calculations, lattice dynamics and molecular dynamics simulation at a wide range of temperatures and/or pressures. For instance, the empirical fitting is useful to construct transferable potentials derived from binary oxides for ternary systems.^{74,75} However, solely the second approach, *i.e.*, fitting to first-principles data, can provide those potential parameters when there are no relevant experimental data available.

2.1.3 Energy Minimisation

The main goal of energy minimisation is to find the minimum point on the potential energy surface of a given structure. Energy minimisation allows the prediction of the likely structure for a given molecule (or solid) that can have multiple stable structures (or phases). In pharmaceutical molecular modelling, energy optimisation based on classical force fields is often referred to as molecular mechanics (MM).

2.1.3.1 Lattice Statics

In lattice statics simulations, vibrational contributions are not taken into account; hence the ‘*internal*’ lattice energy U is equal to Φ and these two quantities are interchangeable in static-limit calculations. Such energy minimisations provide the crystal structure and the corresponding lattice energy. In the static limit, *i.e.*, at absolute zero and zero pressure, the optimised crystal structure is determined by

$$\frac{\partial U}{\partial Z_i} = \frac{\partial \Phi}{\partial Z_i} = 0, \quad (2.5)$$

where Z_i are all the parameters that define the crystal structure, *i.e.*, the lengths of the three lattice constants, the three angles between the three lattice vectors, and the atomic positions in the unit cell. Various fast and efficient energy-minimisation algorithms have been developed and there is a vast literature on this topic (see, *e.g.*, Leach,⁶⁵ Schlegel,⁷⁶ and Jensen⁶⁷ for more details).

Energy minimisation (or structural/geometry optimisation) can either be carried out at constant volume or constant pressure. At constant volume, energy minimisation is undertaken with invariant cell dimensions, *i.e.*, keeping all six lattice parameters fixed. Hence, the set of structural parameters Z comprises only the atomic positions in the simulation cell. On the other hand, both lattice parameters and atomic positions are simultaneously varied during constant-pressure minimisation. In the literature, Φ or U is, in principle, expressed as a function of external or macroscopic (η_λ) and internal or microscopic (ε_k) strains due to the six lattice parameters and atomic coordinates, respectively. The internal strains ε_k can simply be treated as thermodynamic parameters on the same footing as the external strains η_λ comprising a set of strain variables \mathcal{E}_A .^{77,78}

To perform constant-pressure energy minimisation in the static limit at a finite external pressure P_{ext} , the enthalpy $H = U + P_{\text{ext}}V$ is minimised with respect to all structural parameter Z_i instead, where V is the volume. Note that $H = U$ when $P_{\text{ext}} = 0$. Energy minimisations at finite temperatures, on the other hand, can be carried out in several ways. The first approach is to perform direct calculations through Monte Carlo (MC) or molecular dynamics (MD) simulations which will be discussed later. However, these methods cannot evaluate free energies (the Helmholtz and Gibbs energies) accurately as they do not sample high-energy regions of phase space adequately. Second, lattice dynamics simulation can alternatively be used to incorporate the vibrational (or thermal) contributions to lattice statics which gives absolute free energies and their derivatives directly. The latter approach is much computationally cheaper than the former direct simulation approaches. Such lattice dynamics simulation can be performed via the quasi-harmonic approximation (QHA), for instance.

2.1.3.2 Quasi-Harmonic Lattice Dynamics (QHD)

Within the quasi-harmonic approximation (QHA), the key assumption is that the Helmholtz energy A of a system at a given temperature T is expressed as the sum of static and temperature-dependent vibrational energies:

$$A(Z, T) = \Phi_{\text{stat}}(Z) + A_{\text{vib}}(Z, T), \quad (2.6)$$

where Φ_{stat} is the static potential energy of the lattice, and A_{vib} denotes the sum of harmonic vibrational contributions from all the normal modes in a given state with a set of all the structural parameters, Z . Traditionally, static lattice calculations involve solely Φ_{stat} and the vibrational term A_{vib} is completely neglected. For a periodic lattice

structure, A_{vib} at a given temperature T is given by

$$A_{\text{vib}} = \sum_{\mathbf{k}, i} \left(\frac{1}{2} h \nu_i(\mathbf{k}) + k_{\text{B}} T \ln \left\{ 1 - \exp \left[-\frac{h \nu_i(\mathbf{k})}{k_{\text{B}} T} \right] \right\} \right), \quad (2.7)$$

where h and k_{B} are the Planck and Boltzmann constants, respectively. $\nu_i(\mathbf{k})$ denotes the harmonic frequencies of modes i with a wave vector \mathbf{k} which can be obtained by diagonalising the dynamical matrix $D(\mathbf{k})$.⁷⁹ The first term on the right-hand side is called the zero-point energy. The evaluation of the sum over all the wave vectors \mathbf{k} is achieved by taking successively finer uniform grids in reciprocal space, *i.e.*, in the Brillouin zone, until convergence.⁸⁰

For a given periodic structure, the free energy obtained using equation (2.6) is a function of the structural parameters, *i.e.*, the six lattice parameters (three lattice vectors and three angles) as the external degrees of freedom and the atomic positions within the unit cell as the internal degrees of freedom. In other words, the Helmholtz energy (and also the static lattice energy) is, of course, a function of both external or macroscopic (η_{λ}) and internal (ε_k) strains. The equilibrium periodic structure under an external pressure P_{ext} can be obtained by minimising the availability (or the Gibbs energy G) $\tilde{A} = A + P_{\text{ext}} V$ with respect to all the strain parameters.⁸¹ \tilde{A} (or G) reduces to the ordinary Helmholtz energy A when $P_{\text{ext}} = 0$.

Derivatives of the free energy with respect to the geometrical variables are essential for performing the structural optimisation through direct free-energy minimisation. Unlike static energy derivatives, which are not difficult to compute analytically,⁸² free-energy derivatives are less straightforward. However, the analytic expressions for derivatives of the free energy can be obtained using first-order perturbation theory applied to the dynamical matrix.^{61,79,83,84} For large cells, the free-energy derivatives can be approximated using the computationally cheaper and less accurate approaches, for example, (i) the zero static internal stress approximation (ZSISA)⁸⁵ which yields correct cell parameters to the first order, and (ii) the constant internal strain parameter approximation (CISPA).⁸⁶ Furthermore, the vibrational entropy S_{vib} can also readily be evaluated and its explicit expression can be written as

$$S_{\text{vib}} = \sum_{\mathbf{k}, i} \left(\left\{ \frac{[h \nu_i(\mathbf{k})/T]}{\exp[h \nu_i(\mathbf{k})/k_{\text{B}} T] - 1} \right\} - k_{\text{B}} \ln \left\{ 1 - \exp \left[-\frac{h \nu_i(\mathbf{k})}{k_{\text{B}} T} \right] \right\} \right). \quad (2.8)$$

As mentioned earlier, this computational method is much computationally cheaper compared to classical molecular dynamics (MD) and Monte Carlo (MC) simulations for free energies, and is often found to be valid up to approximately two-thirds of the melting

point. It has successfully been used to study theoretically the free energies of different types of crystals at high pressures and temperatures.^{87–89} For this reason, the quasi-harmonic lattice dynamics is a powerful tool as an alternative technique to classical molecular dynamics and Monte Carlo simulations for studying the free energies of solids. The direct free-energy minimisation of periodic structures has well been implemented in several computational codes, *e.g.*, SHELL,⁹⁰ and GULP.⁹¹ This enables the programs to perform a full minimisation of the free energy with respect to all external strains and internal coordinates using the quasi-harmonic approximation for large unit cells with a large number of strains. Free-energy minimisation is, however, more computationally expensive than static calculations.⁶¹

2.1.4 Molecular Dynamics

Molecular dynamics is a powerful computer simulation method used for computing the equilibrium and transport properties of many-body systems. The method was invented by Alder and Wainwright.⁹² For many decades now, the simulation technique has successfully been used in many scientific disciplines including, *e.g.*, materials science, biology, geochemistry, and chemical kinetics.

2.1.4.1 Brief Overview of Statistical Mechanics

Statistical mechanics (also often referred to as statistical thermodynamics) studies the macroscopic properties of large many-body systems by investigating their microscopic behaviour. Those large systems are comprised of a large number of degrees of freedom, *i.e.*, the (atomic) positions and momenta. Sometimes, spins (or magnetic moments) are also taken into account. ‘*Phase space*’ is the space spanned by those degrees of freedom and each of the points in phase space is represented by a particular configuration of the system.

The average of a given property Q of a many-body system with a constant number of particles N at constant temperature T and volume V , *i.e.*, the canonical (NVT) ensemble, is given by the ensemble average $\langle Q \rangle$:

$$\begin{aligned}\langle Q \rangle_{NVT} &= \int Q(Z)P(Z) \, dZ, \\ P(Z) &= \frac{\exp(-U(Z)/k_B T)}{\int \exp(-U(Z)/k_B T) \, dZ},\end{aligned}\tag{2.9}$$

where Z is all possible states of the system, $Q(Z)$ is the system's property of interest as a function of Z , $P(Z)$ represents the Boltzmann weighted probability, and $U(Z)$ is the internal energy.

2.1.4.2 Integrating the Equations of Motion

Molecular dynamics (MD) involves the study of the physical movements or dynamics of atoms and molecules in a given many-body system by solving Newton's equations of motion numerically. A simple numerical procedure of a classical MD simulation is shown as follows.

In the microcanonical ensemble (NVE), *i.e.*, the periodic system represented by a unit cell (see Section 2.1.1) with a constant number of particles (N), at constant volume (V) and conserved energy (E), the initial positions and velocities of all the particles in the simulation box are assigned by \mathbf{x}_i and \mathbf{v}_i , respectively. Velocities \mathbf{v}_i are distributed via a Maxwellian distribution for a given temperature. The force acting on each particle \mathbf{f}_i is then computed using the interatomic potentials. A time step Δt , during which the forces \mathbf{f}_i are kept constant, needs to be specified for updating the positions \mathbf{x}_i and velocities \mathbf{v}_i by solving Newton's equations of motion. The choice of time step is vital for a molecular dynamics simulation. The largest time step that can be used is determined by the process that has the fastest rate in the system of interest. In other words, the time step must be smaller than the time scale of the dynamical process(es) of interest. For example, molecular motions, including vibrations and rotations, occur typically in the frequency range $10^{-11} - 10^{-14} \text{ s}^{-1}$; therefore, time steps of the order of femtoseconds (10^{-15} s) or less are required to capture those molecular motions with sufficient accuracy.⁶⁵

In each of the integration steps, the Leapfrog Verlet algorithm can be used to integrate the equations of motion as follows:

$$\begin{aligned}\mathbf{v}_i(t + \frac{\Delta t}{2}) &= \mathbf{v}_i(t - \frac{\Delta t}{2}) + \frac{\mathbf{f}_i}{m_i} \Delta t, \\ \mathbf{x}_i(t + \Delta t) &= \mathbf{x}_i(t) + \mathbf{v}_i(t + \frac{\Delta t}{2}) \Delta t,\end{aligned}\tag{2.10}$$

where m_i is the atomic mass. Alternative algorithms for integrating the equations of motion can also be employed, *e.g.*, the Velocity Verlet method. The integration step is repeated many times until the system properties, *e.g.*, temperature (T) and pressure (P), reach their equilibrium values and do not vary significantly with further time steps. For instance, the instantaneous simulation temperature is obtained by the sum of the kinetic

energies over all the particles in the system:

$$\frac{3}{2}Nk_{\text{B}}T = \frac{1}{2} \sum_{i=1}^N m_i v_i^2. \quad (2.11)$$

After the equilibration stage, the simulation is continued repeatedly in the production stage. The coordinates and velocities (sometimes forces) of all the particles at successive time steps are recorded in the MD trajectory.

Properties of interest, *e.g.*, the mean-square displacement (MSD) of a particle from its starting position, $\langle r^2 \rangle$, can be obtained from a trajectory analysis. The linearly time-dependent MSD can be used to compute the self-diffusion coefficient (D_{s}): $\langle r^2 \rangle = 6D_{\text{s}}t$. Similar approaches to the above technique can be used in MD simulations in other ensembles, *e.g.*, the canonical (NVT) and isothermal-isobaric (NPT) ensembles. Further details can be found in Frenkel and Smit⁹³ and Allen and Tildesley.⁹⁴

2.1.5 Metadynamics

Metadynamics is a simulation technique used to enhance sampling in ordinary molecular dynamics simulations and reconstruct the free-energy profile as a function of a set of selected structural parameters, *i.e.*, collective variables (CVs), which was first proposed by Laio and Parrinello.⁹⁵ In classical molecular dynamics simulations, the results are meaningful only if the run is long enough for the system to visit (or sample) all the energetically available configurations, *i.e.*, the ergodic hypothesis is obeyed.⁹⁶ However, the relevant configurations might be separated by high free-energy barriers and the transitions between distinct metastable states can be difficult. In addition to the scope of molecular dynamics simulations, where metadynamics enables the possibility to accelerate conformational transitions between different metastable states, approximate the transition-state structures and estimate the relative free energies of complex molecular systems.⁹⁷ Further details of the applications and development progress of the metadynamics technique can be found in Barducci *et al.*,⁹⁶ Sutto *et al.*⁹⁸ and Tiwary and Parrinello.⁹⁹

In each metadynamics run, sampling the space of CVs is enhanced (accelerated) by a history-dependent bias force (or potential) that acts on a set of the CVs, S . Strictly speaking, an external history-dependent bias potential as a function of the CVs is repeatedly added to the total energy of the system. This bias potential can be given by the sum of Gaussians deposited in the CVs space along the MD trajectory to reduce the chance of sampling the configurations that have already been visited. An overview of the basic theory of metadynamics is briefly discussed below.

In order to perform a metadynamics calculation, a meaningful set of collective variables S for distinguishing different steady and transition states must first be defined. At simulation time t , the bias potential can be written as

$$V(S, t) = \int_0^t dt' \omega \exp \left(- \sum_{i=1}^n \frac{(S_i(Z) - S_i(Z(t')))^2}{2\sigma_i^2} \right), \quad (2.12)$$

where ω is a constant and typically expressed as the ratio of a Gaussian height W to a deposition stride τ : $\omega = W/\tau$. σ_i refers to the Gaussian width for the i^{th} CV. The two parameters W and σ_i define the shape of the Gaussians, *i.e.*, the extra bias, added at time intervals of the deposition stride τ . In practice, the parameters W , τ and σ are determined *a priori* and kept constant during the metadynamics simulation. Using large Gaussians, the free-energy surface will rapidly be explored at a fast pace, but the reconstructed free-energy profile will poorly be characterised by large fluctuations.^{96,97,100} Therefore, the speed-accuracy trade-off needs to be first considered by examining and testing the suitable values of those user-defined parameters when performing the metadynamics simulations for the system of interest.

After a long enough simulation time, *i.e.*, when the motion of the S becomes diffusive in the domain of interest, the bias potential V gives an estimated free energy as a function of S :

$$V(S, t \rightarrow \infty) = -F(S) + C, \quad (2.13)$$

where C is a constant and the free energy $F(S)$ is given by

$$F(S) = -\frac{1}{\beta} \ln \left(\int dZ \delta(S - S(Z)) \exp(-\beta\Phi(Z)) \right), \quad (2.14)$$

where $\beta = (k_B T)^{-1}$, $\Phi(Z)$ is the potential energy function and δ is the Kronecker delta.

2.1.6 Quantum Mechanical Methods

Quantum mechanical methods (*aka* first-principles or *ab initio* techniques) involve the calculation of the ground-state energy of a many-body system of interest by solving the time-independent Schrödinger electronic wavefunction equation in which the nuclear positions are fixed, *i.e.*, within the Born-Oppenheimer approximation. The time-independent Schrödinger equation is written as

$$\hat{H}\Psi = E\Psi, \quad (2.15)$$

where the non-relativistic Hamiltonian operator \hat{H} in atomic units is given by

$$\hat{H} = -\frac{1}{2} \sum_i \nabla_i^2 - \sum_i \sum_\alpha \frac{q_\alpha}{|\mathbf{r}_i - \mathbf{d}_\alpha|} + \sum_i \sum_{j \neq i} \frac{1}{|\mathbf{r}_i - \mathbf{r}_j|} + \sum_\alpha \sum_{\beta \neq \alpha} \frac{q_\alpha q_\beta}{|\mathbf{d}_\alpha - \mathbf{d}_\beta|}. \quad (2.16)$$

In equation (2.16), \mathbf{r}_i and \mathbf{r}_j denote the electron positions, \mathbf{d}_α and \mathbf{d}_β represent the nuclear positions, and q_α and q_β are the nuclear charges. The four terms on the right-hand side of equation (2.16) represent the kinetic energy of the electrons, the nuclear-electron attraction, the electron-electron repulsion and the nuclear-nuclear repulsion, respectively. Finding the true wavefunction of a given many-body system is non-trivial. However, it can be represented by a simpler function; hence, making sensible approximations to the wavefunction is one of the main concerns of electronic structure theory.

The total energy of an approximate wavefunction Ψ is given by the expectation value of \hat{H} :

$$E = \frac{\int \Psi^* \hat{H} \Psi \, d\tau}{\int \Psi^* \Psi \, d\tau}. \quad (2.17)$$

The variational principle is one of the methods used to find the best approximate wavefunction Ψ that gives the lowest value of E in equation (2.17). As electrons are fermions, the many-body electronic wavefunction Ψ must obey the Pauli exclusion principle, *i.e.*, possess the right permutation symmetry. Hence, the electronic wavefunction changes sign when any pair of electrons are exchanged:

$$\Psi(x_1, x_2, \dots, x_i, \dots, x_j, \dots) = -\Psi(x_1, x_2, \dots, x_j, \dots, x_i, \dots), \quad (2.18)$$

where $x_i = \{\mathbf{r}_i, \sigma_i\}$ represents the spatial and spin coordinates of an electron i . According to the antisymmetry, no pair of electrons can possess the same set of quantum numbers.

2.1.6.1 Basis Sets

In order to approximate the solutions of the electronic Schrödinger equation (2.15), one needs to make the orbital approximation, *i.e.*, using a set of basis functions to represent the electronic wavefunction. The many-electron wavefunction Ψ can be approximated by the antisymmetrised product of single-electron wavefunctions (spin-orbitals) ψ_i 's:

$$\Psi(x_1, x_2, \dots, x_N) = \mathfrak{A} \prod_{i=1}^N \psi_i(x_i), \quad (2.19)$$

where \mathfrak{A} is the antisymmetrising operator. A more convenient way of writing equation (2.19) is to use a Slater determinant:

$$\Psi(x_1, x_2, \dots, x_N) = \frac{1}{\sqrt{N!}} \begin{vmatrix} \psi_1(x_1) & \psi_1(x_2) & \cdots & \psi_1(x_N) \\ \psi_2(x_1) & \psi_2(x_2) & \cdots & \psi_2(x_N) \\ \vdots & \cdots & \ddots & \vdots \\ \psi_N(x_1) & \cdots & \cdots & \psi_N(x_N) \end{vmatrix}. \quad (2.20)$$

The spin-orbitals are the products of spatial and spin functions, α and β :

$$\begin{aligned}\psi_i(x_i) &= \psi_i(\mathbf{r}_i)\alpha(\sigma_i), \text{ or} \\ \psi_i(x_i) &= \psi_i(\mathbf{r}_i)\beta(\sigma_i).\end{aligned}\tag{2.21}$$

In general, the spatial orbitals $\psi_i(\mathbf{r}_i)$ in equation (2.21) are approximately expanded in a basis set, *i.e.*, a linear combination either of atomic functions or plane waves, $\varphi(\mathbf{r})$:

$$\psi_i(\mathbf{r}) = \sum_{j=1}^{n_{\text{basis}}} c_{ij} \varphi_j(\mathbf{r}),\tag{2.22}$$

where c_{ij} 's are the orbital coefficients. Atomic pseudopotentials, *i.e.*, the simplified atomic orbital, can also be used for the core electrons.¹⁰¹ Given the trial wavefunction, *i.e.*, the Slater determinant (2.20), the energy can then be minimised using the variational principle with respect to the c_{ij} 's.

2.1.6.2 Plane-Wave Basis Sets

As mentioned earlier, the spatial orbitals $\psi_i(\mathbf{r})$ can either be a linear combination of atomic functions or plane-wave functions, $\varphi(\mathbf{r})$, in equation (2.22). For modelling infinite (extended) systems, *e.g.*, a unit cell within the periodic boundary conditions shown in Figure 2.1, the use of plane-wave basis functions, *i.e.*, functions with an infinite range, is more appropriate.⁶⁷ According to Bloch's theorem,¹⁰² the wavefunction $\psi_i(\mathbf{r})$ in equation (2.22) can be written as a product of a cell-periodic part and a wave-like part (φ):

$$\psi_i(\mathbf{r}) = e^{i\mathbf{k}\cdot\mathbf{r}} \varphi_i(\mathbf{r}),\tag{2.23}$$

where, \mathbf{k} is, again, the wave vector, and the kinetic energy of the electron, E_{kin} , depends quadratically on \mathbf{k} : $E_{\text{kin}} = \frac{1}{2}|\mathbf{k}|^2$. Due to the periodicity, $\varphi_i(\mathbf{r})$ can be expanded into a basis set of plane-wave functions:

$$\varphi_i(\mathbf{r}) = \sum_{\mathbf{G}} c_{i,\mathbf{G}} e^{i\mathbf{G}\cdot\mathbf{r}},\tag{2.24}$$

where \mathbf{G} are reciprocal lattice vectors and $c_{i,\mathbf{G}}$ are the plane-wave coefficients. Therefore, the electronic wavefunctions $\psi_i(\mathbf{r})$ is given by

$$\psi_i(\mathbf{r}) = \sum_{\mathbf{G}} c_{i,\mathbf{G}} e^{i(\mathbf{k}+\mathbf{G})\cdot\mathbf{r}}.\tag{2.25}$$

In a unit cell with a volume V , the number of wavefunctions used, N_{PW} , is thus determined by the highest energy wave vector \mathbf{k} included, defining the maximum kinetic energy, $E_{\text{kin}}^{\text{max}}$:

$$N_{\text{PW}} = \frac{1}{2\pi^2} V \sqrt{(E_{\text{kin}}^{\text{max}})^3}.\tag{2.26}$$

The quality of the basis sets for reconstructing the wavefunctions can be increased by increasing the $E_{\text{kin}}^{\text{max}}$ parameter, *i.e.*, the cut-off on the kinetic energy. Note that the size of a plane-wave basis set depends solely on $E_{\text{kin}}^{\text{max}}$ and the size of the unit cell, as shown in equation (2.26), not on the actual system described within the unit cell. Alternatively to the plane-wave functions, the basis set can be chosen as a set of nuclear-centred (or Gaussian) basis functions. However, the size for nuclear-centred basis functions increases linearly with actual system size; therefore, plane-wave basis sets become more suitable and more favourable for large extended systems. There are various famous codes for performing first-principles calculations based on plane-wave basis sets, *e.g.*, Quantum ESPRESSO^{103,104} and VASP.^{105–107} On the other hand, CRYSTAL17^{2,108,109} and CP2K¹¹⁰ can be employed to run *ab initio* simulations based on mixed nuclear-centred (or Gaussian type) and plane-wave basis sets. Further details of the plane-wave basis sets can be found in, for example, Leach⁶⁵ and Jensen.⁶⁷

2.1.6.3 Density Functional Theory (DFT)

Density functional theory (DFT) is the most popular electronic-structure calculation method for modelling large molecules and solids.¹¹¹ DFT is based on the Hohenberg-Kohn theorem, stating that the many-electron system's ground-state properties can be evaluated by minimising an energy functional $E[\rho]$ of the electron density $\rho(\mathbf{r})$.¹¹² The exact ground-state energy is the minimum value of $E[\rho]$ obtained when $\rho(\mathbf{r})$ is the exact ground-state electron density. Kohn and Sham¹¹³ later introduced the concept of a fictitious non-interacting system with the same electron density as the real system of interacting particles. Consequently, the electron density ρ can be expressed in terms of the single-electron wavefunctions ψ_i 's of the ideally non-interacting system:

$$\rho(\mathbf{r}) = \sum_{i=1}^N |\psi_i(\mathbf{r})|^2. \quad (2.27)$$

The energy functional $E[\rho]$ is thus given by

$$\begin{aligned} E[\rho] &= T_S[\rho] + V_{\text{nuc}}[\rho] + J[\rho] + E_{\text{xc}}[\rho] \\ &= -\frac{1}{2} \sum_{i=1}^N \int \psi_i^*(\mathbf{r}) \nabla^2 \psi_i(\mathbf{r}) \, d\mathbf{r} - \sum_{\alpha} \int \rho(\mathbf{r}) \frac{q_{\alpha}}{|\mathbf{r} - \mathbf{d}_{\alpha}|} \, d\mathbf{r} \\ &\quad + \frac{1}{2} \int \int \frac{\rho(\mathbf{r})\rho(\mathbf{r}')}{|\mathbf{r} - \mathbf{r}'|} \, d\mathbf{r} \, d\mathbf{r}' + E_{\text{xc}}[\rho]. \end{aligned} \quad (2.28)$$

On the right-hand side of equation (2.28), the first term gives the Kohn-Sham kinetic energy, the second represents the electron-nuclei interaction, the third is the Coulomb

energy and the last denotes the so-called exchange-correlation energy. The ground-state electron density and energy are obtained by minimising the total energy functional in equation (2.28) via the iterative self-consistent calculations for the ψ_i 's.

The exchange-correlation functional term E_{xc} is unknown; hence, approximate expressions must be used. The simplest form is the local-density approximation (LDA), where the expressions for a uniform electron gas density are employed. Various functional forms of the generalised-gradient approximation (GGA) consider the charge density gradient as well as the density itself.^{114,115} Amongst many variants of the GGA functionals, GGA-PBESol¹¹⁵ is specially designed for modelling bulk solids and their surfaces. GGA-PBESol is expected to yield the more accurate bulk, electronic, structural and other properties of several types of solids.¹¹⁶ Hybrid functionals, *e.g.*, B3LYP,^{117,118} use the combination of the Hartree-Fock exchange with DFT correlation and exchange. Greater details of the simulation techniques for modelling solid-state materials based on DFT can be found in, for instance, Hasnip *et al.*¹¹⁹ and Martin.¹²⁰

There are various DFT-based software packages for modelling solid-state materials and condensed matter such as VASP,^{105–107} Quantum ESPRESSO,^{103,104} CRYSTAL17,^{2,108,109} and CP2K.¹¹⁰ As mentioned earlier, calculations based on plane-wave basis sets can be performed using the VASP and Quantum ESPRESSO codes, while the mixed plane-wave and Gaussian-type basis sets are used in the CRYSTAL17 and CP2K. Those DFT software packages have their own merits and drawbacks in terms of performance and reliability.^{65,67,120} For performing first-principles simulations involving a wide range of atomic species, the availability of consistent sets of basis sets and atomic pseudopotentials is also crucial. For instance, the standard solid-state pseudopotentials (SSSP) library¹²¹ provides consistent sets of optimised atomic pseudopotentials for modelling solid-state materials using the open-source Quantum ESPRESSO software package.^{103,104} For those reasons, one should be aware of the suitability of the program(s) for modelling the systems of interest.

2.1.6.4 *Ab Initio* Molecular Dynamics (AMD)

The theoretical foundation of *ab initio* molecular dynamics (AMD) is similar to that of classical MD discussed earlier; however, instead of using classical force-field potentials, the energy and forces acting on the constituent atoms are obtained by solving the Schrödinger equation. The computer simulation based on AMD is computationally expensive and limited to small simulation cells and time scales of a few picoseconds. Within DFT, the Car-Parrinello MD (CPMD) method is a useful technique where the

dynamics of electrons and nuclei are carried out simultaneously.¹²²

2.1.7 Transition-State Optimisation

For a chemical reaction of interest, steady-state structures, *e.g.*, reactants and products, can be determined by locating minima on the potential energy surface (PES), *e.g.*, using equation (2.5). On the other hand, transition-state geometries can be obtained by searching for saddle points on the PES.^{65–67} Any position on the PES corresponding to a maximum in one direction and a minimum in all other directions is defined as a first-order saddle point. A second-order saddle point, on the contrary, corresponds to a maximum in two directions and a minimum in all other directions, and so forth. Various efficient numerical algorithms used for locating transition-state structures in periodic systems have been developed over recent years, such as nudged elastic band (NEB) and dimer methods,¹²³ and have been implemented in several *ab initio* and classical codes, *e.g.*, VASP,^{105–107} Quantum ESPRESSO,^{103,104} CP2K,¹¹⁰ and GULP.¹²⁴

2.2 Computer Modelling of Point Defects

There are two computational approaches for simulating solids containing point defects that are (i) the two-region approach or embedded-cluster model and (ii) the supercell method. The schematic illustration of these two models is shown in Figure 2.2. The former approach was initially proposed by Mott and Littleton.^{60,125} The latter approach, on the other hand, is commonly used to calculate the properties of crystalline solids in general.¹²⁶ These two approaches have their own merits and limitations.

In the two-region approach, the defective crystal is divided into two separate regions: (i) an inner region (I) which surrounds immediately the point defect and (ii) an outer region (IIb) which locates further away from the defect with an interface or in-between region (IIa). The total energy of the defective crystal is minimised by a relaxation of atomic positions around the point defect. In region I, atomic positions are allowed to be fully relaxed as the elastic force equations for forces acting on each of the atoms are explicitly solved. Thus, the lattice relaxation in this region is assumed to be greatest. On the other hand, the lattice relaxation in region II is assumed to be smaller and the elastic force equations are estimated using the Mott-Littleton approximation.¹²⁵ The total energy of the defective crystal E_{dc} is given by

$$E_{dc}(x, \Delta y) = E_1(x) + E_2(x, \Delta y) + E_3(\Delta y), \quad (2.29)$$

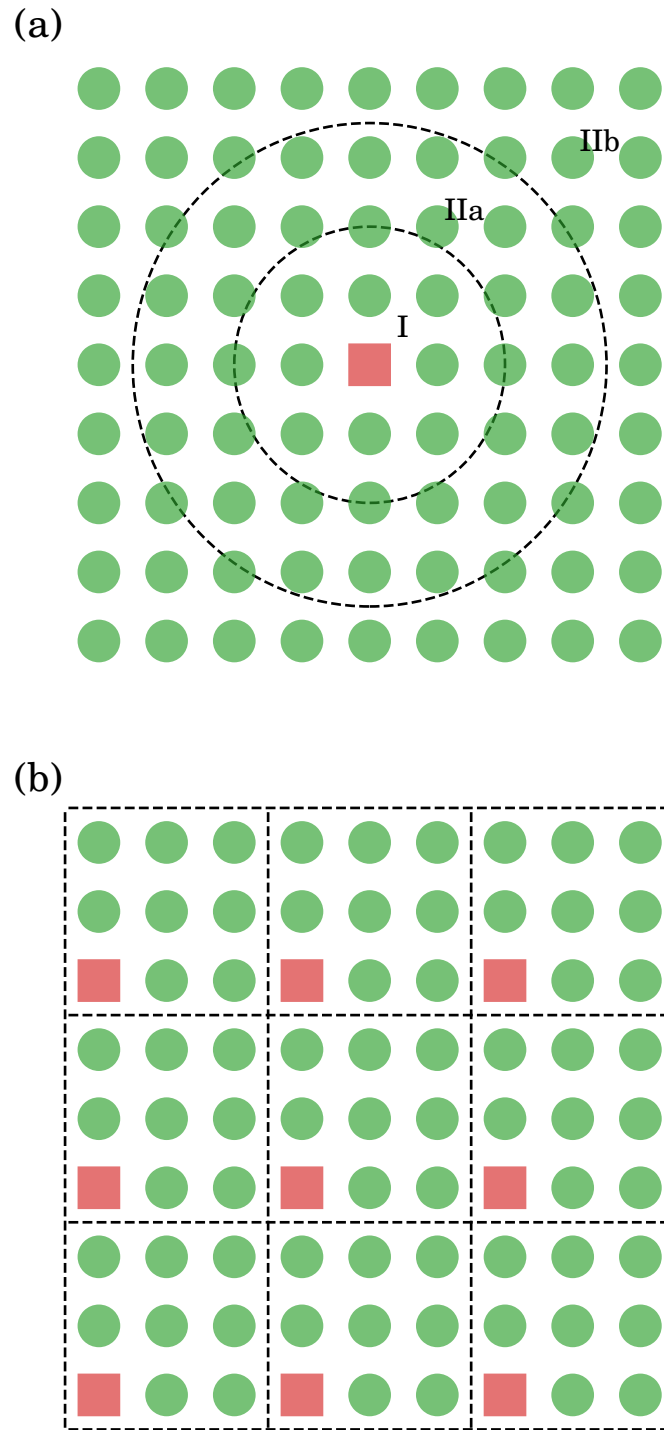


FIGURE 2.2. Two models for defect calculations: (a) two-region and (b) supercell approaches.

where x and Δy represent the atomic coordinates in region I and the atomic displacements in region II, respectively. The terms E_1 and E_3 arise from the interactions within each of the corresponding two regions while E_2 defines the interaction energy between them. The explicit dependence of E_{dc} on E_3 can be eliminated as E_3 can be expressed in terms of the derivatives of E_2 by assuming that E_3 is a quadratic function with respect to Δy together with the condition of $\partial E / \partial y = 0$ at equilibrium. The forces acting on each atom in region I is required to vanish to determine E_{dc} . Theoretically, the defect energy approaches its converged value as the size of region I is increased. Practically, there should approximately be 400-600 constituent atoms or ions in region I to ensure the convergence of E_{dc} with respect to the size of the inner region. The method is a computationally inexpensive approach¹²⁷ and is well implemented in, for example, the General Utility Lattice Program (GULP)⁹¹ which is one of the most widely used software packages for modelling solid-state materials based on classical force fields. However, one important limitation of this method is that the point-defect calculations can solely be done in the static limit as this approach is not able to perform simulations at elevated temperatures.

In the supercell approach, a superlattice of defects is extended repeatedly throughout the macroscopic crystal lattice after introducing a point defect into a perfect lattice. The symmetry of the crystal is completely removed due to the lattice distortion caused by the point defect. Strictly speaking, the equilibrium atomic positions within the crystal are not determined by its corresponding symmetry of the perfect lattice. In this approach, choice of the size of a unit cell or supercell used in a periodic defect calculation is important. If the supercell size is small, there will be a strong defect-defect interaction since the point defect is able to interact with other defects, *i.e.*, itself, in the neighbouring supercell images and the defect concentration in the crystal will be too high. Hence, one is expected to use bigger supercells to avoid these problems. Convergence towards the properties of an isolated point defect is expected as the supercell size or superlattice spacing is increased.

The supercell approach can be used to calculate defect free energies at a wide range of temperatures and pressures. For instance, the entropies and enthalpies of defect formations at finite temperatures and pressures can be evaluated directly, for instance, using the quasi-harmonic approximation. The optimised periodic structures can be obtained by the minimisation of either static energy or free energy of the system with respect to the structural variables. The latter approach is so-called the direct free-energy geometry optimisation. Furthermore, thermodynamic quantities at constant volume and

constant pressure can also be obtained independently in the supercell approach.

2.2.1 Defect Thermodynamics

In the supercell approach, the constant-pressure and constant-volume defect properties at constant temperature T can be computed separately, for instance,

$$\begin{aligned}
 g_p &= [G_{\text{dc}}(P, T) - G_{\text{pc}}(P, T)]/N_d, \\
 f_v &= [F_{\text{dc}}(V, T) - F_{\text{pc}}(V, T)]/N_d, \\
 s_p &= [S_{\text{dc}}(P, T) - S_{\text{pc}}(P, T)]/N_d, \\
 s_v &= [S_{\text{dc}}(V, T) - S_{\text{pc}}(V, T)]/N_d,
 \end{aligned} \tag{2.30}$$

where the subscripts ‘dc’ and ‘pc’ denote the defective and perfect crystals, respectively. The capital letters refer to absolute free energies (G and F) and entropies (S) of the corresponding macroscopic crystals. The subscripts ‘v’ and ‘p’ are used for the defect properties obtained at constant volume V or constant pressure P , respectively. N_d is the total number of point defects within the supercell. Constant-pressure quantities are obtained by allowing all the six lattice parameters to vary during the geometry optimisation as well as the internal coordinates. Constant-volume properties, on the contrary, are obtained by keeping all the lattice parameters fixed.

In addition to free energies and entropies in equation (2.30), changes in enthalpy and internal energy of the defect formation at constant pressure and constant volume can, respectively, be calculated by

$$\begin{aligned}
 h_p &= g_p + Ts_p, \text{ and} \\
 u_v &= f_v + Ts_v.
 \end{aligned} \tag{2.31}$$

The relations between the constant-pressure and constant-volume defect properties in the limit when $(v_p/V \rightarrow 0)$, where v_p refers to the defect volume change have previously been discussed.¹²⁸ The following relations are valid when the defect concentration is extremely small, *i.e.*, in the dilute limit. In this limit, one can obtain constant-pressure defect properties from the corresponding constant-volume quantities:

$$g_p = f_v \tag{2.32}$$

$$h_p = u_v + \left(\frac{\alpha T}{\beta_T} \right) v_p, \tag{2.33}$$

$$s_p = s_v + \left(\frac{\alpha}{\beta_T} \right) v_p, \tag{2.34}$$

where α and β_T are the volumetric thermal expansion coefficient and the isothermal compressibility, respectively. The first-order correction to the equation (2.32)⁶¹ is

$$f_v - g_p = \frac{1}{2} \left(\frac{v_p}{\beta_T} \right) \left(\frac{v_p}{V_{\text{supercell}}} \right), \quad (2.35)$$

and v_p itself is given by

$$v_p = \beta_T V p_v = -\beta_T V \left(\frac{\partial f_v}{\partial V} \right)_T, \quad (2.36)$$

where p_v refers to the change in pressure of the defect formation. The partial derivative $(\partial f_v / \partial V)_T$ on the right-hand side of the equation can be estimated by $(\partial u_v / \partial V)_T$.^{129,130}

2.2.2 Kröger-Vink Notation for Point Defects

For consistency, the Kröger-Vink notation¹³¹ for substitutional point defects is used throughout this work. Here, we summarise only briefly the convention. In NaCl structure, for instance, V'_{Na} and V^\bullet_{Cl} denote sodium-ion and chloride-ion vacancies with the corresponding final net charges of -1 (indicated by ') and +1 (indicated by \bullet), respectively. $\text{Ca}^\bullet_{\text{Na}}$ refers to a substitutional Ca^{2+} cation onto a Na^+ site leaving a net charge of +1 (\bullet). A superscript x indicates either a neutral substitution, *e.g.*, Au^x_{Ag} for the substitution of a Ag atom by a Au atom, or a defect formation with no effective charge, *e.g.*, Ba^x_{Mg} for the substitution of a Mg^{2+} ion by a Ba^{2+} ion. The symbol x is essentially useful for substitutional defects involving neutral (or non-ionic) species in order to avoid ambiguity.

2.3 List of Software Packages

2.3.1 GULP

The General Utility Lattice Program (GULP) is a molecular mechanics and molecular dynamics code designed for modelling a variety of materials based on classical force-field methods.⁹¹ The program provides a vast choice of empirical potentials. Apart from the ordinary static-energy geometry optimisation, the package can also perform the direct free-energy minimisation for both periodic and non-periodic structures.¹²⁴

2.3.2 DL_POLY4 and DL_Software

DL_POLY4 is a general purpose massively parallel classical molecular dynamics (MD) simulation package for modelling a variety of materials ranging from small molecules to

large systems.¹³² DL_FIELD is a support tool for converting force-field models and creating the input files (FIELD and CONFIG) for DL_POLY4.¹³³ DL_ANALYSER is a general tool for analysing the output files (*e.g.*, HISTORY and STATIS) from DL_POLY4.¹³⁴

2.3.3 CRYSTAL17

CRYSTAL17 is a general-purpose *ab initio* software package for studying the electronic structures and properties of crystalline solids, surfaces and molecular systems using Hartree-Fock, density functional theory and various hybrid methods.^{2,108,109} The QHA module implemented in CRYSTAL17 is particularly useful for performing *ab initio* free-energy minimisation.

2.3.4 Quantum ESPRESSO

Quantum ESPRESSO is an integrated suite of multi-purpose open-source software packages for electronic-structure calculations and materials atomistic modelling based on density functional theory (DFT), plane-wave basis sets and atomic pseudopotentials.^{103,104}

2.3.5 CP2K

CP2K is a quantum chemical software package for performing *ab initio* atomistic simulation of various chemical systems, including solid-state materials, liquids, molecules and isolate atoms.¹¹⁰ CP2K can perform various modelling methods, such as density functional theory (DFT) using the mixed Gaussian and plane-wave approaches (GPW and GAPW), semi-empirical methods, classical force-field based methods, and quantum mechanics/molecular mechanics (QM/MM) methods. CP2K can also perform *ab initio* molecular dynamics (AMD) simulation.

2.3.6 PLUMED

PLUMED is an open-source software package for performing free-energy calculations, enhanced-sampling molecular dynamics simulation, *e.g.*, metadynamics and umbrella sampling techniques.¹³⁵ PLUMED can be used as a tool for analysing the output files, *e.g.*, trajectories, produced by molecular dynamics (MD) simulations. PLUMED can be combined with various MD engines, including DL_POLY4, CP2K and Quantum ESPRESSO.

2.3.7 VASP

The Vienna *Ab initio* Simulation Package (VASP) is one of the most famous software packages for performing electronic-structure calculations of solid-state materials based on density functional theory (DFT) with various types of DFT functional forms, atomic pseudopotentials and plane-wave basis sets.^{105–107}

2.3.8 Structure Visualisers

The crystal and molecular structures in this work were edited and visualised using VESTA¹³⁶ and Avogadro.¹³⁷ Molecular dynamics (MD) trajectories were visualised and analysed by the Visual Molecular Dynamics (VMD) program.¹³⁸

DEFECT THERMODYNAMICS IN CRYSTALLINE SOLIDS AND CLUSTERS

In this chapter, we use computer simulation based on classical force fields and first-principles density functional theory (DFT) to investigate the temperature and finite-size effects on the free-energy of formation of substitutional point defects in crystalline solids. The free-energies and other related thermodynamic quantities such as entropies and heat capacities have been computed using quasi-harmonic lattice dynamics. Periodic structures of bulk solids are represented by supercells with various shapes and sizes. Under the periodic boundary conditions, the calculation of defect properties can be carried out at either constant volume or constant pressure. Amongst these defect properties, constant-pressure heat capacities prove more difficult to compute compared to constant-volume heat capacities. Here, we provide possible solutions for estimating constant-pressure heat capacities via numerical calculations. Furthermore, we have also demonstrated that the substitutional defect free-energies depend strongly on temperature. The choice of the simulation model, for instance, employing periodic supercells or finite-size clusters, size of the system, and so forth, has significant influences on those defect quantities. We highlight that the defect properties calculated via *ab initio* and classical simulations yield similar results for the same solid. Furthermore, we present also the defect properties in a metal as a different type of solids described by another different classical potential model. The effects of defect clustering on the defect thermodynamics will be briefly illustrated. Comments on potential applications of the

calculation of free-energies of substitutional defect formation in crystals in the field of geochemistry, such as trace-element partitioning in minerals and melts, and solid solutions, have also been made.

3.1 Introduction

Previously, the free-energy of formation of Ba^{2+} substitutional defects in MgO was comprehensively studied by Taylor and co-workers.⁶¹ The work employed the supercell approach, quasi-harmonic lattice dynamics, and direct free-energy minimisation to observe the variation of the substitutional defect free-energies with temperature and supercell size, using a classical interionic potential model. The study shows that the quantities obtained at constant volume and constant pressure, which can be obtained separately, are significantly different. This simulation technique proves valid up to two-thirds of the melting point and is certainly useful for computing defect free-energies under a wide range of temperatures and pressures.^{89,139,140} However, interatomic forces are in fact anharmonic; hence, the harmonic approximation would not appropriately be used to describe the interatomic potentials at distances further away from the equilibrium values. Therefore, at higher temperatures, *e.g.*, above the two-thirds of the melting point,^{61,89,139,140} the quasi-harmonic approximation would fail in explaining various phenomena such as thermal expansion, the temperature variations of elastic constants and phonon frequencies, phase transitions and thermal conductivity, due to the anharmonic and phonon interactions.¹⁴¹

The critical paper of Taylor *et al.*⁶¹ has therefore been chosen as the key reference and the inspiration of the present study. However, the paper does not provide any information on changes in heat capacity of defect formation. In addition to this prior work, we also examine the changes in heat capacity of substitutional defect formation at both constant volume and constant pressure. According to fundamental statistical thermodynamics, the constant-volume heat capacity of a given solid at a finite temperature can be readily calculated from its vibrational partition function, but the calculation of the constant-pressure heat capacity proves more difficult. In this work, we have highlighted the merits and limitations of various numerical models for obtaining constant-pressure heat capacities of defect formation.

Apart from the effects of temperature and system size used in the simulation, we aim to investigate finite-size effects on the defect thermodynamics, comparing finite-sized (or molecular) clusters with the periodic model. In addition, we further provide numerical

TABLE 3.1. Buckingham pair-potential parameters of $X\text{-O}^{2-}$ for modelling a Ba^{2+} substitutional defect in MgO .

X	A (eV)	ρ (Å)	C (eV Å ⁶)
O^{2-}	22764.3	0.1490	20.37
Mg^{2+}	1346.6	0.2984	-
Ba^{2+}	757.8	0.4105	-

TABLE 3.2. Supercells of MgO used in this work and their corresponding mole fractions of a single Ba in the defective supercells, X_{Ba} .

Number of ions	X_{Ba}	Shape	Number of ions	X_{Ba}	Shape
32	0.06250	bcc	686	0.00292	fcc
54	0.03704	fcc	864	0.00231	bcc
64	0.03125	cub	1000	0.00200	cub
128	0.01563	fcc	1024	0.00195	fcc
216	0.00926	cub	1458	0.00137	fcc
250	0.00800	fcc	1728	0.00116	cub
256	0.00781	bcc	2000	0.00100	fcc
432	0.00463	fcc	2048	0.00098	bcc
512	0.00391	cub	2744	0.00073	cub

results obtained from *ab initio* DFT calculations rather than a pair-potential model. The results for a different type of solid, a metal, described by a different classical potential model, *i.e.*, a Lennard-Jones solid which has no long-range electrostatic contribution, are also presented in order to ensure the validity of the simulation technique when using other types of classical potential models. We also illustrate the effects of defect clustering on the defect properties. Finally, we highlight the potential applications of the computation of defect free-energies in geochemistry, for instance, trace-element partitioning between minerals and melts, and solid solutions.

3.2 Models and Computational Details

3.2.1 Classical Simulation

All the classical calculations in this work were carried out using the General Utility Lattice Program (GULP).⁹¹ The Buckingham potential parameters for the study of the substitution of a Mg^{2+} by a Ba^{2+} ion in MgO crystal, Ba_{Mg}^x , are listed in Table 3.1.¹⁴² We have used the rigid-ion model and a cut-off radius of 9.0 Å for all the pair potentials.

TABLE 3.3. 12-6 Lennard-Jones pair-potential parameters for modelling the Ag substitutional defect in Cu metal.

Species	ϵ (eV)	σ (Å)
Cu	0.4079	2.3374
Ag	0.3453	2.6376

The Broyden–Fletcher–Goldfarb–Shanno (BFGS) minimisation algorithm^{143–146} with a stopping criterion on the gradients (forces) of 1.0×10^{-4} Hartree Bohr⁻¹ ($\sim 5.1 \times 10^{-4}$ eV Å⁻¹) was used for the geometry optimisation. In the supercell calculations, cubic symmetry is preserved if the superlattice of Ba²⁺ itself is cubic.¹²⁷ For instance, after replacing one of the Mg²⁺ ions in a simple cubic supercell of MgO with a Ba²⁺ ion, the symmetry of the Ba²⁺ superlattice is also simple cubic. On the contrary, if a Mg²⁺ ion is replaced with a Ba²⁺ ion in a face-centred cubic supercell of MgO, the symmetry of the Ba²⁺ is face-centred cubic. In the present study, we consider three different shapes of supercells, *i.e.*, simple cubic (cub), face-centred cubic (fcc) and body-centred cubic (bcc), with supercell sizes ranging from 32-2744 ions. The supercells used and their corresponding mole fraction of Ba²⁺ in the defective crystals, X_{Ba} , are shown in Table 3.2. The initial crystal structures were prepared using the VESTA visualiser program.¹³⁶ The vast series of the defective structures were generated using a simple Python script written in the Jupyter Notebook,¹⁴⁷ as an implementation in the Anaconda Software Distribution.¹⁴⁸ Defect properties such as the constant pressure defect free-energy g_p can be calculated from the lattice free energies of a supercell containing x ions:

$$g_p = G_{\text{BaMg}_{0.5x-1}\text{O}_{0.5x}}(P, T) - G_{\text{Mg}_{0.5x}\text{O}_{0.5x}}(P, T), \quad (3.1)$$

where there is only a single Ba²⁺ in the supercell, *i.e.*, N_d in equation (2.30) equals 1.

For observing finite-size effects on the defect properties, we also simulated the substitution of a copper (Cu) atom by a silver (Ag) atom in bulk copper metal, *i.e.*, the Ag_{Cu}^x defect. The Lennard-Jones pair-potential parameters with the 12-6 exponent for Cu and Ag atoms were taken from Zhen and Davies,¹⁴⁹ as listed in Table 3.3. The pair-potential parameters between Ag-Ag, Cu-Cu and Ag-Cu were truncated at distances above 9.0 Å and calculated using the Waldman-Hagler combining rules¹⁵⁰ as follows

$$\begin{aligned} \epsilon_{\text{Ag-Cu}} &= 2\sqrt{\epsilon_{\text{Ag}}\epsilon_{\text{Cu}}} \left(\frac{\sigma_{\text{Ag}}^3 \sigma_{\text{Cu}}^3}{\sigma_{\text{Ag}}^6 + \sigma_{\text{Cu}}^6} \right), \text{ and} \\ \sigma_{\text{Ag-Cu}} &= \left(\frac{\sigma_{\text{Ag}}^6 + \sigma_{\text{Cu}}^6}{2} \right)^{\frac{1}{6}}. \end{aligned} \quad (3.2)$$

3.2.2 First-Principles Simulation

To compare with the classical results, we have also performed some analogous calculations *ab initio*. The *ab initio* calculations based on first-principles density functional theory (DFT) were conducted using the CRYSTAL17 code.^{108,109} Note that, similar to the GULP program, CRYSTAL17 is also able to model non-periodic finite-size clusters without the use of the supercell approach. The revised version of the generalised-gradient approximation of Perdew-Burke-Ernzerhof designed for solids and surfaces (GGA-PBESol)¹¹⁵ was used for evaluating the exchange and correlation contributions to the total energy. Atom-centred Gaussian-type-function (GTF) basis sets were employed to represent the atomic wavefunctions. The Hay-Wadt small-core effective-core pseudopotential (ECP) basis set with a 3-1(1d)G¹⁵¹ contraction was used for the Ba atom. All-electron basis sets with 8-511G¹⁵² and 8-411G¹⁵³ contractions, on the other hand, were used to describe the Mg and O atoms, respectively. For the self-consistent field (SCF) calculation of the (electronic) total energy, the convergence criterion on the energy difference between next steps was set to 1.0×10^{-6} Hartree ($\sim 2.7 \times 10^{-5}$ eV). The convergence criteria of the structural optimisation using the Broyden–Fletcher–Goldfarb–Shanno (BFGS) minimisation method^{143–146} were set to 3.0×10^{-4} Hartree Bohr⁻¹ (~ 0.015 eV Å⁻¹) and 1.2×10^{-3} Bohr ($\sim 6.4 \times 10^{-4}$ Å) for the root-mean-square gradients (forces) and displacements, respectively. Additionally, the convergence of the structural minimisation is also checked on the energy difference between consecutive steps using a stopping criterion of 1.0×10^{-7} Hartree ($\sim 2.7 \times 10^{-6}$ eV).

In contrast to the classical defect energies obtained using equation (3.1), one must take the ion energies, E_{ion} , of Mg²⁺ and Ba²⁺ into account when calculating the DFT defect energies. Similar to equation (3.1), for instance, the change in static-limit internal energy at constant volume, u_v , due to the Ba_{Mg}^x defect formation in a supercell of MgO containing x ions is given by

$$u_v = (U_{\text{BaMg}_{0.5x-1}\text{O}_{0.5x}} + E_{\text{Mg}^{2+}}) - (U_{\text{Mg}_{0.5x}\text{O}_{0.5x}} + E_{\text{Ba}^{2+}}), \quad (3.3)$$

where $U_{\text{BaMg}_{0.5x-1}\text{O}_{0.5x}}$ and $U_{\text{Mg}_{0.5x}\text{O}_{0.5x}}$ are the lattice energies of the defective and perfect crystals, respectively. As mentioned above, apart from the energy of periodic lattice systems, the energy of non-periodic isolated systems, *e.g.*, atoms, ions or molecules, can also be obtained using CRYSTAL17.^{108,109} Hence, the isolated-ion energies $E_{\text{Mg}^{2+}}$ and $E_{\text{Ba}^{2+}}$ in equation (3.3) can readily be computed by removing two valence electrons from each of the isolated neutral atoms.

3.3 Results and Discussion

3.3.1 Variation of Defect Quantities with System Size

Figure 3.1(a) illustrates the variation of the defect volume v_p calculated at constant pressure in the static limit as a function of system size for Ba_{Mg}^x in bulk MgO. In the range of system size considered, the figure demonstrates that the values of the defect volume are positive and lie between 20.0-21.4 Å³. The substitution of a Mg^{2+} by the larger Ba^{2+} in MgO accounts for the positive volume change. In other words, the MgO crystal expands to accommodate the bigger Ba^{2+} cation. We can see clearly that the defect volume depends on the size of the supercell. However, the defect volume becomes independent of supercell size when a very large supercell is being used. For all the supercell shapes, the defect volume converges to the value in the dilute limit as the system size is increased, but each of the supercell shapes shows a different convergence rate. Of these three shapes, the fcc and bcc supercells yield the fastest convergence, and that of the simple cubic supercells is the slowest. This is likely due to the more isotropic environment of an isolated defect in the fcc and bcc superlattices.⁶¹ Apart from the defect volume, the dependence of other defect quantities on system size should also be less significant when larger supercells are used, as shown in Figure 3.1(b).

Figure 3.1(b) shows the internal defect energies at constant pressure, $h_p (= g_p)$, and at constant volume, $u_v (= f_v)$, in the static limit as a function of supercell size. The values of the defect energy are all positive, lying between 15.5-16.6 eV, again reflecting the large size of the Ba^{2+} ion. These positive defect energies mainly derive from the short-range repulsive interactions between the Ba^{2+} substitutional defect and its immediate ions. An interesting feature in the graph is that u_v is always greater than h_p for a supercell with the same size due to the volume constraint. Compared to the constant-volume calculation, the geometry optimisation at constant pressure, *i.e.*, all of the cell parameters are allowed to change, involves the relaxation of more degrees of freedom, leading to a lower defect energy. In the dilute limit, we can see that the constant-volume and constant-pressure defect energies converge as the supercell size increases and this is consistent with equation (2.32). The differences $u_v - h_p$ vanish in the limit when $v_p/V_{\text{supercell}} \rightarrow 0$ as the differences in defect energies, in the equation (2.35), are proportional to $v_p/V_{\text{supercell}}$. Equations (2.35) and (2.36) together yield

$$u_v - h_p = \frac{1}{2} p_v v_p, \quad (3.4)$$

and this gives rise to the slower convergence of u_v with respect to supercell size compared

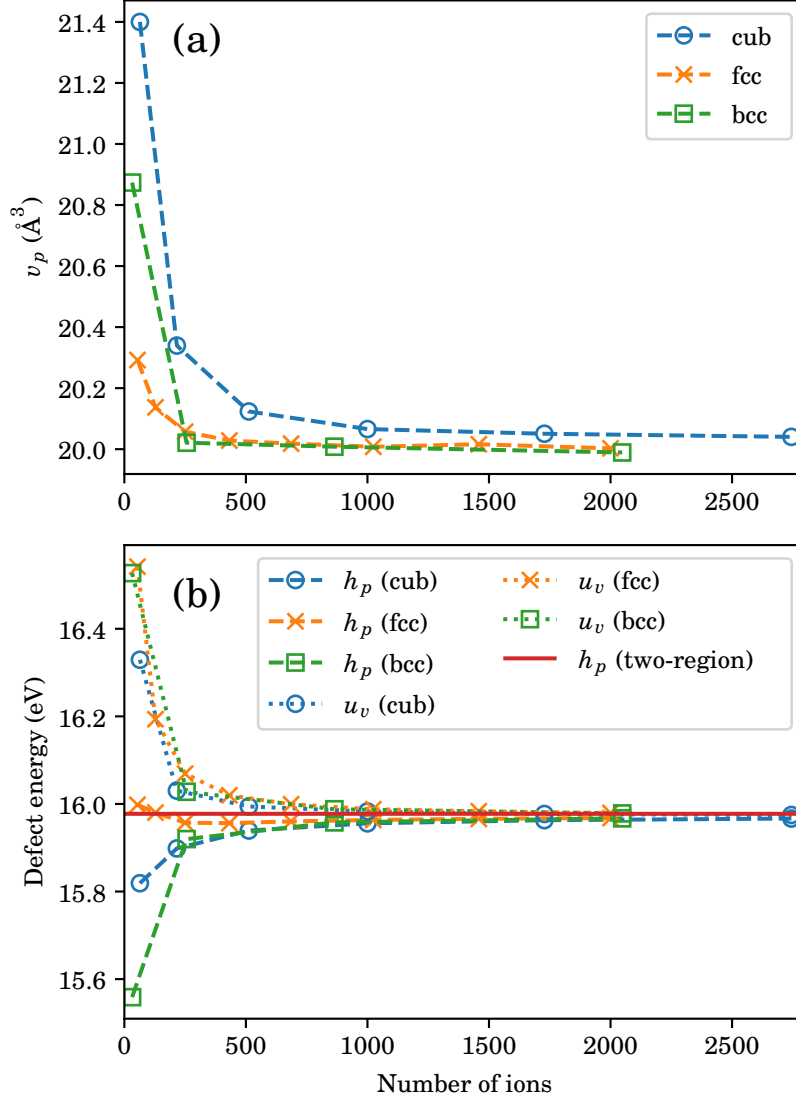


FIGURE 3.1. (a) Defect volume v_p and (b) defect energies at constant pressure h_p (dashed lines) and constant volume u_v (dotted lines) as a function of supercell size for a Ba^{2+} substitutional defect in MgO in the static limit. Defect quantities for the three different shapes of the supercells are plotted using different marker styles. For (b), the defect energy obtained via the two-region approach is marked by a horizontal solid line. The computational details of the classical calculations based on Buckingham interionic potentials are outlined in Subsection 3.2.1.

to that of h_p ; the difference between u_v and h_p is reduced as the supercell size is increased. This is because v_p , as shown in Figure 3.1(a), is larger when a smaller supercell is being used as well as p_v . For substitutional defect formation with a non-zero v_p , p_v vanishes nevertheless as the supercell size is increased. Furthermore, the dilute-limit static defect energies obtained using the supercell approach are in good agreement with the result obtained from the two-region approach.

3.3.2 Effects of Temperature on Defect Properties

The effects of temperature on defect properties are often assumed to be insignificant and hence neglected in the literature.⁶¹ In addition, the computational cost for computing temperature dependent quantities is much more expensive compared to the static-limit calculations, so that the temperature effects have often been ignored. However, here we will show that those defect properties vary with temperature more than almost universally assumed. In this subsection, we aim to probe the temperature effects on the calculated defect quantities for Ba_{Mg}^x , *e.g.*, defect free-energies and entropies, using lattice dynamics within the quasiharmonic approximation together with the direct free-energy minimisation in the supercell approach. We use a simple cubic supercell containing 216 ions of MgO as our case study and the defect properties have been observed in the temperature range 500-1500 K.

Figure 3.2(a) shows the plots of the crystal volumes V_{pc} and V_{dc} for the perfect and defective crystals, respectively, and Figure 3.2(b) illustrates the volume change, v_p , of the Ba_{Mg}^x substitution in MgO as a function of temperature in the temperature range considered. In Figure 3.2(a), the crystal volumes V_{pc} and V_{dc} increase by 3.2% and 3.4%, respectively, over the range 500-1500 K. The increase in crystal volume at elevated temperatures implies that the average interionic distance in both crystal structures increases. However, the increase in V_{pc} is slightly smaller than V_{dc} since the Ba–O distances grow slightly more rapidly than the Mg–O distances as the temperature is increased. The horizontal solid and dashed lines represent V_{pc} and V_{dc} in the static limit, respectively. On the other hand, Figure 3.2(b) shows the temperature variation of the defect volume $v_p = V_{\text{dc}} - V_{\text{pc}}$. From 500 K to 1500 K, v_p increases by approximately 21%. v_p in the static limit is also plotted using a solid line for comparison.

Defect free-energies and entropies are shown in Figures 3.3(a) and 3.3(b), respectively. Figure 3.3(a) shows that the defect free-energies g_p and f_v and the internal energy at constant volume u_v decrease as the temperature increases while the enthalpy h_p is increased. Over the temperature range 500-1500 K, g_p , f_v and u_v decrease approximately

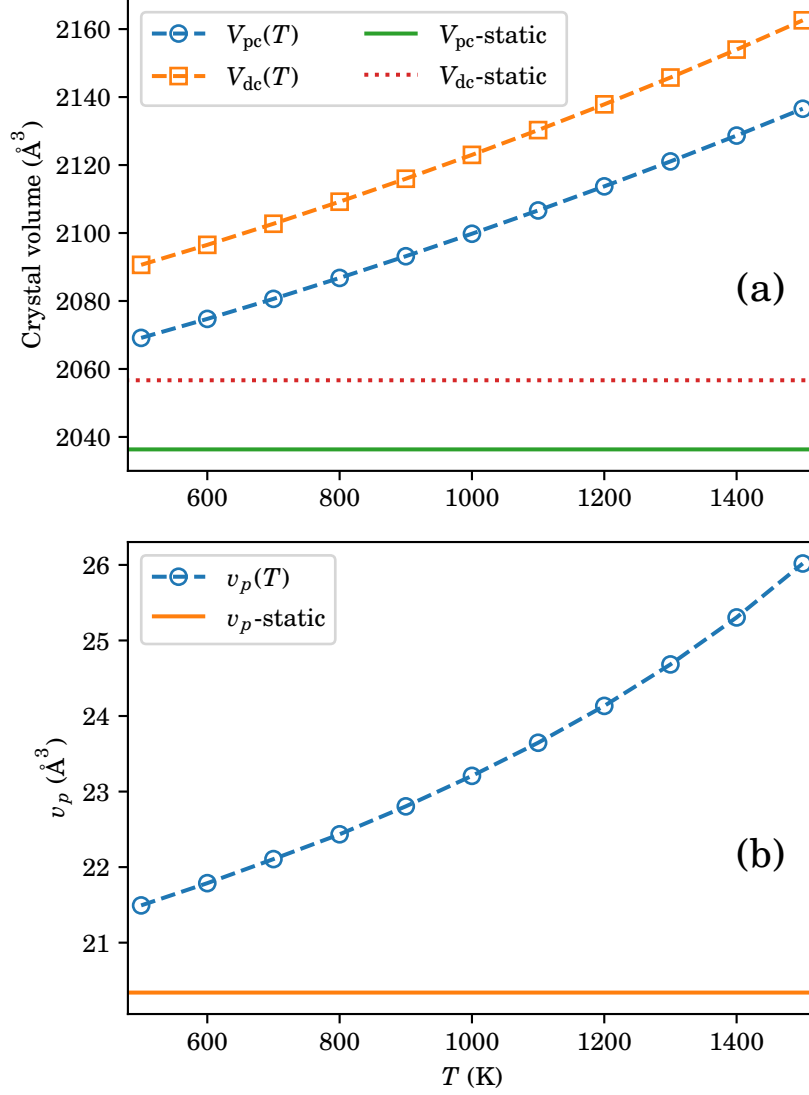


FIGURE 3.2. (a) Crystal volumes of perfect crystals, V_{pc} , and defective crystals, V_{dc} , (b) defect volume v_p of Ba_{Mg}^x substitutional defect using a 216-ion supercell of MgO at elevated temperatures compared with the corresponding values in the static limit marked by horizontal lines. The computational details of the classical calculations based on Buckingham interionic potentials are outlined in Subsection 3.2.1.

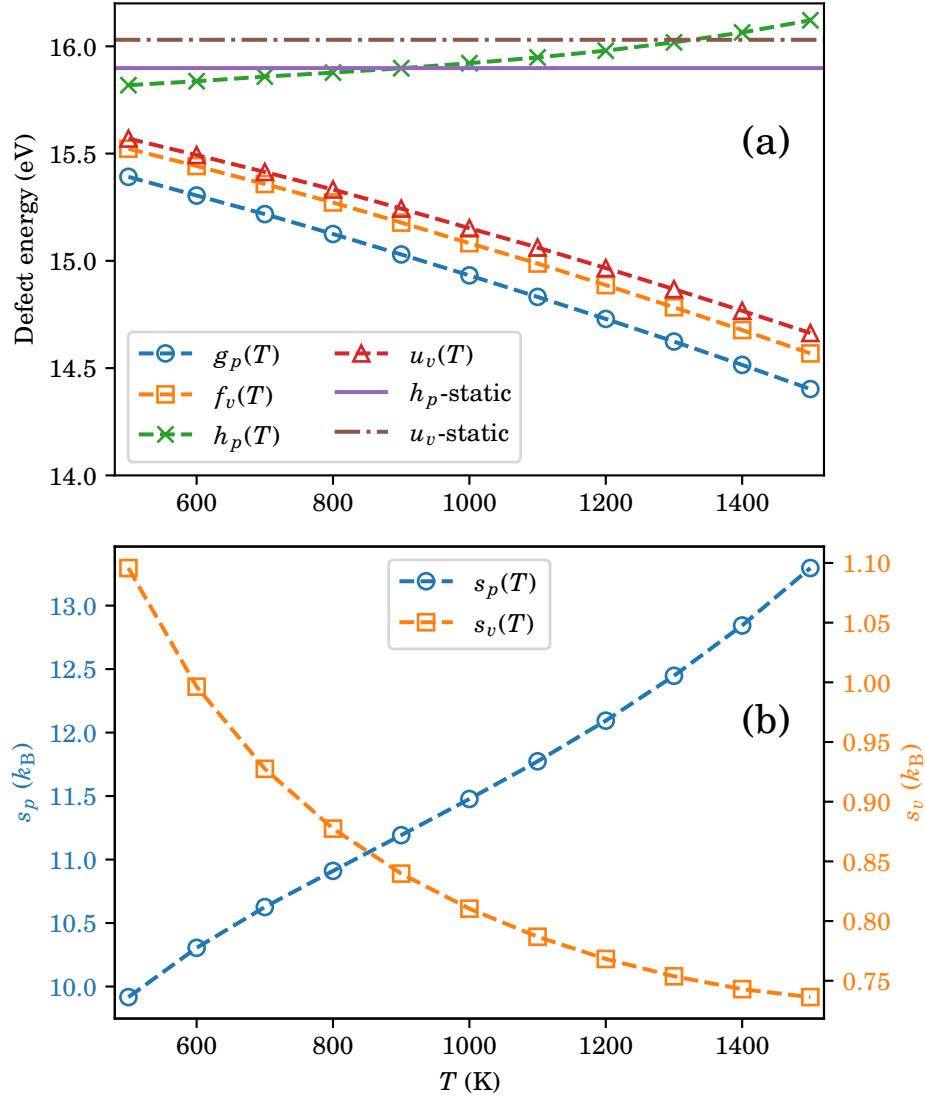


FIGURE 3.3. Temperature variation of (a) defect energies and (b) entropies for Ba_{Mg}^x using a 216-ion supercell of MgO. The computational details of the classical calculations based on Buckingham interionic potentials are outlined in Subsection 3.2.1.

by 6.4%, 6.1% and 5.8%, respectively, while h_p is raised by *ca.* 1.9%. The values of f_v and u_v at each temperature are only slightly different, compared to the larger differences between g_p and h_p , since s_v is very much smaller than s_p , *i.e.*, in equation (2.31).

According to equation (2.8), the entropy of a given structure at T depends solely on the vibrational frequencies which rely on two factors: (i) the interatomic force constants and (ii) the atomic masses, *i.e.*, the stronger force constants with the lighter masses are responsible for the higher vibrational frequencies which lead to the lower entropies, and vice versa. In the case of Ba_{Mg}^x , there are two competing effects for the constant-volume calculations. At constant volume, the substitution of a Mg^{2+} by a much heavier Ba^{2+} decreases the frequencies, while the volume constraint increases interionic forces leading to higher frequencies. For s_p , on the other hand, the volume constraint is less significant as the equilibrium pressure is optimised to zero. Hence, for Ba_{Mg}^x , s_v is generally small and always much smaller than s_p , as shown in Figure 3.3(b). Additionally, the change in s_p with respect to temperature is also greater than the change in s_v and with an opposite trend. Over the range 500-1500 K, s_p increases by 34%, while s_v decreases by 33%.

At a given temperature, the changes in entropy of defect formation, s_p and s_v , depend solely on the change in magnitude of vibrational frequencies, as discussed above. In order to observe the change in magnitude of vibrational frequencies of the Ba_{Mg}^x defect formation explicitly, one can compare the phonon density of states (DOS) plot of the bulk MgO to that of the defective structure, as shown in Figure 3.4. Overall, in Figure 3.4(a), most of the vibrational states in all the structures lie in the range 300-450 cm^{-1} . Additionally, the DOS plots for the three structures are very similar in the high-frequency range, *e.g.*, above 500 cm^{-1} . This implies that the majority of the changes (or shifts) in magnitude of vibrational frequencies due to the defect formation occurs in the frequency range below 500 cm^{-1} , as shown in the plots of the difference in DOS in the defective and perfect structure shown in Figure 3.4(b).

In Figure 3.4(b), the DOS of the optimised defective structures at both constant volume and constant pressure are all lower than that of the perfect crystal over 300-450 cm^{-1} . It implies a significant reduction of the population of vibrational states in the defective systems compared to the perfect crystal over that frequency range. From 450 to $\sim 700 \text{ cm}^{-1}$, there are also small rises in the number of vibrational states due to the defect formation. Noticeably, there is a significant increase in number of vibrational states below *ca.* 200-285 cm^{-1} as a result of the defect formation. In general, the numbers of vibrational states in the defective structures are greater than those of the perfect crystal in the frequency range below 300 cm^{-1} . Subsequently, the considerable reduction

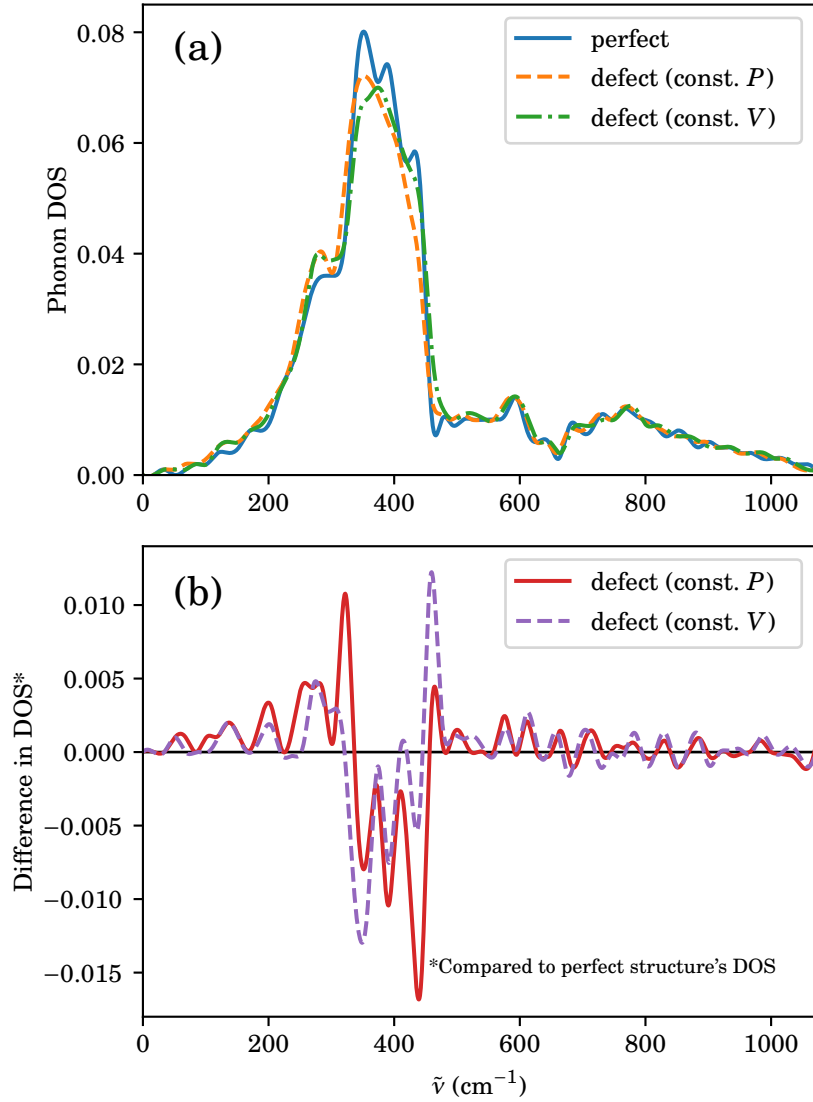


FIGURE 3.4. (a) Phonon density of states (DOS) plots of bulk MgO and Ba_{Mg}^x defective structures at both constant pressure and constant volume at 1000 K using a supercell containing 216 ions. (b) The difference in DOS in the defective and perfect structures. The phonon DOS for each structure is labelled by a different line style. The computational details of the classical calculations based on Buckingham interionic potentials are outlined in Subsection 3.2.1.

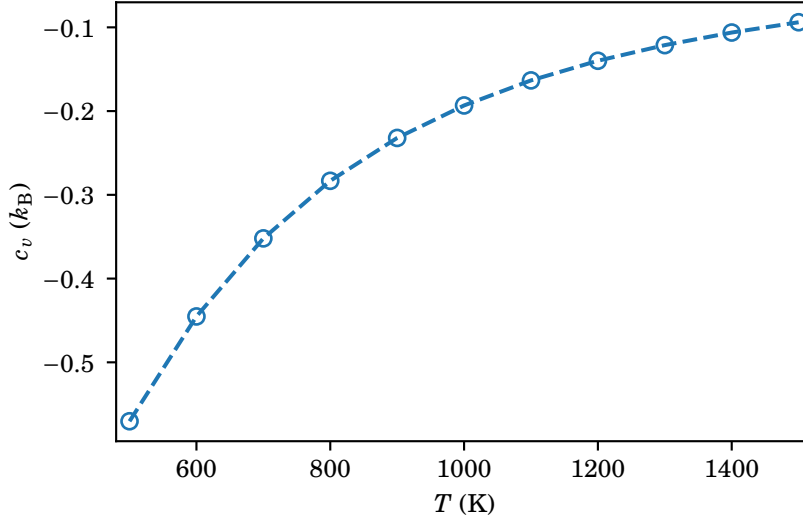


FIGURE 3.5. Temperature dependence of the change in constant-volume heat capacity of the Ba_{Mg}^x defect formation using a 216-ion supercell of MgO. The computational details of the classical calculations based on Buckingham interionic potentials are outlined in Subsection 3.2.1.

in the number of higher-frequency vibrational modes, *e.g.*, mainly from $300\text{-}450\text{ cm}^{-1}$ to lower-frequency modes (a redshift), gives rise to higher entropies in the defect structures, leading to positive s_p and s_v of the Ba_{Mg}^x defect formation in MgO, as shown in Figure 3.3(b).

The phonon DOS plots for the optimised defective structures at constant pressure and constant volume, as shown in Figure 3.4, provide also further information on the difference in magnitude of s_p and s_v for the Ba_{Mg}^x defect formation in MgO. In the frequency range below 400 cm^{-1} , the DOS of the optimised defective structure at constant pressure is higher than that of the structure at constant volume, while the opposite trend in the DOS for these two defective structures can be observed in the frequency range above 400 cm^{-1} . This is the implication of the effect of the volume constraint on the vibrational frequencies at constant volume, leading to a larger number of high-frequency vibrational modes and hence a lower entropy.

Apart from the other properties mentioned above, one can also observe the temperature dependence of the change in the constant-volume heat capacity of defect formation, c_v , as shown in Figure 3.5. It is worth noting that c_v in this case is the difference between the C_V of the perfect MgO supercell with an equilibrium volume at a given temperature T and that of the defective supercell with the same volume as the perfect structure, *i.e.*,

the crystal volume at each T is different. Therefore, c_v cannot directly be obtained from $(\partial u_v / \partial T)$ as the crystal volume is not constant when calculating U_V at each temperature.

Figure 3.5 demonstrates that the constant-volume heat capacity of the perfect crystal is always higher than that of the defective one. Hence, c_v for Ba_{Mg}^x is negative at all temperatures between 500 and 1500 K. Like entropy, heat capacity depends on the frequencies of the vibrational modes in a given material at a particular T , *i.e.*, higher vibrational frequencies result in a lower heat capacity. For a given temperature at constant volume in Figure 3.5, a negative c_v for Ba_{Mg}^x in MgO implies that the volume constraint, which makes the force constants stronger, dominates the vibrational frequencies. Overall, the vibrational modes shift to the lower-frequency regime due to the defect formation at constant volume, as clearly shown in Figure 3.4(b), leads to a negative change in constant-volume heat capacity. Therefore, the present discussion concerning c_v agrees with the earlier discussion regarding s_p and s_v , as evidenced by the phonon DOS plots in Figure 3.4.

Over the temperature range considered, c_v increases by 84% as the temperature is raised. The difference in constant-pressure heat capacity c_p proves more difficult to work out than c_v . According to statistical thermodynamics, the heat capacity of a crystal at constant volume C_V can be obtained by the derivatives of the vibrational partition function Z_{vib} or by the first derivative of the internal energy with respect to temperature:

$$C_V(T) = \left(\frac{\partial U}{\partial T} \right)_V \quad (3.5)$$

$$= RT \left[2 \left(\frac{\partial \ln Z_{\text{vib}}}{\partial T} \right) + T \left(\frac{\partial^2 \ln Z_{\text{vib}}}{\partial T^2} \right) \right]. \quad (3.6)$$

Using equation (3.6), C_V for a given periodic structure at a finite temperature can directly be computed after a phonon calculation in the GULP program, for example. However, to acquire the heat capacity at constant pressure C_P from that calculated C_V , the numerical values of the volumetric thermal expansion coefficient α and the isothermal compressibility β_T (the inverse of the bulk modulus K_T) need to be examined first.¹⁵⁴ The relationship between C_P and C_V can be expressed as

$$C_P = C_V + VT \left(\frac{\alpha^2}{\beta_T} \right), \quad (3.7)$$

where $\alpha = \frac{1}{V} \left(\frac{\partial V}{\partial T} \right)_P$, and $\beta_T = \frac{1}{K_T} = -\frac{1}{V} \left(\frac{\partial V}{\partial P} \right)_T$. Additionally, an approximate form of equation (3.7) is given by the Nernst-Lindemann relation:

$$C_V \approx C_P - C_P^2 T \left(\frac{V \alpha^2}{\beta_T C_P^2} \right)_{T=T_{\text{ref}}}, \quad (3.8)$$

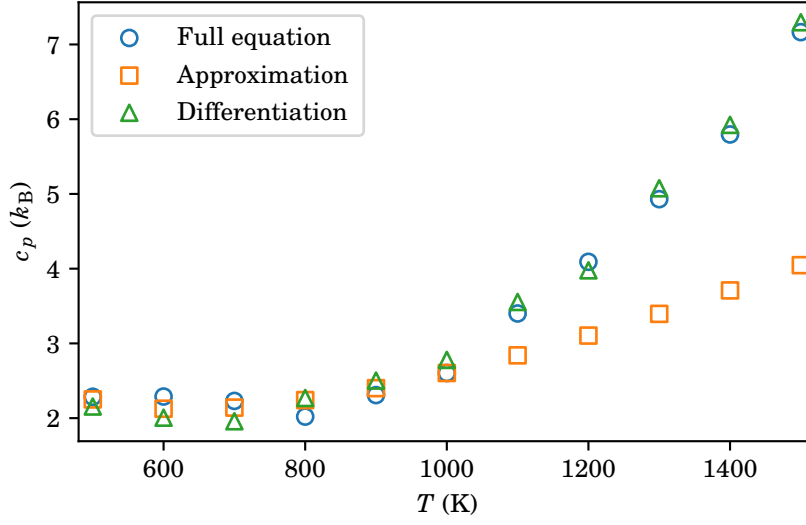


FIGURE 3.6. Temperature dependence of the change in constant-pressure heat capacity of the Ba_{Mg}^x defect formation using a 216-ion supercell of MgO. Different marker styles are used for different methods for calculating C_P : \circ (full equation), \square (approximation), and \triangle (differentiation) refer to equations (3.7), (3.8) and (3.9), respectively. T_{ref} was set at 1000 K for C_P 's obtained using equation (3.8). The computational details of the classical calculations based on Buckingham interionic potentials are outlined in Subsection 3.2.1.

where T_{ref} is any convenient temperature where the necessary data are available.¹⁵⁵ One subtle drawback of using equations (3.7) and (3.8) is that they are not suitable for evaluating the C_P for finite-size (or molecular) clusters as the parameters α and β_T cannot be defined. More importantly, one needs to perform a large number of phonon calculations in order to obtain reasonably adequate numerical results. For these reasons, converting the calculated C_V of both periodic system or finite-size system into C_P through equations (3.7) and (3.8) proves impractical. However, there is another simpler and more fundamental approach to compute the C_P of either a periodic structure or a finite-size cluster via the first derivative of the enthalpy H with respect to temperature T :

$$C_P = \left(\frac{\partial H}{\partial T} \right)_P, \quad (3.9)$$

where $H = G + TS$. The calculation of C_P for a given structure using equation (3.9) can easily be done via a computer code with the implementation of the direct free-energy minimisation approach such as the GULP program.^{91,156}

Figure 3.6 shows the temperature variation of the change in constant-pressure heat capacity c_p of Ba_{Mg}^x substitutional defect formation in MgO calculated through the three

different approaches mentioned earlier: (i) the full $C_V - C_P$ conversion (equation (3.7)) (ii) the approximate expression of the $C_V - C_P$ conversion (equation (3.8)) and (iii) the first derivative of H with respect to T (equation (3.9)). In case (ii), T_{ref} was set at 1000 K. Overall, all the three approaches show that the values of c_p for the $\text{Ba}_{\text{Mg}}^{\times}$ defect are positive at all temperatures between 500 K and 1500 K. This implies that C_P of the defective structure is always higher than that of the perfect crystal in the temperature range considered. Remarkably, the numerical results from equation (3.9) are in good agreement with the ones obtained using equation (3.7) at all temperatures, while the calculated c_p 's from the approximate equation (3.8) are significantly lower than those obtained using the other two expressions at higher temperatures, *i.e.*, above T_{ref} . c_p changes only slightly around $1.9\text{-}2.5k_B$ in the temperature range of 500-1000 K, while it increases rapidly with temperature above 1000 K. At 1500 K, c_p calculated from equations (3.7) and (3.9) increases by approximately 3.5 times the value at 500 K, while c_p from equation (3.8) increases only approximately 1.5 times the value at 500 K.

As expected, the full $C_V - C_P$ conversion equation (3.7) and the fundamental thermodynamic equation (3.9) work equally well to estimate the c_p of the $\text{Ba}_{\text{Mg}}^{\times}$ substitutional defect formation in MgO at any given finite temperature. These two approaches give also a better estimation of c_p than the approximate approach via equation (3.8) at higher temperatures. However, compared to equation (3.7), equation (3.9) needs very much less effort and it is a convenient strategy to calculate C_P or c_p as this requires only H or h_p , respectively, as a function of T from only a few phonon calculations, *e.g.*,

$$c_p = \left(\frac{\partial h_p}{\partial T} \right) = T \left(\frac{\partial s_p}{\partial T} \right). \quad (3.10)$$

Additionally, the conversion between C_P and C_V through the full conversion equation (3.7) relies on the quality of the numerical methods for obtaining the terms α and β_T . Hence, insufficient datasets for the numerical fittings may lead to inadequate numerical results. For example, the fluctuating temperature variation of c_p obtained from equation (3.7) at temperatures below 800 K has been observed, which might be due to the poor numerical fittings.

3.3.3 Finite-Size Effects

So far, we have focused on the defect properties which are obtained from periodic structures using the supercell approach. Alternatively, one can also use the non-periodic model, *i.e.*, switching off the periodicity and instead using finite-size clusters of crystalline solids, to study computationally the defect thermodynamics. The key advantages of using the

non-periodic model are that (i) it is computationally cheaper and (ii) this can be modelled by any other widely used *ab initio* software packages designed for molecular systems such as Gaussian16,¹⁵⁷ ORCA,¹⁵⁸ and so on. Hypothetically, the defect properties obtained by the two strategies should be comparable when a very large finite-size cluster is used. In other words, the defect quantities of a finite-size cluster are expected to converge with respect to system size, and those properties of an extremely large cluster should be comparable with the bulk limit. However, in this subsection, we will show that there will always be differences between the defect properties of solid clusters and those of the periodic systems due to the existence of interfaces.

To observe initially the influence of finite-size effects on defect properties, it is worth considering an analogous system of the Ba_{Mg}^x in MgO we have discussed earlier. We choose the substitution of a Cu atom by a bigger Ag atom in Cu metal as a study case for two main reasons: (i) the constituent and substituent atoms are neutral and held together solely by short-range repulsive and attractive interactions in the classical approach and (ii) the crystal structure of Cu belongs to the same space group as MgO ($Fm\bar{3}m$, conventional space group number 225). Consequently, we can then expect that, apart from the existence of the interfaces, there should be no major difference between the periodic bulk and non-periodic cluster. In contrast, in the Ba_{Mg}^x in MgO case, for instance, an electrically neutral cubic cluster itself may have a non-zero electric dipole moment.

The exploration of finite-size effects on the Ag substitutional defect formation energy in Cu metal and finite-size Cu clusters as a function of system size ranging from 32 to 4000 atoms is illustrated in Figure 3.7. Here, we solely focus on the comparison of simple cubic superlattices of the defective solid with the clusters terminated by (100) surfaces with the same sizes. In a given Cu cluster, one Cu atom situated nearest to the centre of the cluster is replaced by an Ag atom to form the defective structure. With this strategy, the environment of the defect is as isotropic as possible. The data shown in Figure 3.7 can be divided into two sets: the substitutional defect energies for (i) relaxed and (ii) unrelaxed structures which appear in the higher- and lower-energy regions, respectively. More precisely, the defect energies labelled with the unrelaxed flag are the differences in energy of the defective and perfect structures without any geometry optimisation, while the other dataset is obtained in the same fashion but from the fully optimised structures instead.

The Ag substitutional defect formation energies in the Cu solid lie between 1.6-3.1 eV depending on the system size and whether the calculation includes structural relaxation.

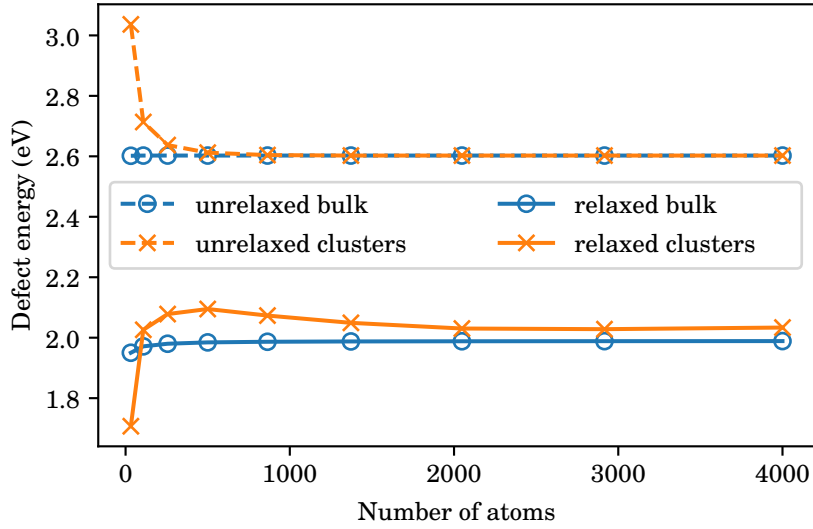


FIGURE 3.7. Finite-size effects on the Ag substitutional defect energy, Ag_{Cu}^x , in Cu metal and finite-size Cu metallic clusters as a function of system size ranging from 32-4000 atoms in the static limit. The solid and dashed lines represent the defect energies obtained before and after performing full geometry optimisation of the corresponding structures, respectively. Defect energies of the periodic and non-periodic systems are highlighted by different marker styles. The computational details of the classical calculations based on Lennard-Jones interatomic potentials are outlined in Subsection 3.2.1.

Again, replacing a smaller Cu atom with a bigger Ag atom is responsible for a positive value of the substitutional defect energy which is similar to the case of Ba_{Mg}^x in MgO. As mentioned above, the main contributions to these positive defect energies are from the short-range repulsion between the new atom and its immediate neighbours. As expected, the defect energies obtained using the unrelaxed structures are all higher than those computed via the fully relaxed ones.

The defect energies for the unrelaxed periodic structures are all approximately 2.6 eV and almost identical for all system sizes, while the computed defect energies using the relatively small unrelaxed clusters are strongly size dependent. For the unrelaxed structures, the defect energies of relatively smaller clusters are higher than those of the larger clusters due to stronger repulsive interactions between the substituent atom and the atoms at the surfaces, which are not allowed to move. However, the defect energy in the unrelaxed clusters approaches the limit of the bulk when using a cluster bigger than 500 atoms. As the cluster size is increased, the defect energies decrease and approach

the converged value as the surface atoms are located further away from the defect and only weakly interact with (or are almost uninfluenced by) the defect itself. The very good agreement between the defect energy of a very large unrelaxed cluster and that of an unrelaxed bulk structure further implies that the effects of the substitution itself, *e.g.*, in terms of the strength of interactions between the defect and its neighbours, are the same in both cases.

The lower-energy region in Figure 3.7, compared to the higher region, shows clearly how geometry relaxation impacts on the substitutional defect energy. For the bulk, the defect energy is largely constant with respect to the supercell size except for the smaller ones. In the bulk structure with a relatively small supercell size, the defect energy tends to be lower than that in the dilute limit due to the stronger defect-defect interactions leading to a lower defect energy, and we shall discuss this effect later in the next section. Note that, as shown in Table 3.3, Ag–Ag interactions are weaker than those of the Ag–Cu and Cu–Cu, respectively (see the ϵ 's). In the $\text{Ag}_{\text{Cu}}^{\text{x}}$ case, there are two competing effects contributing to the defect energy in the opposite way: (i) size constraints increase the defect energy and (ii) an increase in number of Ag–Cu or Ag–Ag interacting pairs decreases the defect energy. A smaller cluster leads to a bigger impact of (ii) in the non-periodic model as we can see the sharp fall in defect energy of the relaxed 32-atom cluster. However, the effect (i) dominates in all other cases as the positive defect energies signify.

The most interesting feature of the plots of the defect energies for the fully relaxed structures in the lower-energy region is that there will always be a difference in defect energy of the cluster model compared to the periodic approach even though a very large finite-size cluster is being used. For instance, the results for the 4000-atom supercell and cluster in the graph are slightly different. At this stage, compared to the unrelaxed models, we can conclude that geometry relaxation after introducing a point defect into a perfect structure results in the difference in defect energy of the bulk and finite-size cluster. One possible explanation of this is that the atomic displacements around the point defect in the periodic and non-periodic models are different which leads eventually to the difference in computed defect energy from the two approaches due to the absence or presence of the interfaces.

In addition, the larger surface area of a larger cluster (*i.e.*, with more atoms at the surfaces) results in a greater degree of structural relaxation at (and near) the interfaces and, therefore, higher surface energy. As the cluster size is increased, the degree of structural relaxation at (and near) the surfaces in a defective cluster should be very

similar to that of its perfect structure. Strictly speaking, the atoms at (and near) the surfaces are hardly influenced by the point defect located at the centre. This might lead to very similar surface areas and surface energies. Since the influence of the point defect on the atomic relaxation at (and near) the surfaces becomes much smaller in an extremely large cluster, the population of atoms at (and near) the interfaces grows rapidly as the size is increased. Hence, the accumulation of these small effects can eventually become significant. For this reason, the calculated defect properties of the finite-size systems are always different from those of the periodic systems due to the existence of interfaces in the non-periodic model. Here, the effects resulting from the existence of interfaces are so-called finite-size effects.

Now, let us go back to study the finite-size effects in our $\text{Ba}_{\text{Mg}}^{\text{x}}$ in MgO case. Figure 3.8 illustrates the variation of defect energies (g_p and f_v) and changes in entropy of defect formation (s_p and s_v) with respect to system size for $\text{Ba}_{\text{Mg}}^{\text{x}}$ substitution in bulk MgO and cubic-shaped MgO clusters, *i.e.*, clusters terminated by (100) surfaces, with the size ranging from 216-2744 ions at 1000 K. The constant-volume defect quantities for the cubic clusters are obtained by keeping the coordinates of all the outermost atoms fixed at their equilibrium positions in their corresponding perfect structures at each temperature, while those of the remaining atoms are allowed to relax fully. In this way, the surface area (or the volume) of a particular cluster at a given temperature does not change during geometry relaxation.

Overall, we can clearly observe that the defect properties for the periodic structures converge rapidly to their dilute-limit values as the superlattice spacing is increased, while those of the clusters show slower convergence rates. Over the range of system sizes considered, the defect properties of the finite-size clusters are different from those of the bulk due to the finite-size effects, as discussed earlier. Figure 3.8(a) points out that the defect energies in the clusters are all higher than those in the bulk and it shows also that the differences in g_p , h_p , f_v and u_v of the bulk and the clusters depend on system size. For instance, f_v of the 216-ion cluster is ~ 1.5 eV higher than that of the bulk, while the difference in f_v is approximately 1 eV for the systems with 2744 ions. The differences in g_p , h_p , and u_v show similar trends. On the contrary, the changes in entropy for the defect formation (s_p and s_v) of the clusters are all smaller than those of the bulk, as shown in Figure 3.8(b). For our biggest systems, *i.e.*, the supercells and clusters containing 2744 ions, the differences in s_p and s_v are approximately $2k_B$ and $0.5k_B$, respectively.

Additionally, Figures 3.9 and 3.10 show the temperature dependence of the defect

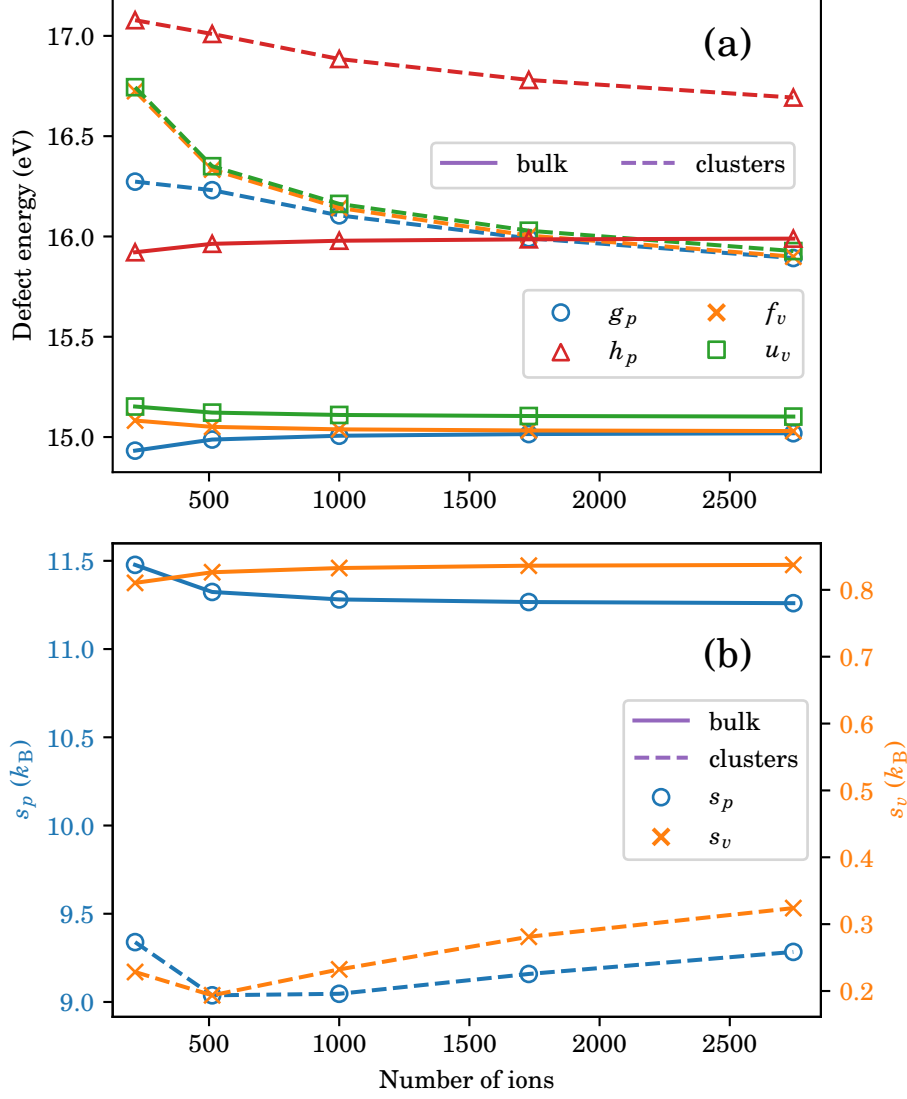


FIGURE 3.8. Variation of (a) defect energies and (b) entropy changes of defect formation with system size for Ba_{Mg}^x in bulk MgO and cubic-shaped clusters with the system size ranging from 216-2744 atoms at 1000 K. Solid and dashed lines represent the defect properties of the bulk and clusters, respectively. Different defect quantities are marked with different marker styles. The computational details of the classical calculations based on Buckingham interionic potentials are outlined in Subsection 3.2.1.

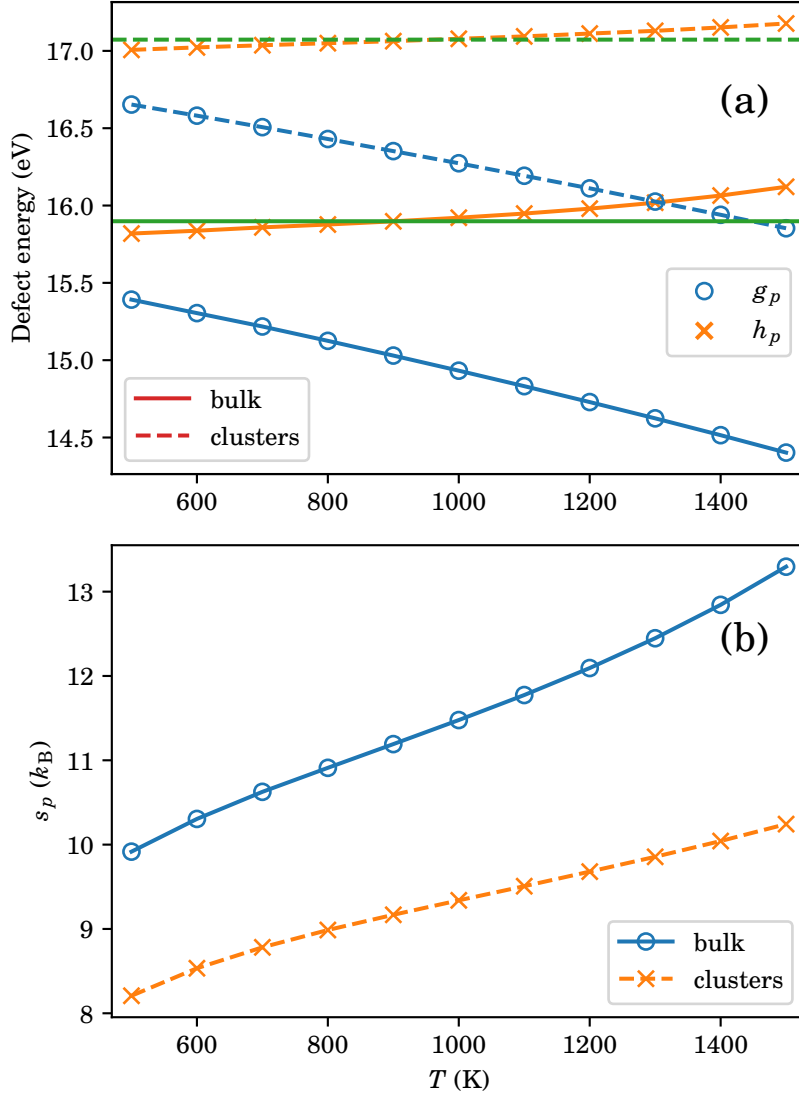


FIGURE 3.9. Variation of (a) defect energies and (b) entropy changes of defect formation with temperature for Ba_{Mg}^x in bulk MgO and MgO cluster at constant pressure. The numerical results were obtained using a supercell and a cluster of MgO containing 216 ions. Solid and dashed lines are used for the defect properties of the bulk and cluster, respectively. In (a), different defect energies are highlighted by different symbols and horizontal straight lines denote the defect energies at the static limit. The computational details of the classical calculations based on Buckingham interionic potentials are outlined in Subsection 3.2.1.

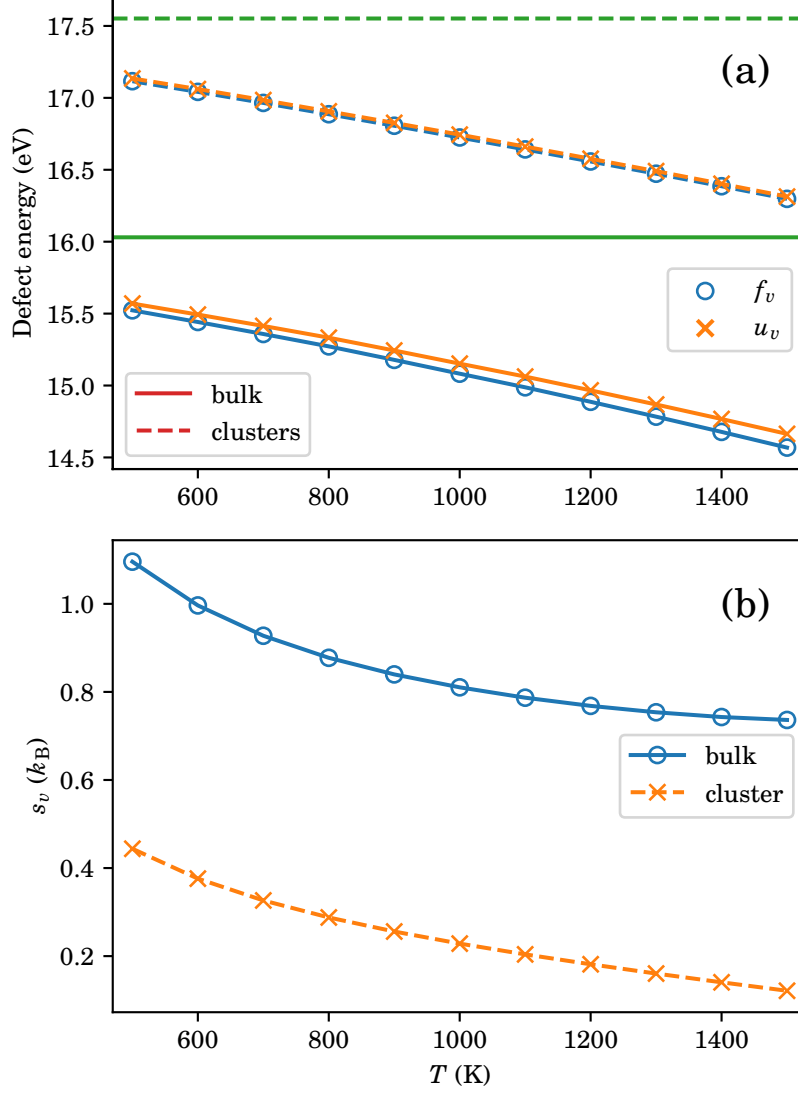


FIGURE 3.10. Variation of (a) defect energies and (b) entropy change of defect formation with temperature for Ba_{Mg}^x in bulk MgO and MgO cluster at constant volume. The numerical results were obtained using a supercell and a cluster of MgO containing 216 ions. Solid and dashed lines are used for the defect properties of the bulk and cluster, respectively. In (a), different defect energies are highlighted by different symbols and horizontal straight lines denote the defect energies at the static limit. The computational details of the classical calculations based on Buckingham interionic potentials are outlined in Subsection 3.2.1.

properties of $\text{Ba}_{\text{Mg}}^{\text{x}}$ in bulk MgO and a MgO cluster both with the system size of 216 ions at constant pressure and constant volume, respectively. In the range of 500-1500 K, the increasing or decreasing trends in both the constant-pressure and constant-volume defect quantities of the finite-size cluster are all consistent with those of the bulk. At all temperatures, all the defect energies of the cluster are higher than those of the bulk, while the defect entropies for the bulk are larger than those of the cluster.

In terms of defect energies, Figures 3.9(a) and 3.10(a) show that the differences in g_p , f_v and u_v of the bulk compared to those of the cluster are temperature independent. Strictly speaking, the differences in those three defect parameters are almost identical at all temperatures, *i.e.*, g_p , f_v and u_v of the cluster are respectively *ca.* 1.3 eV, 1.6 eV and 1.6 eV higher than those of the bulk over 500-1500 K. However, this is not the case for the difference in h_p as shown in Figure 3.9(a). The difference in h_p for the bulk and the cluster becomes smaller as the temperature is increased, *e.g.*, the differences in h_p for the cluster and the bulk are *ca.* 1.2 eV at 500 K and 1.0 eV at 1500 K.

The temperature variation of the constant-pressure and constant-volume entropy changes (s_p and s_v) of the defect formation are shown in Figures 3.9(b) and 3.10(b), respectively. In Figure 3.9(b), s_p 's of the bulk and cluster both increase at elevated temperatures over 500-1500 K. In contrast, s_v 's of the bulk and the cluster both decrease over 500-1500 K. At constant pressure, s_p of the bulk increases more rapidly than that of the cluster, *e.g.*, s_p of the bulk are $1.8k_{\text{B}}$ and $3.2k_{\text{B}}$ higher than that of the cluster at 500 K and 1500 K, respectively. Values of s_v of the bulk and the cluster, on the other hand, show the same decreasing rate, *e.g.*, s_v of the bulk is approximately $0.6k_{\text{B}}$ higher than that of the cluster at all temperatures from 500-1500 K. A more minor change in entropy of the $\text{Ba}_{\text{Mg}}^{\text{x}}$ substitutional defect formation (either s_p or s_v) for the finite-size cluster compared to that of the bulk suggests that there are fewer low-frequency vibrational modes (or more high-frequency vibrational modes) due to the substitution in the cluster than the periodic bulk structure.

The phonon DOS plots and the differences in DOS of the MgO cluster containing 216 ions and its optimised defective analogues at both constant pressure and constant volume at 1000 K are shown in Figure 3.11(a) and 3.11(b), respectively. Figure 3.11 can be compared with the phonon DOS plots of the bulk in Figure 3.4. In comparison with the vibrational phonon DOS of the bulk, the change of vibrational frequencies due to the defect formation in the clusters is less obvious. Overall, there should be more red-shifted vibrational modes than the blue-shifted ones in the defective clusters compared to the perfect structures, as the positive signs of s_v and s_p implies. In comparison with s_p and

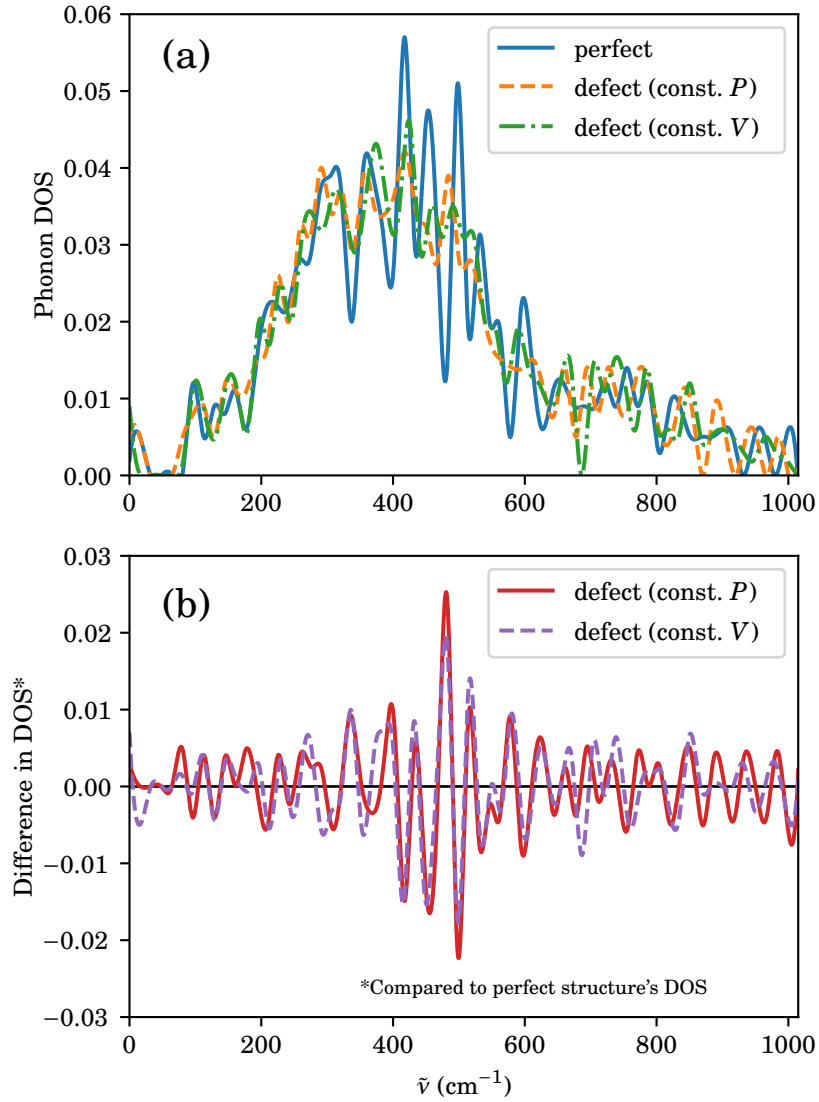


FIGURE 3.11. (a) Phonon density of states (DOS) plots of a perfect 216-ion MgO cluster and the optimised Ba_{Mg}^x defective structures at constant pressure and constant volume at 1000 K. (b) The difference in DOS in the defective and perfect structures. The phonon DOS for each structure is labelled by a different line style. The computational details of the classical calculations based on Buckingham interionic potentials are outlined in Subsection 3.2.1.

s_v of the bulk, on the other hand, the smaller (positive) magnitude of the defect entropies for the clusters is mainly due to a smaller redshift and a greater blueshift, as shown in Figures 3.9(b) and 3.10(b), respectively.

As we mentioned earlier, there are two competing factors influencing vibrational frequencies: (i) the atomic masses and (ii) the strength of interatomic interactions. For Ba_{Mg}^x in MgO, the heavier mass of the Ba^{2+} cation decreases the magnitude of the frequencies leading to a higher entropy, while its bigger ionic radius increases the strength of the interionic interactions, *i.e.*, especially when modelled at constant volume, resulting in a lower entropy. Modelling the defect formation at constant pressure, on the other hand, implies that the volume constraint due to the Ba^{2+} substitution is small and only the mass effect dominates the vibrational frequencies. Consequently, for the Ba_{Mg}^x substitution in periodic bulk MgO, we have previously shown that s_v is always smaller than s_p for all system sizes and at all temperatures, *e.g.*, in Figures 3.3(b) and 3.8(b). Remarkably, it is also the case for all the finite-size clusters considered in the temperature range 500-1500 K as shown in Figures 3.8(b), 3.9(b), and 3.10(b).

So far, we have emphasised that the substitution of a Mg^{2+} by a Ba^{2+} in bulk MgO, compared to a finite-size cluster of MgO, leads to a smaller number of high-frequency vibrational modes and, hence, a greater entropy change from their perfect structures, *i.e.*, for both s_p and s_v . However, the contribution of the mass effects to the change of vibrational frequencies in both defective systems compared to their corresponding perfect structures are expected to be approximately identical. In other words, the differences in both s_p and s_v for the bulk compared to those of the cluster are almost solely due to the change of the force constants or, in general, the so-called volume constraint, and this can be clearly explained by reference to Figure 3.12.

Figures 3.12(a) and 3.12(b) illustrate the temperature dependence of s_p and s_v , respectively, of Ba_{Mg}^x in bulk MgO and cluster. At this stage, we probe the mass effects on the change in entropy of the defect formation using two types of the Ba^{2+} cation: (i) an ordinary (more massive) barium ion with the atomic mass of 137 denoted by ^{137}Ba and (ii) an artificially modified lighter barium ion with the same atomic mass of 24 as a Mg^{2+} denoted by ^{24}Ba . Generally, we can observe clearly that substituting a Mg^{2+} ion by a lighter Ba^{2+} ion reduces s_p or s_v compared to the substitution by the ordinary (heavier) Ba^{2+} ion. A lighter mass increases vibrational frequencies and eventually results in a lower entropy, as discussed earlier. Interestingly, the degree of the contribution of the mass effects to s_p and s_v for the bulk and the cluster are approximately equal. In all cases, substituting a Mg^{2+} by a ^{24}Ba , compared to ^{137}Ba , lowers s_p and s_v equally by $\sim 2.3k_B$.

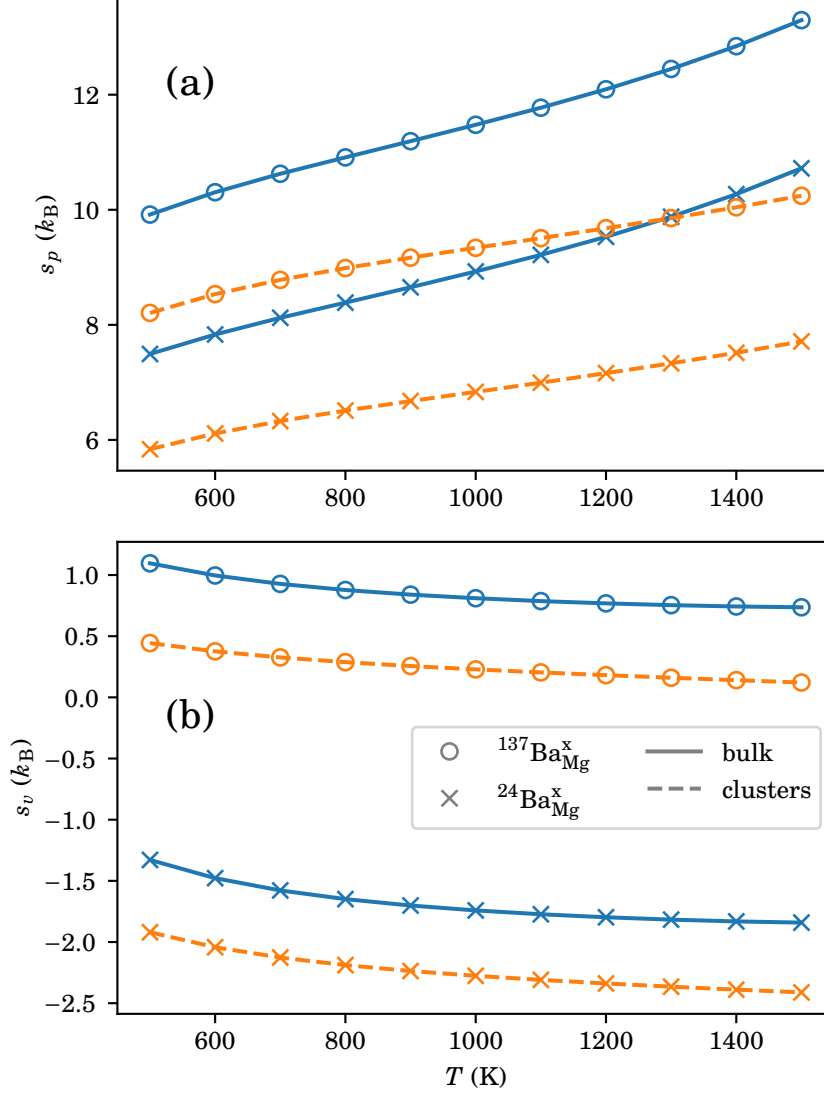


FIGURE 3.12. Temperature variation of (a) s_p and (b) s_v for Ba_{Mg}^x in bulk MgO and MgO cluster containing 216 ions. Different marker styles are used to represent the two types of the Ba^{2+} cation with the atomic masses of 137 and 24 (^{137}Ba and ^{24}Ba) and solid and dashed lines are used to highlight the defect entropies of the bulk and the cluster, respectively. The computational details of the classical calculations based on Buckingham interionic potentials are outlined in Subsection 3.2.1.

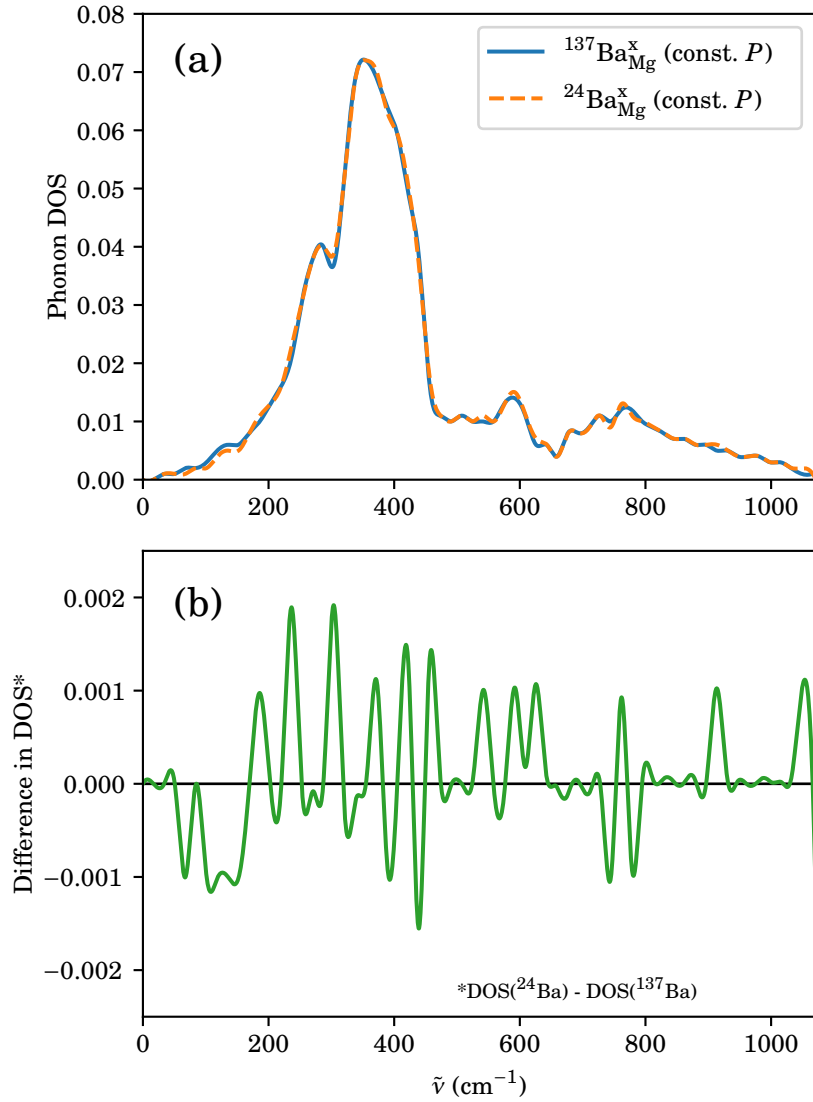


FIGURE 3.13. (a) Phonon density of states (DOS) plots of $^{137}\text{Ba}_{\text{Mg}}^x$ and $^{24}\text{Ba}_{\text{Mg}}^x$ substitutional defects in bulk MgO in a 216-ion supercell at constant pressure at 1000 K. (b) The difference in DOS in the defective structure with ^{24}Ba compared to the structure with ^{137}Ba . In (a), the phonon DOS for each structure is labelled by a different line style. The computational details of the classical calculations based on Buckingham interionic potentials are outlined in Subsection 3.2.1.

The bottom of Figure 3.12(b) illustrates that the volume constraint itself accounts for the the negative s_v of the $^{24}\text{Ba}_{\text{Mg}}^x$ for both the periodic and finite-size systems.

In addition, the influence of the mass effect on vibrational frequencies should be evident in the vibrational DOS plot, shown in Figure 3.13. Figure 3.13(a), shows only a slight difference in the number of vibrational modes in the two defect structures. However, the difference in the density of states in these two defective structures in Figure 3.13(b) shows more clearly the shifts of vibrational modes due to the lighter dopant. For example, it indicates a substantial decrease in number of vibrational states in the frequency region below 180 cm^{-1} and also a considerable increase in number of vibrational states in the frequency range above *ca.* 900 cm^{-1} . Even though these changes are slight, *e.g.*, the almost identical phonon DOS plots in Figure 3.13(a) and the magnitude of the DOS difference in Figure 3.13(b), s_p can still very well reflect this small change. In other words, the magnitude of the entropy change is sensitive to the small difference in the magnitude and number of vibrational frequencies in the frequency and temperature ranges we consider here.

The current discussion regarding the effect of a change in the magnitude of vibrational frequencies due to the substitutional defect on the change in entropy should also be a good basis to understand further the change in heat capacity in a similar fashion, *i.e.*, higher vibrational frequencies result in a lower vibrational heat capacity and vice versa. The changes in heat capacity at constant volume, c_v , for Ba_{Mg}^x in bulk MgO and MgO clusters as a function of system size are shown in Figure 3.14(a). At 1000 K, c_v is negative for all the system sizes considered ranging from 216-2744 ions. This suggests that all the defective structures have lower heat capacities than those of their corresponding perfect analogues, implying that the volume constraint dominates the vibrational frequencies, as discussed earlier. Surprisingly, in contrast to the trends in s_v shown in Figure 3.8(b), where s_v for the bulk is higher than that of the cluster, c_v for the clusters is higher than that of the bulk. One possible reason for these opposite trends for the s_v and c_v for the bulk and the clusters might be that the sensitivities of the magnitudes of c_v and s_v to the change in the magnitude of high-frequency vibrational modes (or the volume constraint, in general) are different.

The effect of the change in the magnitude of a vibrational frequency on the magnitude of these two vibrational properties, *i.e.*, S_{vib} and C_{vib} , can be illustrated by the thermodynamic expressions of S and C for a harmonic oscillator with identical frequency,

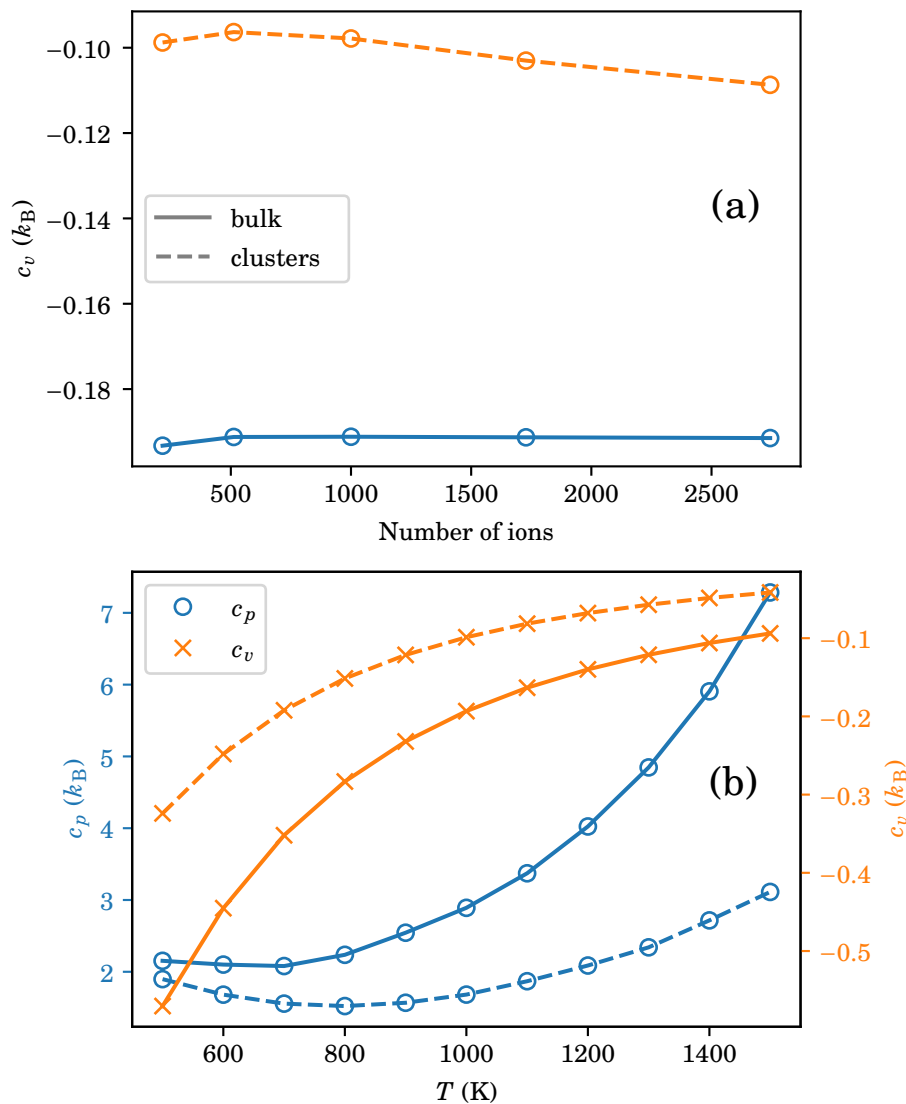


FIGURE 3.14. Variation of heat capacity changes of Ba_{Mg}^x in MgO with (a) system size and (b) temperature. For (a), c_v of each system size was calculated at 1000 K. For (b), a supercell and a cluster of MgO containing 216 ions were used for all temperatures in order to obtain c_p and c_v which are highlighted using different marker styles. Solid and dashed lines with different marker symbols represent the heat capacity changes for the bulk and clusters, respectively. The computational details of the classical calculations based on Buckingham interionic potentials are outlined in Subsection 3.2.1.

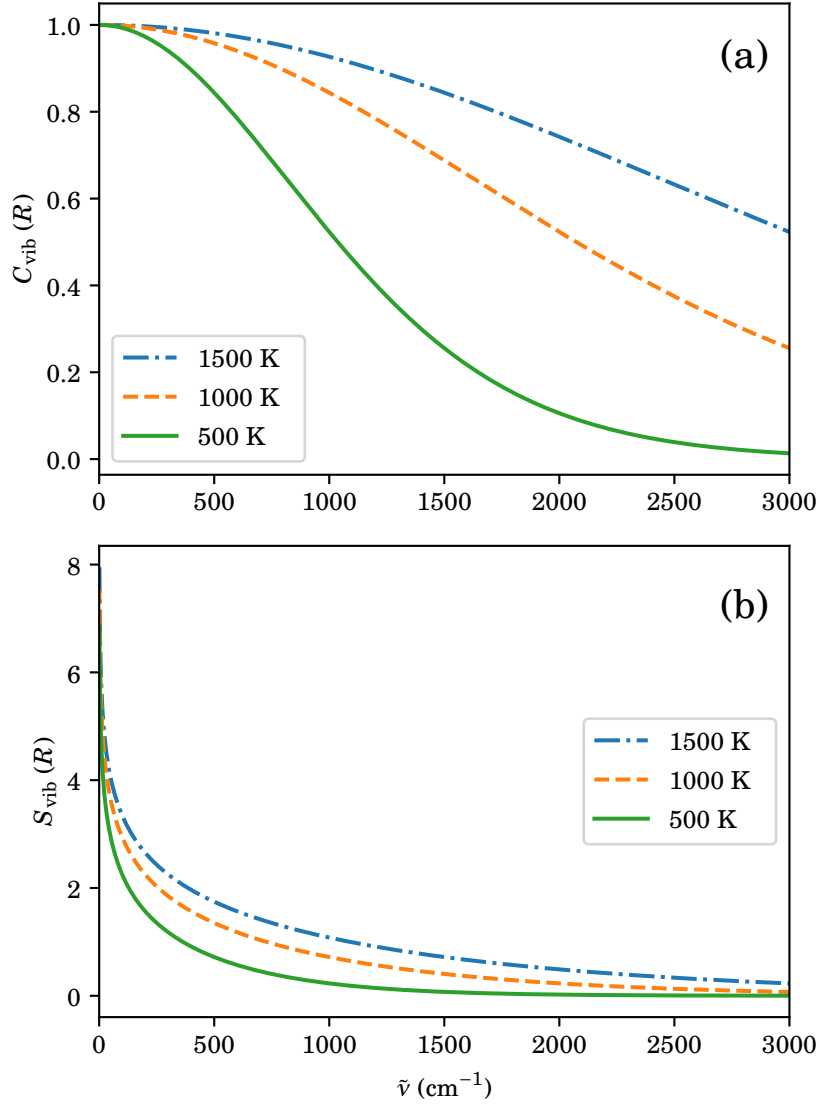


FIGURE 3.15. (a) Vibrational heat capacity C_{vib} and (b) vibrational entropy S_{vib} as a function of wavenumber $\tilde{\nu}$ at 500, 1000, and 1500 K according to equations (3.11) and (3.12). The vibrational quantities at three different temperatures are highlighted by different line styles.

ν :

$$S_{\text{vib}}(x) = R \left\{ \frac{x \exp(-x)}{[1 - \exp(-x)]} - \ln[1 - \exp(-x)] \right\}, \text{ and} \quad (3.11)$$

$$C_{\text{vib}}(x) = R \left\{ \frac{x^2}{[\exp(x) + \exp(-x) - 2]} \right\}; \text{ where } x = \frac{h\nu}{k_B T}. \quad (3.12)$$

Here, R is the gas constant, h is Planck's constant, k_B is the Boltzmann constant, and T is temperature. Using equations (3.11) and (3.12) at 300 K, S_{vib} and C_{vib} decrease approximately by 47% and 12%, respectively, when the vibrational frequency ν is increases from 500 to 1000 cm^{-1} . Note that the decreasing rate of S_{vib} or C_{vib} with respect to frequency depends on the change in the magnitude of the vibrational frequency and temperature, as shown in Figure 3.15. Moreover, one can evaluate analytically the change in S_{vib} and C_{vib} due to the change in vibrational frequency through the first derivatives of S_{vib} and C_{vib} in equations (3.11) and (3.12), respectively, with respect to ν :

$$\begin{aligned} \left(\frac{\partial S}{\partial \nu} \right)_T &= -\frac{h}{k_B T} R \left\{ \frac{x \exp(x)}{[\exp(x) - 1]^2} \right\}, \text{ and} \\ \left(\frac{\partial C}{\partial \nu} \right)_T &= -\frac{h}{k_B T} R \left\{ \frac{x \exp(x)[x + \exp(x)(x - 2) + 2]}{[\exp(x) - 1]^3} \right\}. \end{aligned} \quad (3.13)$$

Figure 3.14(b) shows the temperature dependence of c_v and c_p for Ba_{Mg}^x in bulk MgO and a MgO cluster with a system size of 216 ions in the temperature range of 500-1500 K. Note that c_p is calculated using equation (3.10). As expected, over the temperature range considered, c_p for all cases is positive, whereas c_v is negative. As in the discussion concerning s_v and s_p , the difference in magnitude (and sign) of c_v and c_p is due to the volume constraint predominantly controlling the vibrational frequencies in the c_v case, while the mass effect, on the other hand, dominates the frequencies in the case of c_p .

Over 500-1500 K, c_v increases as the temperature is elevated. c_v for the bulk and the cluster both increase more rapidly over 500-1000 K than 1000-1500 K. The difference between c_v of the bulk and the cluster varies with temperature and becomes smaller when the temperature is increased, *e.g.*, c_v for the cluster is approximately $0.50k_B$ and $0.25k_B$ greater than that of the bulk at 500 and 1500 K, respectively. From 500-1500 K, c_v for the bulk and the cluster both increase by *ca.* 83%. On the other hand, c_p of the bulk and the cluster decrease only slightly over \sim 500-800 K and then increase over 800-1500 K. At higher temperatures, c_p for the bulk increases faster than that of the cluster. The difference in c_p of the bulk and the cluster, unlike c_v , becomes larger as the temperature increases, *i.e.*, c_p of the bulk is approximately $0.1k_B$ and $4.2k_B$ higher than that of the cluster at 500 and 1500 K, respectively. Over 500-1500 K, c_p for the bulk and the cluster increase by \sim 243% and 58%, respectively.

In conclusion, this subsection has focused mainly on the difference between defect properties obtained from the periodic and non-periodic models. All the defect properties of finite-size clusters are closer to the bulk values when the system size is increased. Even though a very large solid cluster may be used, the evaluated defect properties of that finite-size cluster will always be different from those of the bulk limit due to the existence of the interfaces. These are so-called finite-size effects. There are two main possible explanations for the difference between the defect thermodynamics of the bulk and clusters. Firstly, the influence of the substitutional defect on the structural relaxation of atoms at (and near) the surfaces becomes much more similar to, but not exactly the same as, the surface relaxation of the perfect structure as the cluster size is increased. Note that, however, the number of atoms at (and near) the surfaces grows rapidly as the system size is increased. Secondly, due to the interfaces, the degree of the structural relaxation around the defect in the cluster might be different from that in the bulk. These accumulating effects, therefore, may give rise to the difference in the defect properties of the periodic and non-periodic systems. For these reasons, one should always be aware of these effects when choosing between the periodic and non-periodic models for modelling defect formation in crystalline solids, as the two strategies have their own limitations and merits in terms of computational cost and software availability.

3.3.4 *Ab Initio* Calculations for Ba-Substitutional Defect in MgO

In the previous subsection, we presented the defect thermodynamics of the $\text{Ba}_{\text{Mg}}^{\times}$ defect formation in MgO calculated using classical potential parameters. In this subsection, we now show those defect properties obtained from analogous *ab initio* calculations based on density functional theory (DFT) instead. One of the major advantages of *ab initio* or first-principles calculations is that they do not rely on any empirical parameters from fittings. Furthermore, compared to the classical simulation where electrons are not explicitly considered as individual particles, *ab initio* simulation gives insights into the electronic structure and many other related properties of the system of interest. Therefore, the first-principles approach is believed to be more accurate and reliable for complex systems depending on the level of theory that has been employed. However, these *ab initio* calculations are much more computationally expensive, and hence are limited to small systems.

TABLE 3.4. Experimental and calculated lattice parameters of MgO and BaO. The computational details of the classical calculations based on Buckingham interionic potentials and DFT (GGA-PBESol) calculations are outlined in Subsections 3.2.1 and 3.2.2, respectively.

Compound	Lattice parameter a (Å)		
	Buckingham Potentials	DFT-PBESol	Experimental
MgO	4.225	4.222	4.216 ^(a)
BaO	5.543	5.439	5.536 ^(b)

^(a)Hirata *et al.*,¹⁵⁹ ^(b)Elo *et al.*,¹⁶⁰

TABLE 3.5. Observed interionic distances in bulk MgO and BaO from classical and DFT calculations in the static limit. Note that the reported interionic spacing of each ion-pair is measured in the first five nearest-neighbouring shells only. The number of the neighbouring ions (NN) in each shell appears in a parenthesis. The computational details of the classical calculations based on Buckingham potentials and DFT (GGA-PBESol) calculations are outlined in Subsections 3.2.1 and 3.2.2, respectively.

Structure	Ion pair	Shell (NN)	Interionic distance (Å)	
			Classical	DFT
MgO	Mg–O	1 st (6)	2.113	2.111
		2 nd (8)	3.659	3.656
		3 rd (24)	4.724	4.720
		4 th (30)	6.338	6.333
		5 th (24)	7.006	7.001
	Mg–Mg	1 st (12)	2.988	2.985
		2 nd (6)	4.225	4.222
		3 rd (24)	5.175	5.171
		4 th (12)	5.975	5.971
		5 th (24)	6.680	6.676
BaO	Ba–O	1 st (6)	2.772	2.720
		2 nd (8)	4.800	4.710
		3 rd (24)	6.197	6.081
		4 th (30)	8.315	8.159
		5 th (24)	9.192	9.020
	Ba–Ba	1 st (12)	3.920	3.846
		2 nd (6)	5.543	5.439
		3 rd (24)	6.789	6.661
		4 th (12)	7.839	7.692
		5 th (24)	8.764	8.600

TABLE 3.6. Observed distances between the Ba^{2+} and its neighbouring ions in the first few nearest-neighbouring shells, *i.e.*, within half the supercell dimension, in the optimised defective structures of bulk MgO with sizes of 64 (cub), 128 (fcc) and 216 (cub) ions from classical and DFT calculations at constant pressure in the static limit. The number of the neighbouring ions (NN) in each shell appears in a parenthesis. Calculated relative displacements indicate the differences between the ionic distances before and after the geometry relaxation, as shown in Figure 3.16. Note that all the neighbouring ions considered move away from the Ba. The computational details of the classical calculations based on Buckingham interionic potentials and DFT (GGA-PBESol) calculations are outlined in Subsections 3.2.1 and 3.2.2, respectively.

Size	Ion pair	Shell (NN)	Interionic distance (Å)		Displacement (%)	
			Classical	DFT	Classical	DFT
64	Ba–O	1 st (6)	2.355	2.381-2.385	11.46	12.79-12.98
		2 nd (8)	3.699	3.700-3.702	1.09	1.18-1.26
	Ba–Mg	1 st (12)	3.106	3.115-3.117	3.96	4.33-4.39
		2 nd (6)	4.274	4.287-4.290	1.17	1.53-1.60
128	Ba–O	1 st (6)	2.350	2.387-2.388	11.23	12.98-13.11
		2 nd (8)	3.673	3.673	0.39	0.37
		3 rd (24)	4.782	4.789-4.790	1.24	1.38-1.47
	Ba–Mg	1 st (12)	3.085	3.091	3.25	3.46
		2 nd (6)	4.293	4.322	1.60	2.30
		3 rd (24)	5.214	5.218	0.75	0.83
216	Ba–O	1 st (6)	2.355	2.387-2.390	11.46	13.09-13.20
		2 nd (8)	3.670	3.664-3.665	0.29	0.22-0.25
		3 rd (24)	4.787	4.789-4.790	1.34	1.45-1.47
		4 th (30)	6.359-6.367	6.360-6.367	0.33-0.47	0.43-0.54
		5 th (24)	7.035	7.036	0.40	0.49
	Ba–Mg	1 st (12)	3.088	3.091-3.092	3.36	3.52-3.56
		2 nd (6)	4.295	4.320-4.321	1.65	2.32-2.35
		3 rd (24)	5.208	5.208	0.65	0.72
		4 th (12)	6.025	6.026-6.027	0.83	0.92-0.93
		5 th (24)	6.710	6.712-6.713	0.44	0.54-0.56

3.3.4.1 Variation of Static-Limit Defect Properties with System Size

The simulated and experimental lattice parameters for bulk MgO and BaO are listed in Table 3.4. For both crystals, the calculated lattice parameters from the classical calculations are in good agreement with the experimental values. The DFT lattice constant of MgO is also in line with that from the experimental observation, while the calculated lattice parameter of BaO is approximately 0.1 Å shorter than that of the experimental value. The discrepancy between the experimental and calculated structural parameters is expected to be mainly affected by the choice of density-functional approximations, *i.e.*, DFT functionals, for estimating the electronic exchange and correlation terms.^{116,161,162} The static-limit classical and DFT interionic distances in the first five nearest-neighbouring shells in the optimised perfect and defective structures at constant pressure appear in Table 3.5. The number of the nearest neighbours (NN) in each spherical shell is also indicated in parenthesis. As the calculated lattice constants of MgO from the classical and DFT calculations are almost identical, the interionic separations are therefore very similar. On the contrary, the Ba–O and Ba–Ba distances in bulk BaO from the classical simulation are longer than those obtained from the DFT calculation, as the calculated lattice constants suggest.

The simulated static-limit interionic distances between the Ba²⁺ substitutional defect and its neighbouring ions in the first few nearest-neighbouring shells within the optimised defective 64-, 128- and 216-ion supercells of MgO from the classical and DFT simulations at constant pressure are listed in Table 3.6. Here, we only consider the nearest-neighbouring shells within half the length of the supercell. All the neighbouring ions move further away from the Ba²⁺ substitutional defect as the lattice expands to accommodate the bigger Ba²⁺ cation. The Ba–O and Ba–Mg interionic distances in each neighbouring shell in a given defective structure are always shorter than the Ba–O and Ba–Ba distances, respectively, in the same shell in bulk BaO, as shown in Table 3.5. Note that most interionic distances between the Ba²⁺ defect and its neighbouring ions in the DFT simulation are slightly longer than the classical distances, as listed in Table 3.6.

The percentages in the displacement of the neighbouring ions in the nearest shells from the Ba²⁺ defect, *i.e.*, the difference in interionic distance of the Ba²⁺ defect and its neighbouring ions before and after the geometry optimisation, are also listed in Table 3.6. A schematic illustration in Figure 3.16 shows the measurement of the ionic displacements in the two closest-neighbouring shells in the defective structure after the geometry relaxation with reference to the initially unrelaxed defective structure. From Table 3.6, one can observe that the displacements of the neighbouring ions around

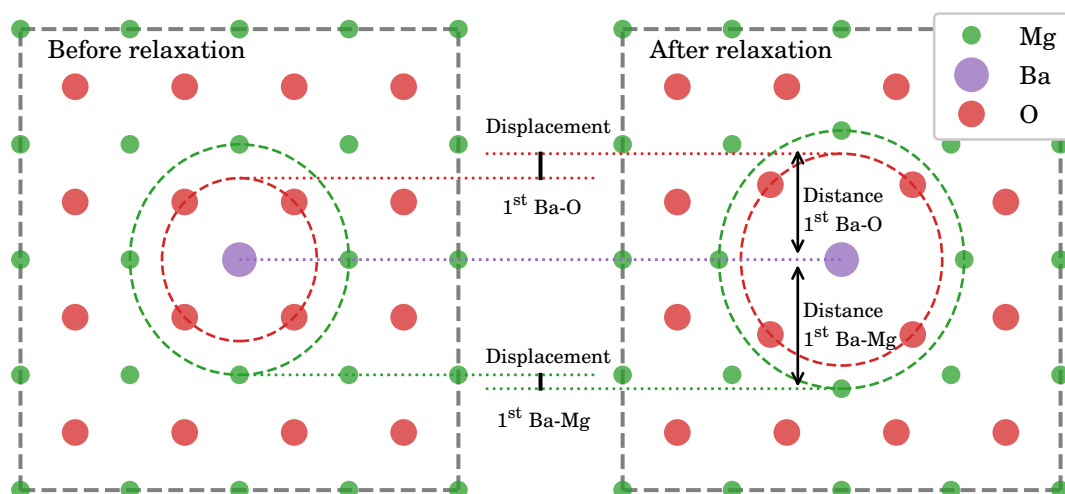


FIGURE 3.16. Schematic illustration of the optimised distances between the Ba^{2+} and its neighbouring ions in the first nearest-neighbouring shells in a defective supercell of bulk MgO, and the relative shell displacements after geometry relaxation.

the $\text{Ba}_{\text{Mg}}^{\text{x}}$ defect tend to be more isotropic in the classical simulation than in the DFT simulation. For instance, the classical and DFT Ba–O distances of the six O^{2-} ions in the first neighbouring shell in the 216-ion defective supercells are 2.355 and 2.387–2.390 Å, respectively. These computed values indicate that the O^{2-} ions are displaced further away from the Ba^{2+} ion by 11.46% and 13.09–13.20% after the structural relaxation at constant pressure in the classical and DFT approaches, respectively. Moreover, the DFT Ba–O distances for the eight O^{2-} ions in the second closest shell lie between 3.664–3.665 Å, which have relative displacements of *ca.* 0.22–0.25%, while an identical Ba–O interionic distance of 3.670 Å with an isotropic atomic displacement of 0.29% is observed in the analogous classical simulation.

The scatter plot of absolute ionic displacements from the Ba^{2+} cation (in Å) on the logarithm scale as a function of the initial interionic distance between the Ba^{2+} defect and its neighbours in the nearest-neighbouring shells within 6 Å from the Ba^{2+} defect in a 216-ion supercell of MgO from both DFT and classical calculations is shown in Figure 3.17. Note that the relaxations in the classical simulations are more symmetrical with less spread and thus more overlap of points in Figure 3.17, *e.g.*, all the six neighbouring O^{2-} ions originally located at around 2.1 Å from the Ba^{2+} have an identical displacement

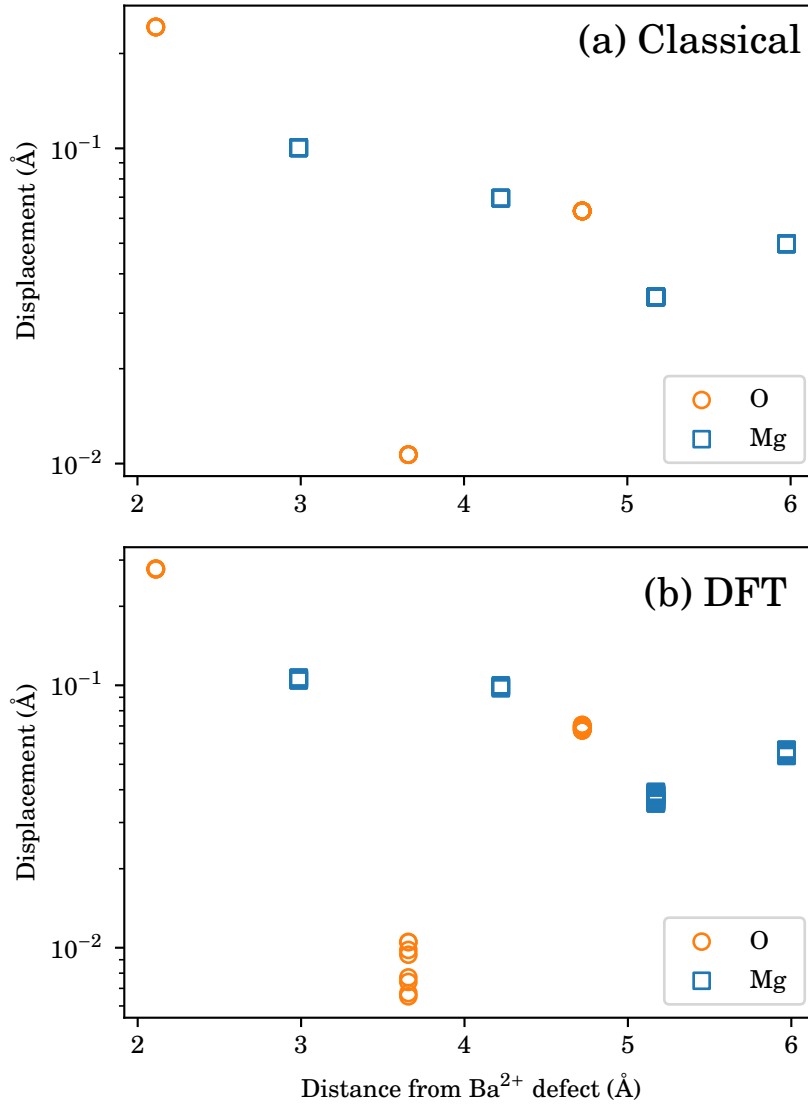


FIGURE 3.17. Atomic displacements of Mg^{2+} and O^{2-} in the first few nearest-neighbouring shells on the logarithm scale as a function of initial ionic distance from the Ba^{2+} defect in a 216-ion supercell of MgO from constant-pressure (a) DFT and (b) classical simulations, respectively. Points overlap due to lattice symmetry, *e.g.*, all the twelve nearest Mg^{2+} ions initially located at *ca.* 3 Å from the Ba^{2+} defect have an approximate displacement of 0.1 Å in both classical and DFT calculations. Only nearest-neighbouring shells within 6 Å from the Ba^{2+} defect are considered. The computational details of the classical calculations based on Buckingham interionic potentials and DFT (GGA-PBESol) calculations are outlined in Subsections 3.2.1 and 3.2.2, respectively.

of ~ 0.25 Å in the classical calculation. Therefore, the non-overlapping points for ions in a given shell indicate the anisotropic displacement of the ion shell. For instance, an obvious non-isotropic displacement is noticeable for the twelve O^{2-} neighbours in the second nearest-neighbouring shell in the DFT simulation, in contrast to those in the classical simulation. Furthermore, the anisotropic atomic displacements in the DFT calculations still occur when a convergence threshold on forces of 1.5×10^{-4} Hartree Bohr $^{-1}$, *i.e.*, half the default value, is used. Hence, decreasing the convergence criterion on forces in the DFT calculation makes only a slight difference in the atomic displacements in the defective structure. However, the displacements are plotted on the logarithm scale; therefore, the absolute values of the atomic displacements are very small, *e.g.*, the largest atomic displacement on the second O^{2-} shell is *ca.* 0.01 Å.

In general, the calculated relative and absolute displacements after the structural relaxation of the ions in the inner shells closer to the defect are much greater than those in the more remote shells, as shown in Table 3.6 and Figure 3.17. For example, the displacements of the O^{2-} ions in the first and second nearest-neighbouring shells of the 64-ion supercell in the classical simulation are 11.46% and 1.09%, respectively. Similarly, the Mg^{2+} ions in the first two nearest-neighbouring shells are displaced by 3.96% and 1.17%, respectively. In all defective supercells, the displacements of the Mg^{2+} ions in the further subsequent shells are smaller than those in the previous inner shells. Interestingly, for the 216-ion defective supercell in the classical simulation, as shown in Figure 3.17, the O^{2-} ions in the third nearest shell (originally situated at ~ 4.7 Å from the defect) are displaced from the Ba^{2+} by 1.34%, while those in the second shell (initially located at *ca.* 3.7 Å from the defect) are only displaced by 0.29% due to the crystal symmetry. This will be briefly discussed and illustrated below. Furthermore, the classical results in Table 3.6 show that the O^{2-} ions in the fourth and fifth shells are slightly displaced from the Ba^{2+} defect, *i.e.*, by 0.33-0.47% and 0.40%, respectively. The general discussion concerning the atomic displacements in the classical simulation also applies to the DFT calculations.

In Table 3.6, with increasing supercell size, we observe that the displacements of the O^{2-} ions in the second nearest-neighbouring shell and the Mg^{2+} ions in the first neighbouring shell from the Ba^{2+} defect in the DFT simulations are slightly smaller than those in the classical calculations. For instance, the displacements of the second-shell O^{2-} neighbours in the 216-ion supercell are 0.22-0.25% and 0.29% in the DFT and classical calculations, respectively. For the 128-ion supercells, the second-shell O^{2-} neighbours are displaced from the Ba^{2+} ion by 0.39% and 0.37% in the classical and DFT simulations,

respectively. The displacements of the O^{2-} ions in the first and third nearest-neighbouring shells in the DFT calculations are similar in supercells considered, while the classical results suggest otherwise. For example, in the DFT calculations, the displacements of the first-shell O^{2-} ions are 12.79-12.98%, 12.98-13.11% and 13.09-13.20% for supercells with increasing size. On the other hand, the displacements in the analogous classical calculations are 11.46%, 11.23% and 11.46%, respectively. The O^{2-} ions in the third neighbouring shell of the optimised 128- and 216-ion supercells in the DFT approach displace from the Ba^{2+} defect by 1.38-1.47% and 1.45-1.47%, respectively. In contrast, the atomic displacements in the classical calculations are 1.24% and 1.34%, respectively.

Here, we investigate further the atomic displacements around a $\text{Ba}_{\text{Mg}}^{\text{x}}$ substitutional defect in a cubic supercell consisting of 2744 ions of MgO with a supercell dimension of 29.575 Å, *i.e.*, the largest MgO supercell considered in this work, in a static-limit classical calculation at constant volume. The atomic positions in the initial lattice configuration are depicted in Figure 3.18. The directions of the atomic displacements of the neighbouring ions from the Ba^{2+} defect after structural relaxation at constant volume are marked by arrows. The size of an arrow on each neighbouring ion indicates the relative magnitude of the displacement; hence is not observable for a very small displacement. Also, we use a colour heatmap to quantify the magnitude of the absolute atomic displacement at each initial atomic position (in Å). The calculated atomic displacements have been refined using linear interpolations between the adjacent atoms. The colour spectrum spreads from red to blue for the greatest and smallest displacements. In analogy to Figure 3.17, the plot of atomic displacements around the Ba^{2+} defect within a spherical radius of 14 Å as a function of initial interionic separation between the Ba^{2+} and neighbouring ions is shown in Figure 3.19.

In Figure 3.18, one can observe that neither the magnitudes nor the directions of the atomic displacements around the incorporated Ba^{2+} ion into MgO are spherically radial. To be more precise, the displacements of all ions are not always pointing away from the Ba^{2+} defect, especially for the ions located on the supercell's edges and at the supercell's corner. Due to crystal symmetry and the artefacts of periodic boundary conditions, the atomic displacements of neighbouring ions are anisotropic (or spherical), *e.g.*, the smaller atomic displacements of the ions situated along the axes aligned with the Ba^{2+} defect can be observed. The ions whose atomic positions are located precisely at the centre of the two Ba^{2+} defects (in the two adjacent images of the supercell) are barely displaced, *e.g.*, the displacements of the ions at the corner and the centre of each of the supercell's edges are small, as indicated by the blue colour contour. As expected, the O^{2-} ions in the

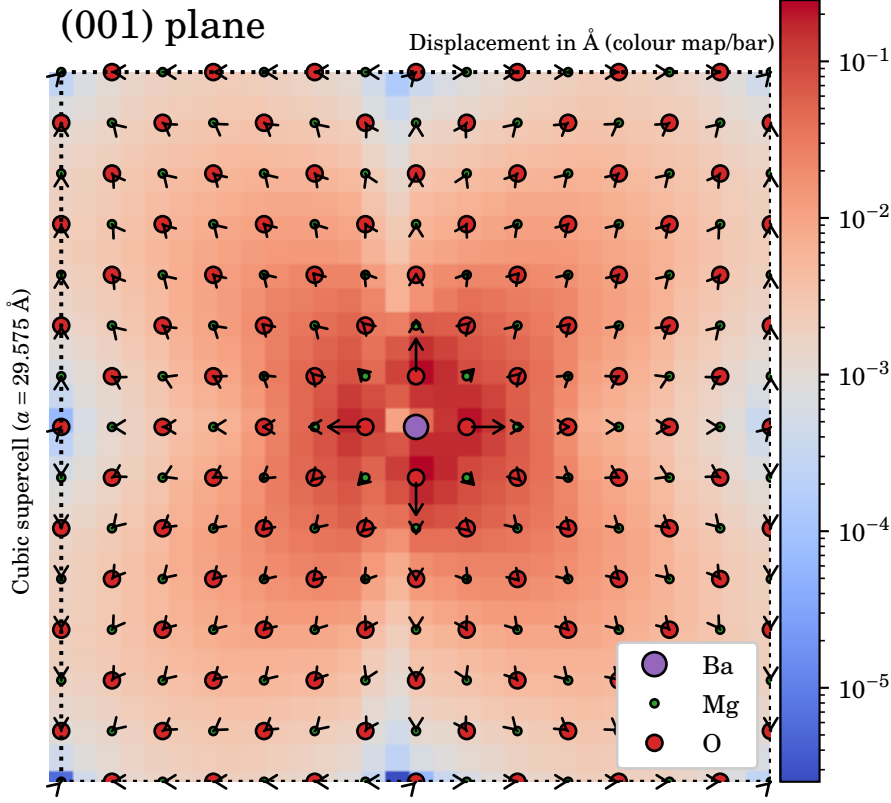


FIGURE 3.18. Atomic displacements around a Ba_{Mg}^x substitutional defect along the (001) plane of an optimised cubic 2744-ion supercell of MgO with a dimension of 29.575 Å in a constant-volume classical calculation in the static limit. The head of the arrow on each of the neighbouring ions indicates the direction of the ionic displacement. The arrow size represents the relative magnitude of the displacement and appears to be absent for very small displacements. The colour spectrum (in the contour map) are also used to display the magnitudes of the atomic displacement (in Å) on the logarithm scale (on the colour bar), *i.e.*, spreading from red to blue for the largest to smallest displacements, respectively. The magnitudes of the atomic displacements have been linearly interpolated between adjacent atoms. Note that the different types of neighbouring ions are plotted at their initial positions using dots with different sizes. The boundaries of the supercell are marked by the dotted lines. The computational details of the classical calculations based on Buckingham interionic potentials are outlined in Subsection 3.2.1.

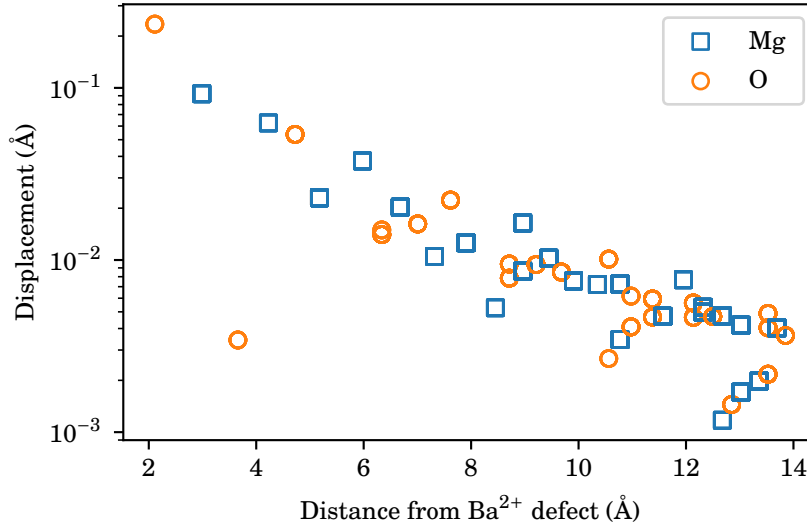


FIGURE 3.19. Plot of atomic displacements around a $\text{Ba}_{\text{Mg}}^{\times}$ substitutional defect in an optimised cubic 2744-ion supercell of MgO with a cell length of 29.757 Å as a function of initial interionic distance from the Ba^{2+} defect in a constant-volume classical calculation in the static limit. Only nearest-neighbouring shells within 14 Å from the Ba^{2+} defect are plotted. Points overlap due to crystal symmetry. The computational details of the classical calculations based on Buckingham interionic potentials are outlined in Subsection 3.2.1.

closest shell to the Ba^{2+} defect show the greatest displacement. Then, the displacement of the ions in a more remote neighbouring shell decreases rapidly with initial interionic distance from the Ba^{2+} defect, as shown in Figure 3.19.

Overall, similar trends and magnitudes of the atomic displacements in the neighbouring shells within a defective supercell size have been observed for both DFT and classical simulations. In both simulation approaches, the degree of atomic relaxation (or displacements) in the first nearest-neighbouring shells is greatest and is much smaller for those in the subsequent shells. As the system size increases, the ions' displacements in a particular shell of interest are only slightly different in the DFT calculations, while the displacements of a given shell may differ significantly in supercells with increasing size in the classical simulation.

Figure 3.20(a) illustrates the defect volume v_p as a function of system size for the $\text{Ba}_{\text{Mg}}^{\times}$ defect formation in bulk MgO in the static limit. These *ab initio* results can directly be compared with those obtained from the classical calculations shown in Figure 3.1(a). Overall, v_p converges as the system size is increased. Compared to the classical v_p as a

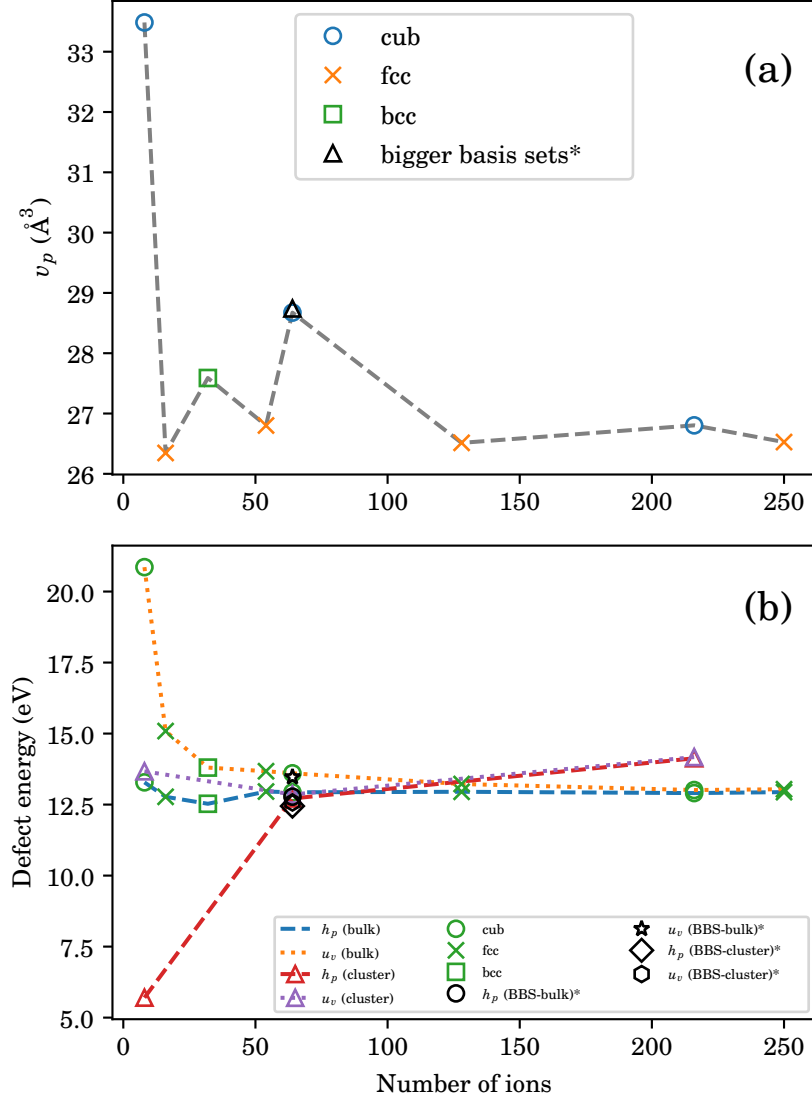


FIGURE 3.20. (a) Defect volume v_p and (b) constant-pressure and constant-volume defect energies (h_p and u_v , respectively) as a function of system size ranging from 8-250 ions for a Ba^{2+} substitutional defect in MgO in the static limit. In (a), v_p was obtained from the periodic bulk only. For the bulk, defect quantities for the three different shapes of the supercells are marked by different symbols. Calculated v_p for a 64-ion supercell using bigger basis sets is also highlighted. In (b), different line styles represent different defect energies.

*The black markers highlight the calculated defect quantities in the supercell and cluster containing 64 ions using bigger basis sets: Hay-Wadt pseudopotential basis set with a 6-3111(2d)G¹⁶³ contraction for Ba, all-electron basis set with a 8-511d1G¹⁶⁴ contraction for Mg, and all-electron basis set with a 8-411d11G¹⁶⁵ contraction for O.

function of system size in Figure 3.1(a), the *ab initio* values show a significantly faster convergence with system size, implying the more localised ions located further away from the point-defect during structural relaxation after the substitution, *i.e.*, a smaller degree of structural deformation due to the $\text{Ba}_{\text{Mg}}^{\times}$ defect, as discussed above. The defect volume is much higher for the smallest system containing only eight ions than those of the bigger supercells due to the higher defect concentration and the stronger defect-defect interactions. We will discuss these effects in the next subsection. Except for the v_p of the smallest system containing eight ions, Figure 3.20(a) shows that the values of v_p are positive and lie between *ca.* 26-29 Å³, while the classical values are only around 20-21 Å³. The discrepancy between these numerical results arise from the longer Ba–O (and Ba–Mg) interatomic distances in the *ab initio* calculations than those in the classical approach, as shown in Table 3.5. Again, the face-centred cubic and body-centred cubic supercells show faster convergence than the simple cubic ones. Here, the v_p of 26.5 Å³ for the largest supercell containing 250 ions, which is a face-centred cubic supercell, should well represent the value of the defect volume in the dilute limit.

For the bulk with a 64-ion supercell, we have also compared the calculated v_p with the one obtained using bigger basis sets for all the three atomic types, which has been included in the plot in Figure 3.1(a). A Hay-Wadt pseudopotential basis set with a 6-3111(2d)G contraction was used for the Ba atom,¹⁶³ while all-electron basis sets with 8-511d1G¹⁶⁴ and 8-411d11G¹⁶⁵ contractions were used for the Mg and O atoms, respectively. Notably, the calculated v_p from the smaller basis sets is in good agreement with the one obtained using the larger basis sets, indicating that the smaller basis sets are already adequate for calculating the defect properties of this system. This is also the case for h_p and u_v shown in Figure 3.20(b).

Figure 3.20(b) shows the variation of the constant-pressure and constant-volume defect energies, *i.e.*, h_p and u_v , respectively, in the static limit with system size. In the system-size range 16-250 ions, the defect energies for the bulk and clusters are all positive, lying between 12.5-15.0 eV and reflecting the substitution of a smaller Mg^{2+} ion by a larger Ba^{2+} ion. These *ab initio* values are in reasonable agreement with those obtained via the classical approach of 15.5-16.5 eV. Consistent with equation (2.35) for smaller systems, the volume constraint results in a higher u_v than h_p . The difference between these two energies vanishes or u_v than h_p both approach the dilute limit as the system size is increased (see equation (2.32)). Furthermore, the calculated h_p and u_v in the 64-ion supercell and cluster using the bigger basis sets are also in line with the ones obtained from the smaller basis sets.

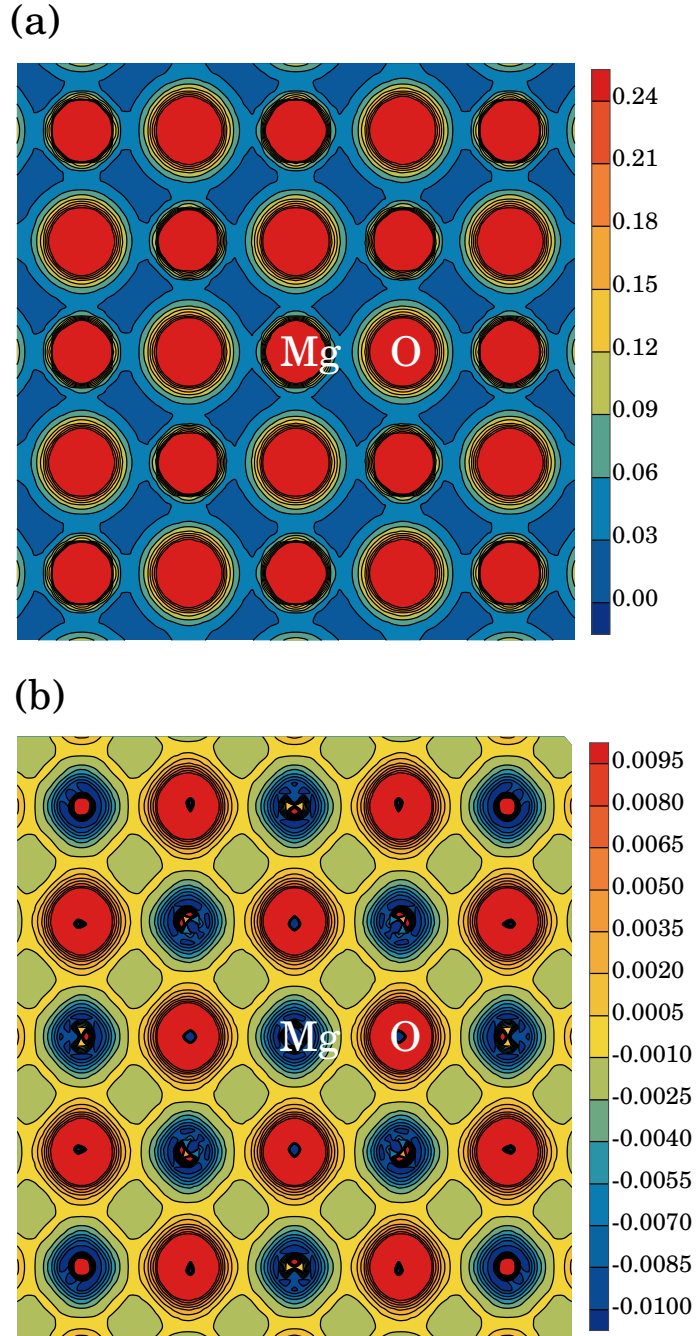


FIGURE 3.21. Electron density of bulk MgO: (a) total electron density and (b) electron-density difference maps in a (100) plane. In each plot, the black isolines represent the values of electron density in atomic units, *i.e.*, electrons/Bohr³. Different electron density ranges are shaded by different colours. The computational details of the DFT (GGA-PBESol) calculations are outlined in Subsection 3.2.2.

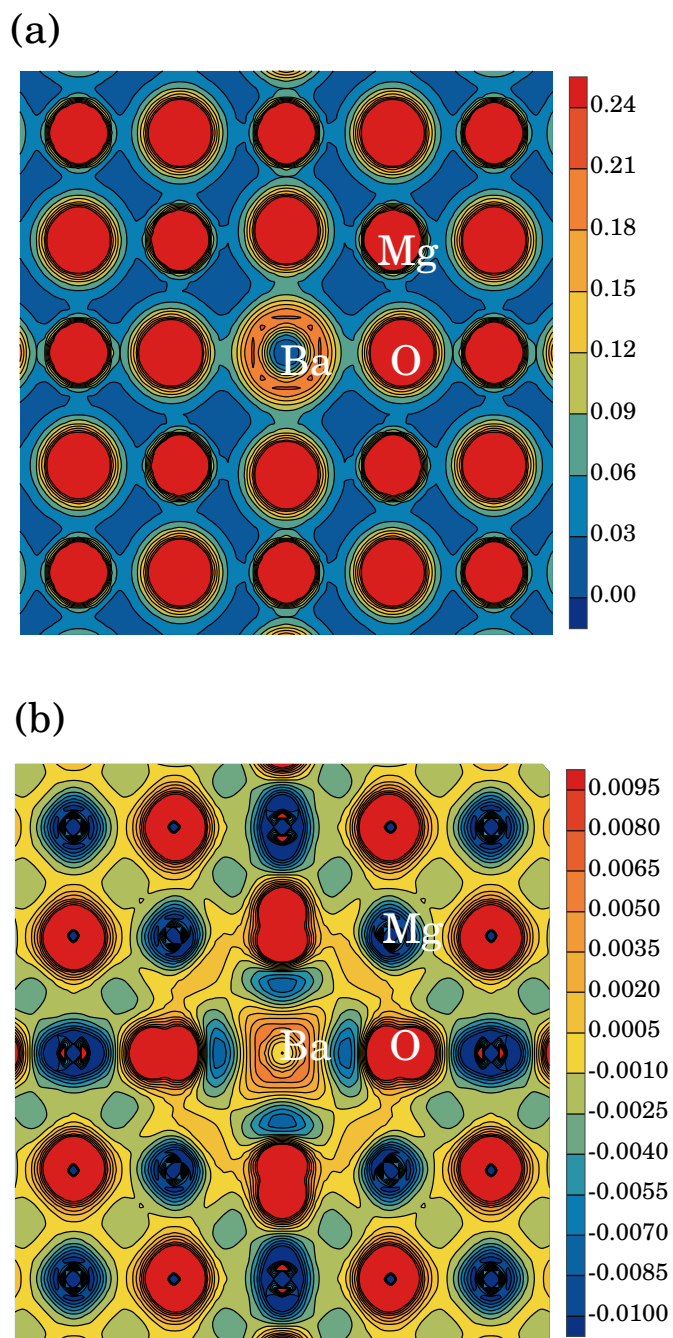


FIGURE 3.22. Electron density of defective bulk MgO with a Ba_{Mg}^x substitutional defect: (a) total electron density and (b) electron-density difference maps in a (100) plane. In each plot, the black isolines represent the values of electron density in atomic units, *i.e.*, electrons/Bohr³. Different electron density ranges are shaded by different colours. The computational details of the DFT (GGA-PBESol) calculations are outlined in Subsection 3.2.2.

One of the major advantages of the first-principles approach is that it provides insight into the electronic structure of a given system of interest, as mentioned earlier. The total electron density maps for the bulk MgO and the defective structure with the $\text{Ba}_{\text{Mg}}^{\times}$ defect are depicted in Figures 3.21(a) and 3.22(a), respectively. The plots were produced using the CRYSPLOT visualisation tool.¹⁶⁶ Compared to the electron density map of bulk MgO in Figures 3.21(a), the electron density map of the defective structure in 3.22(a) shows also the obvious displacements of atoms next to the bigger Ba^{2+} cation to be further away from it. Additionally, the charge- or electron-density difference maps in Figures 3.21(b) and 3.22(b) for the perfect and defective structures, respectively, provide also crucial information on their electronic properties.

The charge-density difference maps are obtained from the difference in electron density in the crystals and the superposition of atomic (or ionic) electronic distributions as the reference charge densities. Strictly speaking, an electron-density difference map is given by subtracting the super-imposed densities of the non-interacting constituent atoms (or ions) from the actual crystal electron density. For a given system, the electron-density difference map provides a pictorial representation of the chemical bonding in the molecule or solid. In bulk MgO, as a polar solid, the change in electron density in the vicinity of the Mg atoms must be negative, while that of the O atoms is positive due to the formation of Mg^{2+} and O^{2-} ions, as shown in Figure 3.21(b). One can also use the same concept for considering the nature of ionic bonding of the defective structure in Figure 3.22(b). Compared to Figure 3.21 for bulk MgO, the density maps for the defective structure in Figure 3.22 show that one can observe the non-spherical electron densities of ions in the vicinity of the substituted point defect. This indicates that the Ba^{2+} ion is much more polarisable than Mg^{2+} .

3.3.4.2 Temperature Variation of DFT Defect Quantities using QHA

To investigate the temperature dependence of the defect thermodynamics of $\text{Ba}_{\text{Mg}}^{\times}$ in MgO computationally, we first determine the lattice parameter of MgO as a function of temperature over 500-1500 K using the quasi-harmonic approximation implemented as the QHA module in CRYSTAL17.^{108,109,168–171} The temperature variation of the lattice parameter a of MgO, referring to the conventional unit cell containing eight ions, is shown in Figure 3.23(a). Furthermore, the temperature variations of the volumetric thermal-expansion coefficient, α_V , and the bulk modulus, K_T , are shown in Figure 3.23(b). These computed QHA properties are in line with the previous theoretical work of Erba and co-workers.¹⁷⁰ Furthermore, the calculated QHA quantities are also in reasonable

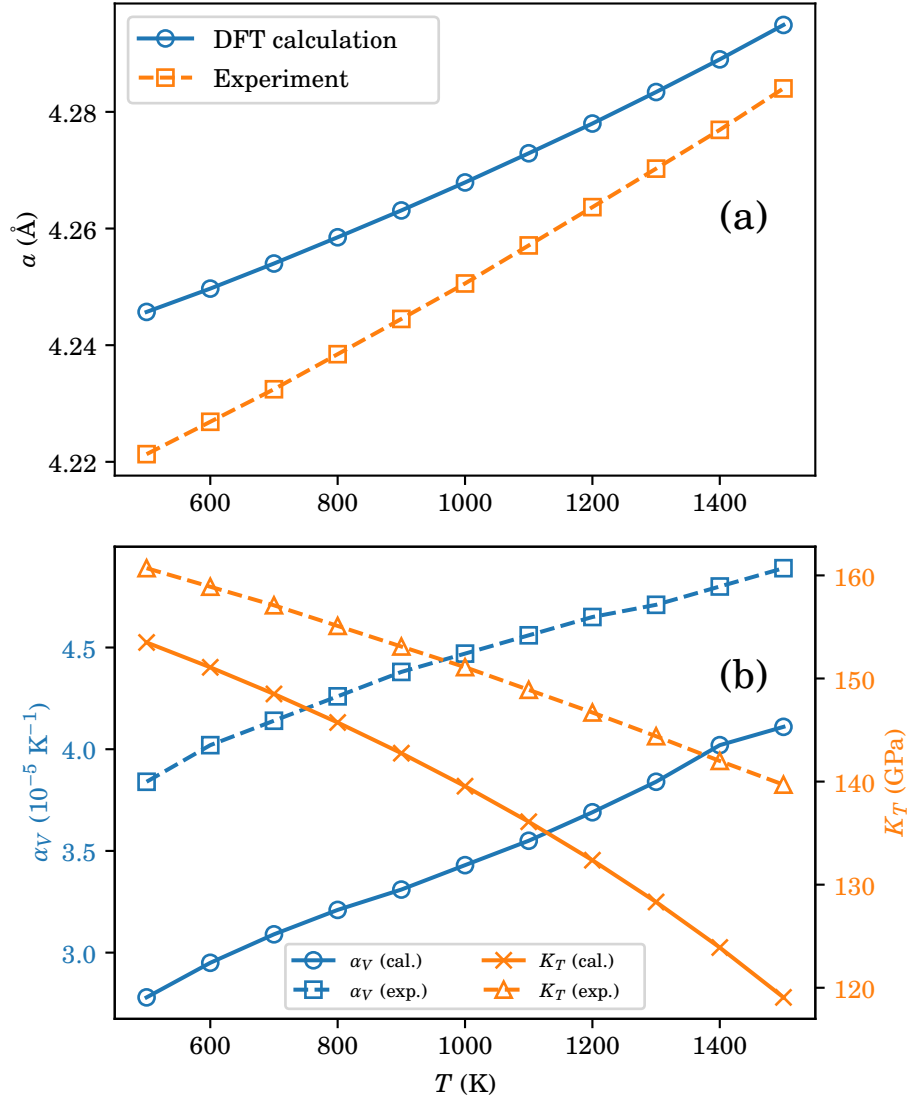


FIGURE 3.23. Temperature variation of experimental and DFT-QHA calculated (a) lattice constant and (b) volumetric thermal-expansion coefficient α_V and bulk modulus K_T of MgO. The experimental values are taken from Anderson and co-workers.¹⁶⁷ The computational details of the DFT (GGA-PBESol) calculations are outlined in Subsection 3.2.2.

agreement in terms of trends and magnitudes with those from the experimental work of Anderson and co-workers.^{167,172} Although the implementation of the QHA module in CRYSTAL17 proves very useful for computing temperature-dependent thermodynamic properties, these calculations are computationally expensive. Therefore, the DFT-QHA calculations are limited to small systems. For these reasons, the DFT calculation of the constant-pressure defect quantities in large supercells is practically non-trivial. Here, we can only present the variation of the *ab initio* defect properties of the $\text{Ba}_{\text{Mg}}^{\text{x}}$ defect formation in bulk MgO at constant volume at each temperature, *i.e.*, making some additional assumptions.

In order to approximate the constant-volume defect quantities of $\text{Ba}_{\text{Mg}}^{\text{x}}$ in MgO at various temperatures, we first construct supercells of bulk MgO with the equilibrium volumes obtained from the QHA calculation mentioned above and replace a Mg^{2+} ion with a Ba^{2+} ion in each structure. After that, we optimise the defective structures with respect to the internal energy U while keeping all the six lattice parameters fixed in the static limit before performing phonon calculations at each volume, *i.e.*, at different temperatures, to evaluate the corresponding vibrational contributions, *i.e.*, using the zero static internal stress approximation (ZSISA).⁸⁵

Using the numerical procedure outlined above, the variation of *ab initio* constant-volume defect properties of the $\text{Ba}_{\text{Mg}}^{\text{x}}$ defect formation in bulk MgO using a simple cubic supercell containing 64 ions over 500-1500 K can then be estimated, and the results are shown in Figure 3.24. In Figure 3.24(a), u_v is higher than f_v at all temperatures over 500-1500 K due to the positive change in constant-volume entropy of defect formation, s_v , as shown in Figure 3.24(b). The difference between u_v and f_v is slightly temperature-dependent as f_v decreases slightly faster than u_v . For instance, u_v is *ca.* 0.1 and 0.3 eV higher than f_v at 500 and 1500 K, respectively. From 500-1500 K, u_v , f_v and s_v decrease approximately by 7.4%, 9.0% and 12%, respectively, while c_v increases by $\sim 85\%$.

These first-principles results can directly be compared to the classical calculations in Figures 3.3 and 3.5. Surprisingly, although the degrees of structural relaxation in both approaches are slightly different, as shown in Table 3.6, the trends and magnitudes of all other constant-volume defect quantities obtained from the DFT calculations are in line with those obtained from the classical simulation. Therefore, this good agreement implies that the computational approaches we have considered here, *i.e.*, the atomistic simulation based on classical crystal-potential models and *ab initio* simulation based on DFT, are both appropriate for studying the defect thermodynamics in crystalline solids and their temperature dependence within the quasi-harmonic approximation

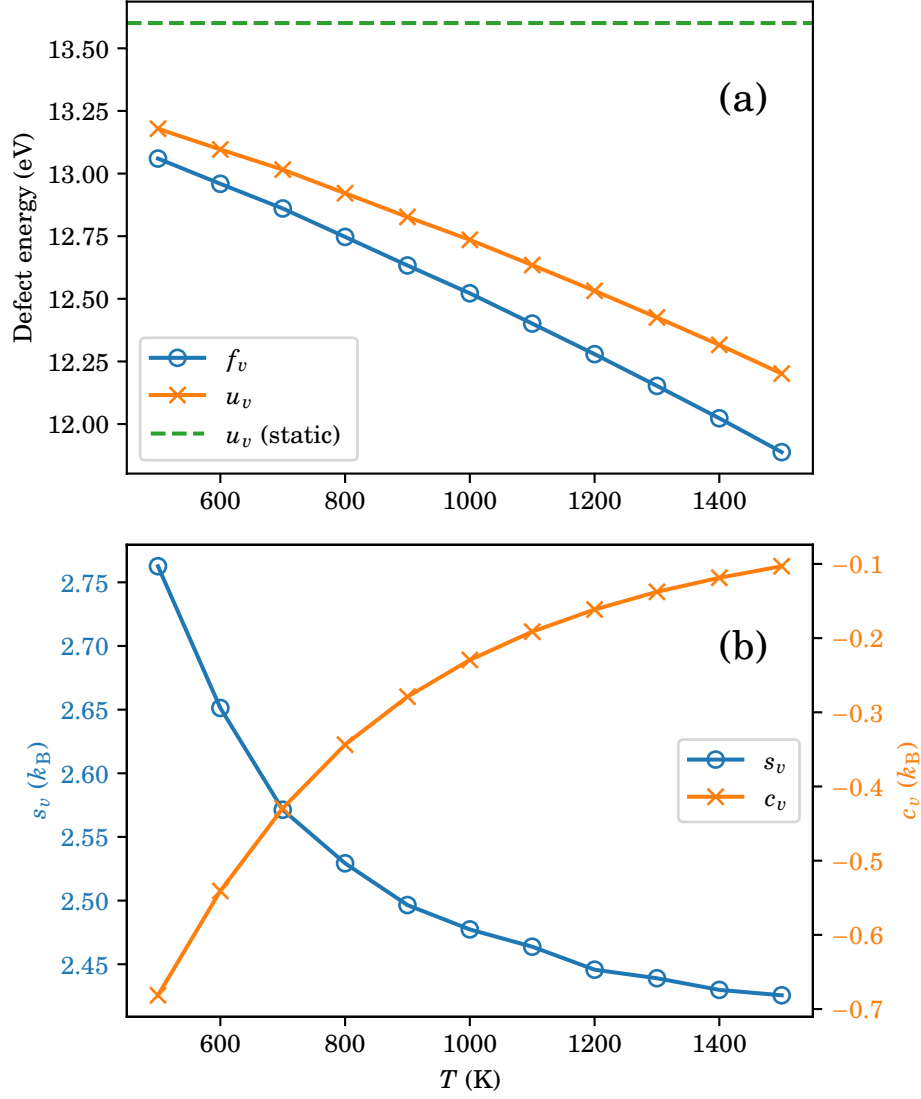


FIGURE 3.24. Temperature variations of (a) defect energies and (b) changes in entropy and heat capacity of Ba_{Mg}^x defect formation in bulk MgO at constant volume. The results were obtained using a 64-ion supercell of MgO. Different defect properties are marked by different symbols. In (a), the horizontal dashed line represents the constant-volume defect energy in the static limit. The computational details of the DFT (GGA-PBESol) calculations are outlined in Subsection 3.2.2.

since they yield exceptionally comparable numerical results. Previously, there have been only a few direct comparisons between calculated defect energies from force-field based and first-principles quantum mechanical approaches,¹⁷³ *e.g.*, De Vita *et al.*¹⁷⁴ reported that the calculated defect formation and migration energies in MgO obtained from DFT calculations are in very good agreement with those obtained using classical calculations based on empirical pair potentials.

3.3.5 Defects in Metals

Previously, we have mainly been concerned with the thermodynamics of a substitutional defect formation in a polar solid, *i.e.*, the $\text{Ba}_{\text{Mg}}^{\text{x}}$ defect in MgO. We have, so far, investigated the effects of (i) temperature, (ii) system size, and (iii) periodicity of the simulation model on defect thermodynamics. Owing to the fact that the quality of the numerical results depends greatly on the description of the interatomic interactions (or *aka* the potential model) for a given solid of interest. However, with the same strategy for modelling the substitutional point-defect formation outlined above, one should be able to evaluate the defect thermodynamics of a particular system adequately by employing any well-developed and high-quality potential model.

In this subsection, we present the defect thermodynamics of the substitution of a Cu atom by a larger Ag atom, $\text{Ag}_{\text{Cu}}^{\text{x}}$, in Lennard-Jones Cu metal and its finite-size clusters as an example of different kinds of solids, a metal, in order to compare the numerical results to those of the $\text{Ba}_{\text{Mg}}^{\text{x}}$ defect in MgO, an ionic solid. Again, in this case, we employ the classical Lennard-Jones potential parameters listed in Table 3.3 and the mixing rules in equation (3.2), which have already been used in the earlier subsection. Here, we consider solely cubic supercells and finite-size clusters of Cu metal.

Figure 3.25 shows the variation of (a) the defect energies (g_p and f_v) and (b) changes in the entropy of defect formation (s_p and s_v) with system sizes ranging from 256-2048 atoms for $\text{Ag}_{\text{Cu}}^{\text{x}}$ in bulk Cu and cubic-shaped Cu clusters at 350 K. These defect thermodynamics as a function of system size can directly be compared with those of the $\text{Ba}_{\text{Mg}}^{\text{x}}$ defect in MgO, as shown in Figure 3.8. As expected, the trends of defect energies for the $\text{Ag}_{\text{Cu}}^{\text{x}}$ defect in bulk Cu and clusters, as shown in Figure 3.25(a), are all consistent with those of the $\text{Ba}_{\text{Mg}}^{\text{x}}$ defect in MgO, as shown in Figure 3.8(a). Consequently, one can use the earlier discussion concerning the defect formation energies for the $\text{Ba}_{\text{Mg}}^{\text{x}}$ defect as a function of system size to explain variations of the defect energies of the $\text{Ag}_{\text{Cu}}^{\text{x}}$ defect in the same fashion. This is also the case for the defect energies of the finite-size Cu clusters.

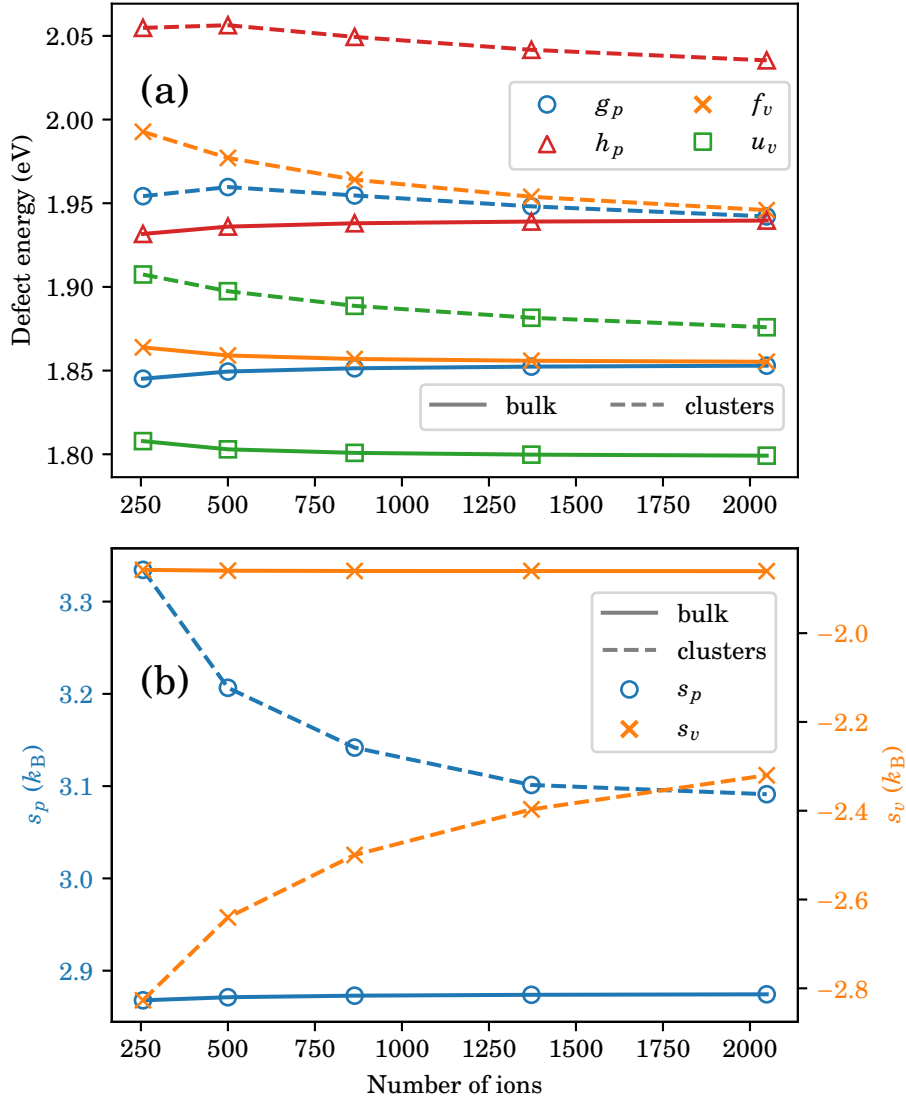


FIGURE 3.25. Variation of (a) defect energies and (b) entropy changes of defect formation with system size for Ag_{Cu}^x in bulk Cu metal and cubic-shaped Cu clusters with system sizes ranging from 256-2048 atoms at 350 K. Solid and dashed lines represent the defect properties of the bulk and clusters, respectively. Different defect quantities are marked with different marker styles. The computational details of the classical calculations based on Lennard-Jones interatomic potentials are outlined in Subsection 3.2.1.

The defect energies for the $\text{Ag}_{\text{Cu}}^{\text{x}}$ defect in Cu metal and its finite-size clusters lie between 1.80-2.05 eV, whose magnitudes are much smaller than those of the $\text{Ba}_{\text{Mg}}^{\text{x}}$ defect (~ 15 -17 eV). This is due to the weaker interatomic interactions in the Lennard-Jones solid than those in the ionic solid. In addition, the size mismatch is smaller in this case, *i.e.*, the van der Waals radius of Ag is only *ca.* 23% bigger than Cu,¹⁷⁵ while the ionic radius of Ba^{2+} is $\sim 88\%$ bigger than Mg^{2+} .¹⁷⁶ In Figure 3.25(a), the defect energies of the clusters are all higher than those of the bulk, and they converge slowly to the bulk limit as the system size is increased. For the largest system size with 2048 atoms, the defect energies of the finite-size cluster are all ~ 0.1 eV higher than those of the bulk.

Additionally, the variation of s_p and s_v with system size is shown in Figure 3.25(b). Again, the smaller (negative) s_v than (positive) s_p can be explained by the previous discussion regarding the influence of the mass effects and the volume constraint on vibrational frequencies, *i.e.*, the mass effects dominate the vibrational frequencies at constant pressure, while the volume constraint dominates the vibrational modes at constant volume. In the case of the $\text{Ag}_{\text{Cu}}^{\text{x}}$ defect, s_v for the bulk is higher than that of the clusters, while the $\text{Ba}_{\text{Mg}}^{\text{x}}$ case suggests otherwise. For the systems with 2048 atoms, s_p for the cluster is *ca.* $0.25k_{\text{B}}$ higher than that of the bulk, whereas s_v for the bulk is approximately $0.20k_{\text{B}}$ higher than that of the cluster.

The temperature variation of the defect properties of the $\text{Ag}_{\text{Cu}}^{\text{x}}$ defect in bulk Cu metal and Cu cluster with a system size of 216 atoms at constant pressure and constant volume are shown in Figures 3.26 and 3.27, respectively. Overall, the trends in both constant-pressure and constant-volume defect quantities are consistent with those of the $\text{Ba}_{\text{Mg}}^{\text{x}}$ defect, as shown in Figures 3.9 and 3.10. Note that the defect volume v_p rises from 7.17 to 7.27 \AA^3 or increases approximately by 1.4% over 150-350 K. In terms of the defect energies, Figures 3.26 and 3.27 show that the difference in each of the defect energies of the bulk compared to that of the cluster depends hardly on temperature. The differences in those four defect quantities are almost identical at all temperatures, *i.e.*, all the four defect energies of the cluster are *ca.* 0.1 eV higher than those of the bulk over 150-350 K.

Over the temperature range considered, s_p for the $\text{Ag}_{\text{Cu}}^{\text{x}}$ defect in Cu metal and Cu cluster consisting of 256 atoms lies between 1.75-3.27 k_{B} , and it increases as the temperature is elevated. The difference between s_p of the cluster and that of the bulk appears to be marginally temperature-dependent. For example, s_p of the cluster is approximately 0.47 k_{B} and 0.52 k_{B} higher than that of the bulk at 150 and 350 K, respectively. On the other hand, s_v for both systems lies between -0.8 k_{B} and -2.9 k_{B} , and decreases as the temperature is raised from 150-350 K. s_v of the bulk is $\sim 1k_{\text{B}}$ higher than that of the

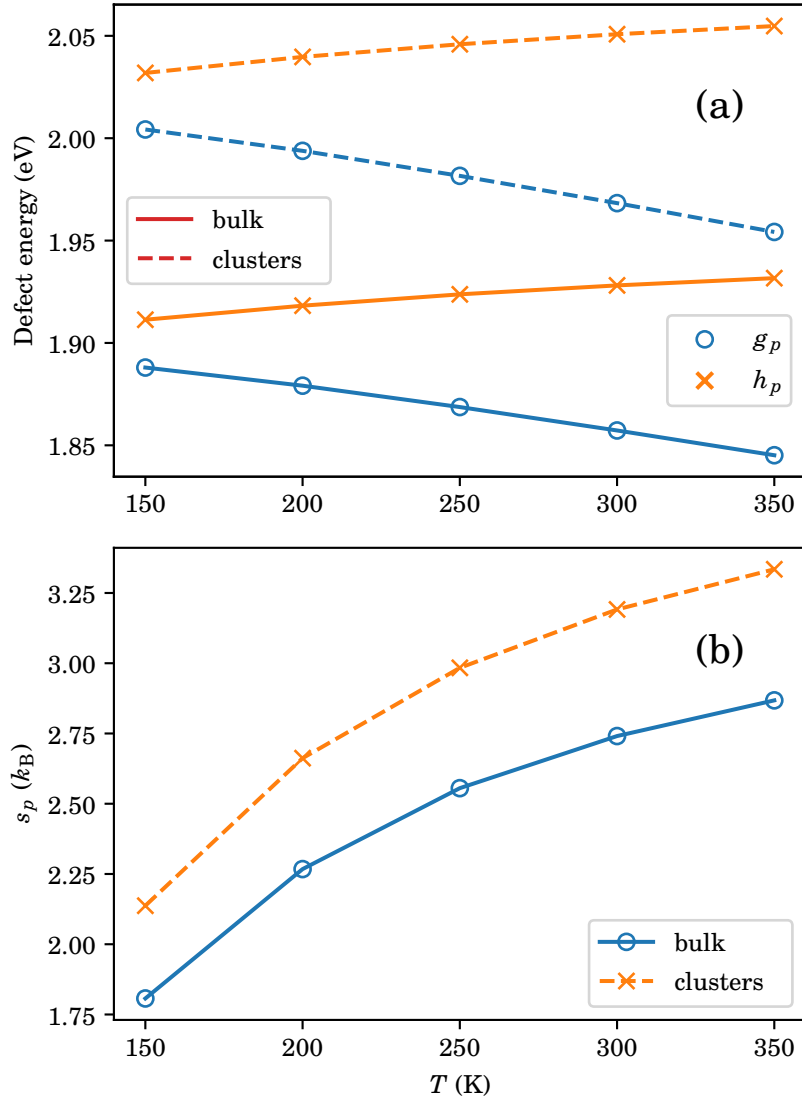


FIGURE 3.26. Temperature variation of (a) defect energies and (b) entropy changes of Ag_{Cu}^x in bulk Cu metal and Cu cluster containing 256 atoms at constant pressure. Solid and dashed lines represent the defect properties of the bulk and cluster, respectively. In (a), different defect energies are marked by different symbols. The computational details of the classical calculations based on Lennard-Jones interatomic potentials are outlined in Subsection 3.2.1.

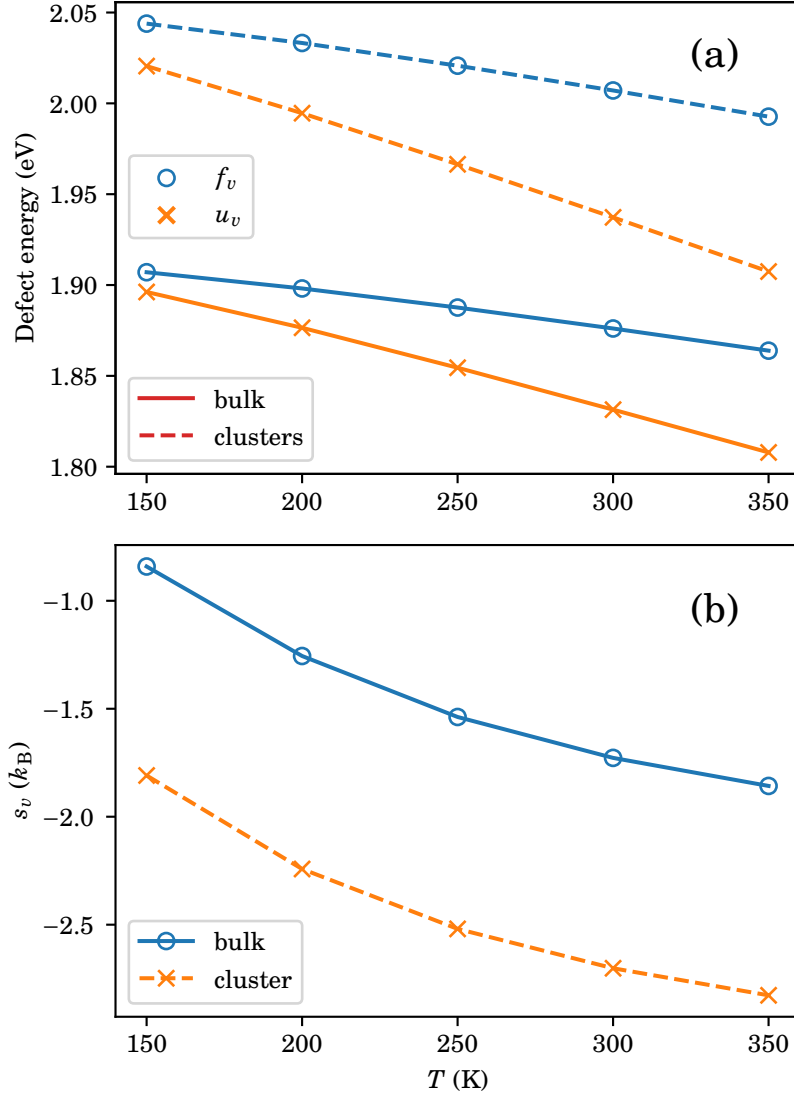


FIGURE 3.27. Temperature variation of (a) defect energies and (b) entropy change of Ag_{Cu}^x in bulk Cu metal and Cu cluster containing 256 atoms at constant volume. Solid and dashed lines represent the defect properties of the bulk and cluster, respectively. In (a), different defect energies are marked by different symbols. The computational details of the classical calculations based on Lennard-Jones interatomic potentials are outlined in Subsection 3.2.1.

cluster at all temperatures.

The changes in constant-volume heat capacity, c_v , for the Ag_{Cu}^x defect in bulk Cu metal and clusters as a function of system size ranging from 256-2048 atoms at 350 K are shown in Figure 3.28(a). In the range of system size considered, c_v for the clusters is higher than that of the bulk. For the smallest and largest systems, c_v of the cluster is $0.09k_B$ and $0.05k_B$ higher than that of the bulk, respectively. Again, c_v for all systems is negative since the volume constraint dominates the vibrational frequencies at constant volume, as discussed previously.

Moreover, Figure 3.28(b) shows the temperature variation of c_p and c_v of the Ag_{Cu}^x defect in bulk Cu metal and cluster with a system size of 256 atoms in the temperature range 150-350 K. Note that c_p is calculated using equation (3.10). At all temperatures, c_v is negative, while c_p is positive, again implying the dominance of the volume constraint and the mass effects over the vibrational frequencies at constant volume and constant pressure, respectively. From 150-350 K, c_v of the bulk and the cluster increase approximately by 50% and 62%, respectively. Noticeably, c_v for the bulk is higher than that of the cluster at 150 K, while it is otherwise at higher temperatures. On the contrary, c_p for the bulk and the cluster decrease by *ca.* 56% and 59%, respectively, over 150-350 K.

So far, we have clearly shown that the defect thermodynamics of another type of solids, *e.g.*, the Ag_{Cu}^x defect in Cu metal and clusters modelled by a classical Lennard-Jones potential force field, can successfully be investigated. For this case, one can well apply the previous analysis of the effects of temperature, system size and periodicity on the defect thermodynamics of the Ba_{Mg}^x defect in MgO. Hence, the quasi-harmonic approximation proves very useful for calculating defect free-energies and investigating the crucial effects on defect thermodynamics regardless of the type of solid of interest when a well-developed and high-quality classical potential model is in use.

3.3.6 Effects of Defect Clustering

So far, we have considered the simulation of substitutional defects in crystalline solids with only a single defect in their periodic supercells. With the periodic-boundary conditions, a smaller defective supercell results in a higher defect concentration and, more importantly, a stronger defect-defect interaction. To avoid the unnecessary (or artificially) high defect concentration and strong defect-defect interaction within the supercell approach, one must perform a convergence test of the defect properties with respect to supercell size before choosing a large enough and suitable supercell for modelling the defect. In this subsection, however, we investigate systematically the dependence of de-

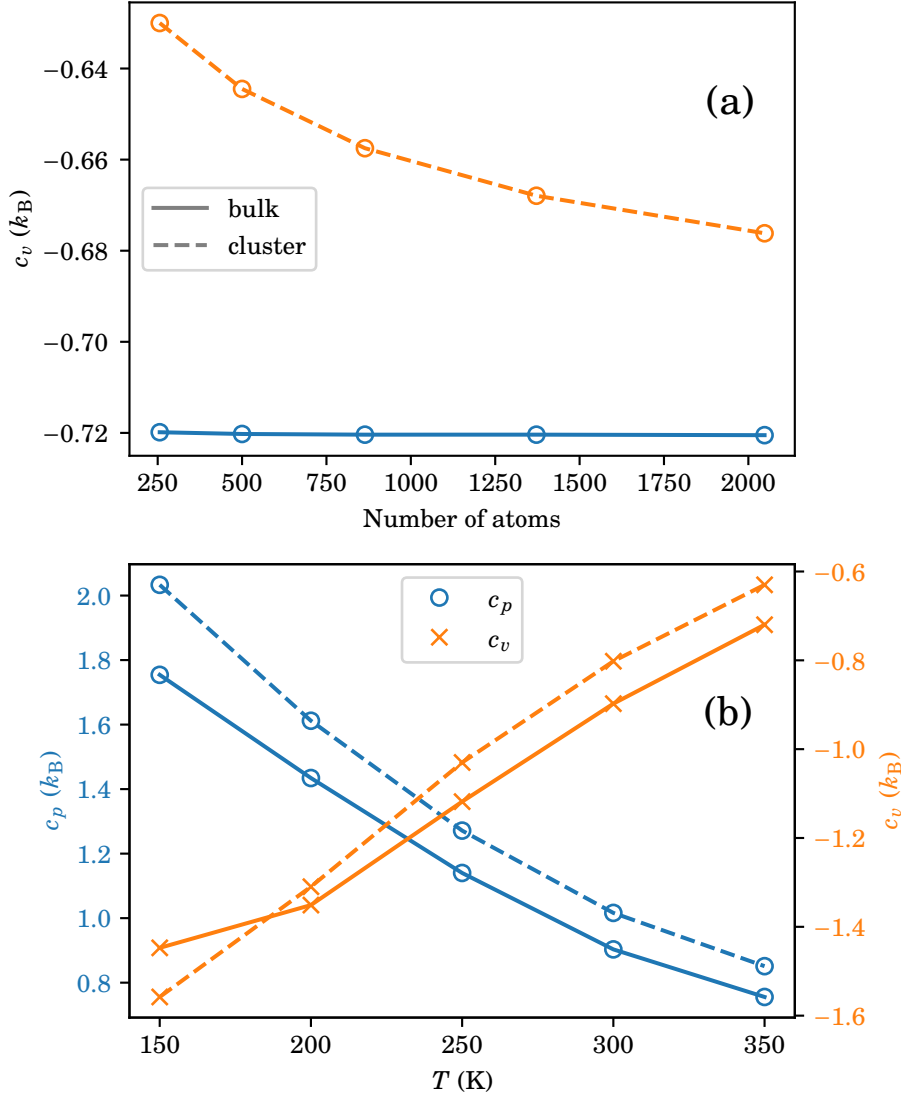


FIGURE 3.28. Variations of changes in heat capacity of Ag_{Cu}^x in Cu metal and cluster with (a) system size and (b) temperature. For (a), c_v of each system size was calculated at 350 K. For (b), a supercell and a cluster of Cu metal consisting of 256 atoms were used for all temperatures in order to obtain c_p and c_v , which are highlighted by different symbols. Solid and dashed lines represent the change in heat capacity for the bulk and clusters, respectively. The computational details of the classical calculations based on Lennard-Jones interatomic potentials are outlined in Subsection 3.2.1.

fect thermodynamics on defect clustering, *i.e.*, the assembling of multiple substitutional point-defects in crystals in the static limit.

Firstly, we study the dependence of three defect properties, *i.e.*, v_p , h_p and u_v , of the Ba_{Mg}^x defect in a 1000-ion supercell of MgO containing two Ba^{2+} ions on Ba–Ba interionic spacing, $d_{\text{Ba–Ba}}$. In this case, we intend to explore systematically the dependence of those defect quantities on the interionic separation between the two Ba^{2+} substitutional defects defining the strength of the defect–defect interaction, *i.e.*, a shorter defect-defect distance accounts for a stronger defect-defect interaction. Secondly, we illustrate briefly the dependence of the Ba_{Mg}^x defect thermodynamics in MgO on Ba^{2+} defect concentration. In the latter case, there might be a number of possible defective structures at a given defect concentration. However, in this present work, we take only the supercell with the closest packing of the defects at each concentration into account.

To observe the dependence of v_p , h_p , and u_v on Ba–Ba distance, 23 different defective 1000-ion supercells of MgO containing two Ba^{2+} substitutional defects with various interionic separations ($d_{\text{Ba–Ba}}$) varying from *ca.* 3.0–17.5 Å have been first constructed. The schematic representations of the first four structures with the shortest $d_{\text{Ba–Ba}}$ are shown in Figures 3.30(a)–(d), respectively. Note that the $d_{\text{Ba–Ba}}$ distances are measured in the optimised structures. Using these initial structures, the defect thermodynamics as a function of $d_{\text{Ba–Ba}}$ at constant pressure and constant volume in the static limit can separately be computed.

The variation of v_p per defect with Ba–Ba spacing is shown in Figure 3.30(a). The horizontal dashed line marks the calculated v_p from the same supercell containing only a single Ba^{2+} substitutional defect. Overall, v_p per defect tends to decrease as the Ba–Ba spacing is increased. This implies that the aggregation of substitutional defects tend to enlarge the defective crystal volume. Interestingly, v_p per defect of the second structure with a Ba–Ba distance of *ca.* 4.5 Å is $\sim 0.32 \text{ Å}^3$ larger than the first structure, whose $d_{\text{Ba–Ba}}$ is approximately 2.5 Å. The sudden increase in v_p per defect arises from the more strained central O^{2-} ion confined in the Ba–O–Ba linear alignment, as shown in Figure 3.29(b). The huge structural strain causes the longer interionic separations in the relaxed structure and results eventually in a greater amount of structural distortion and a larger v_p per defect. This is also the case for the third structure in Figure 3.29(c), where there is a perfectly in-between Mg^{2+} ion in the linear arrangement of Ba–Mg–Ba, leading to a larger v_p per defect than the single-defect limit. However, v_p per defect for the first structure with the linear Ba–O–Ba arrangement is approximately 0.1 Å^3 larger than that of the third structure with the linear Ba–Mg–Ba alignment due to the stronger

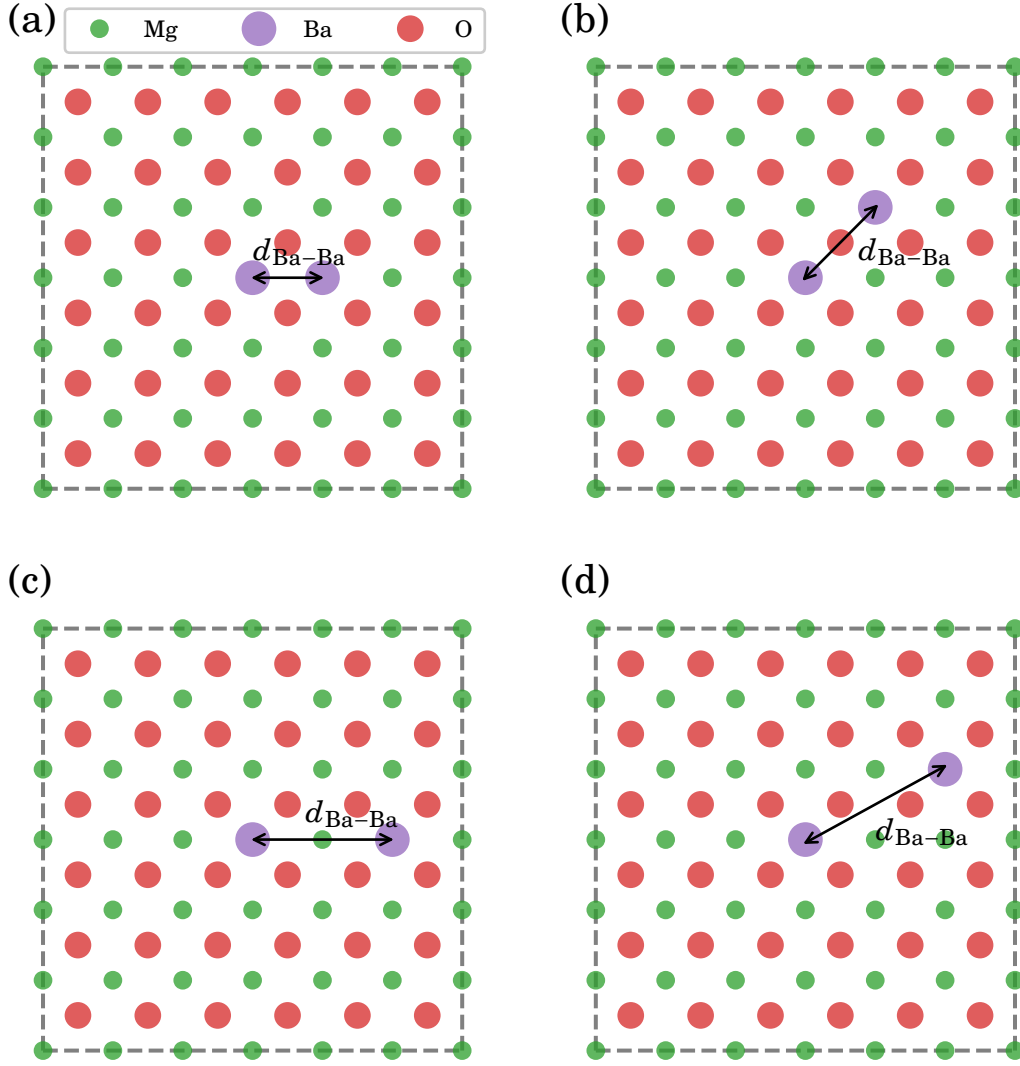


FIGURE 3.29. Schematic illustration of the first four initial defective 1000-ion supercells of bulk MgO with two Ba^{2+} ions of the Ba_{Mg}^x substitutional defects. The interionic separation of the two Ba^{2+} ions ($d_{\text{Ba-Ba}}$) are marked by the two-headed arrows. Mg^{2+} and Ba^{2+} ions are represented by the smallest and largest dots, respectively.

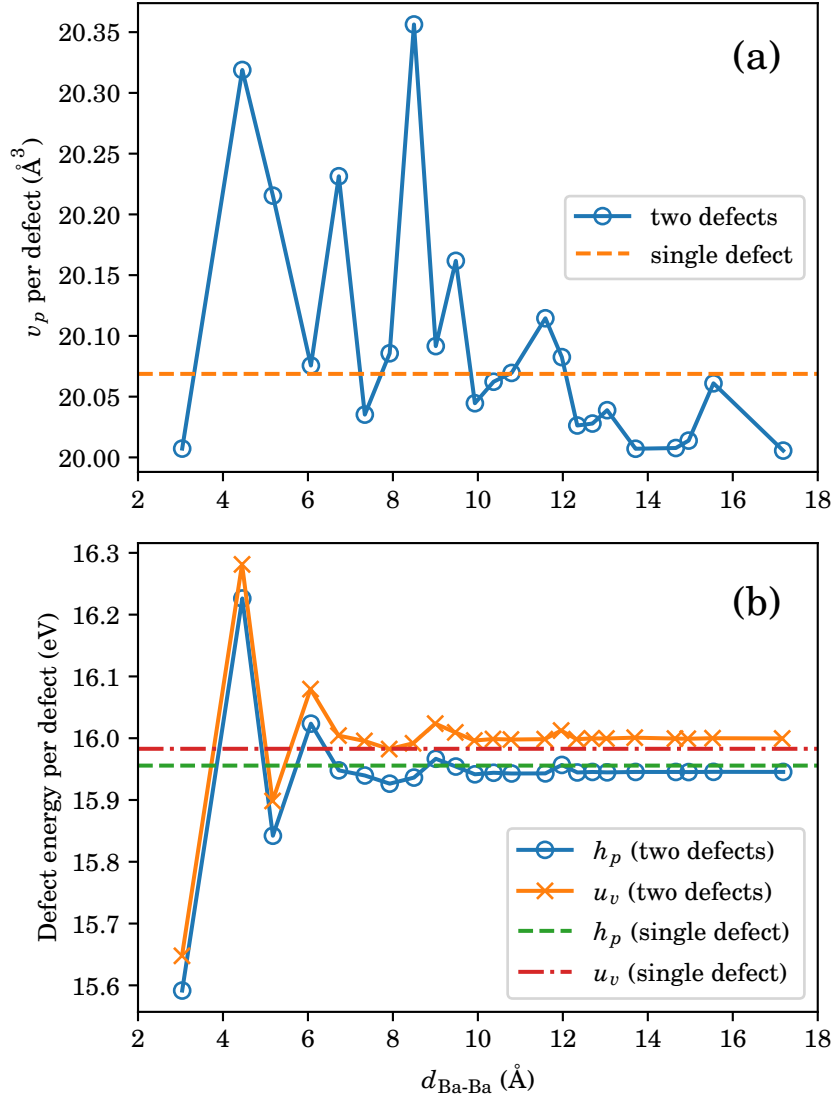


FIGURE 3.30. Variation of (a) defect volume and (b) defect energies per defect with interatomic distance of two Ba^{2+} ions of the $\text{Ba}_{\text{Mg}}^{\text{x}}$ substitutional defects ($d_{\text{Ba-Ba}}$) in bulk MgO with a supercell containing 1000 ions in the static limit. In both plots, the horizontal dashed lines represent the defect quantities obtained from the same supercell consisting only one $\text{Ba}_{\text{Mg}}^{\text{x}}$ defect. Different defect energies are highlighted by different markers. The construction of the initial defective supercells is consistent with Figure 3.29. The computational details of the classical calculations based on Buckingham interionic potentials are outlined in Subsection 3.2.1.

short-range repulsion between the oppositely charged Ba^{2+} and O^{2-} ions. The idea can also be used to explain the sudden increases in v_p per defect, *e.g.*, v_p of the fifth and eighth structures in Figure 3.30(a). Furthermore, the larger v_p for smaller supercells can also be explained by this concept, *e.g.*, in Figures 3.1(a) and 3.20(a). For the structures with $d_{\text{Ba-Ba}}$ larger than *ca.* 10 Å, the increases in v_p per defect, if any, are not dramatic due to the smaller structural strain.

In Figure 3.29(a) for the first structure with the shortest $d_{\text{Ba-Ba}}$ possible, on the contrary, there is no ion between the two Ba^{2+} ions. In this case, there is no enormous repulsive interaction between pairs of ions, leading to a less strained structure and smaller v_p per defect than the single-defect limit. One could also imagine that the combination of the two Ba^{2+} defects located very close to each other gives rise to a single substitutional defect with a charge of +4, leading to stronger cation-anion attractive interactions, shorter interionic distances and, hence, a smaller v_p per defect compared to the single-defect limit. Apart from the special cases for the structures with linear alignments of ions with the two defects, a larger defect-defect separation results in a smaller v_p per defect than the single-defect limit. Strictly speaking, the further apart two defects tend to decrease the defective crystal volume.

Figure 3.30(b) shows the variation of h_p and u_v per defect with $d_{\text{Ba-Ba}}$. As expected, as the defect-defect spacing is increased, the defect energies are in better agreement with their single-defect limits. The two defects that are situated very far away from each other, *i.e.*, with a very large $d_{\text{Ba-Ba}}$, can be viewed as completely-separated two Ba_{Mg}^x point-defects. Again, u_v per defect is higher than h_p per defect at all Ba-Ba distances as a direct consequence of the volume constraint in the constant-volume calculations. The defect energies per defect for the first structure, in Figure 3.29(a), are much lower than their single-defect limits due to the stronger attractive interactions between the (approximately) more positive (combined) substitutional defect cation with the surrounding anions. This concept can also be used to describe the decrease in defect energies per defect of the third structure, in Figure 3.29(c). The defect energies per defect for the second and the fourth structures, in Figures 3.29(b) and 3.29(d), on the other hand, are higher than the single-defect limits due to the strong repulsive interactions between the Ba^{2+} cations and their O^{2-} neighbours.

The variation of defect quantities per defect with mole fraction (concentration) of Ba_{Mg}^x defects, X_{Ba} , in a 1000-ion supercell of MgO is shown in Figure 3.32. In this study, X_{Ba} ranges from 0.002 to 0.064 for 1-32 Ba_{Mg}^x defects in the supercell of bulk MgO containing 1000 ions in total. Note that X_{Ba} indicates the number of the Ba^{2+} ions divided

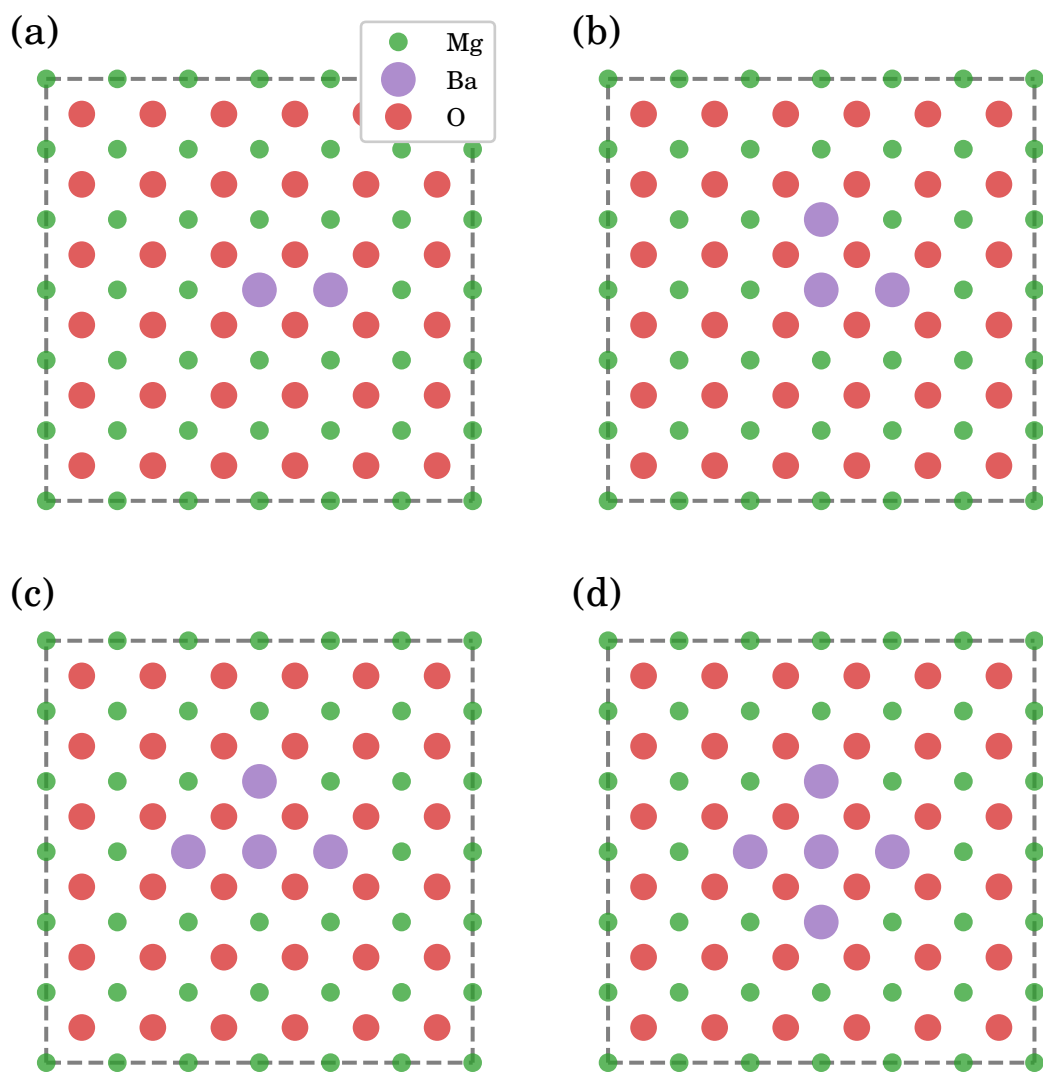


FIGURE 3.31. Schematic illustration of the first four initial defective 1000-ion supercells of bulk MgO with multiple (2-5) Ba^{2+} ions of the Ba_{Mg}^x substitutional defects. The successive substitution is done by replacing any of the Mg^{2+} ions located closest to the existing defect cluster by a Ba^{2+} . Mg^{2+} and Ba^{2+} ions are represented by the smallest and largest dots, respectively.

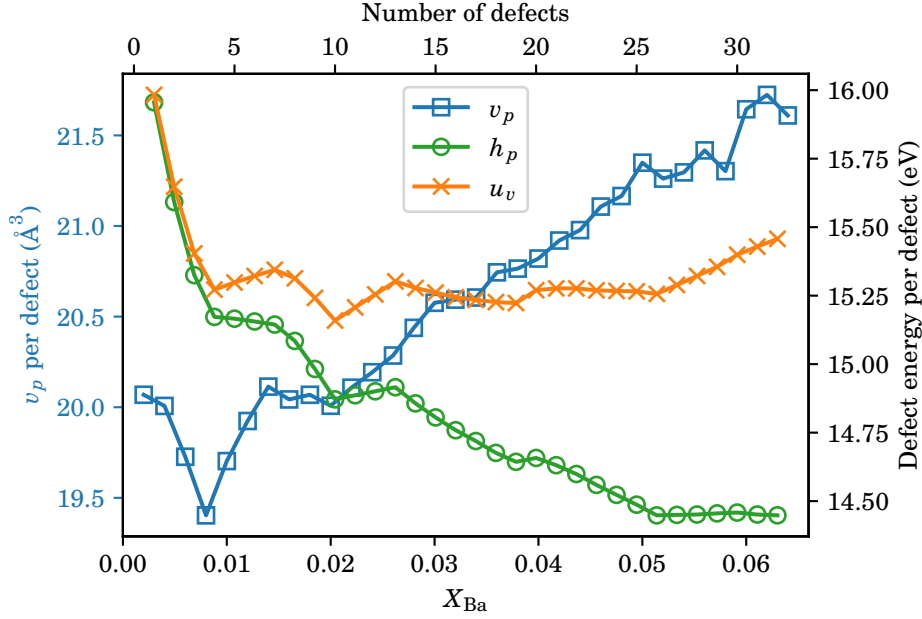


FIGURE 3.32. Variation of defect volume and defect energies per defect with mole fraction (or number) of the Ba^{2+} ions of the multiple Ba_{Mg}^x substitutinal defects (X_{Ba}) in bulk MgO with a supercell containing 1000 ions in the static limit. Different defect quantities are highlighted by different markers. The construction of the initial defective supercells is consistent with Figure 3.31. The computational details of the classical calculations based on Buckingham interionic potentials are outlined in Subsection 3.2.1.

by 500, the total number of the cations in the supercell. At a given mole fraction, only the supercell with the closest packing of the Ba_{Mg}^x defects is used to calculate the defect thermodynamics. Figures 3.31(a)-(d) show schematically the first four initial defective structures with 2-5 Ba_{Mg}^x defects, *i.e.*, with X_{Ba} ranging from 0.002-0.010, respectively.

In Figure 3.32, u_v per defect is higher than h_p per defect at all Ba^{2+} concentrations due to the volume constraint in the constant-volume calculations. At constant pressure, h_p per defect decreases rapidly, while v_p per defect rises dramatically, *i.e.*, for supercells with X_{Ba} higher than 0.008, as X_{Ba} is increased. The previous discussion concerning the significant reduction in v_p per defect for supercells with two Ba_{Mg}^x defects can be used to describe the decrease in v_p per defect for the supercells with low X_{Ba} here in this case. The dramatic decrease in h_p per defect with the increasing X_{Ba} indicates that the defects prefer thermodynamically to aggregate or cluster together, while the defect volume per defect increases (or the volume of the defective crystal expands) to accommodate more

of the bigger Ba^{2+} cations. At low X_{Ba} , u_v per defect decreases as X_{Ba} is increased and remains approximately constant when the concentration of the Ba_{Mg}^x defects is higher. However, u_v per defect increases gradually when X_{Ba} is higher than 0.050, again due to the volume constraint.

3.3.7 Applications

So far, we have shown that we can calculate defect free-energies in solids and clusters via atomistic simulation based on classical potential models and first-principles DFT using quasi-harmonic lattice dynamics (QLD). The simulation technique is not only appropriate for computing defect thermodynamics over a wide range of temperatures, *i.e.*, up to two-thirds of the melting points, but the approach also proves very useful for the calculation of defect quantities under a wide range of pressures.^{89,139,140,177} Moreover, this simulation technique can generally be employed to study crystalline solids' temperature- and pressure-dependent properties. For more than two decades now, our research group, in particular, has extensively been using this fruitful technique to study computationally the properties and behaviour of numerous types of crystalline solids at various temperatures and pressures.

For instance, in combination with *ab initio* Hartree-Fock theory and classical molecular dynamics (MD), QLD can give insightful information on the superionic properties of Li_2O at high temperatures.¹⁷⁸ Apart from bulk properties of metal oxides, *e.g.*, MgO , Li_2O and NiO , one can use the lattice dynamics within the quasi-harmonic approximation to calculate their surface free-energies at elevated temperatures.¹⁷⁹ Most recently, the properties of Fe_3S under the condition of planetary cores at high temperatures and pressures have been explored via *ab initio* DFT calculations using the QHA.¹⁸⁰

However, in the following chapter, we focus mainly on two geochemical applications of the calculation of defect thermodynamics or particularly defect formation energies in crystalline solids: (i) trace-element partitioning in minerals and melts, and (ii) solid solutions and highly-disordered systems. Previously, the atomistic computer simulation of the incorporation of trace elements including noble gases in minerals and melts has comprehensively reviewed by, *e.g.*, Allan and co-workers,^{127,173,181} and more recently by Dubacq and Plunder.¹⁸² The simulation technique based on QLD for studying the properties of solid solutions and highly-disordered systems has also previously been summarised in review articles by members of our research group.^{183,184}

3.4 Conclusions

The quasi-harmonic approximation proves very useful for computing constant-pressure and constant-volume defect free-energies in various types of crystalline solids within the supercell approach both classically and *ab initio*. Quasi-harmonic lattice dynamics can be used to probe the effect of temperature on those defect thermodynamics, which has often been neglected in previous studies. We have shown that the defect properties, *i.e.*, for a substitutional Ba^{2+} defect in MgO as a study case, are strongly temperature-dependent; hence, the temperature effect is not negligible as universally assumed. We have shown that defect thermodynamics depend on system size when small supercells are used, and the defect quantities converge to their dilute limit as the system size increases. For that reason, large supercells are required to ensure convergence towards the dilute-limit values. The difference between constant-pressure and constant-volume defect properties in the dilute limit becomes negligible.

In the quasi-harmonic approach, at a given temperature, the vibrational entropy and heat capacity of a particular system depends solely on the vibrational frequencies, which rely on the interatomic force constants and atomic masses. For the incorporation of a larger (and heavier) substitutional defect in a lattice crystal, there are two competing effects on the changes in entropy and heat capacity of the defect formation at constant volume. The volume constraint increases the vibrational frequencies resulting in a lower entropy and heat capacity, whereas the heavier substitutional defect decreases the frequencies leading to a higher entropy and heat capacity. On the contrary, the volume constraint is much less significant at constant pressure; hence the mass effect dominates. Amongst the defect thermodynamics of our interest, the constant-pressure heat capacity is the least straightforward to compute as the parameters relating to the lattice expansion are required. However, we have shown that the numerical calculation of the constant-pressure heat capacity can be done in various ways. Evaluating the constant-pressure heat capacity via the partial derivatives of enthalpy with respect to temperature is the most fundamental and convenient approach. Plots of phonon density of states can be used to observe and compare the changes in entropy and heat capacity of defect formation at constant volume and constant pressure.

Alternatively, non-periodic finite-size clusters of solids can be used instead of periodic supercells when modelling the substitutional defects in crystals. Compared to the supercell approach, calculating the defect thermodynamics of non-periodic clusters is computationally cheaper, and this can be performed via many widely used *ab initio* codes

for molecular modelling. The defect properties obtained from the two models are expected to be comparable when a large finite-size cluster is in use, *i.e.*, the defect quantities of larger finite-size clusters are closer to the bulk limit. However, there will always be differences between the defect properties of clusters and periodic systems due to the interfaces in the non-periodic model. The discrepancy between the defect thermodynamics obtained from the two models arises from the different degrees of structural relaxation at (or near) the surfaces in defective and perfect non-periodic structures. Furthermore, the degrees of structural relaxation around the point defect in the periodic and non-periodic models might also be significantly different. For clusters with increasing size, the degrees of the surface relaxation in defective and perfect clusters are expected to be very similar but not identical. As the number of atoms at (and near) the surfaces and those atoms that surround the incorporated defect grows very rapidly as the cluster size is increased, these accumulating effects are the direct consequence of the significant difference in defect properties of clusters and periodic bulk systems. Therefore, one should be aware of these finite-size effects when choosing between the periodic and non-periodic models for simulating defects in crystals. The two approaches have their own merits and drawbacks regarding software availability and computational cost.

In addition to the computation of the defect thermodynamics via the classical approach based on empirical force-field parameters, we have also performed analogous calculations via first-principle methods based on density functional theory (DFT) in order to compare the numerical results obtained from these two simulation approaches directly. Although the DFT calculations are much more computationally expensive than the classical simulation, they can provide insights into the electronic structures and related properties of the systems of interest. For instance, electron density plots can be used to study the nature of the chemical bonding and the polarisability of different atomic types in crystalline solids. The atomic displacements of the neighbouring ions due to the Ba^{2+} substitutional defect in MgO in both simulation approaches have thoroughly been investigated. Similar trends and magnitudes of the atomic displacements in the neighbouring shells within the defective supercells have been found in both simulation techniques. Ions in the inner neighbouring shells displace away from the incorporated defect more greatly than the more remote ones. The atomic displacements around the defect in the classical simulation are more isotropic than those in the DFT calculation. However, neither the magnitudes nor the directions of the atomic displacements are spherically radial and isotropic due to crystal symmetry and the artefacts of periodic boundary conditions. Even though the structural relaxations around the point defect in

both approaches are slightly different, the defect thermodynamics obtained from the two methods agree well with each other.

The temperature and system-size dependence of the defect thermodynamics in metals, where the bonding is very different from ionic oxides, has also been examined. For example, we have investigated the substitution of a Cu atom by a Ag atom in classical Lennard-Jones Cu metal and clusters. Interestingly, we have found that the trends of the defect thermodynamics in different types of crystalline solids are similar. Accordingly, the quasi-harmonic approximation proves very useful for computing defect free-energies and studying the defect thermodynamics (*i.e.*, valid up to two-thirds of the melting point) regardless of the type of a solid as long as a well-developed and high-quality classical potential model is being used.

The concentration of substitutional point defects also plays a crucial role when calculating the defect properties since there will be stronger defect-defect interactions in systems with higher defect concentrations, *e.g.*, in small supercells or supercells with several substituted defects. In the case of a supercell with a couple of substitutional defects, we observe that the defect properties vary with the distance between a pair of substitutional defects, *i.e.*, especially when they aggregate or cluster together, and the trends of those defect properties depend strongly on crystal symmetry. As expected, the defect properties converge to their dilute limit when the pair of substitutional defects are more isolated, *e.g.*, located further away from each other. For the case of supercells with various numbers of defects, the defect quantities vary significantly with the defect concentration. In our case, a larger number of substitutional Ba^{2+} ions in MgO results in a larger defect volume per defect in general which, again, depends also on the crystal symmetry. On the contrary, the defect energies (per defect) tend to decrease as more defects cluster together.

Within the quasi-harmonic approximation, the computational technique outlined in this chapter has successfully been used for modelling defects in crystalline solids and clusters over a wide range of temperatures, *i.e.*, up to two-thirds of the melting point, and a wide range of pressures through both classical and first-principles approaches. The following chapter will show its potential geochemical applications for studying the partitioning behaviour of trace elements between minerals and melts and investigating the properties of solid solutions and highly-disordered systems.

TRACE-ELEMENT PARTITIONING IN MINERALS AND MELTS

This chapter first discusses the crucial factors that control the partitioning of trace elements into minerals and a simple geological model for explaining the experimental partitioning data. After that, we review fundamental thermodynamic approaches before discussing the use of simple lattice strain models for studying the incorporation of trace elements into minerals and melts. The following sections concern the limitations of the simple lattice strain models and the use of atomistic modelling to explore those limitations. Finally, we comment briefly on the connection of these approaches to the study of solid solutions and highly-disordered systems.

4.1 Partitioning Controlling Factors

According to the well-known qualitative Goldschmidt rules, the primary controls on trace-element partitioning between a solid and melt at a given temperature T and pressure P are the dissimilarity or mismatch in electrical charge (or valence) and ionic radius between the substituent ion (dopant) and substituted (host) species.¹⁸⁵ We can summarise these rules as follows:

1. Substituting a given ionic type in a polar solid by other ions with similar ionic radii, *e.g.*, the difference in ionic radius is less than $\sim 15\%$, can extensively occur. The

insertion of smaller ions into the crystal occurs more favourably than the larger ones. Note that the substitution by much larger ions is very limited.

2. Substituting a given type of ions by ions with similar electrical charges, *e.g.*, ions whose charges differ by ± 1 , can slightly occur. Ions with higher electrical charges enter the solid more readily. Note that any substitution can occur only when the crystal's electrical neutrality is preserved.
3. One of the two competing ions occupying a particular lattice site with higher ionic potential interacts more strongly with its surrounding anions. Note that the ionic potential of a given cation is the ratio of the electrical charge to its ionic radius.

As trace-element partitioning is a thermodynamic process, it depends fundamentally on temperature and pressure. Furthermore, apart from the mismatch in ionic radius and valence of the dopant and host ion, as mentioned above, substitutions at intrinsic or extended defects might also be important.¹²⁷ Additionally, oxygen fugacity (f_{O_2}) is also crucial for controlling partition coefficients of trace elements with various valence states, *e.g.*, vanadium (V) and rhenium (Re).^{186,187} Slow diffusion has also been found to control the partitioning process kinetically.^{188,189}

For almost three decades now, an extensive number of experimental studies of the influence of these controlling factors on partitioning coefficients for various minerals (*e.g.*, olivine, garnet, clinopyroxene, calcite, orthopyroxene, wollastonite and amphibole) and melts (such as silicate and carbonate) over a wide range of temperatures and pressures have been carried out.^{33,190–213} The overview picture of the experimental studies of trace-element partitioning in minerals and melts and the crucial contributing factors to their partition coefficients have comprehensively been reviewed by Blundy and Wood,^{29,214–216} and recently by Mollo and co-workers.²¹⁷

4.2 Onuma Diagrams of Experimental Partition Coefficients

According to Onuma *et al.*,³² a curve of the experimental partition coefficients for iso-valent cations as a function of ionic radius can be observed.^{32,218} A schematic Onuma diagram is illustrated in Figure 4.1(a), and the experimental Onuma diagram for clinopyroxene equilibrated with silicate melts in the diopside-albite system is shown in Figure 4.1(b). The experimental data are taken from the DC23 run in the work of Blundy and

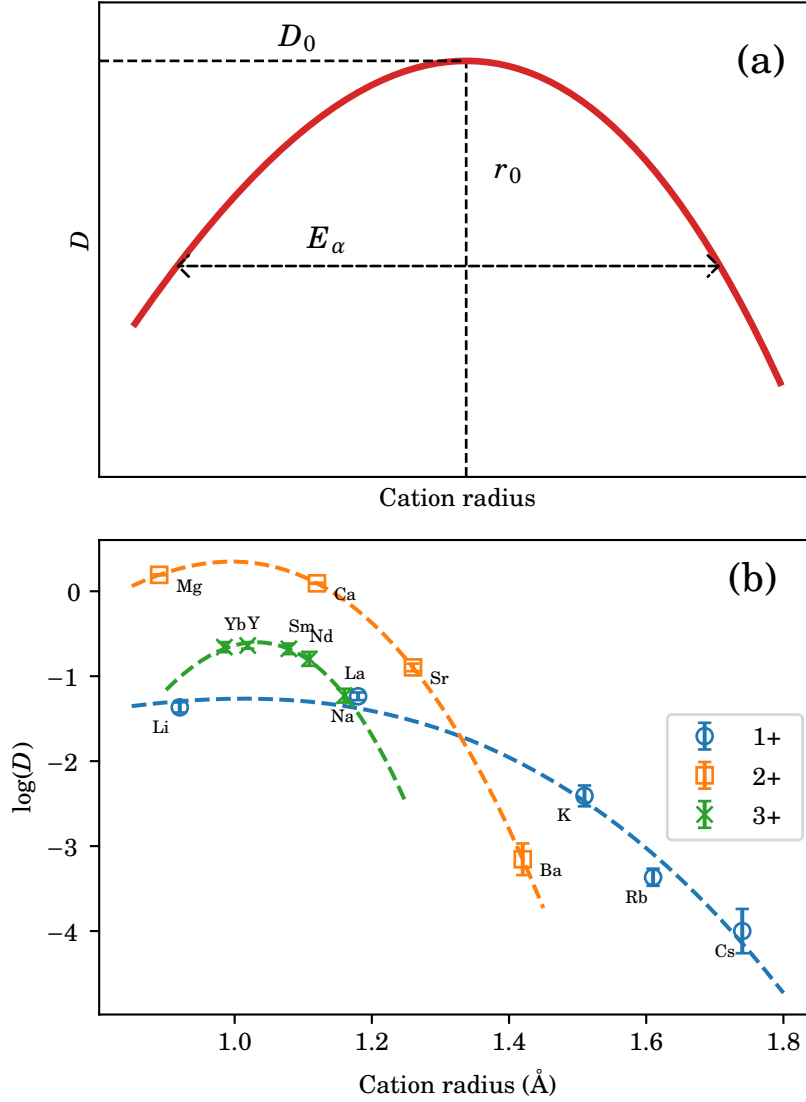


FIGURE 4.1. (a) Schematic illustration of an Onuma diagram: the plot of experimental partition coefficients D as a function of cation radius. In (a) the labelled parameters are obtained from fitting the data into equation (4.18) and described by equation (4.13) using a lattice strain model. (b) The experimental Onuma diagram for clinopyroxene equilibrated with silicate melts in the diopside-albite system.¹⁹⁶ Error bars of ± 1 standard deviation for multiple analyses are shown. Again, the curve for each isovalent cation series represents fits to equation (4.18).

Dalton.¹⁹⁶ In the DC23 experiment, a mixture of 80% diopside and 20% albite ($\text{Di}_{80}\text{Ab}_{20}$) was used as the starting composition resulting in the co-existing phases of clinopyroxene crystal and silicate melt at 0.8 GPa and 1375°C. Further details on experimental methods and conditions can be found in Blundy and Dalton.¹⁹⁶ Monovalent (+1), divalent (+2) and trivalent (+3) cations entering the large $M2$ -site are considered. The Shannon ionic radii of VIII-coordinated cations are used.¹⁷⁶ The three parameters in Figure 4.1(a) and the curve for each isovalent cation series in Figure 4.1(b) can be obtained from fitting the data into equation (4.18) using a lattice strain model. However, we will thoroughly discuss this lattice strain model for explaining trace-element partitioning in solid minerals and melts later in the next section.

The experimental Onuma diagram in Figure 4.1(b) shows, as expected, that the partition coefficients of the divalent cations tend to be greater than those of the trivalent or monovalent cations with similar ionic radii as Ca^{2+} is the host ion on the $M2$ -site of clinopyroxene. The curvature of a given Onuma diagram tends to become tighter with increasing valence, *e.g.*, the Onuma curve of the trivalent ions has a greater (or tighter) curvature than the divalent and monovalent cations, respectively. For solid minerals containing various crystallographic sites available for substitutions, the overlap of multiple curves can experimentally be observed for each isovalent species.^{30,32,218} These minerals include, for example, clinopyroxene,^{219–221} olivine,²²² and many silicates. One can distinguish the series of the overlapping curves in an Onuma diagram for a given cation valence in minerals with several sites prone to exchange by different maxima corresponding to the optimal radii of the various substituted sites. However, greater overall partition coefficients for some cations than would have been expected can be observed due to their ability to distribute between two (or more) different sites in a given crystal. In this case, considering the size mismatch on a single site alone would be insufficient.

In the following sections, we outline the thermodynamic foundation of trace-element partitioning in minerals and melts and then discuss the use of simple elastic lattice strain models in crystalline solids to justify those observations. However, those simple lattice strain models have several limitations, and we will explore those limitations via the mean of atomistic modelling. Despite those limitations, we will also demonstrate that the calculation of defect thermodynamics via atomistic simulation, which has been comprehensively discussed in Chapter 3, can be used to provide insights into partitioning experimental observations through computer simulation.

4.3 Thermodynamic Foundation of Trace-Element Partitioning

As mentioned earlier in Chapter 1, an equal partial molar Gibbs free energy is required for the distribution of a given trace element in the co-existing crystal and melt phases at equilibrium. Therefore, the fundamental thermodynamics of the incorporation of trace cation or cation defect into the solid and melt phases must be addressed in any discussion concerning trace-element partitioning. Trace-element partitioning can be viewed as substituting a host cation a^{m+} by a trace cation b^{n+} on a particular lattice site α in the crystal. From a thermodynamic viewpoint, it is vital to adopt the appropriate stoichiometry (or charge-balance mechanism) to construct activity-composition formulae, even though the partition coefficient D of a single trace element is required in most geochemical models. This is particularly essential for heterovalent substitutions, *i.e.*, where $n \neq m$. We use B and A to denote trace and host mineral components, respectively. For isovalent substitutions ($n = m$), components A and B have the same stoichiometry, such as Mg_2SiO_4 and Ni_2SiO_4 for Ni^{2+} incorporation into forsterite. On the other hand, component B must incorporate additional cations for balancing the charge for heterovalent substitutions, *e.g.*, $\text{CaMgSi}_2\text{O}_6$ and LaMgAlSiO_6 for La^{3+} incorporation into diopside, which makes the Onuma diagram unclear as two distinct substituent cations are being considered.

The partitioning behaviour of trace elements in minerals and melts has been rationalised via different thermodynamic approaches. Trace-element partitioning can be viewed as either (i) a fusion reaction of a fictive trace-element mineral component (B), with an appropriate charge balancing scheme, or (ii) an exchange reaction between host mineral component A and trace-element mineral B , and their corresponding melt phases. Therefore, the two thermodynamic approaches for describing the incorporation of a trace element in a mineral solid are briefly discussed below.

4.3.1 Fusion Equilibria for Mineral-Melt Partitioning

The fusion reaction of B , a ‘fictive’ trace-element end-member mineral, *e.g.*, $\text{SrMgSi}_2\text{O}_6$ or CeMgAlSiO_6 , is given by



The change in Gibbs energy for the fusion reaction is given by ΔG_B^{fus} , and one can write the equilibrium constant K_B at a given temperature T as

$$K_B = \frac{a_B^{\text{melt}}}{a_B^{\text{crystal}}} = \exp\left(-\frac{\Delta G_B^{\text{fus}}}{RT}\right), \quad (4.2)$$

where a_B 's refer to the activity of the trace-element component B in the melt and crystal phases, and R is the gas constant. If ΔG_B were known, one can readily calculate K_B and convert it into the partition coefficient D_b for b^{2+} via appropriate activity-composition relations for crystal and melt. Unfortunately, data on the free energy of fusion of minerals, e.g., $\text{SrMgSi}_2\text{O}_6$ or CeMgAlSiO_6 , are almost unavailable.¹²⁷ Hence, one must take an alternative approach into account.

Wood and Blundy¹⁹² proposed that ΔG_B is comprised of (i) the structural strain around the '*misfit*' cation and (ii) the strain caused by temperature and exerted pressure. To relate the partition coefficient, D , to the equilibrium constant, K , they define a fictive mineral component as a crystal that is able to accommodate a cation with the proper charge without generating any structural strain. For instance, the crystal component J for clinopyroxene, $j^{2+}\text{MgSi}_2\text{O}_6$, where j^{2+} is a trace cation with an ionic radius of r_0 that fits exactly into the $M2$ -site. Note that r_0 does not need to be identical to that of the host cation, r_a . The fusion equilibrium of the component J is



and associated with the equilibrium constant

$$K_0 = \frac{a_J^{\text{melt}}}{a_J^{\text{crystal}}} = \exp\left(-\frac{\Delta G_J^{0,\text{fus}}}{RT}\right), \quad (4.4)$$

where $\Delta G_J^{0,\text{fus}} = G_{J(\text{melt})}^0 - G_{J(\text{crystal})}^0$. Using activity-composition relationships for solid and melt, one can relate directly K_0 in equation (4.4) to the observed Nernst (and molar) partition coefficient D_0 defined by

$$D_0 = \frac{[j]^{\text{crystal}}}{[j]^{\text{melt}}} = \frac{X_j^{\text{crystal}}}{X_j^{\text{melt}}}, \quad (4.5)$$

where $[j]$'s and X_j 's denote, respectively, the weight and mole fractions of trace-element j in the two co-existing phases.^{190,192,223,224}

Before relating K_0 directly to D_0 , the effect of substituting j^{2+} in the crystal and melt phases by a homovalent b^{2+} with radius r_b present at a very low concentration must

be first considered.¹⁹² In analogy to equation (4.3), the fusion reaction of b^{2+} between crystal and melt is given by



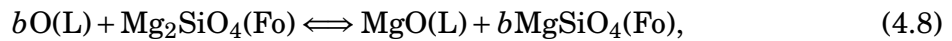
The component B in this case is, however, present at infinite dilution in a host of the pure component J . ΔG^{fus} for the fusion reactions (4.3) and (4.6) would be identical if the b^{2+} and j^{2+} ions had exactly the same ionic radius. On the other hand, in the case when $r_b \neq r_j$, the difference between the free energies of fusion reactions (4.3) and (4.6) is presumably due to the strain energies after introducing the misfit b^{2+} cation into the crystal and melt. This assumption works well for closed-shells cations, *e.g.*, Mg^{2+} , Ca^{2+} and Sr^{2+} , and this is also the case for the lanthanides, where crystal-field effects are small.³³ Using the concept outlined earlier, the change in Gibbs energy of the fusion reaction (4.6) can therefore be given by

$$\Delta G_B^{0,\text{fus}} = \Delta G_J^{0,\text{fus}} - \Delta G_{\text{strain}}^{\text{melt}} - \Delta G_{\text{strain}}^{\text{crystal}}, \quad (4.7)$$

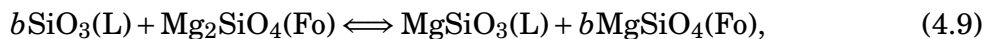
where ΔG_{strain} 's denote the strain energies associated with the substitution of one mole of j^{2+} by b^{2+} in an extremely large amount of the melt and crystal co-existing phases of the essentially pure J . We will discuss the estimation of these strain energies using lattice strain models later on in the following section.

4.3.2 Exchange Equilibria for Mineral-Mineral Partitioning

Apart from the fusion reaction, an exchange reaction involving trace and host (B and J) components in the co-existing melt phase can alternatively be used to explain the trace-element partitioning. Here, in analogy to the fusion equilibria outlined above, we consider the incorporation of b^{2+} trace cation into forsterite (Fo) using oxide species $b\text{O}$ in the melt phase at the given temperature T and pressure P of interest:



or, using pyroxene species instead of the oxide in the melt:



where (L) denotes, in general, species in a liquid phase including melts and metamorphic fluids.¹⁸² The simple exchange reactions (4.8) and (4.9) were used by Purton and co-workers to study computationally and experimentally the homovalent cation incorporation in forsterite at elevated temperatures.^{30,225}

According to Beattie *et al.*,²²⁶ the equilibrium constants (or exchange coefficients) K_D for the exchange reactions (4.8) and (4.9) can be written as

$$K_{D(4.8)}^{b-\text{Mg}} = \frac{a_{b\text{MgSiO}_4}^{\text{Fo}} \cdot a_{\text{MgO}}^{\text{L}}}{a_{\text{Mg}_2\text{SiO}_4}^{\text{Fo}} \cdot a_{b\text{O}}^{\text{L}}} = \exp\left(-\frac{\Delta G_{(4.8)}^{\text{ex}}}{RT}\right) \quad (4.10)$$

$$K_{D(4.9)}^{b-\text{Mg}} = \frac{a_{b\text{MgSiO}_4}^{\text{Fo}} \cdot a_{\text{MgSiO}_3}^{\text{L}}}{a_{\text{Mg}_2\text{SiO}_4}^{\text{Fo}} \cdot a_{b\text{SiO}_3}^{\text{L}}} = \exp\left(-\frac{\Delta G_{(4.9)}^{\text{ex}}}{RT}\right), \quad (4.11)$$

where $\Delta G_{(4.8)}^{\text{ex}}$ and $\Delta G_{(4.9)}^{\text{ex}}$ refer to the changes in Gibbs free energy for the exchange reactions (4.8) and (4.9), respectively. ΔG^{ex} is the free energy required to remove a Mg^{2+} from the solid mineral, and then insert it into the melt phase, while extracting a b^{2+} ion from the melt and incorporating it into the same crystal at the same time. In this case, on the contrary to the fusion equilibrium constant in equation (4.4), $K_D^{b-\text{Mg}}$, *i.e.*, in equations (4.8) and (4.9), involves both dopant and substituted species. Therefore, $K_D^{b-\text{Mg}}$ includes the partition coefficients of both b^{2+} and Mg^{2+} cations. As a consequence, the free energies of fusion for both fictive trace (B) and host (J) mineral components are explicitly included in the exchange-equilibrium approach.

As two similar mineral components, *i.e.*, in terms of stoichiometry, tend to have similar changes in entropy of fusion (ΔS^{fus}), the exchange coefficients is generally less temperature-dependent than partition coefficients.¹²⁷ This consideration proves very useful when comparing computational and experimental results. According to the previous study on forsterite-melt partitioning by Purton *et al.*,²²⁵ several simplifications have been made in order to relate directly the computed exchange enthalpies (ΔH^{ex}) to experimentally-observed partition coefficients for a large number of divalent trace cations using equation (4.9). These assumptions include (i) the cations in the octahedral sites in crystal and melt are disordered at high temperatures,²²⁷ (ii) ΔS^{ex} in equation (4.9) is omitted as a result of similar ΔS^{fus} of several olivines,²²⁸ and (iii) the averaged molecular weights of the crystal and melt are almost the same. Note that b^{2+} is at infinite dilution in forsterite and melt. Consequently, the simplified expression of equation (4.9) is given by

$$K_{D(4.9)}^{b-\text{Mg}} = \frac{X_b^{\text{Fo}} \cdot X_{\text{Mg}}^{\text{L}}}{X_{\text{Mg}}^{\text{Fo}} \cdot X_b^{\text{L}}} = \frac{D_b}{D_{\text{Mg}}} = \exp\left(-\frac{\Delta H^{\text{ex}}}{RT}\right), \quad (4.12)$$

where D_b and D_{Mg} refer to the partition coefficients for b^{2+} and Mg^{2+} cations, respectively, ΔH^{ex} is the exchange enthalpy, and X 's denote the mole fractions. The calculated D_{Mg} is 1.43 as a result of the choice of melt composition. Using equation (4.12), D_b can readily

be calculated by computing ΔH^{ex} for each trace divalent cation and directly compared with the experiments. Again, ΔH^{ex} can be estimated using a lattice strain model.

4.4 Lattice Strain Models

For a given series of isovalent trace cations, the curvature of the Onuma diagram varies from crystal to crystal and is characterised by the crystal's elastic modulus,³³ *i.e.*, a crystal with a larger bulk modulus tends to results in a tighter Onuma curve. This implies that the exchange of misfit trace cations occurs more preferentially in crystals with smaller elastic moduli. With this concept, there will always be an elastic response of the crystalline solid or mineral to strain when incorporating misfit trace cations whose ionic radii are different from the host cation. Therefore, this elastic response quantifies the ability of a particular trace cation to exchange in a given solid-melt system. As crystals are typically more rigid than melts, they are less tolerant of misfit trace cations. For this reason, the crystal lattice is assumed to predominate the trace-element partitioning energetically.

Blundy and Wood³³ have proposed an elastic lattice strain model to describe the dependence of experimentally-determined partition coefficients D on ionic radius for an isovalent trace-cation series in a mixture of mineral and melt in an Onuma curve, *e.g.*, in Figure 4.1(b). The model employs the cubic polynomial for the strain energy U_{strain} (per mole of trace element b) previously introduced by Brice,³⁴ which quantifies the extent of the size mismatch between the trace-cation radius r_b and the radius of a given spherical crystallographic site α with Young's modulus (or elasticity) of Y_α normally occupied by a host cation with an ionic radius of r_0 in a particular solid mineral:

$$U_{\text{strain}} = 4\pi Y_\alpha N_A \left[\frac{r_0}{2} (r_b - r_0)^2 + \frac{1}{3} (r_b - r_0)^3 \right], \quad (4.13)$$

where N_A is the Avogadro's number. Several studies have shown that the equation (4.13) appears to explain the dependence of D_b on r_b adequately for, *e.g.*, clinopyroxene, plagioclase, amphibole, and many other minerals.^{33,192,193,195,196,198,208,209,229–236}

However, the estimation of strain energy around the misfit cation b^{n+} using the expression of Brice³⁴ in equation (4.13) does not take shear and volumetric strains into account, as solely the Young's modulus is used in the formulation. Hence, the model of Brice³⁴ is inadequate and oversimplified for describing strains in the strained crystal. Consequently, this oversimplification gives rise to one of the several limitations of the lattice strain model of Blundy and Wood,³³ which will be discussed in more detail below.

An analogous approach to the strain model of Brice³⁴ has previously been proposed by Nagasawa²³⁷ which is given by

$$U_{\text{strain}} = 6\pi r_0^3 \phi_\alpha K_\alpha \Omega, \quad (4.14)$$

where

$$\Omega = \epsilon^2 \left[1 + \frac{\epsilon(1 + \sigma_\alpha)}{3(1 - \sigma_\alpha)} \right], \quad \phi_\alpha = \frac{2(1 - 2\sigma_\alpha)}{3(1 - \sigma_\alpha)}, \quad \text{and } \epsilon = \frac{r_b - r_0}{r_0}.$$

Here, for a given lattice site α in a crystal, K_α and σ_α are the site's bulk modulus and Poisson's ratio, respectively. The previous work of Beattie,²²² for instance, shows that the model of Nagasawa,²³⁷ *i.e.*, in equation (4.14), can well be used to study the partitioning behaviour of divalent and trivalent trace elements in olivine and silicate melts.

Silicate melts have a zero shear modulus; hence, the corresponding strain energy in equations (4.13) and (4.14) is zero. The strain energies obtained from the models of Brice³⁴ and Nagasawa²³⁷ are similar, as they differ no more than *ca.* 10% for the largest misfit ions.^{30,127} In spite of the fact that several simplifications have been made in their formulations, these two lattice strain models enable us to quantify conveniently the partitioning of an isovalent series of trace cations on a specific lattice site as a function of a small set of parameters, *e.g.*, as shown in Figure 4.1(a).

For a crystal with various lattice sites prone to exchange, *i.e.*, where multiple substitutions can occur, the overall partition coefficient for a given trace cation is the sum of its partition coefficients on all the individual sites, each of which is characterised by an optimal radius and an effective Young's modulus. Nevertheless, these two lattice strain models have their own merits and drawbacks. The lattice strain model of Brice³⁴ is more convenient to use. In contrast, the Nagasawa²³⁷ model provides a more complete description of the lattice strain formation process as non-radial stresses around the misfit trace ion are explicitly considered. However, in the present work, we focus mainly on the Brice³⁴ lattice strain model.

One can now incorporate the cubic function of Brice³⁴ in equation (4.13) into the developed thermodynamic scheme discussed above. This can be done by either: (i) setting $\Delta G_{\text{strain}}^{\text{melt}}$ to zero and equating U_{strain} with $\Delta G_{\text{strain}}^{\text{crystal}}$ in equation (4.7) or (ii) equating U_{strain} with ΔH^{ex} in equation (4.12). Consequently, for case (i), the relationship between equilibrium constants of the fusion reactions (4.3) and (4.6) can be given by

$$K_B = \frac{a_B^{\text{melt}}}{a_B^{\text{crystal}}} = \exp \left(\frac{-\Delta G_J^{0,\text{fus}} + \Delta G_{\text{strain}}^{\text{crystal}}}{RT} \right) = K_0 \exp \left(\frac{\Delta G_{\text{strain}}^{\text{crystal}}}{RT} \right). \quad (4.15)$$

In equation (4.15), given the assumption that strain energy terms dominate the free energy of fusion, it gives the relationships between the fusion reactions of the trace

substituent cation b and host substituted species j . Wood and Blundy¹⁹² relate K_B in equation (4.15) to the partition coefficient D_b for trace element b by setting the activity coefficient for J in the crystal $\gamma_J^{\text{crystal}}$ to be 1, *i.e.*, in Raoult's law region, and the identical activity coefficient for B and J in the melt is assumed, *i.e.*, $\gamma_B^{\text{melt}} = \gamma_J^{\text{melt}}$. Using equations (4.4) and (4.5), the proportionality between D_0 and K_0 depends on the activity coefficient of J in the melt, γ_J^{melt} , and the correction term for mean molecular weights of the melt and crystal:

$$D_0 = \frac{\gamma_J^{\text{melt}}}{K_0} \left(\frac{\overline{M}_w^{\text{melt}}}{\overline{M}_w^{\text{crystal}}} \right), \quad (4.16)$$

where \overline{M}_w 's denote the mean molecular weights of the two phases on a six-oxygen basis. Given these assumptions, one can convert the relationship between K_B and K_0 in equation (4.15) into a relationship between D_b and D_0 written as:³³

$$D_b = D_0 \exp \left(-\frac{\Delta G_{\text{strain}}^{\text{crystal}}}{RT} \right). \quad (4.17)$$

Equating $\Delta G_{\text{strain}}^{\text{crystal}}$ and U_{strain} from equation (4.13) gives

$$D_b = D_0 \exp \left\{ \frac{-4\pi Y_\alpha N_A}{RT} \left[\frac{r_0}{2} (r_b - r_0)^2 + \frac{1}{3} (r_b - r_0)^3 \right] \right\}, \quad (4.18)$$

where D_0 , *i.e.*, the strain-compensated (or strain-free) partition coefficient for a particular lattice site α , is the maximum value of D_b .

As we have seen earlier, the experimentally-determined partition coefficients for a series of isovalent cations on a particular lattice site α of a given mineral equilibrated with a melt phase as a function of ionic radius, *e.g.*, data shown in Figure 4.1(b), can be fitted to equation (4.18) of Blundy and Wood³³ model. Using this approach, all partition coefficients for a series of isovalent trace cations on a given lattice site α , for instance, lanthanides entering the $M2$ -site in clinopyroxene,²²³ can be described by three fit parameters: (i) the optimal radius r_0 , (ii) the lattice site's effective Young's modulus Y_α , and (iii) the strain compensated partition coefficient D_0 . The schematic plot of the simple model of Blundy and Wood³³ is illustrated in Figure 4.1(a). Figure 4.1(a) shows that the '*most compatible*' or '*best-fit*' trace cation has an ionic radius of r_0 and a partition coefficient of D_0 corresponding to the peak of the curve. The partition coefficient of a particular trace cation b^{n+} , whose ionic radius r_b deviates away from r_0 in either positive or negative directions, will generally be smaller than D_0 . The curvature and the derivative $\partial D / \partial r_b$ increase with increasing Y_α , the site's Young's modulus.

TABLE 4.1. Lattice strain parameters for the experimental partition coefficients of cations entering the $M2$ -site of diopside equilibrated with silicate melts, as shown in Figure 4.1(b). The data are taken from the DC23 run in a diopside-albite system at 0.8 GPa, 1375°C by Blundy and Wood.³³ One standard deviation error for each of the parameters is indicated, and is absent if it is zero in the place of the least significant digit. Note that the experimental bulk modulus K_T for diopside mineral is 113 GPa.²⁴²

Cations	Y_α (GPa)	r_0 (Å)	D_0
Monovalent (+1)	30±11	1.014±0.136	0.05±0.02
Divalent (+2)	127	0.995	2.23±0.01
Trivalent (+3)	283±34	1.032±0.006	0.25±0.01

Although the lattice strain model of Blundy and Wood³³ has successfully been employed for describing the partitioning of trace elements on a single site, the model is basically insufficient in cases where the substitution can occur on multiple lattice sites prone to exchange.²³⁸ In those cases, the overall partition coefficient of a given trace cation is the sum of the partition coefficients on all the individual lattice sites, *e.g.*, REEs (rare-earth elements) entering $M1$ - and $M2$ -sites in pyroxenes.^{207,239} When necessary, it is possible to parameterise the three fit parameters, *i.e.*, r_0 , D_0 , and Y_α , in terms of changes in pressure P , temperature T , and mineral and melt compositions.^{192,195,240,241} D_0 and to a much lesser degree Y_α , vary with pressure and temperature, and r_0 varies primarily with mineral composition.¹²⁷

As presented above, Figure 4.1(b) shows fits to the experimentally-determined partition coefficients of trace cations entering the large $M2$ -site in clinopyroxene equilibrated with silicate melts in a diopside-albite system from the DC23 experiment by Blundy and Dalton¹⁹⁶ using equation (4.18). The fit parameters for each series of isovalent cations are listed in Table 4.1. Note again that Ca^{2+} is the host ion occupying the $M2$ -site of clinopyroxene. Hence, the partition coefficients of the divalent cations tend to be larger than trivalent or monovalent cations with similar ionic radii. Y_{M2} for the monovalent cations is the largest, whereas that of the trivalent cations is the smallest, reflecting the curvatures of their Onuma diagrams in Figure 4.1(b). According to numerous experimental partitioning data, the applications and main features of these three fit parameters from the lattice strain model of Blundy and Wood³³ are briefly summarised below.

The best-fit ionic radius r_0 is one of the crystallographically meaningful parameters from fittings as it reflects well the known metal-oxygen interionic separation for the lattice site in a crystal of interest after considering the ionic radius of 1.38 Å for four-

coordinated O^{2-} .¹⁷⁶ Again, note that r_0 is not necessary to be identical to that of the host cation at the lattice site of interest. As shown in Table 4.1, r_0 for the $M2$ -site of clinopyroxene is comparable with the ionic radius of eight-coordinated Ca^{2+} normally resident at that site, as several previous experiments on partitioning in clinopyroxene and melts have suggested.^{192,193,196} This is also the case for various solid solution series, *e.g.*, garnets¹⁹⁵ and plagioclases.³³ Several observations of the partitioning of trace cations with varying charges from +1 to +4 in, *e.g.*, garnet,¹⁹⁵ clinopyroxene,¹⁹⁶ and wollastonite,¹⁹⁷ have shown that r_0 decreases with increasing ionic charge. However, the decreasing variation is non-linear as the r_0 flattens out at higher charges than +3.¹⁹⁷ Allan *et al.*¹²⁷ and Karato,²⁴³ for example, suggest that the shorter optimal radius of the site (r_0) for a series of highly-charged cations might be a direct consequence of the relaxation of the neighbour oxygen ions to become closer to the positively-charged dopant. On the contrary, a cation series with a lower ionic charge is expected to yield a longer r_0 due to the weaker electrostatic interactions resulting in the longer interionic separations with their O^{2-} neighbours compared to those of the dopants with a higher positive charge.¹²⁷

By definition, for a given material, the Young's modulus Y quantifies the degree of the material's resistance to the change in length along the axis of interest, while the bulk modulus K_T refers to its ability to resist the change in volume. In an isotropic material, the relationship between the two moduli is given by

$$Y = 3K_T(1 - 2\sigma), \quad (4.19)$$

where σ is Poisson's ratio. In the literature, most oxides and minerals are assumed to be ideal Poisson solids, *i.e.*, isotropically elastic materials, with $\sigma \approx 0.25$; hence, equation (4.19) gives $Y \approx 1.5K_T$. However, it is worth noting that the crystal lattices of solid minerals are not isotropically elastic media in general.^{244–247}

Given the definitions above, for a given crystallographic site α in a crystal of interest, the apparent Young's modulus Y_α quantifies the site's elasticity (or stiffness), *i.e.*, a stiffer site has a larger Y_α . On the other hand, the apparent site's bulk modulus K_α for an isotropically elastic lattice site α specifies the site's volumetric elasticity, which can also be related to Y_α using equation (4.19). The results in Table 4.1 show that Y_α increases with increasing ionic charges. Y_α of a given site is found to exhibit an approximately linear variation with cation charge,^{29,127} and it relates directly to the material's bulk modulus K_T as their elastic response to strain is consistent with the known bulk moduli of oxides and minerals.²⁴⁸ Hence, the magnitude of fitted Y_α is often compared to that

of K_T in the literature. For homovalent substitution, *e.g.*, the incorporation of divalent cations (+2) onto the $M2$ -site in clinopyroxene,¹⁹⁶ trivalent cations (+3) onto the X -site in garnet,¹⁹⁵ and divalent cations (+2) onto the M -site in plagioclase,^{33,191} the magnitude of Y_α appears to be in good agreement with that of K_T for the crystal. For instance, the magnitude of the fitted Y_α of 127 GPa for the incorporation of divalent cations onto the $M2$ -site of clinopyroxene in Table 4.1 is close to that of the experimental bulk modulus K_T of 113 GPa for diopside mineral.²⁴² However, the definitions of Young's and bulk moduli are fundamentally different, hence making a direct comparison between these two parameters is ambiguous as there are evidently several exceptions.

Hill and co-workers, for instance, have found that the fitted Y_{M1} for the substitution of tetravalent cations (4+) at the $M1$ -site in clinopyroxene is unrealistically large, *i.e.*, 5870 ± 314 GPa,^{198,208} and this is also the case for the Zr-site in Zircon.²⁴⁹ In those cases, heterovalent substitutions result in charged defects which would definitely not give a fitted Y_α close to the experimental elastic moduli. Moreover, van Westrenen *et al.*^{195,200,250} have observed that Y_X of the X -site in garnet does not show linear variations with cation charge along the pyrope-grossular join. The implication of these findings is that the observed elastic properties of the crystal are often controlled broadly by the elastic properties of the large cation lattice site, although some smaller cation lattice sites might deform due to the distortion of the rigid tetrahedral framework of Si–O(–Al). According to the computational work of van Westrenen *et al.*,²⁵¹ the anomalous partitioning behaviour along the pyrope-grossular solid solution is mainly due to the local ordering in the crystal. Nonetheless, these experimental findings emphasise that the elasticity of the rigid crystal, rather than the more flexible melt, controls the partitioning behaviour of trace elements primarily.

Lastly, the strain-free partition coefficient D_0 also varies with cation charge, *e.g.*, as shown in Table 4.1. D_0 is typically smaller for heterovalent substitution than for homovalent substitution. D_0 exhibits a parabolic dependence on cation charge, similar to Onuma diagrams, where the peak of the curve corresponds to the optimal ionic charge at the lattice site of interest.²⁵² Several studies show that D_0 , as expected for a thermodynamic parameter, is temperature- and pressure-dependent.²⁹

4.5 Limitations of Lattice Strain Models

For a few decades now, lattice strain models, *e.g.*, the simple strain model of Blundy and Wood³³ in equation (4.18), have been used for studying the partitioning of trace elements

between solid minerals and melts. The lattice strain models provide an apparent link between experimentally-determined partition coefficients D and the mismatch in ionic radius of the trace and host cations in crystals, and it relates also the D 's to the mineral's elastic properties. The approach has successfully advanced the conventional constant- D strategy for studying the partitioning of trace elements between minerals and melts by enabling the potential to vary systematically D 's in response to changes such as temperature, pressure, and mineral composition.²¹⁵

However, the simple lattice strain model of Blundy and Wood³³ has several limitations in terms of the inadequate definition of lattice strains, arising mainly from the simplifications made in the formulation of the expression for the lattice strain energy, *i.e.*, the strain model of Brice³⁴ in equation (4.13).^{127,182} The use of continuum mechanics in the model of Brice³⁴ is also deficient for studying microscopic structural deformation in minerals, *e.g.*, oxides and silicates, as the lattice strain around incorporated point defects is non-continuous. Strictly speaking, explaining strain energies using the expression of Brice³⁴ in the strain model of Blundy and Wood,³³ *i.e.*, in equations (4.13) and (4.18), is said to be oversimplified in various aspects for estimating lattice strain due to the incorporation of a trace cation in a solid mineral.

In the strain model of Brice,³⁴ the total strain around the substituted cation with an ionic radius of r_b at the site of a host cation with a radius of r_0 is given by $\int_{r_b}^{\infty} \epsilon \, dr = r_b - r_0$, corresponding to the sum of the displacements of all constituent particles within the strained crystal. However, this expression goes against the fundamental definition of strain, which is defined as a dimensionless quantity scaled to the original volume (or length), *i.e.*, $\epsilon = (V_b - V_0)/V_0$ or $\epsilon = (r_b - r_0)/r_0$. In an extremely large strained material (or at a given remote distance from the incorporated cation), the strain resulting from the atomic displacements around the substitutional defect tends to vanish, which contradicts the definition of Brice.³⁴

Describing strains (or expressing the strain energies) in elastically isotropic crystal lattices in terms of a Young's modulus and Poisson's ratio is inadequate. The model of Brice³⁴ does not give a complete description of the overall lattice strain as non-radial strains are not taken into account explicitly, in contrast to the strain model of Nagasawa,²³⁷ as briefly discussed earlier. According to Eshelby,^{244–246} after incorporating a misfit cation at the origin of an infinite-sized isotropic crystal, the elastic displacement along a given direction depends also on the materials' bulk and shear moduli. For instance, Figure 3.18 depicts clearly the anisotropic atomic displacements around the incorporated point-defect Ba^{2+} cation in MgO crystal. In other words, the function for the

strain energy is strongly asymmetric around the misfit cation. Hence, in addition to the Young's modulus, the bulk and shear moduli must also be included in an expression of the strain energy in order to describe the lattice strain process fully, even in an isotropic material.^{182,243} Apart from the strain arising from the mismatch between the ionic radii of the trace and host cations, the environment of the lattice site of exchange also has a great influence on the lattice strain. For instance, some structural deformation of the lattice may occur through other mechanisms, *e.g.*, twisting of surrounding Si–O(–Al) rigid polyhedra, rather than the simple elastic strain process, especially in anisotropic and vacancy-rich minerals.^{127,173,182,195,250,251,253}

Furthermore, when evaluating the strain energy due to the incorporation of a misfit cation in a perfect crystal lattice using equation (4.13), the use of a hard-sphere model with fixed size for O^{2-} and cations (and fixed ionic separations), *e.g.*, employing the ionic radii derived by Shannon,¹⁷⁶ is also seemingly unrealistic. Moreover, calculated strain energies using the model of Brice³⁴ depends strongly on the choice of empirical assumptions about the substitution mechanism (or the charge-compensation mechanism), especially in the case of heterovalent substitutions where there might be ordering between the dopant and its compensating species,³¹ which affects the formulation of activity-composition relationship directly.^{31,127,173,250,254} Furthermore, there are a large number of possible charge-balancing mechanisms for heterovalent substitutions. For instance, the incorporation of a La^{3+} trace cation into diopside mineral ($CaMgSi_2O_6$) can occur through two different possible mechanisms: (i) replacing three divalent (+2) host cations by two trivalent (+3) cations 'and' leaving one divalent-cation vacancy or (ii) substituting two divalent host cations by a La^{3+} ion 'and' an additional monovalent (+1) cation, *e.g.*, Li^+ or Na^+ , as a charge-balancing ion.^{31,173} As a result, these numerous possibilities give rise to one of the major complications for quantifying and modelling the partitioning behaviour of trace elements in minerals.^{31,127,173,182} Again, the use of only one effective Young's modulus Y_α for describing strains due to the simultaneous incorporation of two heterovalent cations is questionable since Y_α is charge-dependent.

More importantly, the lattice strain model does not take the role of the melt phases into account explicitly.^{127,182,243} Again, this is oversimplified as several studies suggest that the structure and composition of the melt phases play also a crucial role in trace-element partitioning between solid minerals and melts.^{255–262}

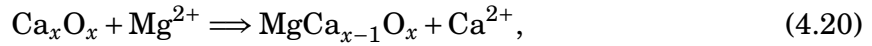
Each of these oversimplifications and assumptions limits the application of the lattice strain model. The theoretical insight into these limitations can be provided by state-of-the-art computer simulation techniques that have been developed and employed to study

the incorporation of cation defects in the structures of various solid minerals at the trace levels,¹²⁷ as briefly summarised in Chapter 2 (Section 2.2). In the previous section, we have comprehensively investigated the incorporation of a Ba^{2+} ion in periclase mineral (cubic MgO) as a simple case study to illustrate the application of those simulation techniques for studying important factors on the thermodynamics of the substitutional defect formation. Using the same approach, in the subsequent subsection, we present the relaxation energies (as the equivalent of strain energies), defect formation energies, and solution energies for the incorporation of trace-element cations in lime (cubic CaO) and diopside minerals via both classical and *ab initio* DFT atomistic simulations (in regard of continuum mechanics) to investigate more fully and illustrate more clearly the limitations of the lattice strain model.

4.6 Defect, Relaxation and Solution Energies

4.6.1 Definitions of Energy Terms

In this subsection, we shall first define the three important computed thermodynamic quantities for studying the solid-solid partitioning of trace elements theoretically: (i) defect energies, (ii) relaxation energies, and (iii) solution energies. In the previous chapter, *i.e.*, in Section 3.3, we have thoroughly discussed the computation of ‘*defect energies*’ of Ba_{Mg}^x in MgO , *e.g.*, using equations (2.30) and (3.1) in the supercell approach. We have used g_p and f_v for the defect free energies at constant pressure and constant volume, respectively. In this section, however, as we will solely concentrate on the constant-volume defect energies in the static limit within the supercell approach, and we use E ’s to denote those energy terms for simplicity. For example, the substitution of a Ca^{2+} ion by a Mg^{2+} ion, Mg_{Ca}^x , in an optimised supercell of CaO (lime mineral) containing $2x$ ions is



with the corresponding defect energy

$$E_{\text{def}}(\text{Mg}_{\text{Ca}}^x) = [E_{\text{lat}}(\text{MgCa}_{x-1}\text{O}_x) + E_{\text{ion}}(\text{Ca}^{2+})] - [xE_{\text{lat}}(\text{CaO}) + E_{\text{ion}}(\text{Mg}^{2+})], \quad (4.21)$$

where $E_{\text{lat}}(\text{MgCa}_{x-1}\text{O}_x)$ refers to the ‘*final lattice energy*’ of the ‘*relaxed*’ defective $\text{MgCa}_{x-1}\text{O}_x$ structure, and $E_{\text{lat}}(\text{CaO})$ is the ‘*lattice energy*’ per formula unit of the optimised perfect structure of CaO . Hence, the term $xE_{\text{lat}}(\text{CaO})$ is equivalent to the lattice energy of a supercell of CaO containing $2x$ ions. E_{ion} refers to the ‘*ion energy*’. Note that

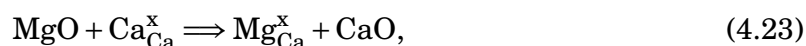
E_{ion} 's are zero in the classical approach, whereas they are non-zero in the first-principles simulation. Hence, E_{ion} 's must be taken into account when calculating *ab initio* defect energies.

In the defective structure of $\text{MgCa}_{x-1}\text{O}_x$ the ‘relaxation energy’, E_{rel} , for the incorporation of a Mg^{2+} substitutional defect in CaO is defined as the difference between $E_{\text{lat}}(\text{MgCa}_{x-1}\text{O}_x)$ before and after structural relaxation or the difference in energy of the initial (unrelaxed) and final (relaxed) $\text{MgCa}_{x-1}\text{O}_x$ structures:

$$E_{\text{rel}}(\text{Ca}_{\text{Mg}}^{\text{x}}) = E_{\text{lat}}^{\text{initial}}(\text{MgCa}_{x-1}\text{O}_x) - E_{\text{lat}}^{\text{final}}(\text{MgCa}_{x-1}\text{O}_x). \quad (4.22)$$

As we have discussed in the previous section, the lattice strain energies, U_{strain} , *e.g.*, in equations (4.13) and (4.14), relate most closely to the relaxation energies, E_{rel} , obtained from the atomistic simulations. U_{strain} can be approximated by E_{rel} from computer simulations. The application of the simulated E_{rel} to the lattice strain model of Brice³⁴ will be discussed below.

In other oxides and ceramics, E_{def} can be used to determine ‘solution energy’, which does not involve only the defect energy, but also the lattice energies of the host and substituent species.^{263–266} For instance, using the notation of Kröger and Vink,¹³¹ the simple exchange reaction of Mg^{2+} and Ca^{2+} in CaO as the host solid oxide is written as



and this gives the solution energy

$$E_{\text{sol}}(\text{Mg}_{\text{Ca}}^{\text{x}}) = E_{\text{lat}}^{\text{final}}(\text{Mg}_{\text{Ca}}^{\text{x}}) + E_{\text{lat}}(\text{CaO}) - E_{\text{lat}}(\text{MgO}). \quad (4.24)$$

Note that this reaction is analogous to the exchange equilibria presented earlier, *e.g.*, in equations (4.8) and (4.9).

4.6.2 Models and Computational Details

Here, we present calculated defect formation, relaxation (approximate strain) and solution energies for the incorporation of homovalent (+2) and heterovalent (+1 and +3) cations into two end-member minerals: (i) lime (solid CaO), and (ii) clinopyroxene diopside ($\text{CaMgSi}_2\text{O}_6$) via both classical and DFT calculations. In many previous computational studies, for example, Purton *et al.*,^{30,31} van Westrenen *et al.*,²⁵⁰ and Allan *et al.*,¹⁷³ those substitutional defect thermodynamics in ionic solids and minerals were computed based solely on the Mott-Littleton model,¹²⁵ as illustrated in Figure 2.2(a), and classical

Buckingham interionic potentials. Hence, in those studies, defect concentration and quantum-mechanical effects have not been explicitly considered and incorporated when evaluating those defect thermodynamic quantities. Here, we intend also to make a direct comparison between the classical and DFT results as there have previously been only a few direct comparisons between calculated defect energies from force-field based and *ab initio* quantum-mechanical approaches.¹⁷³ For example, De Vita *et al.*¹⁷⁴ have previously shown that the calculated defect formation and migration energies in MgO obtained from DFT calculations are in very good agreement with those obtained using classical calculations based on empirical pair potentials. However, the Mott-Littleton approach has not recently been implemented into any widely used DFT software packages for modelling defects in solids. In order to compare the classical and DFT results directly, the supercell approach, as illustrated in Figure 2.2(b) is currently the only choice.

In the present study, all the calculations based on classical force-field potentials were performed using the GULP program.^{91,156} As we are dealing with various types of atomic species (or dopants), a consistent set of atomic pseudopotentials for the first-principles simulation of the incorporation of trace elements in crystals is crucial. Fortunately, as mentioned earlier in Chapter 2, the standard solid-state pseudopotentials (SSSP) library^{121,267} provides consistent sets of pseudopotentials covering most elements across the periodic table optimised for modelling solid-state materials using the Quantum ESPRESSO code.^{103,104} For that reason, the Quantum ESPRESSO program coupled with a consistent set of atomic pseudopotentials provided by the SSSP library were chosen to perform all the plane-wave DFT calculations in the present study. The first-principles elastic constants of CaO and diopside crystals were obtained using the thermo_pw code²⁶⁸ implemented in the Quantum ESPRESSO program.

For the classical calculations, we take the empirical force-field parameters from the previous computational studies of Purton *et al.*,^{30,31} and the full list of those parameters is in Table 4.2. Buckingham potentials, *i.e.*, $\phi_{\text{Buck}}(r_{ij}) = A \exp(-r_{ij}/\rho) - C/r_{ij}^6$, were used for two-body interionic short-range interactions between O^{2-} and cations and a three-body harmonic potential, *i.e.*, $\phi_{\text{angle}}(\theta) = 0.5k_{\theta}(\theta - \theta_0)^2$, was applied for O–Si–O triplets. The shell model of Dick and Overhauser⁷³ was used for polarisable O^{2-} ions, while all the cations were treated as non-polarisable rigid ions; hence, interactions between cations are purely Coulombic. In the core-shell model, an O^{2-} ion consists of a ‘*massless shell*’ and a ‘*massive core*’, connected to each other by a harmonic spring with a spring constant $k_{\text{core-shell}}$. The polarisation effects arise from electric dipoles as a results of the core-shell displacements relative to each other. A cutoff of 12 Å was used throughout the classical

TABLE 4.2. Classical interionic potential parameters used for modelling the incorporation of trace-element cations into lime (cubic CaO) and diopside minerals.

Atom	Charge (e)	Buckingham parameters		
		A (eV)	ρ (Å)	C (eV Å ⁶)
O (shell) ^(a)	-2.86902	22764.0881	0.1490	27.8801
Ca	+2	1090.4020	0.3437	0.0000
Mg	+2	1428.5077	0.2945	0.0000
Sr	+2	1375.0070	0.3500	0.0000
Ba	+2	931.7031	0.3949	0.0000
Mn	+2	1007.4043	0.3262	0.0000
Fe	+2	1207.6020	0.3084	0.0000
Co	+2	1491.7095	0.2951	0.0000
Ni	+2	1582.5116	0.2882	0.0000
Eu	+2	1248.5101	0.3556	0.0000
Li	+1	262.5414	0.3476	0.0000
Na	+1	1266.8457	0.3065	0.0000
K	+1	680.4412	0.3798	0.0000
Rb	+1	919.3840	0.3772	0.0000
Sc	+3	1299.4057	0.3312	0.0000
La	+3	1439.7064	0.3651	0.0000
Nd	+3	1379.9062	0.3601	0.0000
Eu	+3	1358.0053	0.3556	0.0000
Gd	+3	1336.8050	0.3551	0.0000
Ho	+3	1350.2051	0.3487	0.0000
Lu	+3	1347.1051	0.3430	0.0000
Yb	+3	1309.6058	0.3462	0.0000
Si ^(b)	+4	1283.9147	0.3205	10.6546

^(a) $k_{\text{core-shell}} = 74.9238 \text{ eV Å}^{-2}$,^(b) $k_{\theta} = 2.0936 \text{ eV rad}^{-2}$ and $\theta_0 = 109.47^\circ$

TABLE 4.3. Calculated and experimental lattice parameters of CaO and diopside ($\text{CaMgSi}_2\text{O}_6$). The lattice parameters of CaO and diopside refer to their conventional standard unit cells, *i.e.*, eight-atom cubic CaO ($Fm\bar{3}m$ space group) and 40-atom monoclinic $\text{CaMgSi}_2\text{O}_6$ ($C2/c$ space group) crystals, respectively. The computational details for the classical calculations based on Buckingham interionic potentials and the core-shell model and the plane-wave DFT (GGA-PBE) simulation can be found in Subsection 4.6.2.

Solid		a (Å)	b (Å)	c (Å)	β (°)
CaO	Experimental ^(a)	4.815	-	-	-
	DFT	4.830	-	-	-
	Classical	4.807	-	-	-
Diopside	Experimental ^(b)	9.745	8.899	5.251	105.63
	DFT	9.893	9.027	5.333	106.49
	Classical	9.805	9.014	5.242	105.12

^(a)Fiquet *et al.*,²⁷⁰ ^(b)Cameron *et al.*²⁷¹

simulation for the oxygen's shell/cation short-range potentials. A more detailed discussion of interionic potentials can be found in the review article of Allan and Mackrodt.¹⁰ The Broyden–Fletcher–Goldfarb–Shanno (BFGS) minimisation algorithm^{143–146} with a convergence criterion on the forces of 1.0×10^{-4} Hartree Bohr⁻¹ ($\sim 5.1 \times 10^{-4}$ eV Å⁻¹) was used for structural optimisation.

In the DFT simulation, all the atomic potentials were represented by the pseudopotentials taken from the standard solid-state pseudopotentials (SSSP) library optimised for precision.^{121,267} The electronic exchange and correlation energies were evaluated using the generalised-gradient approximation of Perdew-Burke-Ernzerhof (GGA-PBE) DFT functional.¹¹⁴ A kinetic energy plane-wave cutoff of 90 Ry and a charge-density cutoff of 1080 Ry were used. The Monkhorst-Pack **k**-point grids²⁶⁹ of $5 \times 5 \times 5$ and $3 \times 3 \times 5$ were used for the standard conventional unit cells of CaO and diopside, respectively. Gaussian smearing with a spreading width of 0.01 Ry was used throughout the DFT calculations. In the periodic calculations of the energies of isolated cations E_{ion} , the compensating jellium background charge was used to remove the divergences of the electrically non-neutral unit cells.^{103,104} The convergence threshold for the self-consistent field calculation was set to 1.0×10^{-6} Ry ($\sim 1.4 \times 10^{-5}$ eV). For structural optimisation using the BFGS minimisation method, the convergence criteria on the total energy and forces of 1.0×10^{-4} Hartree ($\sim 2.7 \times 10^{-3}$ eV) and 1.0×10^{-3} Hartree Bohr⁻¹ (~ 0.051 eV Å⁻¹), respectively, were used.

A comparison between the experimental and calculated results for the structural

TABLE 4.4. Calculated and experimental elastic properties of CaO and diopside ($\text{CaMgSi}_2\text{O}_6$). K , Y and G denote the mean values of bulk, Young's and shear moduli (in GPa), respectively. σ is Poisson's ratio. The mean values of Y and σ for diopside, as an elastically anisotropic material, are calculated using the Voigt-Reuss-Hill (VRH) approximation.²⁷² The computational details for the classical calculations based on Buckingham interionic potentials and the core-shell model and the plane-wave DFT (GGA-PBE) simulation can be found in Subsection 4.6.2.

Solid		K (GPa)	Y (GPa)	G (GPa)	σ
CaO	Experimental	111.25 ^(a)	181 ^(b)	74.05 ^(b)	0.22 ^(b)
	DFT	103.89	179.69	74.14	0.21
	Classical	136.32	149.17	78.91	0.32
Diopside	Experimental	113 ^(c)	160.5 ^(d)	65.1 ^(c)	0.26 ^(d)
	DFT	107.99	175.98	71.63	0.23
	Classical	125.69	168.46	65.65	0.28

^(a)Chang and Graham,²⁷³ ^(b)Hite and Kearney,²⁷⁴

^(c)Kevien *et al.*,²⁴² ^(d)Aleksandrov *et al.*²⁷⁵

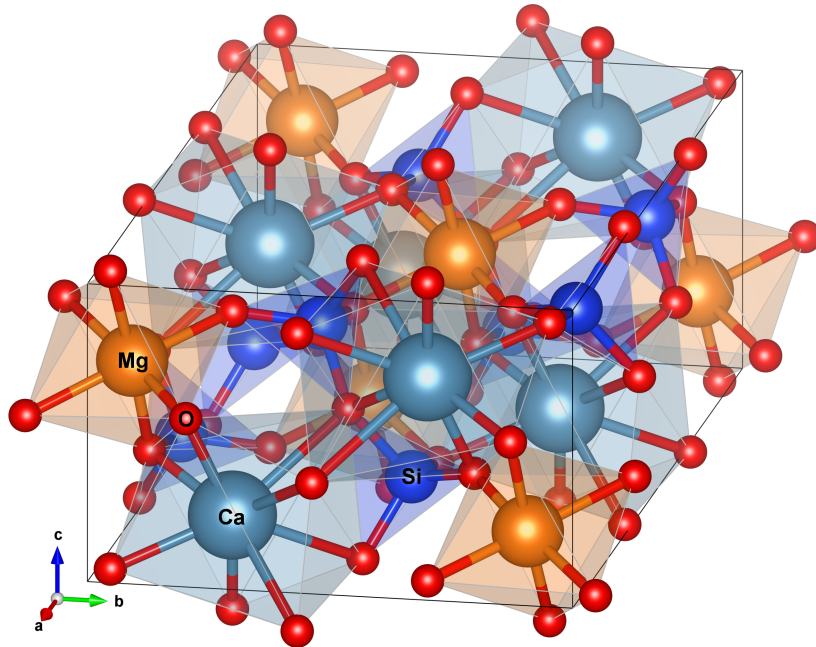


FIGURE 4.2. The crystal structure of the clinopyroxene diopside.²⁷¹

and elastic properties of CaO and diopside is shown in Table 4.3. The experimental and simulated lattice parameters of CaO and diopside refer to their conventional standard unit cells, *i.e.*, eight-atom cubic CaO ($Fm\bar{3}m$ space group) and 40-atom monoclinic $\text{CaMgSi}_2\text{O}_6$ ($C2/c$ space group) crystals, respectively. The crystal structure of diopside²⁷¹ is shown in Figure 4.2. The elastic properties, *i.e.*, the average values of bulk (K), Young's (Y) and shear (G) moduli (in GPa) and Poisson's ratios σ from the experiments and simulations are listed in Table 4.4. The clinopyroxene diopside is, in fact, an elastically anisotropic mineral.^{242,275,276} However, the reported experimental and calculated Young's modulus Y and Poisson's ratio σ for diopside in Table 4.4 are the averaged values from the Voigt-Reuss-Hill (VRH) approximation.²⁷² Overall, the magnitudes of the calculated structural and elastic parameters obtained from both computational approaches are in reasonable agreement with experimental data.

For modelling the incorporation of a trace cation (or cations for heterovalent substitutions) into CaO, cubic supercells containing 512 atoms ($4 \times 4 \times 4$ supercell) and 64 atoms ($2 \times 2 \times 2$ supercell) of CaO were used in the classical and DFT simulations, respectively. On the other hands, supercells of $\text{CaMgSi}_2\text{O}_6$ consisting of 640 atoms ($2 \times 2 \times 4$ supercell) and 80 atoms ($1 \times 1 \times 2$ supercell) were used for simulating the substitutional defect formation in diopside in the classical and DFT calculations, respectively. For both crystals, the initial geometries were prepared using the VESTA visualiser program.¹³⁶ The vast series of defective crystal structures with incorporated trace-element cations were generated using a simple Python script written in the Jupyter Notebook,¹⁴⁷ as an implementation in the Anaconda Software Distribution.¹⁴⁸ A uniform $3 \times 3 \times 3$ Monkhorst-Pack \mathbf{k} -mesh was used for the reciprocal space summations for both structures in the DFT calculations. In both computational approaches, the static-limit defect formation and relaxation energies, *i.e.*, E_{def} and E_{rel} , were obtained at constant volume, *i.e.*, all the six lattice parameters were kept fixed during the geometry optimisation. In all cases, however, the atomic positions are not fixed by their initial crystal symmetry during the structural relaxation.

The three calculated thermodynamic quantities, *i.e.*, (i) defect formation, (ii) relaxation (as equivalent to strain energies) and (iii) solution energies, of the incorporation of trace cations into CaO and diopside as a function of ionic radii are now used to investigate the partitioning behaviour of trace elements and the limitations of the simple lattice strain models theoretically. In order to compute the solution energies, as mentioned earlier, the lattice energies of binary oxides are required. The oxides of divalent (+2), monovalent (+1) and trivalent (+3) have the forms of MO ($Fm\bar{3}m$ space group), M_2O

TABLE 4.5. Six-fold and eight-fold coordinated cation radii (in Å) taken from Shannon,¹⁷⁶ calculated lattice energies per formula unit, and DFT ion energies (all in eV) for studying the incorporation of trace cations in CaO and diopside. The lattice energies of the binary oxides are used for calculating the solution energies, while the ion energies are used for calculating the DFT defect energies. The classical and DFT lattice energies of diopside are also provided for computing the solution energies. The computational details for the classical calculations based on Buckingham interionic potentials and the core-shell model and the plane-wave DFT (GGA-PBE) simulation can be found in Subsection 4.6.2.

Cation	Ionic radius (Å) ^(a)		Lattice energy (eV)		DFT ion energy (eV)
	VI-fold	VIII-fold	Classical	DFT	
Divalent (<i>MO</i>)					
Ca ²⁺	1.00	1.12	-35.95	-116.88	-73.86
Mg ²⁺	0.72	0.89	-41.31	-167.24	-123.93
Sr ²⁺	1.18	1.26	-33.88	-112.07	-69.19
Ba ²⁺	1.35	1.42	-31.33	-478.07	-435.33
Mn ²⁺	0.83	0.96	-38.79	-252.91	-209.61
Fe ²⁺	0.78	0.92	-40.21	-370.92	-327.49
Co ²⁺	0.75	0.90	-40.91	-340.09	-296.61
Ni ²⁺	0.69	N/A ^(a)	-41.68	-384.87	-341.33
Eu ²⁺	1.17	1.25	-33.77	-684.47	-641.65
Monovalent (<i>M</i> ₂ O)					
Li ⁺	0.76	0.92	-29.69	-70.87	-14.04
Na ⁺	1.02	1.18	-26.25	-212.18	-84.82
K ⁺	1.38	1.51	-22.50	-267.77	-112.72
Rb ⁺	1.52	1.61	-21.66	-139.57	-48.66
Trivalent (<i>M</i> ₂ O ₃)					
Sc ³⁺	0.75	0.87	-145.27	-439.79	-154.44
La ³⁺	1.03	1.16	-126.73	-1042.28	-456.35
Nd ³⁺	0.98	1.11	-129.83	-1200.57	-535.37
Eu ³⁺	0.95	1.07	-132.19	-1410.72	-640.36
Gd ³⁺	0.94	1.05	-132.80	-1493.84	-681.93
Ho ³⁺	0.90	1.02	-135.49	-1785.03	-827.42
Lu ³⁺	0.86	0.98	-138.27	-2286.19	-1077.96
Yb ³⁺	0.87	0.99	-137.45	-2147.88	-1008.79
Diopside (CaMaSi ₂ O ₆)	-	-	-337.53	-6454.22	-

^(a)Shannon¹⁷⁶

TABLE 4.6. The calculated final defect formation, relaxation and solution energies for the incorporation of homovalent dopants into CaO obtained from both classical and DFT simulations. All energy values are in eV. The computational details for the classical calculations based on Buckingham interionic potentials and the core-shell model and the plane-wave DFT (GGA-PBE) simulation can be found in Subsection 4.6.2.

Dopant cation	Defect energy (eV)		Relaxation energy (eV)		Solution energy (eV)	
	Classical	DFT	Classical	DFT	Classical	DFT
Mg ²⁺	-4.2138	-3.2601	0.6100	0.1903	1.1493	0.7014
Sr ²⁺	2.3705	2.3122	0.2436	0.1699	0.2993	0.2820
Ba ²⁺	5.8911	5.0785	0.9835	0.9823	1.2702	1.2503
Mn ²⁺	-2.4437	-3.7050	0.2230	0.0833	0.3958	0.1278
Fe ²⁺	-3.4813	-4.7789	0.4241	0.1405	0.7819	0.7196
Co ²⁺	-3.9864	-5.5844	0.5342	0.1681	0.9794	0.6425
Ni ²⁺	-4.4612	-6.5795	0.6766	0.1711	1.2737	0.4592
Eu ²⁺	2.4835	3.1663	0.2394	0.0730	0.3053	0.4167

($Fm\bar{3}m$ space group) and M_2O_3 ($Ia\bar{3}$ space group), respectively, where M 's denotes the corresponding metal cation. In the DFT calculations, the energies of the isolated metal ions are also needed to calculate the defect formation energies. The six-fold and eight-fold coordinated ionic radii from Shannon,¹⁷⁶ classical and DFT lattice energies per formula unit, and DFT ionic energies for all cations considered in this work are listed in Table 4.5. The ionic radii for the six-fold coordination are used for the cation substitutions in CaO and the cation exchange at the $M1$ -site of diopside, which is normally occupied by a Mg²⁺ ion. The eight-fold coordinated ionic radii, on the contrary, are used for the substitutions at the $M2$ -site of a Ca²⁺ ion in diopside. The calculated classical and DFT lattice energies of the clinopyroxene diopside are also given in Table 4.5 for computing the solution energies.

4.6.3 Homovalent Trace Elements in CaO and Diopside

We first concentrate on the energetics of the incorporation of divalent (or homovalent +2) trace cations in CaO. For example, equations (4.21), (4.22) and (4.24) are used to compute the thermodynamics of the incorporation of a Mg²⁺ into CaO within the supercell approach. The calculated final defect formation, relaxation and solution energies for all the homovalent substitutions in CaO and diopside from both the classical and DFT methods are tabulated in Tables 4.6 and 4.7, respectively. In the case of diopside, the substitution can occur at both $M1$ - and $M2$ -sites of the six-fold coordinated Mg²⁺ and

TABLE 4.7. The calculated final defect formation, relaxation and solution energies for the incorporation of homovalent dopants into the clinopyroxene diopside obtained from both classical and DFT simulations. All energy values are in eV. The computational details for the classical calculations based on Buckingham interionic potentials and the core-shell model and the plane-wave DFT (GGA-PBE) simulation can be found in Subsection 4.6.2.

Dopant cation	Defect energy (eV)		Relaxation energy (eV)		Solution energy (eV)	
	Classical	DFT	Classical	DFT	Classical	DFT
<i>M2-site (Ca²⁺ Site)</i>						
Mg ²⁺	-3.9031	-2.9907	0.6965	0.6375	1.4601	0.9709
Sr ²⁺	2.0609	1.8530	0.2152	0.2007	-0.0103	-0.1772
Ba ²⁺	5.6573	4.1509	0.9845	1.1249	1.0364	0.3227
Mn ²⁺	-2.1918	-3.0842	0.2288	0.3976	0.6477	0.7487
Fe ²⁺	-3.1844	-4.2387	0.4613	0.6809	1.0789	1.2598
Co ²⁺	-3.6791	-4.9378	0.5923	0.8533	1.2866	1.2891
Eu ²⁺	2.2152	3.2160	0.2181	0.2032	0.0370	0.4664
<i>M1-site (Mg²⁺ Site)</i>						
Ca ²⁺	5.6580	4.2653	1.2595	0.9779	0.2949	0.3038
Sr ²⁺	8.6637	7.0498	3.5145	3.0903	1.2294	1.0580
Ba ²⁺	12.8771	10.2056	6.2031	7.6936	2.8931	2.4158
Mn ²⁺	2.3904	0.3708	0.1738	0.1409	-0.1332	0.2421
Fe ²⁺	0.9983	-0.8591	0.0306	0.0560	-0.1016	0.6778
Co ²⁺	0.3406	-1.7046	0.0068	0.0166	-0.0568	0.5608
Ni ²⁺	-0.3298	-2.7672	0.0026	0.0115	0.0419	0.3099
Eu ²⁺	8.7937	8.3346	3.4190	2.9878	1.2523	1.6235

eight-fold coordinated Ca²⁺ host cations, respectively, as shown in Figure 4.2; hence, the energetics of the incorporation of trace-element cations at the two lattice sites in diopside are reported separately.

4.6.3.1 Defect Energies

Figures 4.3 and 4.4 show the variations of the final relaxed defect energies, E_{def} , with ionic radius for divalent trace-element cations entering CaO and diopside, respectively. In both minerals, the calculated values of E_{def} show a linear variation with cation radius in the classical approach. In contrast, the E_{def} 's obtained from the DFT calculations show two separate linear trends for the closed-shell cations, *i.e.*, Mg²⁺, Ca²⁺, Sr²⁺ and Ba²⁺, and for the open-shell cations, including Ni²⁺, Co²⁺, Fe²⁺, Mn²⁺ and Eu²⁺. This could possibly arise from the use of the inappropriate (fixed) ionic radii for the 3*d*-block 4*f*-block ions. According to Shannon,^{176,277} the determination of these cation radii is less

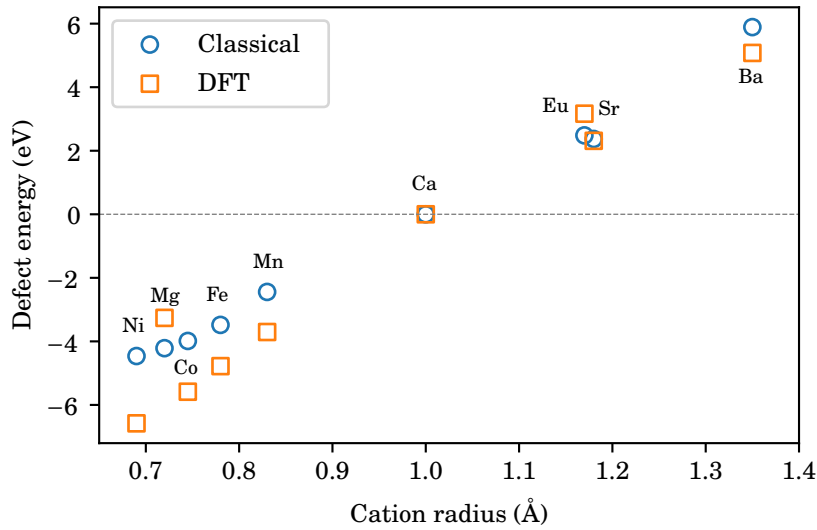


FIGURE 4.3. Variation of calculated final relaxed defect energies with ionic radius for homovalent substitutions in CaO. The computational details for the classical calculations based on Buckingham interionic potentials and the core-shell model and the plane-wave DFT (GGA-PBE) simulation can be found in Subsection 4.6.2.

straightforward compared to the other main-group (close-shell) cations due to various factors, *e.g.*, the crystal-field and ligand-field stabilisation effects. For Mn^{2+} , Fe^{2+} , and Co^{2+} , the size of each cation depends on its spin state; for example, the VI-fold coordinated ionic radii of Mn^{2+} are 0.67 and 0.83 Å in low-spin and high-spin complexes, respectively. Furthermore, the size of a given open-shell cation depends greatly on the nature of its local environment, *i.e.*, the strength of the ligand field surrounding the ion determines its size due to the non-spherical electron distribution (see more details in, *e.g.*, Orgel²⁷⁸ and Figgis and Hitchman²⁷⁹).

It is important to note that E_{def} can either be positive or negative depending on the difference in ionic radius of the size compared to the host cation, *i.e.*, E_{def} of a dopant smaller than the host cation is expected to be negative and vice versa. However, the negative values of DFT relaxation energies for the incorporation of Co^{2+} and Fe^{2+} whose six-fold coordinated Shannon radii are larger than the host cation Mg^{2+} at the $M1$ -site have been observed, as shown in Figure 4.4(b). This is, again, possibly due to the artefact of using the inappropriately fixed cation radii.

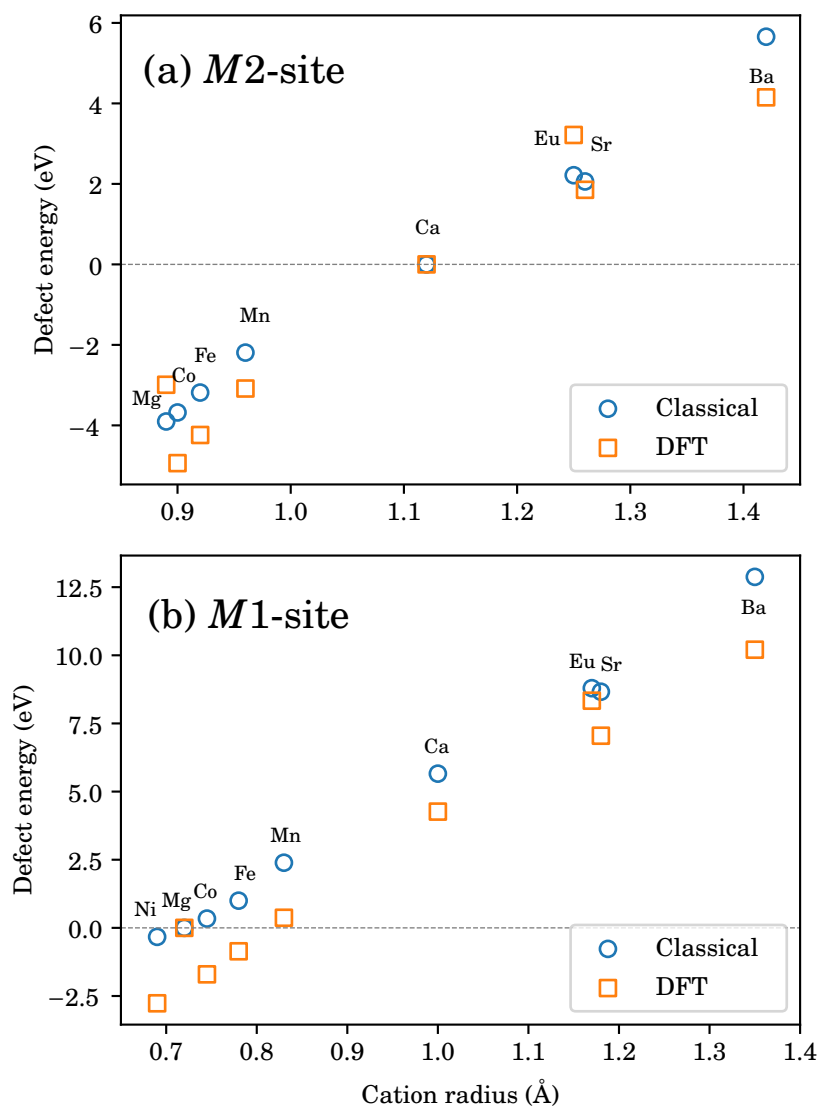


FIGURE 4.4. Variation of calculated final relaxed defect energies with ionic radius for homovalent substitutions in the clinopyroxene diopside. The computational details for the classical calculations based on Buckingham interionic potentials and the core-shell model and the plane-wave DFT (GGA-PBE) simulation can be found in Subsection 4.6.2.

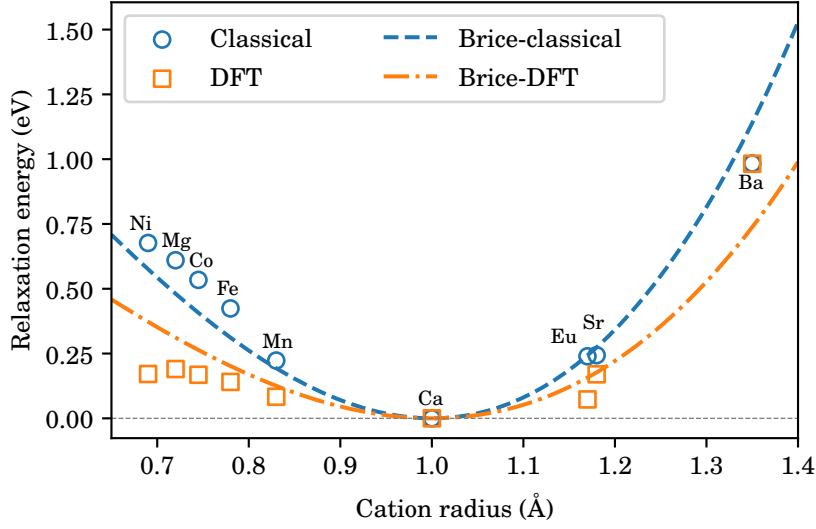


FIGURE 4.5. Variation of calculated relaxation energies with ionic radius for divalent substitutions in CaO. The dashed lines represent fits of the relaxation energies from both simulation approaches to equation (4.13) of Brice.³⁴ The computational details for the classical calculations based on Buckingham interionic potentials and the core-shell model and the plane-wave DFT (GGA-PBE) simulation can be found in Subsection 4.6.2.

4.6.3.2 Relaxation Energies

Plots of the relaxation energies, E_{rel} , as a function of cation dopant size for the divalent substitutions in CaO and diopside are shown in Figures 4.5 and 4.6, respectively. In contrast to the E_{def} , which can either be positive or negative, the E_{rel} of any substitution is always positive as the energy falls as all other constituent ions move in order to accommodate the new substituent cation. In all cases, E_{rel} must be zero (*i.e.*, no relaxation) for the host cation, while the more positive E_{rel} 's are generally expected for the cations whose ionic radii differ more from that of the host cation. Strictly speaking, the greater is the size mismatch between the host and homovalent substituent cations, the higher is E_{rel} . As mentioned above, these E_{rel} 's can roughly be used as approximate strain energies, U_{strain} , *e.g.*, in the Brice³⁴ strain model in equation (4.13). Analogously to E_{rel} , a greater value of U_{strain} is expected for a larger difference in cation radii. In Figures 4.5 and 4.6, the dashed lines represent fits of E_{rel} from both simulation approaches to the cubic equation (4.13).

For the divalent substitutions in CaO, as shown in Figure 4.5, the fitted r_0 is identical for both classical and DFT simulations, *i.e.*, at 1.0 Å corresponding to the ionic radius of

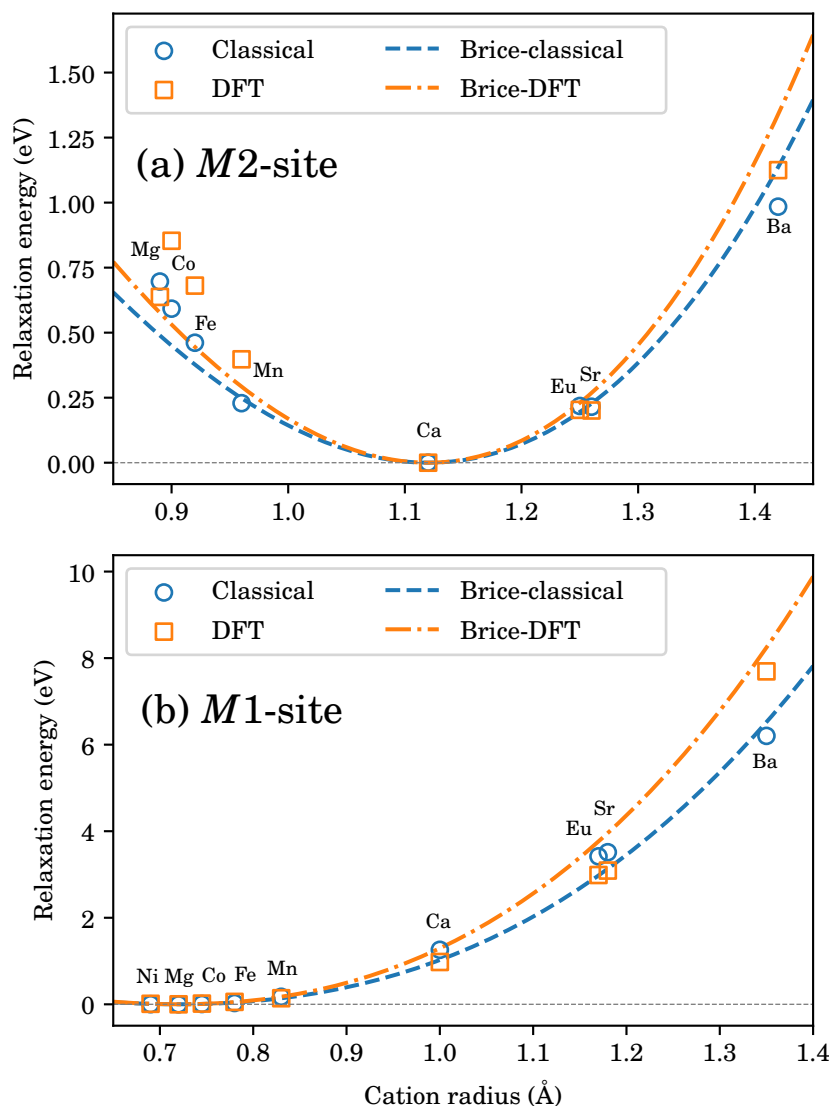


FIGURE 4.6. Variation of calculated relaxation energies with ionic radius for divalent substitutions at (a) *M2*-site and (b) *M1*-site of the clinopyroxene diopside. The dashed lines represent fits of the relaxation energies from both simulation approaches to equation (4.13) of Brice.³⁴ The computational details for the classical calculations based on Buckingham interionic potentials and the core-shell model and the plane-wave DFT (GGA-PBE) simulation can be found in Subsection 4.6.2.

Ca^{2+} host cation. On the other hand, the fitted Ca-site Young's moduli, Y_{Ca} , are considerably different in the two simulation approaches, *i.e.*, 194 and 126 GPa in the classical and DFT calculations, respectively. The significantly larger Y_{Ca} in the classical approach, *i.e.*, resulting in a tighter curve, implies that the classical Ca-site is less elastically compressible or stiffer than that in the DFT simulation. Note that the experimental '*crystal*' Young's modulus is 181 GPa.²⁷⁴ From our calculations, the crystal of CaO is elastically isotropic with the calculated Poisson ratios of 0.21 and 0.32 in the DFT and classical approaches, respectively. Using the relationship between the bulk and Young's moduli in equation (4.19), the fitted '*site*' Young's moduli can be converted to the '*site*' bulk moduli, K_{Ca} . As a result, the DFT and classical K_{Ca} are approximately 72 and 180 GPa, respectively. Note also that the experimental '*crystal*' bulk modulus is 111.25 GPa.²⁷³

For divalent substitutions in diopside, as shown in Figure 4.6, the fitted r_0 's are consistent with the six-fold and eight-fold coordination ionic radii of the host cations Mg^{2+} (0.72 Å) at the *M1*-site and Ca^{2+} (1.12 Å) and the *M2*-site, respectively. The curvature of each cubic function varies from site to site in a manner consistent with their elastic compressibilities determined from high-pressure crystal structure observations. The fitted *M1*-site's modulus, Y_{M1} , is larger than Y_{M2} in both simulation approaches, *i.e.*, the classical and DFT Y_{M2} are *ca.* 246 and 291 GPa, respectively, whereas the classical and DFT Y_{M1} are approximately 372 and 470 GPa. The larger Y_{M1} compared to Y_{M2} results in a tighter curve, which implies that the *M2*-site is more compressible than the *M1*-site of the clinopyroxene diopside. This is in line with the experimental work of Levien and Prewitt,²⁸⁰ which emphasises that the *M1*-site is relatively less compressible than the *M2*-site. The previous computational study of Purton *et al.*³⁰ has shown that the plots for Mg-sites in diopside and forsterite are similar. Therefore, it is clear that the rigidity or stiffness of the site's local environment rather than that of the bulk determines the relaxation (approximate strain) energy. Explicit consideration of the variations in the size of dopant and oxygen ions with bond length may improve the application of the lattice strain model.¹⁸²

In Figure 4.6(a), the relaxation energies for the incorporation of Mn^{2+} , Fe^{2+} and Co^{2+} at the *M2*-site of diopside deviate slightly from the trend for other cations as we have seen earlier in the case of the defect energies. Again, this arises from the use of the fixed unrealistic ionic radii. Therefore, we highlight this as a limitation of the use of the simple strain model of Brice³⁴ in equation (4.13), where the strain energy is expressed as a function of fixed cation radius (with fixed-size O^{2-}) derived by Shannon,¹⁷⁶ to study

trace-element partitioning.

4.6.3.3 Solution Energies

The defect energies themselves do not relate directly to the incorporation process. Besides, they contribute to the solution energies of the trace-cation exchange reactions, *e.g.*, for the $\text{Mg}_{\text{Ca}}^{\text{x}}$ substitution reaction in equation (4.23) with the solution energy obtained using equation (4.24). Again, note that the calculation of the solution energy does not include only the simulated defect energy $E_{\text{def}}(\text{Mg}_{\text{Ca}}^{\text{x}})$, but also the difference in lattice energies of the two binary oxides, *i.e.*, $E_{\text{lat}}(\text{CaO}) - E_{\text{lat}}(\text{MgO})$. It is also important to note that a negative defect energy does not necessarily mean that the overall solution energy is negative. Here, we use the binary oxides to provide a reference level (simple starting point) for our model for explaining mineral-melt partitioning as the ultimate goal. The explicit incorporation of the heats of fusion of these binary oxides makes only a slight difference.²⁸¹ Using heats of formation of molten oxides instead of solid oxides, the heat of solution for exchanging Sr with Mg at the *M1*-site of diopside, for instance, changes only by ~ 0.1 eV. Although the size of trace-element dopant cation gives a simple rule of thumb, the magnitude of the solution energy cannot always be examined from a sole consideration of its size.

Figure 4.7 shows the variation of classical and DFT solution energies, E_{sol} , with cation dopant size for divalent substitutions in CaO. Overall, the curve of the solution energies as a function of ionic radius exhibits a similar shape to that of the relaxation energies in Figure 4.5, with a minimum at the radius of the Ca^{2+} cation. The shape of the curve is a result of two opposite effects: (i) the increase in defect energy and (ii) the decrease of the difference in lattice energy between CaO and MO with increasing dopant size. The variation of the solution energies with cation radius for homovalent substitutions at the *M2*- and *M1*-sites of diopside is illustrated in Figure 4.8. The minima of the curves for the classical solution energies are more well-defined, in contrast to those of the DFT solution energies. The two minima of the classical solution energies at the two lattice sites are also well-separated as clearly shown in Figure 4.9, *i.e.*, ~ 1.2 Å and 0.8 Å for the *M2*- and *M1*-sites, respectively, indicating the strong site preference of trace-element cations based on their size. Only cations with in-between radii will show equipartitioning between the *M2*- and *M1*-sites. Similarly to the variation of the relaxation energies with dopant size as discussed above, the dependence of the solution energies on ionic radius also varies from site to site, again indicating the importance of the site's local environment in controlling cation exchange.

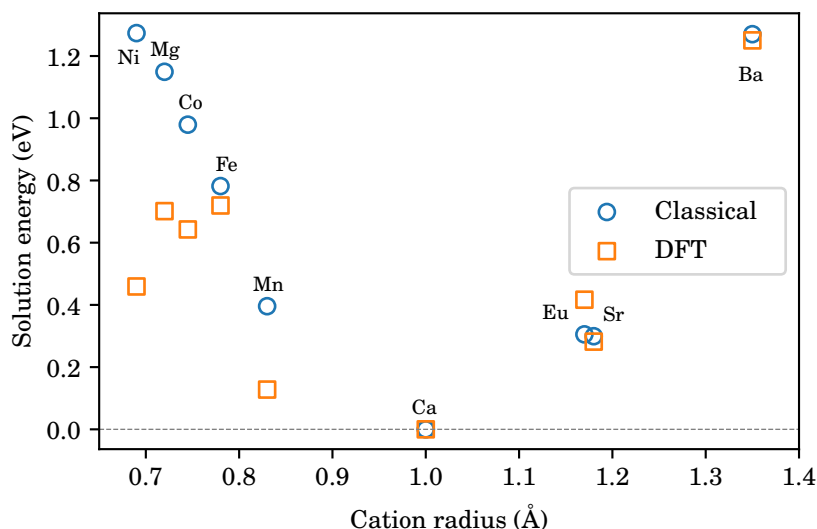


FIGURE 4.7. Variation of calculated solution energies with ionic radius for divalent substitutions in CaO. The computational details for the classical calculations based on Buckingham interionic potentials and the core-shell model and the plane-wave DFT (GGA-PBE) simulation can be found in Subsection 4.6.2.

So far, we have shown that both the classical and DFT simulation techniques are useful for computing the defect, relaxation and solution energies for the incorporation of divalent cations in CaO and diopside in order to investigate the partitioning behaviour theoretically. The magnitudes and trends in these thermodynamic properties obtained from both techniques are also in reasonable agreement. Even though the magnitudes and trends in relaxation energies for the homovalent substitutions in CaO and diopside from both simulation approaches are similar, as shown in Figures 4.5 and 4.6, respectively, the classical and DFT values of the site Young's moduli obtained from the fits of the relaxation energies to the strain model of Brice³⁴ are significantly different. The classical calculations based on empirical force fields are much computationally cheaper than the DFT calculations. However, they cannot provide insights into the electronic properties and other related quantum mechanical effects, *e.g.*, crystal-field and ligand-field stabilisation for the open-shell metal cations. The quality of the numerical results depends strongly on the accuracy of the empirical force fields and atomic pseudopotentials (and basis sets) used in the classical and DFT approaches, respectively. Previously, Purton *et al.*³¹ have extended these classical calculations to heterovalent trace impurities in forsterite and diopside. In the following subsection, we will discuss the calculation of the

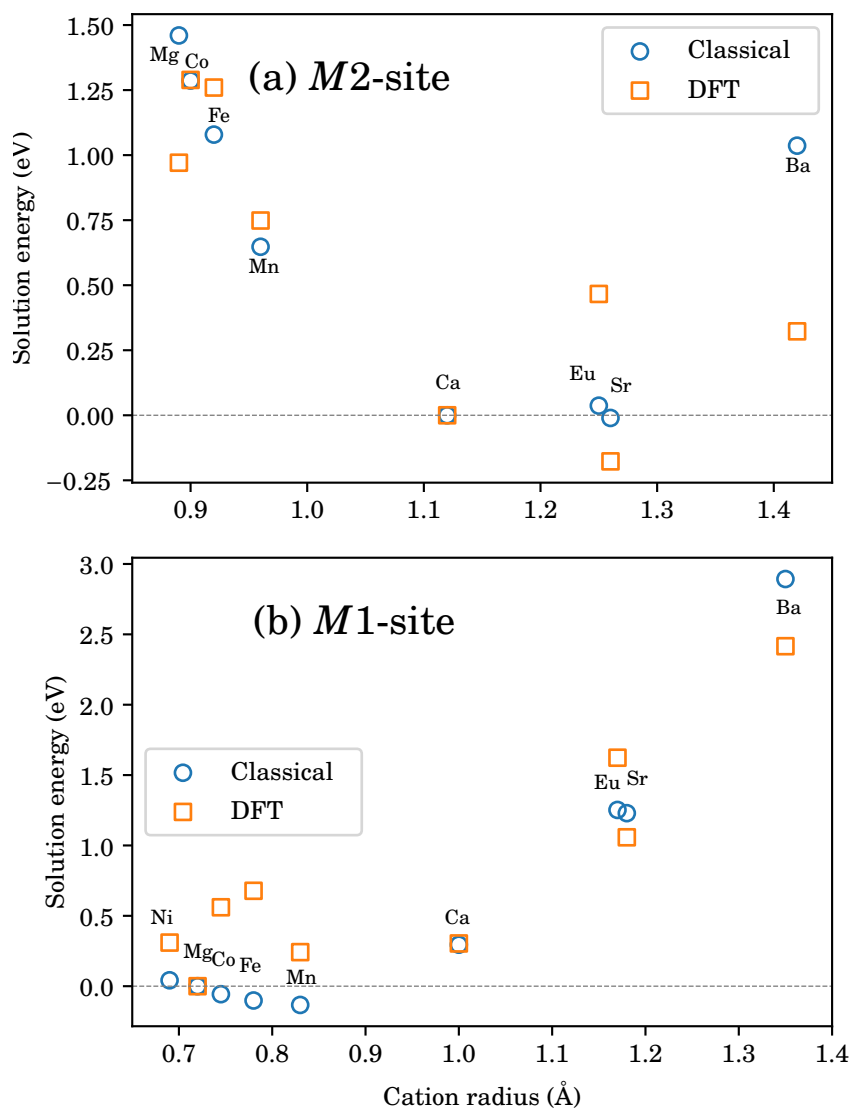


FIGURE 4.8. Variation of calculated solution energies with ionic radius for divalent substitutions in the clinopyroxene diopside. The computational details for the classical calculations based on Buckingham interionic potentials and the core-shell model and the plane-wave DFT (GGA-PBE) simulation can be found in Subsection 4.6.2.

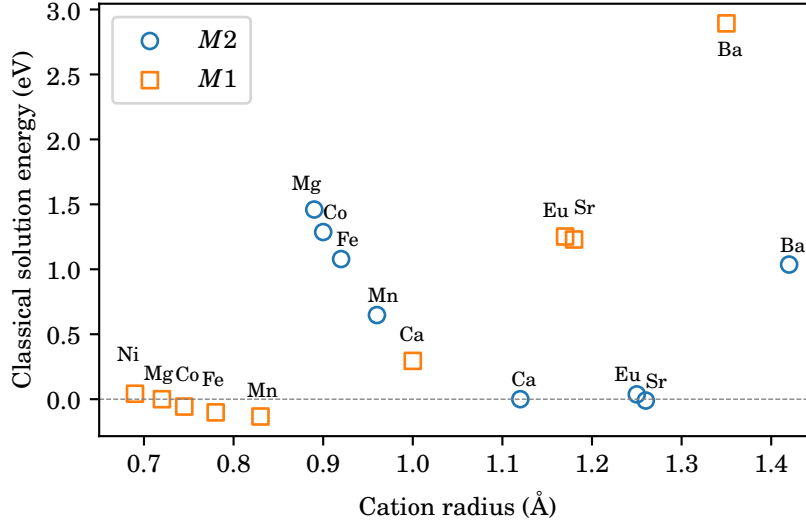


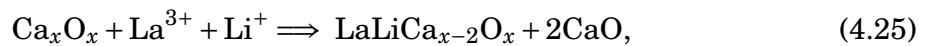
FIGURE 4.9. Variation of classical solution energies with ionic radius for diivalent substitutions at $M1$ - and $M2$ -sites of diopside. The computational details for the classical calculations based on Buckingham interionic potentials and the core-shell model can be found in Subsection 4.6.2.

thermodynamic quantities of heterovalent substitutions in CaO and diopside using the same classical and DFT simulation techniques outlined in the earlier section.

4.6.4 Heterovalent Trace Elements in CaO and Diopside

The incorporation of heterovalent cations involves ions with charges different from that of the host ion in a given mineral. For example, the substitution of Ca^{2+} by Li^+ or La^{3+} . Such heterovalent substitution gives rise to several problems. Firstly, the lattice polarisation due to the charged defect must be taken into account explicitly.^{125,282} Secondly, an appropriate charge-balancing or charge-compensating mechanism must be considered in order to maintain electroneutrality. As mentioned in the previous section, there are a large number of possible charge-balancing mechanisms, *e.g.*, by forming vacancies or incorporating other charge-compensating ions.

As a simple example, in the supercell approach, the incorporation of La^{3+} in a supercell of CaO containing $2x$ ions can occur through various possible charge-compensation mechanisms, for instance, by incorporating Li^+ as a compensating cation:

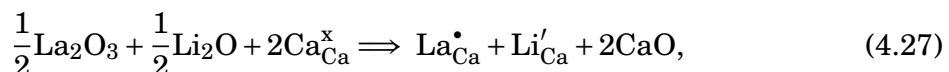


with the corresponding defect energy

$$E_{\text{def}}(\text{La}_{\text{Ca}}^{\bullet} + \text{Li}_{\text{Ca}}') = E_{\text{lat}}(\text{LaLiCa}_{x-2}\text{O}_x) - [(x-2)E_{\text{lat}}(\text{CaO}) + E_{\text{ion}}(\text{La}^{3+}) + E_{\text{ion}}(\text{Li}^+)]. \quad (4.26)$$

In this case, we consider two ‘associated’ substitutional defects of $\text{La}_{\text{Ca}}^{\bullet}$ and Li_{Ca}' situated as close as possible to one another. Alternatively, the two defects can be very far from each other in a given crystal. These are referred to as ‘isolated’ defects. In the latter case, the total defect energy should well be estimated from the sum of the defect energies of two isolated defects, *i.e.*, $E_{\text{def}}(\text{La}_{\text{Ca}}^{\bullet}) + E_{\text{def}}(\text{Li}_{\text{Ca}}')$. In contrast to the defect energies, the relaxation energies, E_{rel} , are ‘not’ additive and they ‘cannot’ be estimated simply from the separate relaxations of the two isolated defects. We shall see in the discussion below that the associated defect energy, denoted as $E_{\text{def}}(\text{La}_{\text{Ca}}^{\bullet} + \text{Li}_{\text{Ca}}')$, will be lower than the isolated defect energy $E_{\text{def}}(\text{La}_{\text{Ca}}^{\bullet}) + E_{\text{def}}(\text{Li}_{\text{Ca}}')$ due to the association energy between the two point defects. In fact, we have already seen the lowering in defect energy per defect for the clustering of multiple $\text{Ba}_{\text{Ba}}^{\times}$ substitutional defects in MgO, *i.e.*, in Figure 3.32. The decrease in defect energy per defect for multiple $\text{Ba}_{\text{Ba}}^{\times}$ defects in MgO is also due to the association energy of those $\text{Ba}_{\text{Ba}}^{\times}$ defects. It is worth noting that the reaction (4.25) can also be viewed as the incorporation of Li^+ into CaO with a charge-compensating La^{3+} cation.

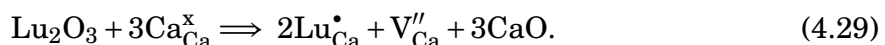
To evaluate the solution energy, using the Kröger and Vink notation,¹³¹ the exchange reaction (4.25) can be expressed as



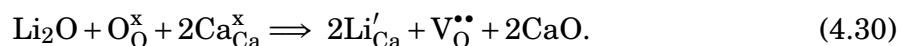
with the corresponding solution energy

$$E_{\text{sol}}(\text{La}_{\text{Ca}}^{\bullet} + \text{Li}_{\text{Ca}}') = E_{\text{lat}}^{\text{final}}(\text{La}_{\text{Ca}}^{\bullet} + \text{Li}_{\text{Ca}}') + 2E_{\text{lat}}(\text{CaO}) - [0.5E_{\text{lat}}(\text{La}_2\text{O}_3) + 0.5E_{\text{lat}}(\text{Li}_2\text{O})]. \quad (4.28)$$

Alternatively to the reaction mechanism (4.27), the incorporation of La^{3+} into CaO can occur by substituting two Ca^{2+} ions by two La^{3+} ions and creating a single Ca^{2+} cation vacancy, denoted by ‘V’:



In addition to reaction (4.27), the incorporation of Li^+ (a monovalent cation) into CaO can occur by exchanging two Ca^{2+} host ions with two Li^+ cations and creating a single O^{2-} vacancy:



In forsterite and diopside crystals, for example, other charge-compensation mechanisms with an effective positive charge involve oxygen interstitials and (for +3 dopants) trivalent exchange with Si coupled with Al substitution for Mg. These reaction mechanisms are much higher in energy than the reactions listed above;^{31,173} hence, they shall not be considered further.

These examples are only a few possibilities amongst many other possible charge-compensating mechanisms for heterovalent substitutions in minerals. For instance, many other charge-balancing cations can be used in the heterovalent substitution reaction (4.27), *e.g.*, using Na^+ instead of Li^+ or using Sc^{3+} instead of La^{3+} . A different charge-compensating cation results in different values of the defect thermodynamic properties.^{31,127,173} As discussed earlier, the (associated) defect-defect distance determines also those calculated defect properties. Consequently, any computational study must consider various possible charge-compensating mechanisms, types of dopants, and their structural arrangements for heterovalent substitutions in a given mineral. The issue becomes more complicated for the incorporation of heterovalent cations in a crystal with several lattice sites prone to exchange. In this study, we consider solely the thermodynamic properties of the heterovalent substitutions with additional heterovalent charge-compensating cations for simplicity.

The classical and DFT defect, relaxation and solution energies for both associated and isolated +1 and +3 trace elements in CaO are listed in Table 4.8. In the case of the associated defects, the two point defects are located as close as possible to each other, whereas the two defects are placed as far as possible from each other in the case of the isolated defects. The calculated thermodynamics for all the monovalent substitutions with a La^{3+} charge-compensating defect are plotted in Figure 4.10, while the calculated energies for the trivalent substitutions with a Li^+ charge-balancing cation are shown in Figure 4.11. As expected, all three classical and DFT thermodynamic quantities for the associated defects are lower than those for the isolated defects due to the association energy between the two incorporated heterovalent cations in each structure.

For the clinopyroxene diopside, the classical and DFT defect, relaxation and solution energies for +1 and +3 trace elements are listed in Table 4.9. Here, we consider solely the three thermodynamic quantities of two ‘*associated*’ defects for a given heterovalent cation of interest and its corresponding charge-compensating defect. Again, the calculated energetics of the heterovalent substitutions at the *M1*-site and *M2*-site of diopside are reported separately. Note that the distances between two closest *M1*–*M1*, *M2*–*M2* and *M1*–*M2* sites in diopside are *ca.* 3.1, 4.4 and 3.2 Å, respectively. These different lattice-

TABLE 4.8. Calculated defect, relaxation and solution energies for heterovalent substitutions in CaO. The computational details for the classical calculations based on Buckingham interionic potentials and the core-shell model and the plane-wave DFT (GGA-PBE) simulation can be found in Subsection 4.6.2.

Dopant cation	Defect energy (eV)		Relaxation energy (eV)		Solution energy (eV)	
	Classical	DFT	Classical	DFT	Classical	DFT
Monovalent (+1) - with associated La^{3+} compensating defect						
Li^+	-5.2778	-0.9547	2.5461	0.5954	1.0365	0.9111
Na^+	-4.2425	0.0995	2.9321	0.6281	0.3514	0.2307
K^+	-1.1997	2.1862	4.2823	1.1366	1.5194	0.9077
Rb^+	-0.0191	3.5560	5.2668	1.8138	2.2789	1.8108
Monovalent (+1) - with isolated La^{3+} compensating defect						
Li^+	-4.9252	-0.7941	4.9041	0.9444	1.3890	1.0716
Na^+	-3.9640	0.2185	5.3642	1.0028	0.6298	0.3496
K^+	-0.9328	2.3056	6.7259	1.4842	1.7864	1.0270
Rb^+	0.2461	3.6757	7.7121	2.1407	2.5442	1.9306
Trivalent (+3) - with associated Li^+ compensating defect						
Sc^{3+}	-14.4527	-10.1706	5.1652	1.3918	1.1317	0.6515
La^{3+}	-5.2778	-0.9547	2.5461	0.5954	1.0365	0.9111
Nd^{3+}	-7.0199	-2.9422	2.7649	0.5509	0.8427	0.6049
Eu^{3+}	-8.2786	-3.9734	3.0066	0.5228	0.7641	0.7316
Gd^{3+}	-8.5951	-3.9430	3.0842	0.6237	0.7513	0.5394
Ho^{3+}	-9.9538	-5.5052	3.4295	0.7108	0.7388	0.4692
Lu^{3+}	-11.3000	-6.0480	3.8546	0.8959	0.7848	0.4823
Yb^{3+}	-10.9070	-5.9489	3.7395	0.8516	0.7668	0.6915
Trivalent (+3) - with isolated Li^+ compensating defect						
Sc^{3+}	-14.2890	-10.0531	7.7120	1.7104	1.2954	0.7690
La^{3+}	-4.9252	-0.7941	4.9041	0.9444	1.3890	1.0716
Nd^{3+}	-6.7087	-2.8138	5.1641	0.9173	1.1539	0.7333
Eu^{3+}	-7.9965	-3.8429	5.4351	0.7925	1.0461	0.8621
Gd^{3+}	-8.3207	-3.8275	5.5203	0.9903	1.0256	0.6549
Ho^{3+}	-9.7096	-5.4118	5.8958	1.0829	0.9830	0.5627
Lu^{3+}	-11.0853	-5.9567	6.3504	1.2681	0.9995	0.5737
Yb^{3+}	-10.6846	-5.9489	6.2277	0.8516	0.9892	0.6915

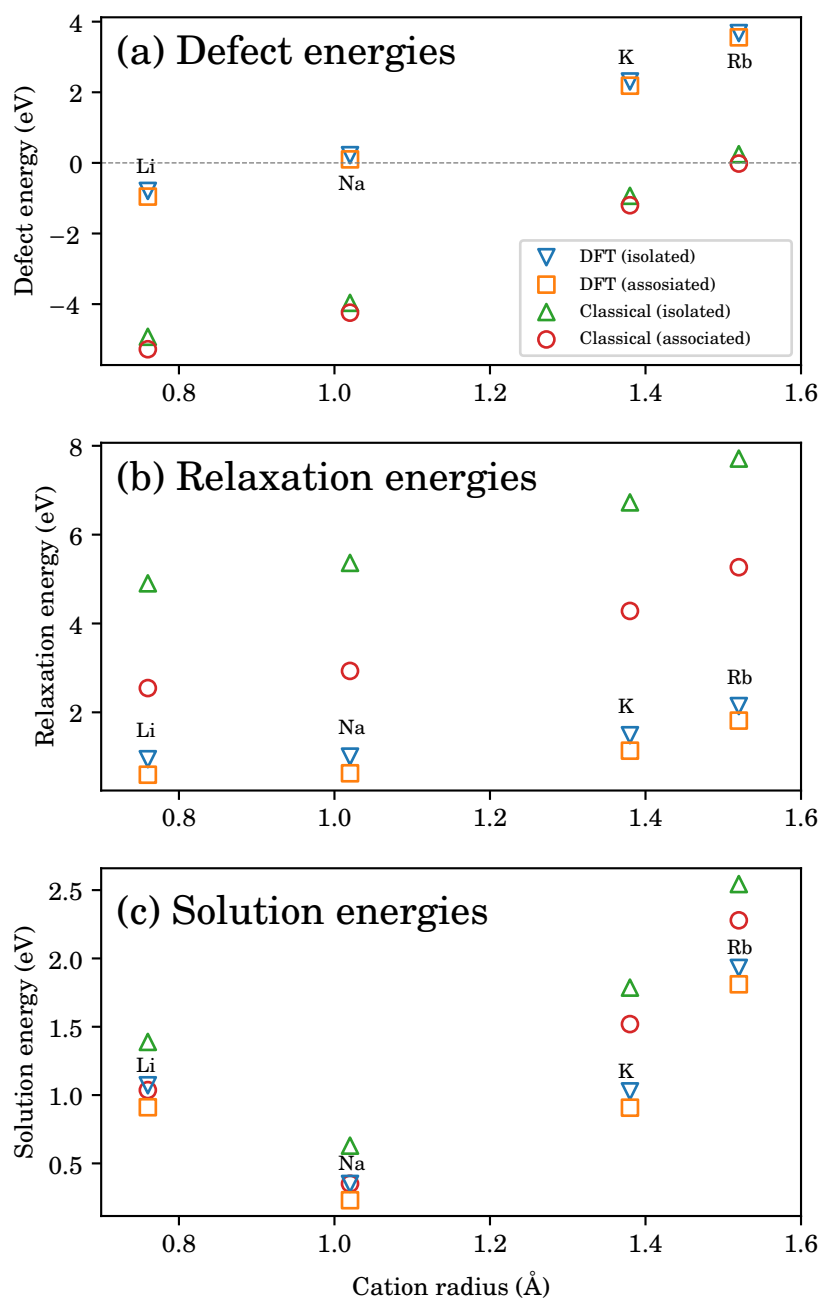


FIGURE 4.10. Variations of calculated (a) defect, (b) relaxation and (c) solution energies with cation radius for monovalent substitutions in CaO with a La^{3+} ion as the compensating defect. The computational details for the classical calculations based on Buckingham interionic potentials and the core-shell model and the plane-wave DFT (GGA-PBE) simulation can be found in Subsection 4.6.2.

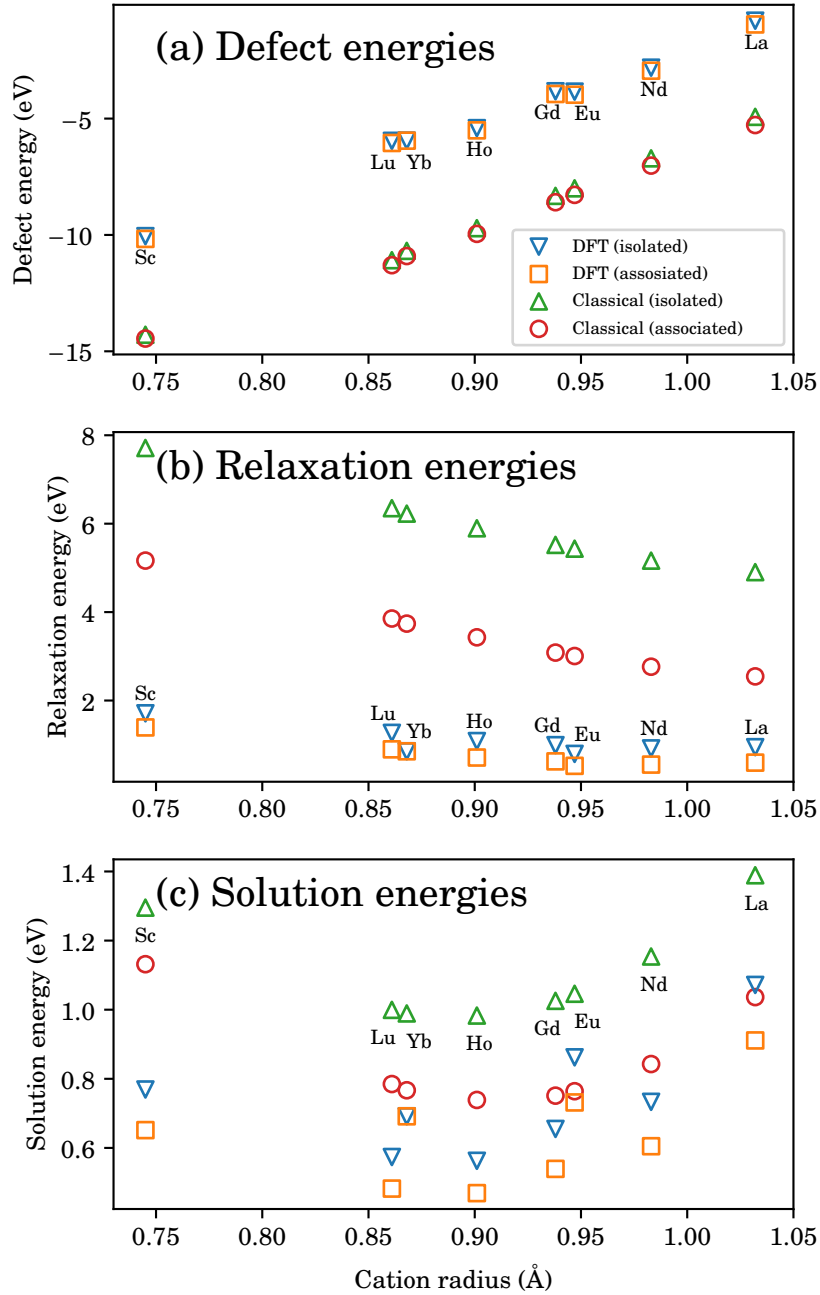


FIGURE 4.11. Variations of calculated (a) defect, (b) relaxation and (c) solution energies with cation radius for trivalent substitutions in CaO with a Li^+ ion as the compensating defect. The computational details for the classical calculations based on Buckingham interionic potentials and the core-shell model and the plane-wave DFT (GGA-PBE) simulation can be found in Subsection 4.6.2.

TABLE 4.9. Calculated defect, relaxation and solution energies for heterovalent substitutions in diopside. The computational details for the classical calculations based on Buckingham interionic potentials and the core-shell model and the plane-wave DFT (GGA-PBE) simulation can be found in Subsection 4.6.2.

Dopant cation	Defect energy (eV)		Relaxation energy (eV)		Solution energy (eV)	
	Classical	DFT	Classical	DFT	Classical	DFT
Monovalent (+1) at <i>M2</i> - with La^{3+} associated compensating defect at <i>M1</i>						
Li^+	0.9705	3.9588	4.6709	4.2704	1.9217	1.8631
Na^+	1.8836	4.9873	4.7936	4.0503	1.1143	1.1569
K^+	4.9884	6.5857	5.8915	4.6045	2.3444	1.3456
Rb^+	6.0909	7.6698	6.6840	5.3717	3.0258	1.9631
Monovalent (+1) at <i>M1</i> - with La^{3+} associated compensating defect at <i>M2</i>						
Li^+	0.0837	2.8704	2.9352	0.5459	1.0349	0.7746
Na^+	1.9974	4.4789	4.5872	1.0625	1.2281	0.6484
K^+	6.1923	7.3450	8.0848	3.8284	3.5483	2.1050
Rb^+	7.7231	9.0004	10.8915	6.8084	4.6580	3.2937
Trivalent (+3) at <i>M2</i> - with Li^+ associated compensating defect at <i>M1</i>						
Sc^{3+}	-7.6529	-5.0747	4.7132	1.3505	2.5684	1.7858
La^{3+}	0.0837	2.8704	2.9352	0.5459	1.0349	0.7746
Nd^{3+}	-1.3629	1.2247	2.9868	0.4696	1.1366	0.8103
Eu^{3+}	-2.4173	0.2691	3.1060	0.4236	1.2622	1.0126
Gd^{3+}	-2.6722	0.4189	3.1496	0.5004	1.3110	0.9397
Ho^{3+}	-3.8285	-0.8531	3.3665	0.4822	1.5010	1.1598
Lu^{3+}	-4.9636	-1.2946	3.6631	0.7397	1.7581	1.2742
Yb^{3+}	-4.6130	-1.4523	3.5792	0.5038	1.6976	1.2266
Trivalent (+3) at <i>M1</i> - with Li^+ associated compensating defect at <i>M2</i>						
Sc^{3+}	-9.3379	-6.2916	2.5263	0.6722	0.8833	0.5689
La^{3+}	0.9705	3.9588	4.6709	4.2704	1.9217	1.8631
Nd^{3+}	-0.9524	1.8716	3.7119	2.8892	1.5471	1.4571
Eu^{3+}	-2.3568	0.7807	3.2080	2.3818	1.3227	1.5241
Gd^{3+}	-2.7118	0.6767	3.0909	2.1213	1.2714	1.1975
Ho^{3+}	-4.2394	-1.0493	2.7466	1.5332	1.0901	0.9636
Lu^{3+}	-5.7611	-1.7989	2.5281	1.1367	0.9606	0.7699
Yb^{3+}	-5.3190	-1.6809	2.5679	1.2688	0.9917	0.9979

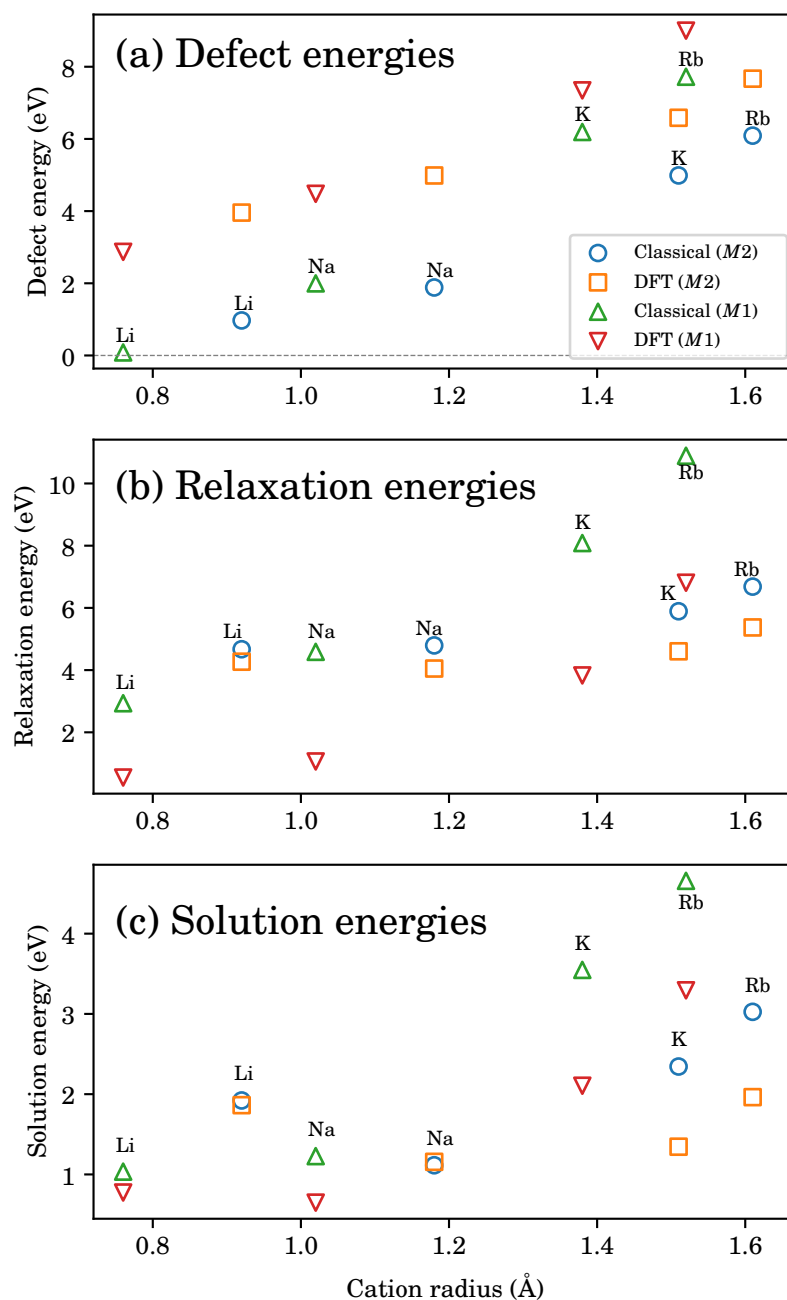


FIGURE 4.12. Variations of calculated (a) defect, (b) relaxation and (c) solution energies with cation radius for monovalent substitutions in diopside with a La^{3+} ion as the compensating defect. $b^+(M1)/\text{La}^{3+}$ (closest $M2$) and $b^+(M2)/\text{La}^{3+}$ (closest $M1$) are considered for monovalent substitutions at $M1$ -site and $M2$ -site, respectively. The computational details for the classical and plane-wave DFT (GGA-PBE) simulation can be found in Subsection 4.6.2.

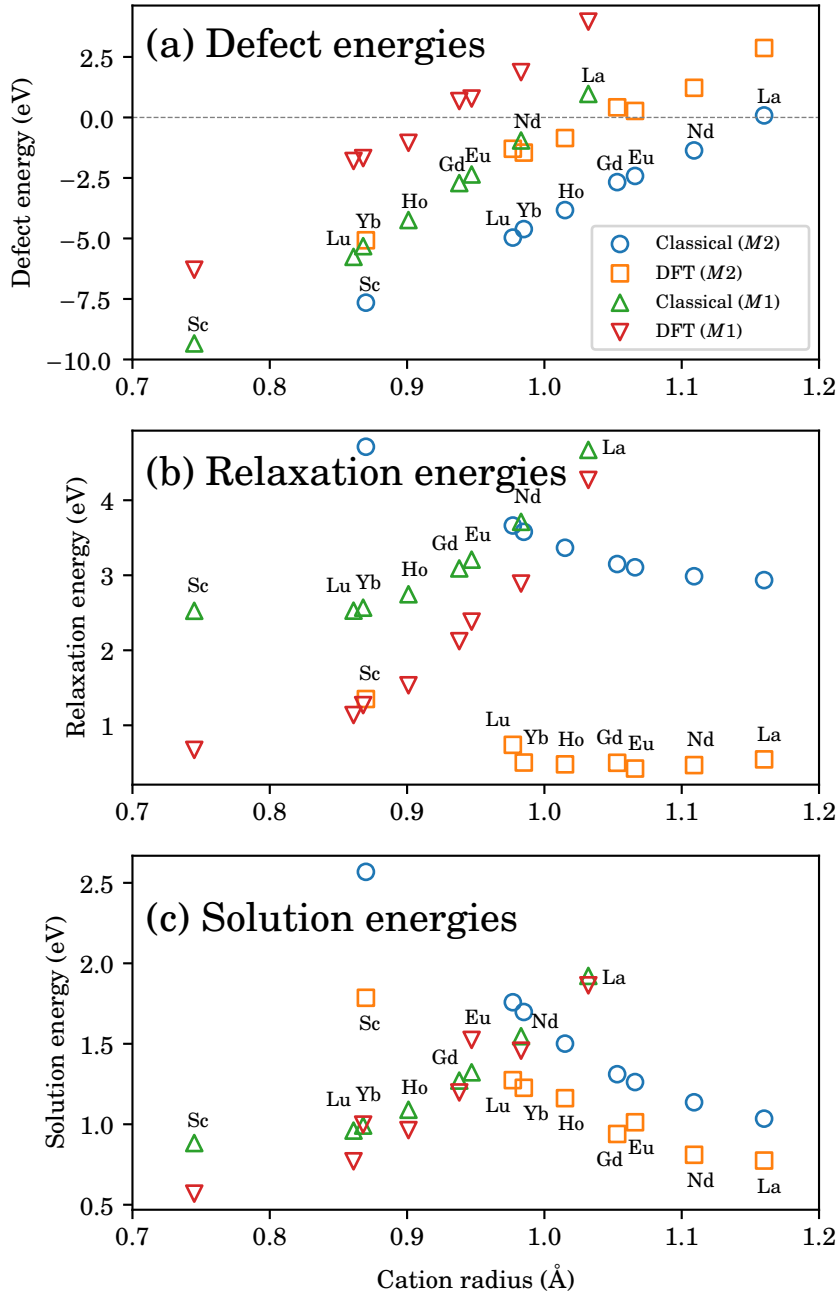


FIGURE 4.13. Variations of calculated (a) defect, (b) relaxation and (c) solution energies with cation radius for trivalent substitutions in diopside with a Li^+ ion as the compensating defect. $b^{3+}(M1)/\text{Li}^+(\text{closest } M2)$ and $b^{3+}(M2)/\text{Li}^+(\text{closest } M1)$ are considered for trivalent substitutions at $M1$ -site and $M2$ -site, respectively. The computational details for the classical and plane-wave DFT (GGA-PBE) simulation can be found in Subsection 4.6.2.

site separations lead to different computed energies. For simplicity, we consider only the heterovalent substitutions at the closest $M1$ – $M2$ sites. For example, a monovalent substitution at an $M2$ -site is coupled with a La^{3+} compensating defect substituted at the closest $M1$ -site, *i.e.*, $b^+(M2)/\text{La}^{3+}(M1)$. On the other hand, a monovalent substitution at an $M1$ -site is coupled with a La^{3+} compensating cation incorporated at the closest $M2$ -site, *i.e.*, $b^+(M1)/\text{La}^{3+}(M2)$. The variation of the three thermodynamic quantities with ionic radius obtained from both classical and DFT calculations for the monovalent substitutions is shown in Figure 4.12. Furthermore, the calculated energies as a function of dopant size for the trivalent substitutions are also plotted in Figure 4.13.

Overall, in contrast to the case of homovalent substitutions in CaO and diopside, the magnitudes of the three thermodynamic quantities, *i.e.*, defect, relaxation and solution energies, for the heterovalent substitutions in CaO and diopside obtained from the classical and DFT approaches can be significantly different, as listed in Tables 4.8-4.9 and illustrated in Figures 4.10-4.13. Those significant differences in the magnitudes of the numerical results might be mainly due to the different magnitudes of computed absolute energy terms from the two computational approaches. However, the trends of those three thermodynamic quantities obtained from the classical and DFT approaches are in good agreement. Due to the similarity of the trends of the numerical results obtained from the classical and DFT methods, we shall solely discuss the DFT defect, relaxation and solution energies for heterovalent substitutions in CaO and diopside beyond this point.

4.6.4.1 DFT Defect Energies

In the previous theoretical work by Purton *et al.*,³¹ all the calculated classical defect energies for isolated heterovalent (+1 and +3) impurities in forsterite and diopside were obtained using the two-region approach with the Mott-Littleton approximation.¹²⁵ In those calculations, the lattice polarisation arising from the incorporated charged defect has been taken into account explicitly. According to Purton *et al.*,^{30,31} as expected from classical electrostatic explanations, the ‘*isolated*’ defect energies follow the order $+3 < +2 < +1$ for a given cation radius in forsterite and diopside minerals. In our calculations based on the supercell approach, on the other hand, the ‘*associated*’ defect energies for the +1 trace-element cations in CaO, as shown in Figure 4.14, are not always higher than those for +2 cation impurities with similar ionic radii. This is due to the incorporation of an additional +3 charge-compensating defect, *i.e.*, La^{3+} , in order to maintain the electroneutrality of the defective supercell. Similarly to the

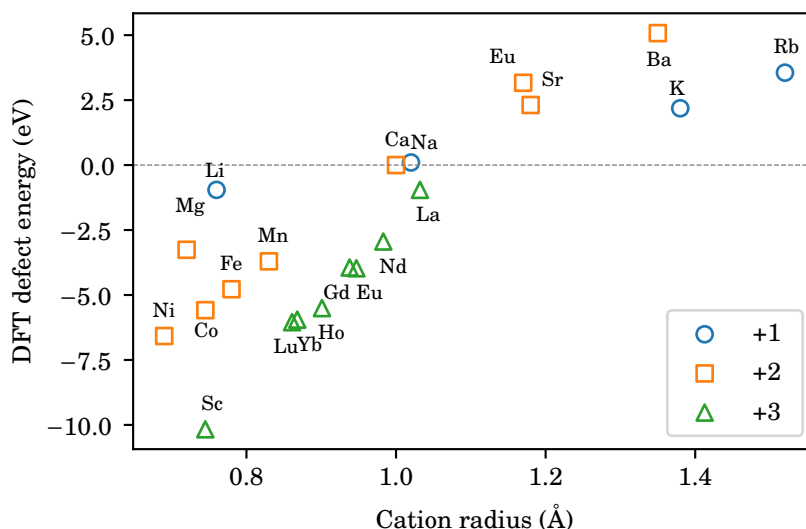


FIGURE 4.14. DFT defect energies of homovalent (+2) and heterovalent (+1 and +3) substitutions in CaO. Only associated defect energies are plotted for the heterovalent substitutions. La^{3+} and Li^{+} are chosen as the compensating defects for monovalent (+1) and trivalent (+3) substitutions, respectively. The computational details for the plane-wave DFT (GGA-PBE) simulation can be found in Subsection 4.6.2.

divalent substitutions in CaO, the variation of defect energy with dopant size for both the monovalent and trivalent cation impurities is approximately linear. The slope of these linear trends increases in order $+1 < +2 < +3$.

Figure 4.15 shows a comparison between the DFT defect energies of homovalent and heterovalent substitutions at the two lattice sites of diopside with cation radius. At both lattice sites, similar to the defect energies of trace-element substitutions in CaO shown in Figure 4.14, the variation of the defect energies of a series of isovalent trace elements is approximately linear and the slope of those linear trends follows the order $+1 < +2 < +3$. Note again that these associated defect energies do not always follow the order $+3 < +2 < +1$ according to the classical electrostatic arguments for isolated defects. This is due to the additional +3 charge-compensating defect also incorporated into the diopside crystal for a monovalent substitution.

4.6.4.2 DFT Relaxation Energies

Using the DFT defect energies of homovalent and heterovalent substitutions in CaO in Figure 4.14, the corresponding DFT relaxation energies are plotted in Figure 4.16(a).

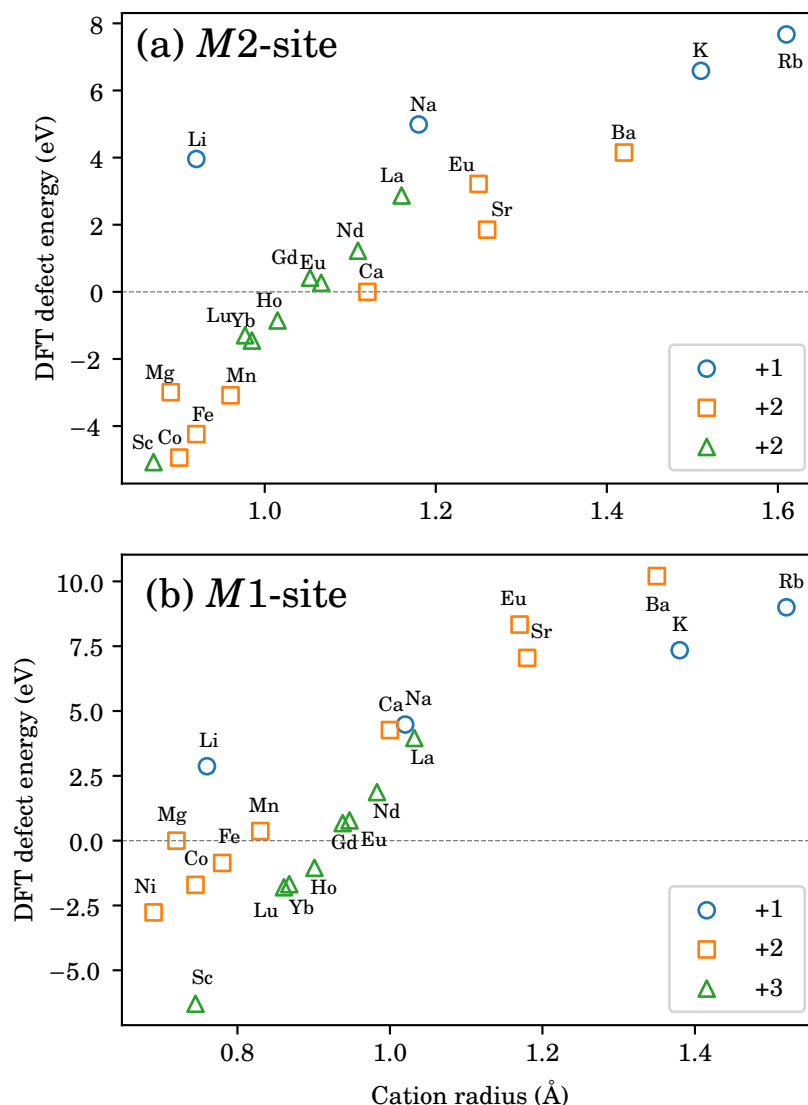


FIGURE 4.15. DFT defect energies of homovalent (+2) and heterovalent (+1 and +3) substitutions at (a) $M2$ -site and (b) $M1$ -site of diopside. Only associated defect energies are computed for the heterovalent substitutions. $b^+(M1)/La^{3+}(\text{closest } M2)$ and $b^+(M2)/La^{3+}(\text{closest } M1)$ are considered for monovalent substitutions at $M1$ -site and $M2$ -site, respectively. $b^{3+}(M1)/Li^+(\text{closest } M2)$ and $b^{3+}(M2)/Li^+(\text{closest } M1)$ are considered for trivalent substitutions at $M1$ -site and $M2$ -site, respectively. The computational details for the plane-wave DFT (GGA-PBE) simulation can be found in Subsection 4.6.2.

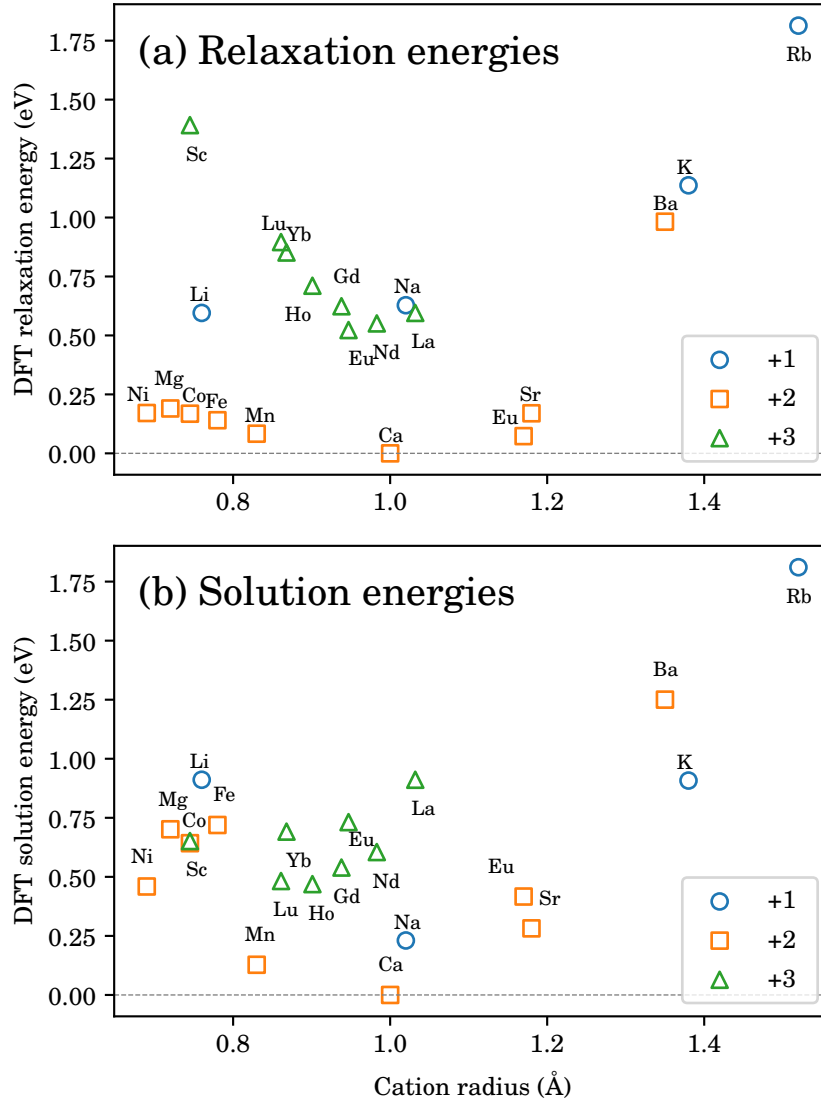


FIGURE 4.16. DFT (a) relaxation and (b) solution energies of homovalent (+2) and heterovalent (+1 and +3) substitutions in CaO. Only associated defect energies are plotted for the heterovalent substitutions. La^{3+} and Li^+ are chosen as the compensating defects for monovalent (+1) and trivalent (+3) substitutions, respectively. The computational details for the plane-wave DFT (GGA-PBE) simulation can be found in Subsection 4.6.2.

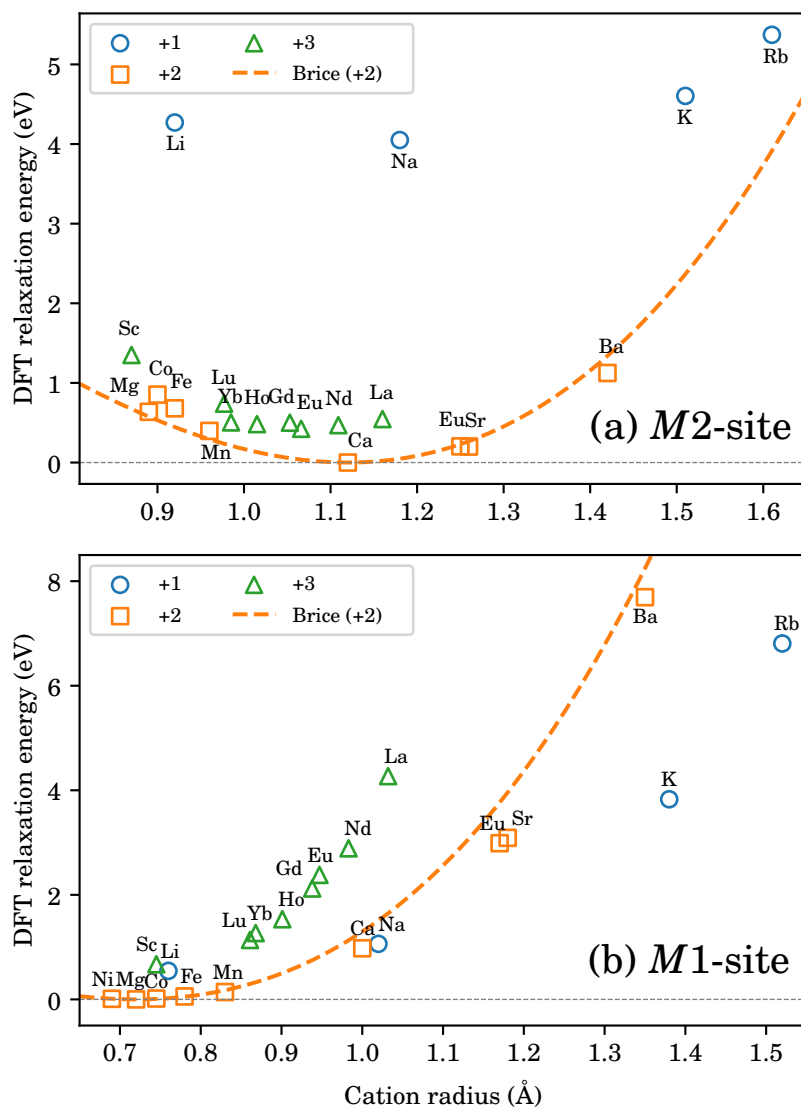


FIGURE 4.17. DFT relaxation energies of homovalent (+2) and heterovalent (+1 and +3) substitutions at (a) $M2$ -site and (b) $M1$ -site of diopside. $b^+(M1)/La^{3+}$ (closest $M2$) and $b^+(M2)/La^{3+}$ (closest $M1$) are considered for monovalent substitutions at $M1$ -site and $M2$ -site, respectively. $b^{3+}(M1)/Li^+$ (closest $M2$) and $b^{3+}(M2)/Li^+$ (closest $M1$) are considered for trivalent substitutions at $M1$ -site and $M2$ -site, respectively. The dashed lines represent fits of the relaxation energies for divalent ions to equation (4.13) of Brice.³⁴ The computational details for the plane-wave DFT (GGA-PBE) simulation can be found in Subsection 4.6.2.

Additionally, the variations of the DFT relaxation energies with ionic radius for homovalent (+2) and heterovalent (+1 and +3) substitutions at both the *M1*-site and *M2*-site of diopside is shown in Figure 4.17. As expected, the relaxation energies for all substitutions are greater than zero as energy is required for the structural relaxation in order to accommodate the misfit cation (or cations). The relaxation energies for heterovalent charged defects are always positive and higher than those for homovalent impurities due to the lattice polarisation. It is worth noting that for the two associated defects at the *M1*- and *M2*-sites of diopside are not additive and cannot simply be approximated from their separate relaxations. For each series of isovalent trace elements, except for the +1 curve in CaO, the minimum of the relaxation energy curve occurs at a radius close to the host cations, *e.g.*, VIII-fold coordinated Ca^{2+} at the *M2*-site and VI-fold coordinated Mg^{2+} at the *M1*-site of diopside, respectively.

An interesting feature of the plots in Figure 4.16(a) and 4.17 is that the curvature of the relaxation energies as a function of dopant size for +1 trace-element cations is smaller (less tight) than that for the divalent dopants, while the +3 curve is much tighter than the other two curves with a larger curvature. In the case of diopside, for each isovalent series, the curvature of the relaxation energy as a function of ionic radius at the *M1*-site is tighter than that at the *M2*-site, reflecting the relative compressibilities of the two sites. As discussed earlier, the curvature for each isovalent cation series reflects the site compressibility. However, fitting the +1 or +3 relaxation energies to equation (4.13) of the lattice strain model of Brice³⁴ in order to obtain a single apparent (or effective) site Young's modulus, Y_{Ca} , proves problematic as two heterovalent cations were incorporated simultaneously in every case. Furthermore, the lattice polarisation is not included in the expression for strain energy in equation (4.13). This is another key limitation of using the strain model of Brice³⁴ for explaining the heterovalent trace-element partitioning in minerals.

4.6.4.3 DFT Solution Energies

We next consider DFT solution energies for the incorporation of trace elements in CaO, as shown in Figure 4.16(b). Note again that the solution energy for each heterovalent substitution was calculated using equation (4.28). The variation of the DFT solution energies of the homovalent and heterovalent substitutions at the two lattice sites of diopside is also shown in Figure 4.18. As we have seen earlier in Figures 4.7, 4.8 and 4.9, the variation of the +2 solution energies with dopant size has a similar shape to that of the corresponding relaxation energies with a minimum at the radius of the Ca^{2+}

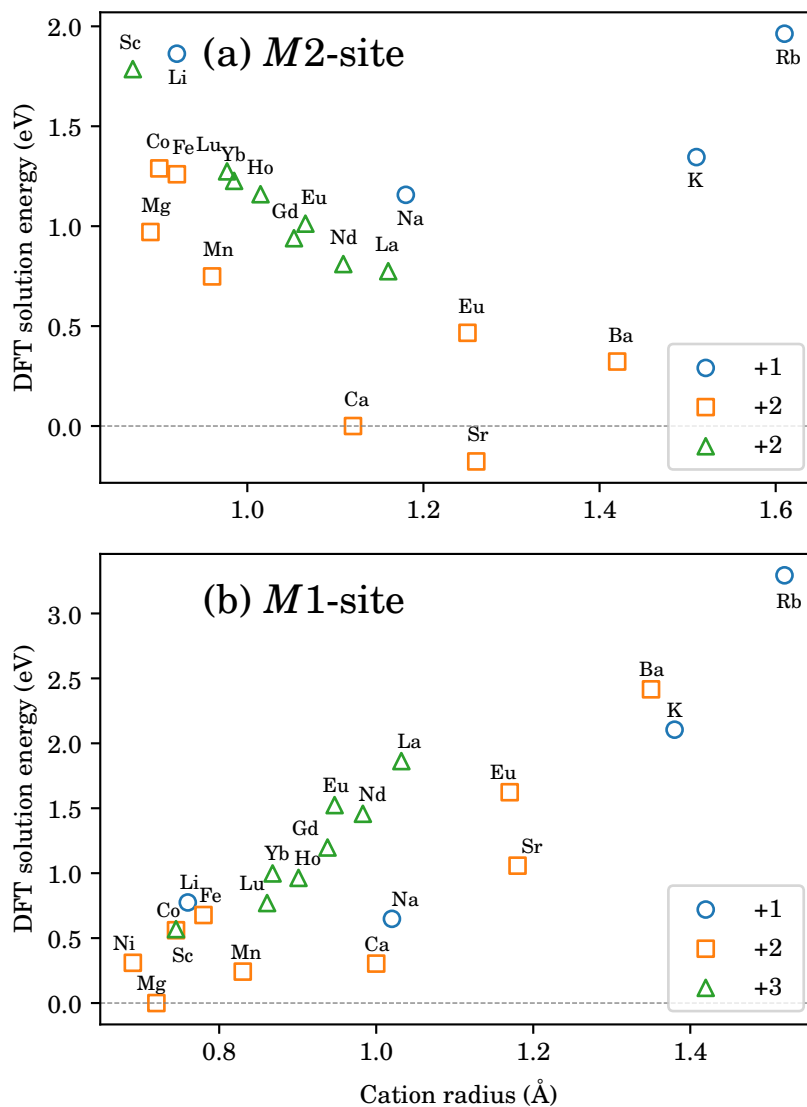


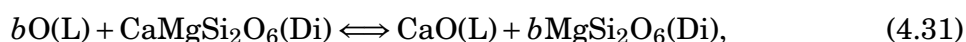
FIGURE 4.18. DFT relaxation energies of homovalent (+2) and heterovalent (+1 and +3) substitutions at (a) *M2*-site and (b) *M1*-site of diopside. $b^+(M1)/La^{3+}$ (closest *M2*) and $b^+(M2)/La^{3+}$ (closest *M1*) are considered for monovalent substitutions at *M1*-site and *M2*-site, respectively. $b^{3+}(M1)/Li^+$ (closest *M2*) and $b^{3+}(M2)/Li^+$ (closest *M1*) are considered for trivalent substitutions at *M1*-site and *M2*-site, respectively. The computational details for the plane-wave DFT (GGA-PBE) simulation can be found in Subsection 4.6.2.

host cation. Roughly, it is also the case for the +1 and +3 curves, *e.g.*, in Figures 4.10(c), 4.11(c), 4.12(c) and 4.13(c). It is important to keep in mind that the overall solution energy depends not only on the defect energies, but also several other contributing terms. Even though the calculated defect energy of a given trace element is lower at the *M2*-site than at the *M1*-site of diopside, a cation may substitute for Ca rather for Mg due to the contribution of these extra terms.

For a given trace element at a particular lattice site, the exchange-reaction mechanism that yields the lowest solution energy should be considered. As stressed previously, exploring all the possibilities theoretically is not trivial. Furthermore, comparing solution energies for different reaction mechanisms can be problematic due to different energy terms contributing to each reaction. According to the classical simulation of Purton *et al.*,³¹ a reaction mechanism involving the association between the dopant and its corresponding charge-compensating defect tends to have low solution energy, for example, the reactions $b^{3+}(M1)/Na^+(M2)$ and $b^{3+}(M2)/Na^+(M2)$ give the lowest solution energies for trivalent substitutions at the *M1*-site and *M2*-site of diopside, respectively.

4.6.5 Implications for Trace-Element Partitioning

In the first section, we have shown that it is possible to explain trace-element partitioning in terms of an exchange reaction between host and trace-element minerals and their corresponding melt species, *e.g.*, in equation (4.8) for the incorporation of a b^{2+} trace cation in forsterite or



for a b^{2+} trace element substituting for a Ca^{2+} host cation at an *M2*-site of diopside. Hence, the partitioning behaviour of b^{2+} in diopside links directly to the solution energy of reaction (4.31). In the literature, the local environment of the cations in the binary oxides is often assumed to be identical to that in the melt in order to compare computed solution energies with experimentally observed partition coefficients conveniently. This is definitely oversimplified since the composition and the structure of the melt phases play a vital role in controlling the trace-element partitioning behaviour between minerals and melts.^{255–262,283}

The variation of experimental partition coefficients of +1, +2 and +3 trace elements in diopside plotted against cation radius is shown in Figure 4.1(b). As the partition coefficient D_b is the ratio of crystal to melt concentration, the greater is the partition coefficient, the greater is the preference of the trace element b for the crystal. The

variation of the partition coefficients for an isovalent cation series with dopant size shows the optimum radius close to the size of the host cation.¹⁹² The curvature of the plots tends to increase with increasing charge, *i.e.*, the +3 curve is tighter than the +2 and +1 curves.³³ This behaviour can also be observed in the plots of solution energies, *e.g.*, in Figures 4.9, 4.12(c) and 4.13(c). Where substitution can occur at several lattice sites, a series of overlapping curves will be observed for each isovalent series.²¹⁹ In addition to the trace-element incorporation in the bulk of a given solid, Pinilla *et al.*²⁸⁴ have also pointed out that the adsorption and incorporation of trace elements at the interfaces also play a vital role when examining the partition coefficients. Incorporation of large trace-element cations may occur more preferentially at the interfaces than in the bulk of a mineral, leading to higher partition coefficients than would have been expected from predictions.²⁸⁴

However, calculated solution energies *cannot* directly be compared with experimental partition coefficients for several reasons. Firstly, finite-concentration effects have not been considered or have even been ignored when evaluating defect energy using the two-region approach. Secondly, these simulation techniques do not take the nature of the melt phases into account explicitly. Hence, the variation of the solution energies for heterovalent substitutions does not always reflect that of their experimentally observed partition coefficients.¹⁷³ Crystal chemistry also has a great impact on trace-element partitioning behaviour. For instance, both Mg^{2+} and Ca^{2+} can occupy the *M2*-site of the clinopyroxene diopside crystal occurred naturally or synthetically.¹⁷³ This results in a shift of the +3 curve's minimum to a smaller cation radius, and the +3 cations are more soluble at the *M2*-site. The experimental study of Wood and Blundy¹⁹² shows that the optimal ionic radius for the *M2*-site in diopside decreases with increasing Ca^{2+} content and decreasing Al^{3+} content of the clinopyroxene composition. We, therefore, make brief comments on the computational techniques for studying the incorporation of trace elements in solid solutions rather than end-member minerals and for predicting partition coefficients in the following subsection. The direct simulation of trace-element partition coefficients will also be discussed briefly.

4.6.6 Brief Comments on Solid Solutions and Direct Simulation Technique

van Westrenen *et al.*^{251,285} have previously extended lattice-static simulations using the Mott-Littleton two-region approach for modelling defects, similar to those outlined

above, of the pyrope ($\text{Py-Mg}_3\text{Al}_2\text{Si}_3\text{O}_{12}$) and grossular ($\text{Gr-Ca}_3\text{Al}_2\text{Si}_3\text{O}_{12}$) garnet end members to calculate the energetics of trace-element incorporation in pyrope-grossular solid solutions.²⁵⁰ The thermodynamic properties were computed using two different approaches: (i) a mean-field approach assuming the presence of one type of hybrid X -site with in-between characteristics of pure Mg^{2+} and Ca^{2+} X -sites, and (ii) a discrete model assuming explicit two cation sublattices of Mg^{2+} and Ca^{2+} X -sites. Numerical results have been compared with a wide range of experimental garnet-melt trace-element partitioning data at high temperatures and pressures in order to understand the controlling factors of the trace-element partitioning into solid solutions. They have found that the hybrid approach is inadequate to explain the partitioning behaviour of trace elements due to local distortions of polyhedra in the garnet structure which are averaged out. Interestingly, the results obtained from the discrete model show that trace elements are more soluble in $\text{Py}_{50}\text{Gr}_{50}$ than in each of both end-member compounds mainly due to the local ordering in the garnet structure. Consequently, large trace cations may substitute for Mg^{2+} and small dopants for Ca^{2+} in $\text{Py}_{50}\text{Gr}_{50}$. The calculated solution energies provide successfully an account of the experimentally observed anomalous partitioning behaviour of trace elements along the pyrope-grossular join.¹⁹⁵ Generally, successful simulation of effects due to non-ideality in solid solutions will provide more realistic and more accurate comparisons between computational results and experimental trace-element partitioning data on natural systems.¹⁷³

According to, *e.g.*, Kanzaki²⁸⁶ and Purton *et al.*,²²⁵ solely enthalpies of substitution in the dilute limit in each phase for mineral-melt trace-element partitioning are considered, and entropic contributions have been neglected entirely. This means that the nature of the melt species has been completely ignored. In our group, however, we have performed direct simulation based on Monte Carlo (MC) simulations in the semi-grand canonical ensemble (NPT), which determines chemical potential differences and thus gives partition coefficients directly.^{127,173,287} The simulation technique proves very useful for studying the phase diagrams of ceramic oxides and minerals.^{184,288,289} Using classical potentials of Lewis and Catlow,⁷⁴ calculated trace-element partition coefficients D_b in solid and melt phases of CaO vary over more than an order of magnitude for a wide range of trace cations. Unfortunately, there are no direct experimental data for comparison. However, the calculations reproduce the shape of an Onuma curve with an optimal radius close to the cation radius of the Ca^{2+} host cation. Again, the calculated partition coefficients can also fit the Brice³⁴ equation (4.13) to obtain an effective site Young's modulus, Y_{Ca} . Nevertheless, the resulting fitted value of Y_{Ca} is significantly larger than that of the

crystal Young's modulus.

4.7 Conclusions

Understanding the partitioning behaviour of trace elements in minerals and melts is crucial for mineralogists and igneous geochemists. According to a many experimental studies, several key factors control the partitioning of trace elements between minerals and melts. The trace-element partitioning processes depend absolutely on temperature and pressure. According to the Goldschmidt rules, another primary control on partitioning is the valence and cation radius mismatch between the dopant and host cations. Importantly, structures and compositions of the solid and melt phases also play a vital role in the trace-element partitioning between the two co-existing phases. The adsorption and incorporation of trace elements at interfaces must also be considered, as large trace-element cations may occur more preferentially at the interfaces than in the bulk of a solid mineral. Oxygen fugacity determines also the partition coefficients of trace elements with various oxidation states. For a few decades now, the influence of those controlling factors on trace-element partition coefficients for different minerals over a wide range of temperatures and pressures has extensively been studied. The variation of experimental coefficients with dopant size for an isovalent cation series at a given lattice site of a crystal of interest shows an *approximately* parabolic curve with a maximum occurring at an ionic radius close to the host cation. Such a partitioning curve is so-called an Onuma diagram. The curvature of an Onuma diagram tends to become tighter with increasing valence. The overlap of multiple curves for each isovalent species can be observed in crystals with several lattice sites available for substitutions.

Different thermodynamic approaches can explain the trace-element partitioning behaviour in solid minerals and melts. A partitioning process can be viewed as either a fusion reaction of a fictive trace-element mineral component or an exchange reaction between host and trace-element mineral components and their corresponding melt species. In both approaches, partitioning coefficients can be derived from the equilibrium constants, which link directly to the change in Gibbs energy of those reactions. By making several assumptions, the changes in Gibbs energy for substitution/exchange reactions can be approximated by lattice strain energies in the solid phase. Computer simulation based on lattice statics and dynamics enables us to calculate the relaxation energies, equivalent to the strain energies, for the trace-element substitutions in certain minerals. A lattice strain model can explain *roughly* the variation of these strain (relaxation)

energies with ionic radius, *e.g.*, the models of Nagasawa²³⁷ or Brice.³⁴

Using the model of Brice,³⁴ Blundy and Wood³³ have proposed an elastic lattice strain model to describe the variation of experimental partition coefficients D_b with ionic radius r_b , *i.e.*, an Onuma curve. Although the simple strain model of Blundy and Wood³³ appears to explain well the Onuma curve for an isovalent series, describing strains using the equation of the Brice³⁴ model is found to be inadequate and oversimplified. In this model, the poor definition of lattice strain arises mainly from the simplifications made in the formulation for the lattice strain energy as a function of ionic radius. Additionally, the Brice³⁴ model employs continuum mechanics to study the lattice's structural deformation microscopically, whereas the lattice strain due to the incorporated defects is strongly non-continuous. Furthermore, the strain energy expression is derived by assuming that the crystal of interest is elastically isotropic; hence, it does not give a complete description of the overall lattice strain since non-radial strains are not considered explicitly. Only one Young's modulus is used to describe lattice strains in the model of Brice,³⁴ which seems very unrealistic. Both shear and bulk moduli should be included in the expression to describe strains more fully. Lattice strains also depend greatly on the local environment of the lattice site, which the model cannot sufficiently probe. The use of the fixed ionic radii derived by Shannon¹⁷⁶ is questionable as a given ion's ionic radius varies from crystal to crystal and lattice site to lattice site, depending mainly on its local environment. And more importantly, the simple strain model of Blundy and Wood³³ underplays the role of the melt phases.

In this chapter, we have comprehensively investigated the calculated defect, relaxation and solution energies of homovalent (+2) and heterovalent (+1 and +3) substitutions in lime (cubic CaO) and diopside ($\text{CaMgSi}_2\text{O}_6$) minerals using classical force-field based and plane-wave DFT simulations; therefore, a direct comparison between the numerical results obtained from the two computational approaches has been made, and the quantum-mechanical effects such as the crystal-field and ligand-field stabilisation effects have explicitly been included in the DFT calculations. In contrast to many previous theoretical studies, our calculations are based on the periodic supercell approach rather than the Mott-Littleton method¹²⁵ for modelling the point-defect formation in the crystals. Using the supercell approach, one can explicitly take the concentration of the point defects (or dopants) into account, and the temperature (or pressure) dependence of the defect thermodynamics can be observed. We observed that the magnitudes and trends of the three defect thermodynamic quantities calculated using the classical simulation are in reasonable agreement with those obtained from the DFT method for homovalent

substitutions in CaO and diopside. However, although the trends of the thermodynamic quantities obtained from both computational approaches for heterovalent substitutions are in good agreement, their magnitudes might significantly differ, potentially due to the more significant differences in the computed absolute energies from the two different methods.

As mentioned above, the strain energies for incorporating trace-cation defects into minerals can be estimated by the computed relaxation energies obtained from classical and first-principles computer simulation techniques based on lattice statics and dynamics outlined in Chapter 2. For homovalent substitutions, analogously to the Onuma diagram, the dependence of the calculated relaxation energies on ionic radius is *approximately* parabolic, with a minimum occurring at cation radii close to that of the host cation. The curvature varies from site to site, reflecting roughly their relative compressibilities. We have shown that the simple lattice strain model of Brice³⁴ can *roughly* describe the variation of those relaxation energies with cation radius. However, the relaxation (and also defect) energies for the incorporation of some open-shell cations, *e.g.*, Mn^{2+} , Fe^{2+} and Co^{2+} , deviate slightly from the prediction by the Brice model, indicating the artefact of using the invariant and unrealistic cation radii in the lattice strain model. Apart from the relaxation energies, the defect formation and overall solution energies for the substitution reactions could well be used to explain the partitioning behaviour of *homovalent* trace elements in *solid* minerals.

However, quantifying the partition coefficients and calculating the thermodynamic properties of *heterovalent* substitutions prove much more complicated due to many possible charge-balancing mechanisms. These affect the activity-composition relationship and the energetics directly. Possible mechanisms often involve the simultaneous incorporation of two heterovalent cations into a crystal. In those cases, the lattice polarisation arising from charged defects must be considered explicitly. Thus, the use of a single effective Young's modulus in the model of Blundy and Wood³³ to describe the lattice strain due to multiple heterovalent defects in all the previous studies is ambiguous. Crystal chemistry is also essential when studying the trace-element partitioning behaviour in complex natural systems, *e.g.*, solid solutions. A computational technique based on Monte Carlo (MC) simulations, where the characteristics of the melt phases are taken into account explicitly, can be used to calculate partition coefficients and make more realistic comparisons with those observed experimentally. However, advances in experimental and computational techniques are still required to thoroughly investigate the partitioning behaviour of trace elements in minerals and melts.

EXPLORING NON-ARRHENIUS REACTION RATES IN SOLID-STATE MATERIALS

The main focus of this chapter is to explore the possible factors that can give rise to the deviation from Arrhenius-like behaviours in solid-state inorganic catalysis based on the concept of the macromolecular rate theory (MMRT) to gain a fuller understanding of both types of catalysis through a unified approach. We first briefly discuss chemical catalysis and the classical models that account for the variation of catalysed reaction rates with temperature. We then review the application of the MMRT in describing the non-Arrhenius behaviour of enzymatically-catalysed reaction rates before discussing the potential of using the MMRT approach to explain also the non-Arrhenius behaviour of reactions and processes catalysed by solid-state materials. Next, based on the MMRT concept, we explore the non-Arrhenius behaviour of reactions catalysed by zeolitic materials, in particular, and possible factors that control the temperature dependence of those zeolite-catalysed reaction rates. Lastly, we will show the calculations of temperature-dependent free energies of activation and diffusivity for diffusion processes in MgO and zeolites using various computer simulation techniques based on both classical and *ab initio* DFT approaches, including quasiharmonic lattice dynamics (QLD), molecular dynamics (MD) and metadynamics. We will comment also on the possible application of *ab initio* metadynamics simulations for accurately examining the temperature dependence of the activation free energy of zeolite-catalysed reactions.

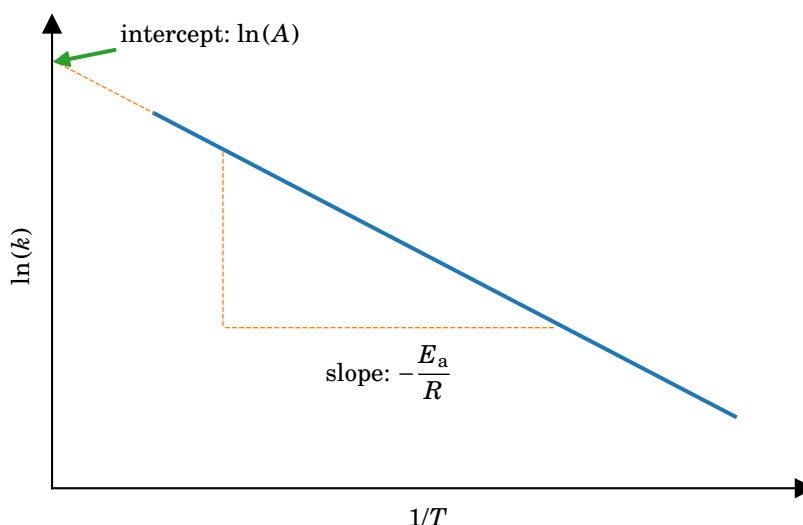


FIGURE 5.1. Schematic plot of the Arrhenius equation.

5.1 Catalysis and Chemical Reaction Rates

The term ‘*catalysis*’ was firstly introduced by Oswald in 1984: “Catalysis is the acceleration of a slow chemical process by the presence of a foreign material”.³⁵ Microscopically, a catalyst accelerates a considerably slow chemical reaction by attaching itself or interacting with the reactant species to lower the activation energy of the process. In this regard, the activation energy can be defined as the minimum amount of energy consumed by the reactant(s) to form the product(s). The classical Arrhenius equation has long been used to explain the rate of a chemical reaction in terms of the rate constant as a function of the activation energy E_a and temperature T ,³⁷ which writes

$$k = A \exp\left(-\frac{E_a}{RT}\right), \quad (5.1)$$

where k is the rate constant, A denotes the pre-exponential factor which is the high-temperature limit of k , and R refers to the gas constant. E_a is empirically assumed to be independent of temperature.

To illustrate the temperature variation of the rate constant k , the Arrhenius equation (5.1) is usually plotted in the logarithm scale, $\ln(k)$, as a function of reciprocal temperature, $1/T$. The plot results in a straight line with a slope of $-E_a/R$ and an intercept of $\ln(A)$, as shown in Figure 5.1. The transition-state theory (TST), *aka* Eyring’s absolute rate, on the other hand, is an extended form of the ordinary Arrhenius equation (5.1), which expresses the rate constant k in terms of the change in Gibbs energy of activation

ΔG^\ddagger , *i.e.*, the difference in Gibbs energy of the transition-state and ground-state species,

$$\begin{aligned} k &= \frac{\kappa k_B T}{h} \exp\left(-\frac{\Delta G^\ddagger}{RT}\right) \\ &= \frac{\kappa k_B T}{h} \exp\left(\frac{\Delta S^\ddagger}{R}\right) \exp\left(-\frac{\Delta H^\ddagger}{RT}\right), \end{aligned} \quad (5.2)$$

where κ represents the transmission coefficient. ΔS^\ddagger and ΔH^\ddagger denote the changes in entropy and enthalpy of activation.^{290,291} It is worth noting that the transmission coefficient κ has contributions from quantum mechanical effects, *e.g.*, dynamical recrossing and tunnelling, and deviations from the distribution of relevant states in equilibrium.²⁹² κ is generally temperature-dependent but is often assumed to equal 1 for simplicity.

5.2 Non-Arrhenius Behaviour of Enzyme Rates and Macromolecular Rate Theory

According to the absolute rate law, *i.e.*, equation (5.2), ΔS^\ddagger and ΔH^\ddagger are often assumed to be independent of temperature. This assumption works adequately for a wide range of relatively simple chemical reactions. Hence, one can determine ΔG^\ddagger very accurately for reactions involving small molecules in the liquid or gas phases through computation.²⁹³ Many research studies, however, suggest that the assumption of the temperature independence of these parameters is not valid for various chemical systems and that the temperature variation of each of the parameters is quite involved.^{38,292,294} The recent study of Roy *et al.*,²⁹⁵ for example, shows clearly that the value of ΔS^\ddagger for enzymatically catalysed reactions is significantly sensitive to temperature as initially proposed more than 70 years ago by Kavanau.²⁹⁶

For some enzyme-catalysed reactions, the curvature of the rate with reciprocal temperature can be negative. This gives rise to an optimal temperature (T_{opt}), as shown in Figure 5.2.^{294,297} In the literature, the negative curvature of the temperature variation of enzymatic rates has been explained by the combination of the Arrhenius-like behaviour in the temperature region below T_{opt} and the fall of the reaction rate in the temperature region above T_{opt} , which is due to enzyme denaturation and/or aggregation.³⁹ Nonetheless, many studies demonstrate that the aggregation or denaturation of enzymes is somewhat inadequate to account for the decrease in enzymatic rates above T_{opt} .^{38,298} For instance, Feller and Gerday²⁹⁹ illustrate that the reaction rates catalysed by some psychrophilic (or cold-adapted) enzymes decrease above T_{opt} in the absence of the aggregation, denaturation or unfolding of those enzymes.

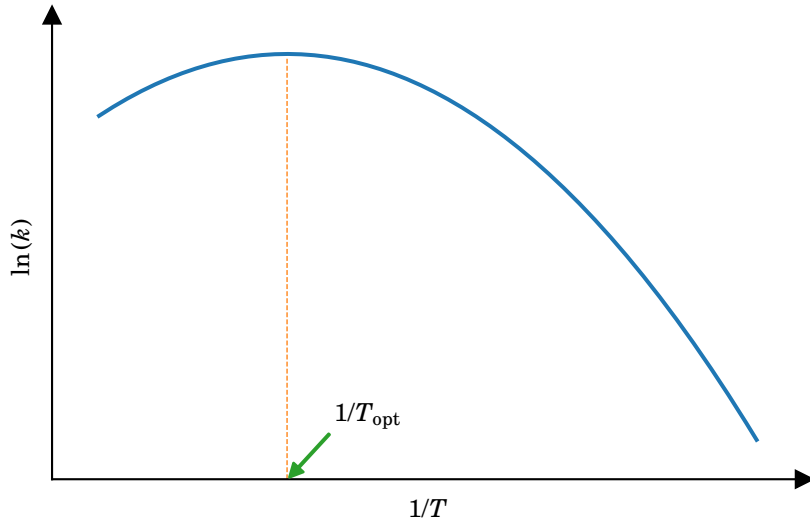


FIGURE 5.2. Schematic plot of some biologically catalysed reaction rates in the logarithm scale as a function of $1/T$.

Hobbs *et al.*³⁹ were the first to propose a theoretical model that incorporates the temperature dependence of the terms ΔS^\ddagger and ΔH^\ddagger into the Eyring's absolute rate equation (5.2), where the rate constant k is expressed as a function of the (non-zero) change in heat capacity of activation at constant pressure, ΔC_p^\ddagger , to describe more fully the temperature variation of biochemically catalysed reaction rates in the absence of enzyme aggregation and denaturation. The hypothetical model was later known as the '*macromolecular rate theory, MMRT*'.²⁹⁷ The MMRT equation is acquired by expanding the absolute rate equation (5.2) using the temperature-dependent expression of $\Delta G^\ddagger (= \Delta H^\ddagger - T\Delta S^\ddagger)$ in terms of ΔC_p^\ddagger using two fundamental thermodynamic relations:

$$\Delta H^\ddagger = \int_{T_0}^T T \Delta C_p^\ddagger dT, \text{ and}$$

$$\Delta S^\ddagger = \int_{T_0}^T \frac{\Delta C_p^\ddagger}{T} dT;$$

hence,

$$\Delta G^\ddagger = \left[\Delta H_{T_0}^\ddagger + \Delta C_p^\ddagger (T - T_0) \right] - T \left[\Delta S_{T_0}^\ddagger + \Delta C_p^\ddagger \ln \left(\frac{T}{T_0} \right) \right], \quad (5.3)$$

where $\Delta H_{T_0}^\ddagger$ and $\Delta S_{T_0}^\ddagger$ are the changes in enthalpy and entropy of activation at an arbitrary reference temperature T_0 , respectively. Using equations (5.2) and (5.3), the

MMRT equation is written as

$$\ln(k) = \ln\left(\frac{k_B T}{h}\right) - \frac{[\Delta H_{T_0}^\ddagger + \Delta C_p^\ddagger (T - T_0)]}{RT} + \frac{[\Delta S_{T_0}^\ddagger + \Delta C_p^\ddagger \ln\left(\frac{T}{T_0}\right)]}{R}. \quad (5.4)$$

By definition, the difference in heat capacity between the ground-state reactant and the transition state, ΔC_p^\ddagger , leads directly to the temperature dependence of the activation parameters ΔH^\ddagger and ΔS^\ddagger . Constant-pressure heat capacity C_p , according to the fundamental thermodynamic relation, is expressed as

$$C_p = \left(\frac{\partial H}{\partial T}\right)_P = T \left(\frac{\partial S}{\partial T}\right)_P. \quad (5.5)$$

The activation heat capacity can be obtained by

$$\Delta C_p^\ddagger = \left(\frac{\partial H}{\partial T}\right)_P^{\text{TS}} - \left(\frac{\partial H}{\partial T}\right)_P^{\text{GS}} = T \left[\left(\frac{\partial S}{\partial T}\right)_P^{\text{TS}} - \left(\frac{\partial S}{\partial T}\right)_P^{\text{GS}} \right], \quad (5.6)$$

where ‘TS’ and ‘GS’ denote the transition and ground states, respectively. Furthermore, the constant-pressure heat capacity C_p relates directly to the fluctuations in enthalpy and entropy:

$$\begin{aligned} C_p &= \frac{\langle \delta H^2 \rangle}{k_B T^2} = \frac{\langle H^2 \rangle - \langle H \rangle^2}{k_B T^2} \\ &= \frac{\langle \delta S^2 \rangle}{k_B} = \frac{\langle S^2 \rangle - \langle S \rangle^2}{k_B}. \end{aligned} \quad (5.7)$$

The change in heat capacity of activation is thus given by

$$\Delta C_p^\ddagger = \frac{\Delta \langle \delta H^2 \rangle^\ddagger}{k_B T^2}. \quad (5.8)$$

When ΔC_p^\ddagger is equal to zero, equation (5.4) reduces to the ordinary absolute rate equation (5.2). The MMRT model emphasises that the variation of enzymatic rates with temperature is explicitly linked to the parameter ΔC_p^\ddagger . The MMRT equation implies further that the magnitude (absolute value) of the term ΔC_p^\ddagger can alter T_{opt} .^{38,298} T_{opt} can then be obtained by taking the first derivative of the absolute rate equation (5.2) and setting that first derivative to zero to find the maximum:

$$T_{\text{opt}} = -\frac{\Delta H^\ddagger}{R} = -\frac{\Delta H_{T_0}^\ddagger + \Delta C_p^\ddagger (T_{\text{opt}} - T_0)}{R}, \text{ and} \quad (5.9)$$

$$T_{\text{opt}} = \frac{\Delta C_p^\ddagger T_0 - \Delta H_{T_0}^\ddagger}{\Delta C_p^\ddagger + R} \approx T_0 - \frac{\Delta H_{T_0}^\ddagger}{\Delta C_p^\ddagger} \text{ for } |\Delta C_p^\ddagger| \gg R. \quad (5.10)$$

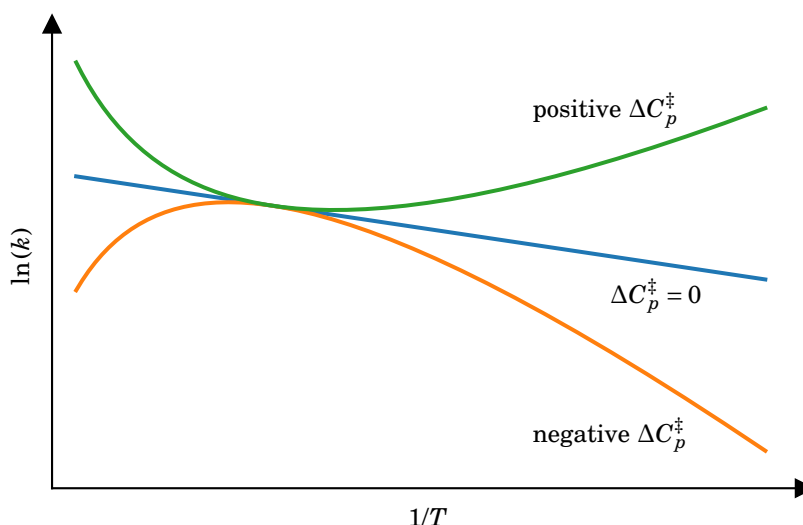


FIGURE 5.3. Effect of the sign of ΔC_p^\ddagger on the temperature variation of chemical reaction rates modelled using the macromolecular rate theory (MMRT)

Consequently, the value of ΔC_p^\ddagger itself tunes T_{opt} which determines the temperature-dependent behaviour of an enzyme-catalysed rate.

With the assumption that the parameters ΔS^\ddagger and ΔH^\ddagger are dependent of temperature in the MMRT approach, *i.e.*, when $\Delta C_p^\ddagger \neq 0$, the hypothesis can account for the negative curvature in several enzymatically catalysed reaction rates in the absence of the enzyme dysfunction. The effect of the sign of ΔC_p^\ddagger on reaction rates, according to the MMRT equation (5.4), is illustrated schematically in Figure 5.3. Practically, to extract ΔC_p^\ddagger of an enzyme reaction by fitting the experimental kinetic data to the MMRT equation (5.4), the rate constant in the logarithm scale $\ln(k)$ needs to be firstly attained as a function of temperature T .

For instance, the MMRT fitting of a reaction rate catalysed by an acid phosphatase observed by Peterson *et al.*^{300,301} yields $\Delta C_p^\ddagger = -3.4 \pm 0.3 \text{ kJ mol}^{-1} \text{ K}^{-1}$, as shown in Figure 5.4.³⁸ The obtained kinetic data are so-called ‘zero-time’, implying that the data are independent of enzyme denaturation. The dataset can easily be taken from the source using the WebPlotDigitizer online tool.³⁰² With the same protocol, ΔC_p^\ddagger of -2.8 ± 0.2 and $-3.6 \pm 0.3 \text{ kJ mol}^{-1} \text{ K}^{-1}$ can be attained for reactions catalysed by adenosine deaminase and β -lactamase, respectively. Generally, studies have shown that the negative curvature of various experimentally-observed enzyme-catalysed rates corresponds to negative values of ΔC_p^\ddagger ranging from -1 to -12 $\text{kJ mol}^{-1} \text{ K}^{-1}$.³⁸ Previously, research studies have

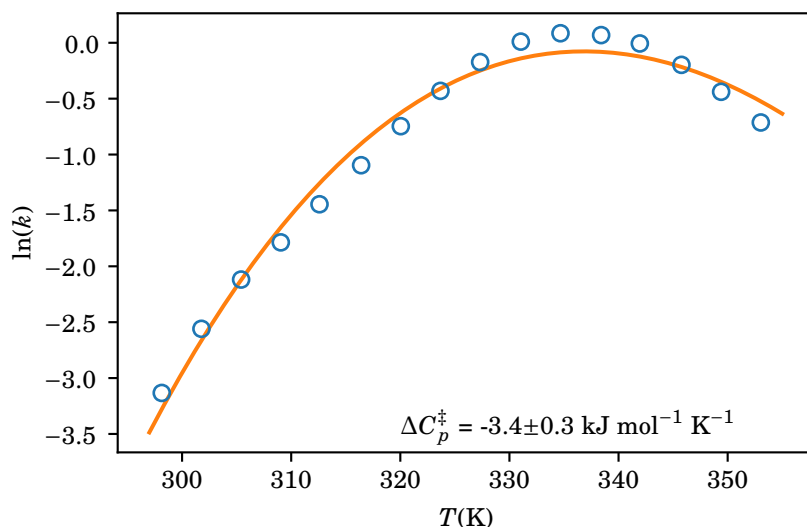


Figure 5.4: MMRT equation fitted to kinetic data of a reaction catalysed by acid phosphatase where enzyme denaturation is negligible and its associated change in heat capacity of activation.

suggested that the catalytic activity of an enzyme is likely to be connected with its heat capacity in some way;^{38,40} the huge mass of enzymes is related to their catalytic power, and the mass is directly related to the heat capacity, *i.e.*, heavier enzymes possess higher heat capacities.³⁰³ Possible explanations for the magnitudes and minus sign of ΔC_p^\ddagger for the enzymatic rates were not uncovered until much later.

Wolfenden and Snider³⁰⁴ showed that the value of ΔG^\ddagger of enzymatically catalysed reactions is much lower compared to the non-catalysed analogues, arising from the tighter binding mode of the enzyme-substrate complex at the transition state. This results eventually in a considerable increase in enzymatic reaction rate. Similarly, one can expect that the value of ΔC_p^\ddagger for an enzyme-catalysed reaction should also be negative as a direct consequence of a tighter binding mode of the transition-state complex compared to the more structurally flexible enzyme-substrate complex in the ground state, as shown in Figure 5.5.

Hobbs *et al.*³⁹ provide two possible explanations for a large negative ΔC_p^\ddagger . Firstly, in terms of statistical thermal physics, a very tight binding mode of the transition state complex and a decrease in the number of available conformational states compared to those in the ground state give rise to such a large negative ΔC_p^\ddagger . Secondly, from the perspective of the transition state theory, the transition state of the enzyme-substrate complex has fewer low-frequency vibrational and rotational modes than those of the

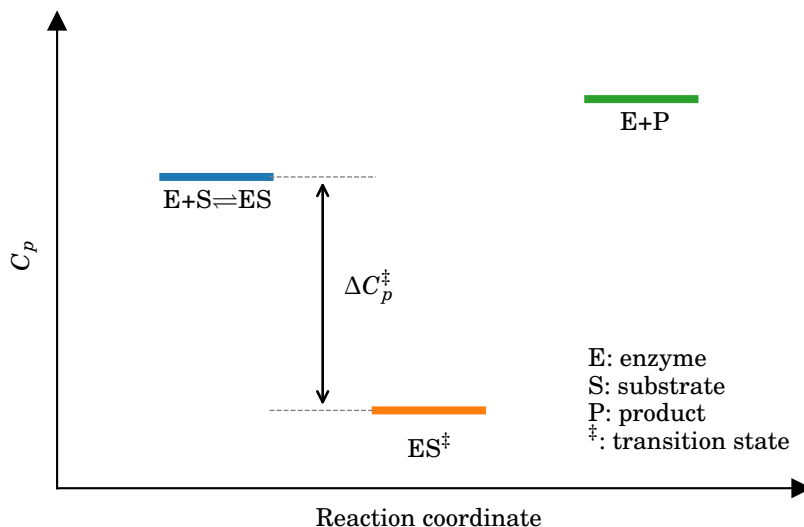


Figure 5.5: Schematic diagram of the change in heat capacity as an enzymatically catalysed reaction proceeds.

ground-state complex resulting in a large negative ΔC_p^\ddagger .

Apart from state-of-the-art experimental techniques, computer simulation also plays a central role in understanding the temperature variation of enzyme catalysis. Currently, several studies using advanced experimental methods and sophisticated computer simulation have been performed to elucidate reaction mechanisms of biologically catalysed reactions and the roots of such highly efficient catalytic power.^{305–309} In addition, the combination of modern experimental methods and advanced computer simulation techniques are being adopted to discover the connection between catalysis, dynamics, and adaptations of enzymes over a wide range of temperatures.^{295,310,311} From a microscopic point of view, the temperature does, of course, affect enzyme dynamics directly. However, the link between the dynamics and catalysis of enzymes has until now been open to discussion.^{292,312}

Previously, van der Kamp *et al.*⁴⁰ were the first who attempted to obtain ΔC_p^\ddagger from equations (5.5) and (5.6) by extensive atomistic molecular dynamics (MD) simulations. This study reveals that the transition-state ensemble fluctuates less than the ground-state ensemble, leading to a large negative value of ΔC_p^\ddagger . The contribution from the tighter binding mode of the enzyme’s active site at the transition state is not solely responsible for the large negative ΔC_p^\ddagger , and one also has to take into account the other parts in the enzyme structure. More importantly, the computed ΔC_p^\ddagger is in good agreement

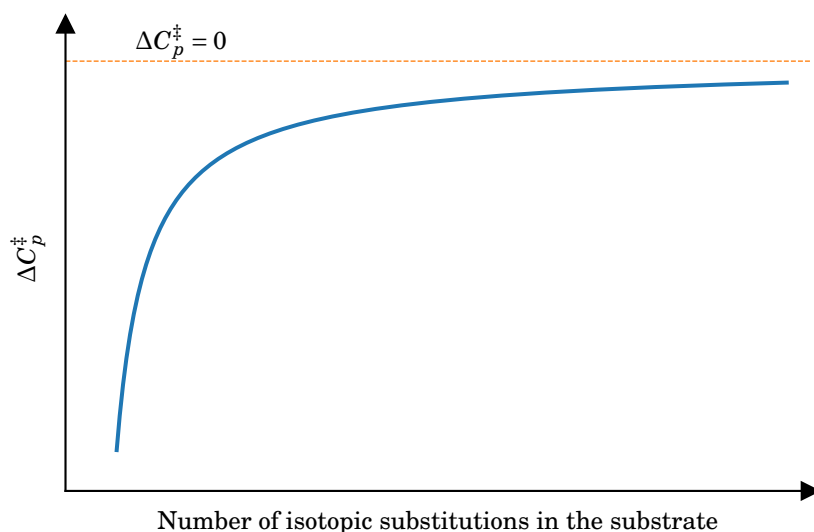


FIGURE 5.6. Schematic illustration of the dependence of the magnitude of the change in heat capacity of activation on the degree of isotopic substitutions in the substrate species in an enzyme-catalysed reaction.

with that obtained by fitting the kinetic data to the MMRT equation.³⁹ A very recent study by Winter *et al.*⁴² also reveals the complex relationship between enzyme-substrate interactions and the dynamics of the protein as a whole. They have found that the protein dynamics and ΔC_p^\ddagger can systematically be mapped to particular enzyme-substrate interactions. The study provides essentially an overall picture of how changes in substrate binding affect global changes in dynamics and structural flexibility extending throughout the whole protein.

Additionally, Jones *et al.*⁴¹ revealed a possible connection between the change in heat capacity of activation and the frequency of vibrational modes of enzymatic reactions through the means of isotope effects experimentally and computationally. The study is based on the premise that substituting a lighter atom with its heavier isotope gives rise to a decrease in vibrational frequency. They found that ΔC_p^\ddagger is significantly sensitive to the isotopic substitution. They emphasised further that the magnitude of ΔC_p^\ddagger is progressively influenced by the increase in the degree of isotopic substitution, *i.e.*, ΔC_p^\ddagger becomes less negative when the degree of isotopic substitution is higher, as shown in Figure 5.6. Furthermore, they demonstrated that even a very small isotopic change in the substrate can cause an enormous change in the temperature variation of biologically catalysed reactions.

The two research studies mentioned above are prime examples for investigating the temperature variation of enzyme rates based on the MMRT approach experimentally and theoretically. However, the discussion of the temperature dependence and the non-Arrhenius behaviour of enzymatically catalysed reaction rates is still ongoing. Two recent critical review papers on the implications of MMRT by Arcus *et al.*^{298,313} provide the detailed underlying theoretical frameworks, experimental and computational evidence, and also a consensus on how these data relate to the thermal adaptation of enzymes or enzyme evolution in general.

In summary, macromolecular rate theory is one of the elegant approaches for explaining the non-Arrhenius behaviour of enzyme-catalysed rates where enzyme aggregation and denaturation or unfolding are negligible and it gives insights into the fundamental origins of enzymes' catalytic performance. With this concept, it can successfully be used as the basis to understand the directed evolution (thermoadaptation) of a *de novo* enzyme and to further computationally design better enzymes^{43,44} as the research area of the computational design of novel enzymes remains active.^{314–316} However, the temperature variation of C_p for the enzyme complexes is still open to question.²⁹⁸

5.3 Similarities between Enzymes and Heterogeneous Catalysts

The previous section shows that changes in magnitude and number of thermally accessible low-frequency vibrational modes are a possible cause of such negative values of ΔC_p^\ddagger of enzymatic reactions. The phenomenon plays a vital role in the temperature dependence of their reaction rates. However, there are strong parallels in materials and inorganic chemistry, *i.e.*, heterogeneous catalysis, which still need to be explored.

In a chemical reaction catalysed by an inorganic solid-state catalyst, the catalytic activity takes place at the surface of the solid. Consequently, a solid-state catalyst with a larger surface area has better catalytic performance than the perfect single crystal. Hence, fine powders and micro- or nanoporous materials are well recognised as highly efficient solid-state catalysts. Even though the characteristics of reaction mechanisms or the prevalent methods used to study heterogeneous and homogeneous catalyses are very distinct, the kinetics of both systems can fundamentally be explained by the same principles.^{36,46,317}

Zeolitic materials are the prime example of heterogeneous catalysts. They might share several common catalytic features with enzymes, as we shall see later. Zeolites are

microporous aluminosilicate materials used as ion exchangers, adsorbents, molecular sieves and gas separators. More importantly, variants of zeolitic compounds can be used as highly efficient solid-state catalysts, mainly in petrochemical industries.⁴⁶ For instance, they prove to be very effective in accelerating the processes of methanol-to-olefins (MTO) or methanol-to-hydrocarbons (MTH) conversion.³¹⁸

The fact that catalytic activities of a zeolite occur at an active catalytic centre within the cavity of its micro-sized pore is a striking resemblance to those occurring within the active site of an enzyme. During a chemical reaction taking place within micron-sized voids in a zeolite framework, the transition-state complexes and reactive transient species are solvated or stabilised via weaker van der Waals and other stronger electrostatic interactions to decrease the activation energy. These solvation or stabilisation effects influence the catalytic power of the zeolitic framework directly. In this particular way, zeolites could be viewed as rigid variants of enzymes used for industrial purposes involving chemical processes at high temperatures.⁴⁶ However, zeolite catalysis is believed to be less effective and less selective than enzyme catalysis due to the rigidity of the zeolitic frameworks and the nature of reaction mechanisms.⁴⁵

Although zeolites are rigid porous materials, all porous frameworks nevertheless exhibit some degree of flexibility.³¹⁹ For example, zeolite frameworks can be deformed upon heating³²⁰ or during adsorption at high pressures of guest molecules.^{321,322} In addition, several research studies have found that even a small degree of framework flexibility results in interesting phenomena, including negative thermal expansion^{323–325} and special diffusion and transport behaviour.^{326–329} Of course, framework flexibility affects their vibrational properties.³³⁰ Therefore, the characteristics of zeolites depend greatly on their framework flexibility which directly affects the chemistry and structural topology of the materials. For instance, Bereciartua *et al.*³³¹ have designed and synthesised novel flexible zeolites to use as gas separators. Several computational studies have shown that allowing zeolitic frameworks to possess some degrees of flexibility using *ad hoc* potential force fields can remove discrepancies between experimentally observed data and theoretical predictions.³³²

To date, several recent review articles show clearly that the zeolite research community is still very active, *e.g.*, Li *et al.*,³³³ Gao *et al.*,³³⁴ Clayson *et al.*,³³⁵ Li and Yu,³³⁶ Lu *et al.*,³³⁷ and Liu and colleagues.³³⁸ All reviews emphasise the importance and recent progress of developing experimental and computational techniques for gaining an in-depth understanding of the structure-function relationship of zeolitic materials. Due to the cumulative development in this research area, modern researchers can systemati-

cally design and synthesise novel and more efficient functionalised zeolitic materials for their intended purposes beyond trial and error approaches.³³⁹

5.4 Exploring Non-Arrhenius Zeolite-Catalysed Reaction Rates

The main focus of this section is to find parallels between the rates of reactions catalysed via enzymes and zeolite frameworks based on the concept of macromolecular rate theory (MMRT). Previously, a number of experimentally observed temperature-dependent kinetic data of the reaction rates catalysed by zeolitic materials have been reported. Interestingly, many of those kinetic data show apparent deviations from the classical Arrhenius behaviour. Here, we consider solely the kinetic data that yield negative values of ΔC_p^\ddagger from the MMRT fittings, *i.e.*, Arrhenius plots of zeolite-catalysed kinetics that exhibit negative curvatures. This section concerns particularly the non-Arrhenius behaviour of a wide range of chemical reactions catalysed by different zeolitic materials.

For a given surface reaction, three elementary steps occur: (i) the reacting molecule adsorbs on an active site at the surface, (ii) the surface reaction undergoes and (iii) the product desorbs from the active site leaving the empty site for a new catalytic cycle.³¹⁷ At low temperatures, the rate-determining step is the desorption process, whereas the adsorption step limits the kinetics at high temperatures. This implies that the energy barrier of the desorption is higher than that of the adsorption at lower temperatures and otherwise in the higher-temperature region. In other words, the reactant molecules diffuse more rapidly at higher temperatures; hence, the occupation of pores with adsorbed molecules is lower in the steady-state to further react. Consequently, the rate is controlled or limited by diffusion at high temperatures. The traditional explanation of the negative curvature of the variation of $\ln(\text{rate})$ with $1/T$ for chemical reactions over zeolitic frameworks is thus due to the change in the rate-determining step, and the activation barriers in the high-temperature and low-temperature regions are reported independently.

Diffusion controls have been used to explain the negative curvature of the Arrhenius plots for various chemical reactions over a wide range of zeolitic frameworks, such as the dehydrogenation of propane over a Na-exchanged Fe-ZSM-5 zeolite,⁴⁹ the oxidation of nitric oxide over a Cu-SSZ-13 framework⁵⁰ and the reduction of NO_x by ammonia over an H-AFX zeolite.⁵¹ Additionally, a change in the property, *e.g.*, structure and deactivation, of the catalytic centre (active site) with temperature could also be the origin of the

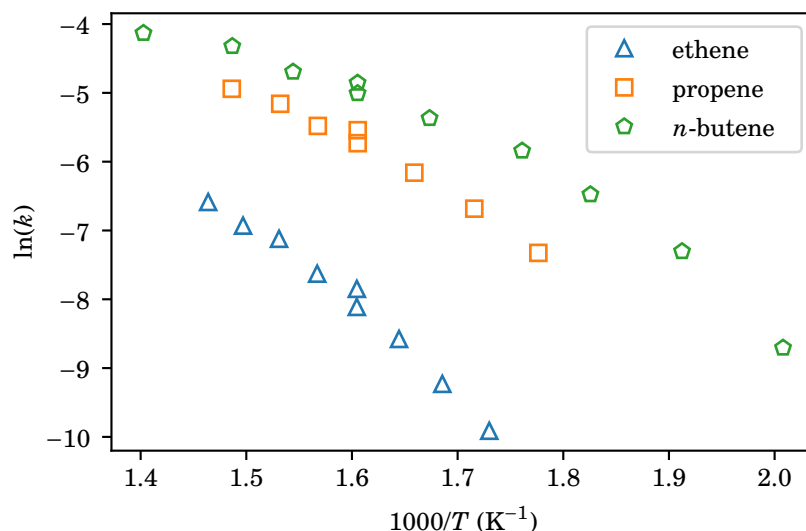


FIGURE 5.7. Arrhenius plots of methylation reactions of ethene, propene and *n*-butene with methanol into propene, butene and pentene, respectively, catalysed by H-ZSM-5 zeolite.^{340,341} Different marker styles are used for the three different methylation reactions.

negative curvature of the temperature variation of many zeolite-catalysed reactions, *e.g.*, the ammonia oxidation over a Cu-SSZ-13 zeolite^{52,53} and the reduction of NO_x by ammonia over an H-AFX zeolite.^{51,54} On the contrary, Modén *et al.*,⁵⁵ Lee,⁵⁶ and Xie *et al.*⁵⁷ have found that the negative curvature of the temperature variation of the nitric oxide decomposition rate over Cu-ZSM-5 zeolites is purely due to kinetic effects rather than the structural changes or deactivation of the Cu catalytic centres.

Nonetheless, several studies state clearly that the reason for the negative curvature of the Arrhenius plots is not obvious for many zeolite-catalysed reactions, *e.g.*, the hydroisomerisation of 3-methylpentane over a Pt-Y zeolite⁵⁸ and the non-selective oxidation of ammonia over Cu-SSZ-13 zeolites,^{52,53,59} as there is no direct evidence of the decrease in rate (or activation energy) at high temperatures. As we have comprehensively discussed earlier, based on the MMRT approach for explaining the non-Arrhenius behaviour of enzyme rates, the deviation from the classical Arrhenius behaviour of those zeolite-catalysed reaction rates might also be the direct consequence of negative values of ΔC_p^\ddagger . Note again that a negative ΔC_p^\ddagger implies the tighter binding mode of the reactive complex in the transition state compared to the ground state. We thus turn to investigate the non-Arrhenius zeolite-catalysed reaction rates using the concept of MMRT.

Much experimental zeolite kinetic data have been published by Svelle and co-

workers.^{340,341} These studies report the temperature variation of methylation reaction rates of ethene, propene and *n*-butene with methanol converted into propene, butenes and pentenes, respectively. All the methylation processes were catalysed by an H-ZSM-5 acidic zeolite. The Arrhenius plots for the three reactions are illustrated in Figure 5.7. All three plots show slight deviations from the linearity as the classical Arrhenius equation suggests theoretically. According to Svelle and co-workers,^{340,341} the change in reaction mechanism due to the difference in the degree of selectivity towards the reacting alkenes at higher temperatures accounts for the slight deviations from the Arrhenius model. Despite the slightly non-linear Arrhenius plot, the activation energy for each methylation reaction was extracted by a single linear fit. Remarkably, as the size of the reactant molecule increases, the methylation reaction rate at a given temperature becomes faster, *i.e.*, the rates of methylation follow the order *n*-butene > propene > ethene. The results are also in good agreement with those of Hill *et al.*,³⁴² where the rates of propene methylation are also higher than those of ethene methylation at the same temperature.

The faster reaction rate of the *n*-butene methylation with methanol might be the direct consequence of tighter confinement at the transition state than the methylation reactions for the other two smaller alkenes. Several studies have previously shown that tighter confinements at the transition states may result in a better catalytic performance.^{343–346} Based on this concept, zeolitic frameworks with smaller pores are expected to reduce the reaction energy barriers more efficiently and accelerate those activated processes more effectively. For instance, the reaction rate of the esterification of acetic acid with ethanol over an H-MFI zeolite is approximately 10^3 times faster than the same reaction over an H-FER zeolite³⁴⁷ since the H-MFI framework is relatively denser and has smaller pores compared to the H-FER framework. According to the Database of Zeolite Structures,³⁴⁸ the purely siliceous MFI and FER frameworks have framework densities (FD_{Si}) of 18.4T and 17.6T per 10^3 \AA^3 , respectively. Note that a T value indicates the average number of silicon tetrahedral sites in the framework. Additionally, the accessible volumes of the MFI and FER frameworks are 9.81% and 10.01%, respectively. This is also the case for, *e.g.*, the conversion of *n*-hexane into benzene over platinum-exchanged K-L and K-Y zeolites,³⁴⁹ the decomposition of nitric oxide over Cu-ZSM-5 and Cu-Y zeolites,³⁵⁰ and the nitric oxide decomposition over Cu-MOR and Cu-SSZ-13 zeolitic frameworks.⁵⁷ In all cases, the zeolitic frameworks that have higher T values and smaller accessible volumes tend to yield faster rates for the same chemical reaction.

After fitting the kinetic data of the three alkene methylation reactions with methanol

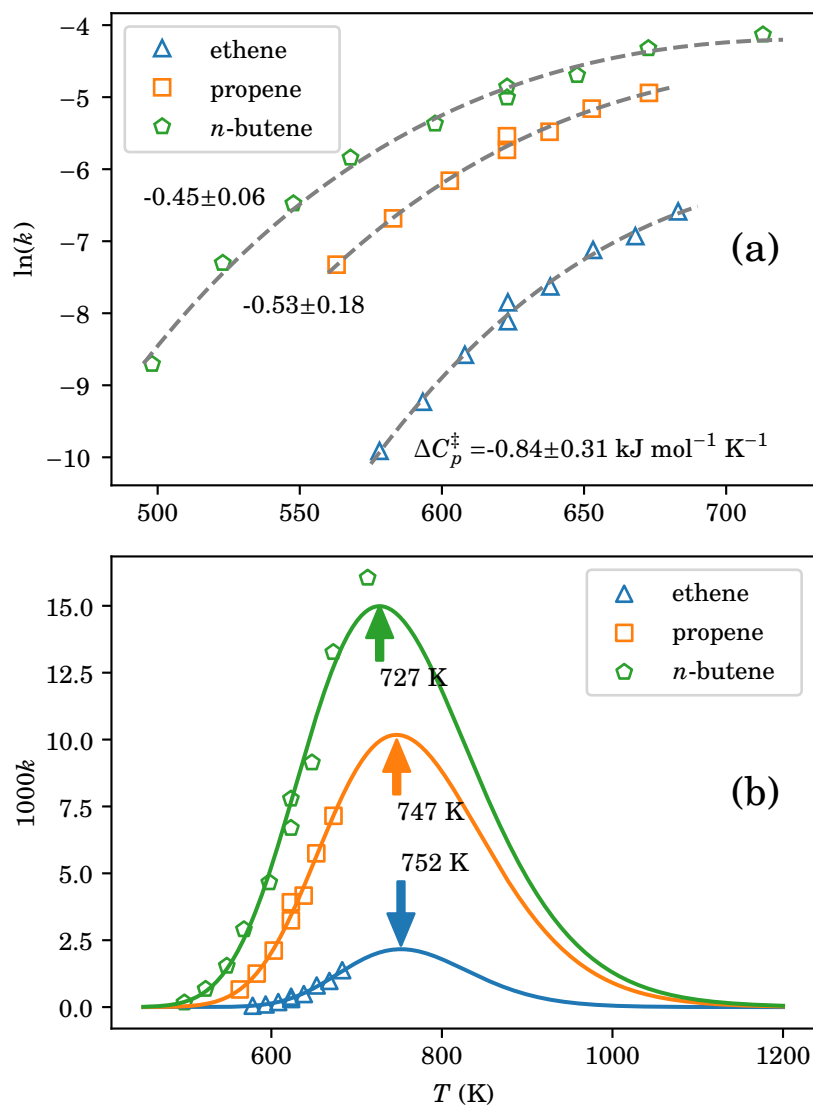


FIGURE 5.8. (a) Fitted kinetic data of ethene, propene and *n*-butene methylation reactions catalysed by acidic zeolite H-ZSM-5 into MMRT equation and their corresponding calculated ΔC_p^\ddagger in $\text{kJ mol}^{-1} \text{ K}^{-1}$. (b) Plots of predicted rate constants for the three methylation processes as a function of temperature and optimum temperatures are marked by arrows.

catalysed by the H-ZSM-5 zeolite into the MMRT equation (5.4), the key thermodynamic parameters ΔC_p^\ddagger and T_{opt} can be extracted as shown in Figure 5.8. In Figure 5.8(a), the magnitude of ΔC_p^\ddagger for the methylation of ethene with methanol is greater than those of the other two larger alkenes, *i.e.*, the smaller reacting alkene leads to the greater magnitude of (negative) ΔC_p^\ddagger . The values of ΔC_p^\ddagger with the corresponding standard errors for the methylation reactions of ethene, propene and *n*-butene with methanol are -0.84 ± 0.31 , -0.53 ± 0.18 and -0.45 ± 0.06 kJ mol⁻¹ K⁻¹, respectively.

As mentioned earlier, ΔC_p^\ddagger for a given reaction indicates the loss of conformational states and translational, vibrational and rotational modes in the transition state compared to the ground state. Therefore, a larger negative value of ΔC_p^\ddagger for the ethene methylation with methanol in the H-ZSM-5 zeolitic framework suggests a greater loss of the vibrational and rotational degrees of freedom in the activated complex compared to those when propene and *n*-butene are the reactants. As *n*-butene is more flexible and has more conformers than propene and ethene, one might expect a greater difference in the number of conformational states between the transition-state and ground-state *n*-butene-methanol complex than those of the propene-methanol and ethene-methanol complexes.

Figure 5.8(b) demonstrates that T_{opt} decreases slightly with the increasing size of the reacting alkene. The values of T_{opt} for the zeolite-catalysed ethene, propene and *n*-butene methylation reactions with methanol are 752 K, 747 K and 727 K, respectively. Furthermore, the plots in Figure 5.8(b) may also provide a compelling link between the predicted kinetic data and the change in entropy of activation ΔS^\ddagger . At T_{opt} , the Gibbs energy of activation ΔG^\ddagger is almost entirely entropic. Strictly speaking, using equation (5.3), the term ΔH^\ddagger gets very close to zero at the optimum temperature and leaves $\Delta G^\ddagger \approx -T\Delta S^\ddagger$, hence $\Delta G^\ddagger \approx -T(\Delta S^\ddagger + \Delta C_p^\ddagger)$ all at T_{opt} . Therefore, with the assumption that the Gibbs energy of activation is completely entropic, the differences in rate are based solely on entropic contributions. One might expect that the ratios of the rates at T_{opt} may also reflect conformational states of the molecules in the zeolites.

For example, in Figure 5.8(b), the ratio of the rates for the three alkene methylation reactions with methanol within the H-ZSM-5 framework at T_{opt} , *i.e.*, the ratio of the peak heights $k_{\text{ethene}} : k_{\text{propene}} : k_{n\text{-butene}}$, is approximately 1.0:4.7:6.9. It suggests that ΔS^\ddagger of the *n*-butene methylation is the greatest, and ΔS^\ddagger of the ethene methylation is the smallest amongst the three methylation reactions. This implies further that the difference in the number of conformational states between the transition-state complex of the methylation of *n*-butene with methanol and its ground-state complex is greater

TABLE 5.1. MMRT kinetic parameters for reactions catalysed by MFI-type zeolitic frameworks

Reaction	Framework	ΔC_p^\ddagger (kJ mol ⁻¹ K ⁻¹)	T_{opt} (K)
Ethene methylation ^(a)	H-ZSM-5	-0.84±0.31	752
Propene methylation ^(b)	H-ZSM-5	-0.53±0.18	747
<i>n</i> -Butene methylation ^(b)	H-ZSM-5	-0.45±0.06	727
Ethene methylation ^(c)	H-MFI	-0.64±0.51	499
Propene methylation ^(c)	H-MFI	-2.54±1.37	425
Propene-1- ¹³ C double-bond shifting ^(d)	Silicalite-1	-1.76±0.50	355

^(a)Svelle *et al.*,³⁴⁰ ^(b)Svelle *et al.*,³⁴¹ ^(c)Hill *et al.*,³⁴²

^(d)Arzumanov and Stepanov³⁵¹

than those of the propene-methanol and ethene-methanol methylation reactions. This is also in line with the interpretation of the obtained ΔC_p^\ddagger 's mentioned above.

The acidic H-ZSM-5 zeolites used for the alkene methylation reactions belong to the MFI framework type.³⁴⁸ Note that the detailed description of the notation used for the zeolitic framework types can be found in Baerlocher and McCusker³⁴⁸ and Bell.³⁵² The MFI-type zeolites can be used as highly efficient catalysts for many petrochemical reactions involving light hydrocarbons.³⁵³ Apart from the methylation reactions we have discussed previously, the Arrhenius plots with negative values of ΔC_p^\ddagger for several other chemical reactions over MFI-type zeolitic frameworks can also be observed. The fitted activation parameters using the MMRT equation (5.4) for reactions catalysed by MFI-type zeolitic materials are listed in Table 5.1.

Previously, Liu *et al.*³⁵⁴ and Lei *et al.*³⁵⁵ have reported the temperature-dependent kinetic data of the conversion reactions of *n*-pentane and neopentane (2,2-dimethylpropane) over Pt-H-MOR zeolites. The Arrhenius plots of these conversion reactions of the two pentane isomers are shown in Figure 5.9. For the two reactant isomers, the structure of *n*-pentane is a long and thin linear chain, while that of the neopentane is more spherical; hence, one can expect that neopentane is smaller (shorter) and less conformationally flexible than *n*-pentane. As the structure of *n*-pentane is more flexible in terms of torsional rotations about the single bonds, it has more conformational isomers and a higher rotational entropy than neopentane.³⁵⁶ Similar to the previous case of the methylation reactions of alkenes as discussed above, the conversion reaction rates of *n*-pentane are expected to be slower than those of neopentane at similar temperatures over the same zeolitic framework due to the tighter confinement in the transition state.

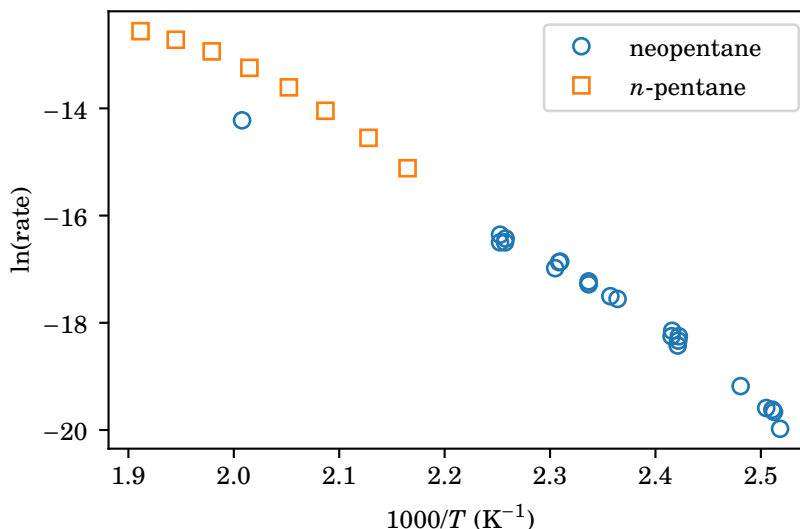


FIGURE 5.9. Arrhenius plots of conversion reactions of neopentane and *n*-pentane catalysed by Pt-H-MOR zeolites.^{354,355} Reaction rates are in mol g⁻¹ s⁻¹ units.

Fits of the reaction rates of the neopentane and *n*-pentane conversion over Pt-H-MOR zeolites to the MMRT equation (5.4) and their corresponding fitted parameters ΔC_p^\ddagger and T_{opt} are shown in Figure 5.10. The fitted T_{opt} of the neopentane conversion is 561 K, while T_{opt} for the *n*-pentane conversion is 544 K. Again, the smaller negative value of ΔC_p^\ddagger for the neopentane conversion over the Pt-H-MOR zeolite of -0.77 ± 0.09 kJ mol⁻¹ K⁻¹ implies a smaller loss of conformational states due to the formation of the transition-state complex compared to the larger negative values of ΔC_p^\ddagger of -1.59 ± 0.06 kJ mol⁻¹ K⁻¹ for the *n*-pentane conversion reaction. Given that ΔG^\ddagger is completely entropic at T_{opt} , the ratio of the peak heights is *ca.* 1.0:3.4. The peak ratio indicates that ΔS^\ddagger of the *n*-pentane conversion reaction over the Pt-H-MOR zeolite is greater than that of the neopentane conversion. Both the activation parameters ΔS^\ddagger and ΔC_p^\ddagger suggest that the conversion of *n*-pentane over the Pt-H-MOR framework shows a more significant loss of conformational states due to the transition-state complex formation than that of the neopentane conversion. The results agree well with those of the alkene methylation reactions discussed earlier.

The recent review articles by, *e.g.*, Shi *et al.*,³⁶⁰ Yeletsy *et al.*,³⁶¹ and Maghrebi *et al.*,³⁶² have emphasised the importance of zeolite-catalysed isomerisation and conversion reactions in various fields, including cosmetics and the production of bio-fuel and

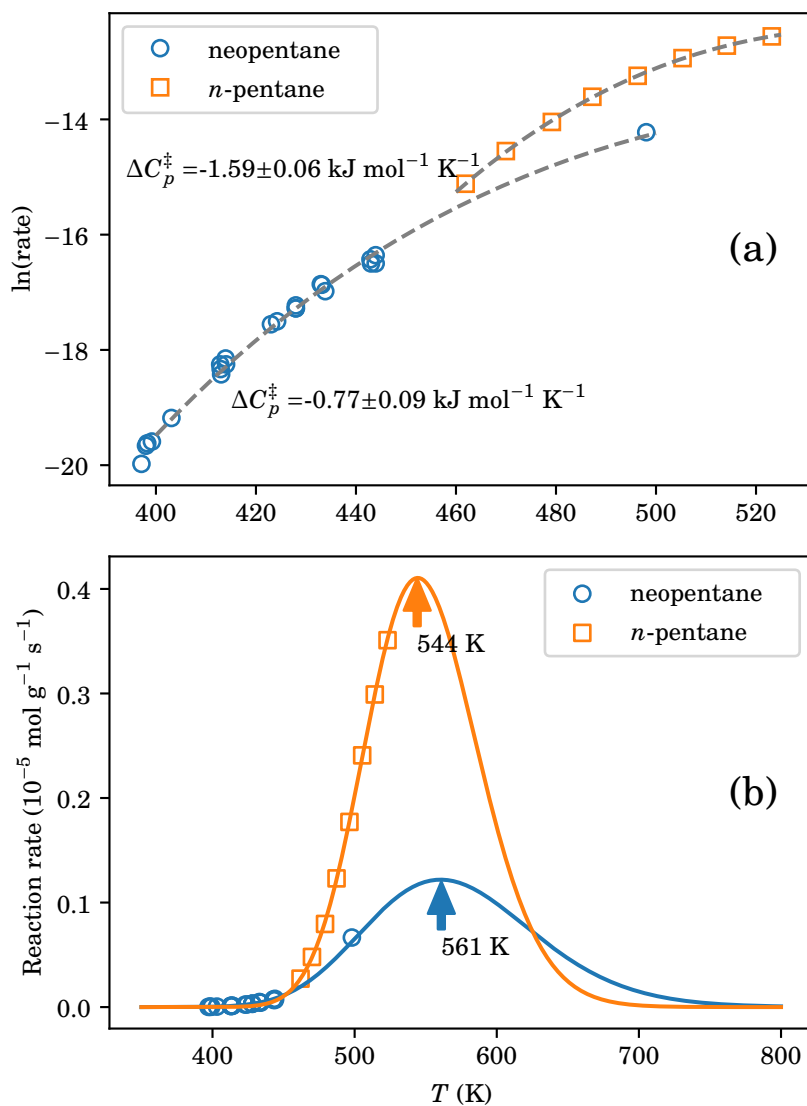


FIGURE 5.10. (a) Fitted kinetic data of neopentane and *n*-pentane conversion reactions catalysed by Pt-H-MOR zeolites into MMRT equation and their corresponding calculated ΔC_p^\ddagger in $\text{kJ mol}^{-1} \text{ K}^{-1}$. (b) Plots of predicted rate constants for the two conversion processes as a function of temperature and optimum temperatures are marked by arrows.

TABLE 5.2. MMRT kinetic parameters for zeolite-catalysed isomerisation and conversion reactions

Reaction	Framework	ΔC_p^\ddagger (kJ mol ⁻¹ K ⁻¹)	T_{opt} (K)
3-Methylpentane hydroisomerisation ^(a)	Pt-Y	-0.89±0.54	586
<i>n</i> -Hexane conversion ^(b)	Pt-K-L	-1.48±0.54	776
	Pt-K-Y	-1.53±0.67	802
Neopentane conversion ^(c)	Pt-H-MOR	-0.77±0.09	561
<i>n</i> -Pentane conversion ^(d)	Pt-H-MOR	-1.59±0.06	544
<i>n</i> -Hexane hydroisomerisation ^(e)	Pt-H- β	-1.92±0.27	564
Isopropanol Conversion ^(f)	Dealuminated H-Y	-1.78±0.32	412
Toluene conversion ^(g)	Y	-0.81±0.05	954
Propene-1- ¹³ C isomerisation ^(h)	Silicalite-1	-1.76±0.50	355

^(a)Martin *et al.*,⁵⁸ ^(b)Lane *et al.*,³⁴⁹ ^(c)Lei *et al.*,³⁵⁵ ^(d)Liu *et al.*,³⁵⁴

^(e)van de Runstraat,³⁵⁷ ^(f)Triantafillidis and Evmiridis,³⁵⁸

^(g)Anis and Zainal,³⁵⁹ ^(h)Arzumanov and Stepanov³⁵¹

petrochemicals. Apart from the propane conversion reactions, the MMRT kinetic parameters of other isomerisation and conversion reactions over various zeolitic materials are listed in Table 5.2. The curvature of the Arrhenius plots of all isomerisation/conversion reactions listed in Table 5.2 is negative, with the values of ΔC_p^\ddagger ranging between *ca.* -0.7 and -2.0 kJ mol⁻¹ K⁻¹. Once again, these negative values of ΔC_p^\ddagger might be evidence of the difference between the number of conformational states in the transition state and that in the ground state.

The temperature variation of many oxidation-reduction reaction rates of nitrogen-containing gases, including ammonia and nitrogen oxides, over various copper-based zeolites show strong deviations from the classical Arrhenius behaviour. For example, the temperature variation of the decomposition rates of nitric oxide over three different Cu-based zeolitic frameworks taken from Xie *et al.*⁵⁷ is shown in Figure 5.11. The negative convex of their Arrhenius plots has traditionally been explained by diffusion controls^{50,51,363} or the deactivation of the Cu catalytic centres.^{52,53,59} However, Li and Hall,³⁵⁰ Modén,⁵⁵ Lee,⁵⁶ and Xie *et al.*⁵⁷ show that the reversibility during temperature cycling of these reaction rates represents pure kinetic effects, *i.e.*, changes in the rate-limiting step, and the decrease in reaction rate at higher temperatures is not definitely due to the catalytic centre deactivation. In the absence of the deactivation of the Cu-centres and no reaction-mechanism change in different temperature ranges, the MMRT approach can also be applied to describe their non-Arrhenius behaviour. Table 5.3 lists

TABLE 5.3. MMRT kinetic parameters for oxidation-reduction reactions of nitrogen oxides and ammonia catalysed by Cu-based zeolitic materials

Reaction	Framework	ΔC_p^\ddagger (kJ mol ⁻¹ K ⁻¹)	T_{opt} (K)
Nitrous oxide decomposition ^(a)	Cu-Na-A	-0.60±0.17	871
Nitric oxide decomposition ^(b)	Cu-ZSM-5	-0.64±0.12	794
	Cu-M	-0.58±0.04	778
	Cu- β	-0.49±0.04	761
	Cu-Y	-0.18±0.06	799
	Cu-ZSM-5 (Cu/Al=0.36)	-1.01±0.13	767
	Cu-ZSM-5 (Cu/Al=0.43)	-1.07±0.14	772
	Cu-ZSM-5 (Cu/Al=0.57)	-0.81±0.09	805
Nitric oxide decomposition ^(c)	Cu-ZSM-5	-0.67±0.11	785
Ammonia oxidation ^(d)	Cu-ZSM-5	-0.27±0.09	664
Ammonia oxidation ^(e)	Cu-SSZ-13 (45% Cu-exch.)	-1.00±0.21	619
	Cu-SSZ-13 (60% Cu-exch.)	-0.62±0.41	667
Ammonia oxidation ^(f)	Cu-SSZ-13 (0.065 wt% Cu)	-1.05±0.17	794
	Cu-SSZ-13 (0.198 wt% Cu)	-1.08±0.10	769
Ammonia oxidation ^(g)	Cu-SSZ-13	-1.09±0.04	841
Nitric oxide oxidation ^(h)	Cu-SSZ-13	-0.68±0.09	584
NO _x reduction ⁽ⁱ⁾	H-AFX	-0.42±0.24	714
Nitrous oxide decomposition ^(j)	Cu-SSZ-13	-0.20±0.16	1304
Nitric oxide decomposition ^(k)	Cu-ZSM-5 (Si/Al=11.5)	-1.09±0.08	774
	Cu-ZSM-5 (Si/Al=20)	-0.93±0.13	740
	Cu-ZSM-5 (Si/Al=30)	-0.63±0.11	699
	Cu-ZSM-5 (Si/Al=50)	-0.62±0.15	702
	Cu-ZSM-5 (Si/Al=100)	-0.61±0.18	701
	Cu-SSZ-13	-0.53±0.08	702
	Cu-MOR-10	-0.50±0.07	685

^(a)Akbar and Joyner,³⁶³ ^(b)Li and Hall,³⁵⁰ ^(c)Modén *et al.*,⁵⁵^(d)Yim *et al.*,³⁶⁴ ^(e)Gao *et al.*,⁵² ^(f)Gao *et al.*,⁵⁹ ^(g)Gao *et al.*,⁵³^(h)Kryca *et al.*,⁵⁰ ⁽ⁱ⁾Kubota *et al.*,⁵¹ ^(j)Lin *et al.*,³⁶⁵ ^(k)Xie *et al.*⁵⁷

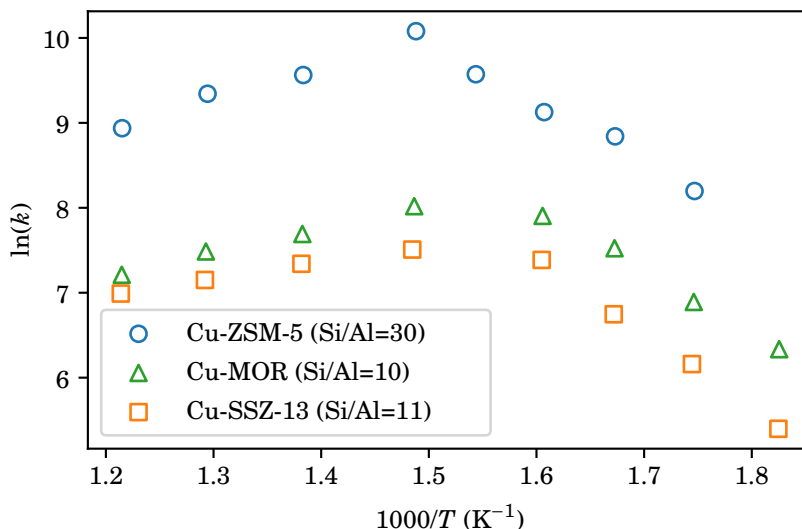


FIGURE 5.11. Arrhenius plots of decomposition reactions of nitric oxide catalysed by Cu-based zeolites.⁵⁷

the MMRT parameters we have calculated for oxidation-reduction reaction rates of small nitrogen-nitrogen molecules catalysed by various Cu-zeolites.

According to Li and Hall,³⁵⁰ Gao *et al.*,⁵² and Xie *et al.*,⁵⁷ a Ca-based zeolite framework with a higher degree of Cu exchange, *i.e.*, a greater number of Cu catalytic centres, tends to give faster rates for a given reaction. From Li and Hall,³⁵⁰ the Arrhenius plots of the decomposition of nitric oxide over Cu-ZSM-5 with three different values of Cu loading are shown in Figure 5.12. The Arrhenius plots in Figure 5.12 illustrate that the Cu-ZSM-5 zeolitic framework with a Cu/Al ratio of 0.57 gives the fastest nitric oxide decomposition rates, whereas the framework with a Cu/Al ratio of 0.36 gives the slowest rates. From Table 5.3, different degrees of the Cu exchange in a given zeolitic framework lead to different values of the MMRT parameters T_{opt} and ΔC_p^\ddagger . However, the dependence of the two fitted kinetic parameters on Cu loading is still unclear.

So far, we have seen that copper-based zeolite catalysts are beneficial for accelerating the oxidation-reduction of small nitrogen-containing gas molecules, including ammonia and nitrogen oxides.³⁶⁶ The MMRT approach could be a possible explanation for the negative convex of the Arrhenius plots of the reduction-oxidation reactions of nitrogen oxides and ammonia over Cu-based zeolites. The MMRT concept can potentially be useful for designing and improving the temperature-dependent catalytic performance of these Cu-based zeolitic materials since several recent reviews, such as Mohan *et al.*,³⁶⁷ Newton

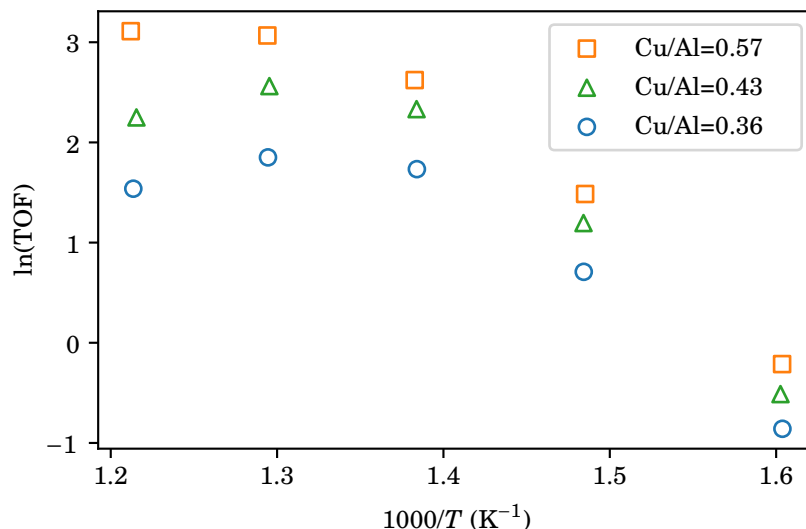


FIGURE 5.12. Arrhenius plots of decomposition reactions of nitric oxide catalysed by Cu-ZSM-5 zeolites with different Cu loadings.³⁵⁰ Turnover frequency (TOF) is in s⁻¹ site⁻¹ units.

et al.,³⁶⁸ Paolucci *et al.*,³⁶⁹ Xu *et al.*,³⁷⁰, Lei *et al.*,³⁷¹ and Shan *et al.*,³⁷² all highlight that the research community of development of Cu-zeolite catalysts is still very much active and growing.

Lastly, ΔC_p^\ddagger and T_{opt} obtained from MMRT fits for other non-Arrhenius reaction rates over various zeolitic frameworks are listed in Table 5.4. Overall, the negative values of ΔC_p^\ddagger of all the zeolite-catalysed reactions tend to be smaller than those of the enzymatic rates. The smaller negative ΔC_p^\ddagger may reflect that zeolite frameworks are generally much more rigid than enzyme structures; hence, one would expect a small difference in the number of conformational states or a small difference in the magnitude of the vibrational frequencies in the ground-state and transition-state complexes. Again, in addition to the non-Arrhenius kinetics of various enzyme-catalysed and zeolite-catalysed reactions we have shown earlier, the fitted MMRT parameters in Table 5.4 suggest that the MMRT approach could be used as a possible explanation of the negative convex of the Arrhenius plots of heterogeneously zeolite-catalysed reactions in the absence of diffusion controls in the high-temperature regime and catalytic centre deactivation. With this idea, the non-Arrhenius behaviour of both biologically and heterogeneously catalysed reaction rates can be understood more fully via the unified approach based on the macromolecular rate theory. In the next section, we will investigate theoretically the non-Arrhenius behaviour

TABLE 5.4. MMRT kinetic parameters of other chemical reactions catalysed by various zeolites

Reaction	Framework	ΔC_p^\ddagger (kJ mol ⁻¹ K ⁻¹)	T_{opt} (K)
Methane oxidation ^(a)	Pd-X	-0.13±0.01	770
Carbon monoxide oxidation ^(b)	Fe-Y	-0.25±0.04	912
Methanol dehydration ^(c)	Dealuminated H-MOR	-3.14±0.46	582
Cumene cracking ^(d)	REY	-0.17±0.04	799
Sodium borohydride hydrolysis ^(e)	Ru(0)-Y	-0.94±0.29	354
Methane combustion ^(f)	Pd-X	-1.12±0.23	690
Styrene oxidation ^(g)	Cr-ZSM-5	-0.37±0.15	366
Acetic acid/ethanol esterification ^(h)	H-FER	-1.31±0.12	413
	H-MFI	-1.49±0.40	407
Glycerol/ <i>n</i> -butanol esterification ⁽ⁱ⁾	H- β	-1.11±0.48	477
Propane dehydration ^(j)	Na-Fe-ZSM-5	-1.39±0.71	849
Y-zeolite formation ^(k)	Ultra-stable Y	-0.36±0.20	527

(a) Rudham and Sanders,³⁷³ (b) Petunchi and Hall,³⁷⁴(c) Bandiera and Naccache,³⁷⁵ (d) Bellare *et al.*,³⁷⁶(e) Zahmakiran and Özkar,³⁷⁷ (f) Wan *et al.*,³⁷⁸ (g) Saux and Pierella,³⁷⁹(h) Bedard *et al.*,³⁴⁷ (i) Nandiwale *et al.*,³⁸⁰ (j) Yun and Lobo,⁴⁹(k) Peng *et al.*³⁸¹

of some activated processes in solid-state materials using classical and first-principles computer simulation techniques.

5.5 Simulation of Activated Processes in Solid-State Materials

This final section will investigate the non-Arrhenius behaviour of some activated processes in solid-state materials using computer simulation based on the MMRT concept. Firstly, we examine the temperature variation of the activation energy of the Mg²⁺ vacancy migration in MgO using classical and DFT quasi-harmonic lattice dynamics (QLD). Secondly, we carry out classical molecular dynamics (MD) simulation and metadynamics to calculate the energy barrier of the guest molecule diffusion through a zeolitic micropore at different temperatures. Next, we use classical MD simulation to study the temperature variation of the self-diffusivity (diffusion rate) of guest molecules in

zeolite frameworks. Additionally, we perform *ab initio* molecular dynamics (AMD) and metadynamics simulations to study the temperature dependence of the energy barrier of the hydrogen hopping or proton jump in an acidic H-LTA zeolite. Finally, we discuss the application of *ab initio* simulation to explore the temperature dependence of the activation energy of zeolite-catalysed reactions theoretically.

5.5.1 Defect Migration in MgO

In Chapter 3, we have comprehensively investigated the temperature variation of the $\text{Ba}_{\text{Mg}}^{\times}$ defect formation energies in MgO using classical and DFT quasi-harmonic lattice dynamics. In those cases, the computed defect free energy is the energy difference between the defective and perfect structures (or product and reactant). In this chapter, on the other hand, we are particularly interested in the temperature variation of the activation energy of chemical reactions and activated processes catalysed by solid-state materials based on the MMRT approach. In other words, we are more interested in the free energy difference between the ground-state and transition-state structures rather than that of the two steady states (reactant and product). According to the MMRT model, a negative value of ΔC_p^{\ddagger} in the MMRT equation (5.4) accounts for the negative curvature of the Arrhenius plot of an enzyme rate in the absence of enzyme denaturation. Given that ΔC_p^{\ddagger} is negative, the plot of ΔG^{\ddagger} versus T should pass through a minimum, as equation (5.3) suggests. Fortunately, as we shall see later, the computational technique based on QLD outlined in Chapter 3 can be employed to compute those activation parameters at different temperatures accurately. In this subsection, we will concentrate on the classical and DFT calculations of the activation free energy of the Mg^{2+} vacancy migration in MgO using quasi-harmonic approximation (QHA).

A Schottky defect in MgO, *i.e.*, a combination of a pair of Mg^{2+} cation and O^{2-} anion vacancies, is schematically illustrated in Figure 5.13. The migration or diffusion of Schottky defects in ionic solids is a direct consequence of their ionic conductivity.^{12,13} For a given Schottky defect in MgO, the Mg^{2+} cation vacancy or O^{2-} anion vacancy can migrate to their adjacent sites occupied by the ions with the same ionic charge as the absent ions. Such defect migration is an activated process. However, Mahmoud *et al.*³⁸² show that the activation energy of the Mg^{2+} vacancy migration in MgO, as marked by the arrow in Figure 5.13, is lower than that of the O^{2-} vacancy migration as a Mg^{2+} ion is smaller than an O^{2-} ion. As a result, the Mg^{2+} vacancy tends to migrate more preferentially than the O^{2-} vacancy. Therefore, we consider the temperature variation of the activation energy of the Mg^{2+} vacancy migration in MgO over the temperature range

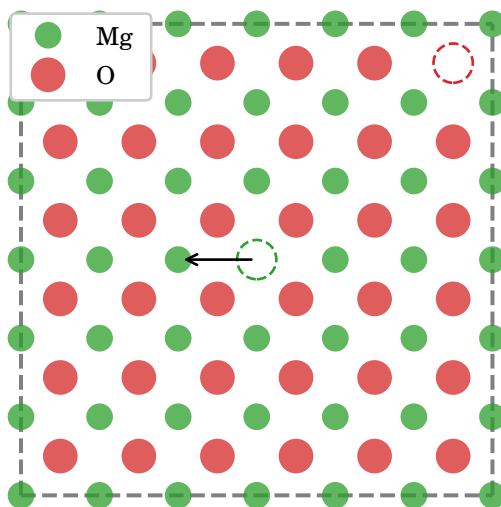


FIGURE 5.13. Schematic illustration of Mg^{2+} vacancy migration in MgO . The two dashed circles represent the Mg^{2+} and O^{2-} vacancies. The migration direction is marked by the black arrow.

100-1500 K.

The classical calculations were performed using the GULP program⁹¹ and the Buckingham potential parameters due to Stoneham and Sangster¹⁴² listed in Table 3.1. A cutoff of 9.0 Å was used for the short-range pair potentials. To investigate the temperature dependence of the activation energies of the Mg^{2+} vacancy migration in MgO , we first determined the lattice parameter of MgO as a function of temperature over 100-1500 K within the QHA. We then constructed 216-ion cubic supercells of MgO with their equilibrium volumes at different temperatures. In a given initial defective supercell, the two Mg^{2+} and O^{2-} vacancies are located as far as possible from each other. Then, all defective structures were optimised with respect to the static internal energy while keeping all six lattice parameters fixed. Then, we performed phonon calculations to evaluate the vibrational contributions of the statically optimised structures, *i.e.*, using the zero static internal stress approximation (ZSISA),⁸⁵ in order to calculate the free energies of all the ground-state structures. A shrink factor of 6 was used for the Brillouin zone integrations when calculating the free energies. The migrating Mg^{2+} ion was placed approximately half-way between its original position and the Mg^{2+} vacancy before executing transition-state search in the static limit to obtain the transition-state structure. Again, the vibrational contribution to the lattice energy of the optimised transition-state

structure was evaluated within the QHA. Note that the imaginary frequencies of the transition-state structures have been neglected in the QHA phonon calculations.

Analogous DFT calculations were conducted using CRYSTAL17.^{108,109} Instead, cubic supercells of MgO containing 64 ions were used in the DFT simulation. The exchange and correlation energies were evaluated using the GGA-PBESol functional.¹¹⁵ All-electron basis sets with 8-411G¹⁵³ and 8-511G¹⁵² were used for the O and Mg atoms, respectively. The QHA module implemented in the CRYSTAL17 code was used to conduct phonon calculations. A shrink factor of 4 was used for the phonon calculations of all 64-ion defective supercells. However, structural optimisation was performed using the Quantum ESPRESSO plane-wave DFT package^{103,104} instead, as performing geometry relaxation using CRYSTAL17 was not successful due to the orthogonality problem of the basis sets used. For geometry optimisation, a plane-wave cutoff of 50 Ry and a density cutoff of 400 Ry were used. The atomic projector-augmented-wave (PAW)³⁸³ pseudopotentials Mg.pbesol-n-kjpaw_psl.0.3.0.UPF and O.pbesol-n-kjpaw_psl.0.1.UPF were used for Mg and O atoms, respectively.³⁸⁴ A uniform $4 \times 4 \times 4$ **k**-grid was used for all structures. The transition-state optimisation was carried out using the nudged elastic band (NEB) method implemented in the Quantum ESPRESSO code. After the structural optimisation, all the optimised geometries were used for performing the phonon calculations through the well-developed QHA module in the CRYSTAL17 software package.

The temperature dependence of ΔG^\ddagger of the Mg^{2+} vacancy migration is shown in Figure 5.14. Interestingly, the variation of ΔG^\ddagger with temperature passes through a minimum at approximately 800 and 300 K in the classical and DFT calculations, respectively. Over 100-1500 K, the calculated DFT ΔG^\ddagger increases approximately by 10%, while the classical ΔG^\ddagger decreases by 2% over 100-800 K and increases by the same degree over 800-1500 K. After fitting the data to equation (5.3), we obtain ΔC_p^\ddagger of -0.0134 ± 0.0004 and -0.0173 ± 0.0009 $\text{kJ mol}^{-1} \text{K}^{-1}$ for the classical and DFT results, respectively. The negative ΔC_p^\ddagger values suggest that the ΔH^\ddagger and ΔS^\ddagger of the defect migration are temperature dependent, as shown in Figure 5.15. Figure 5.15(a) shows that ΔH^\ddagger decreases by $\sim 15\%$ and 23% over 100-1500 K in the classical and DFT simulations, respectively. The classical and DFT ΔS^\ddagger decrease by *ca.* 0.03 and 0.05 $\text{kJ mol}^{-1} \text{K}^{-1}$, respectively, as shown in Figure 5.15(b).

In Figure 5.14, we observe that the fitted ΔC_p^\ddagger for the Mg^{2+} vacancy migration in MgO is much smaller in magnitude than the enzymatic and zeolitic reactions we have shown previously, leading very close to the Arrhenius behaviour. Again, this might be due to a smaller change in the magnitude of the vibrational frequencies in the transition

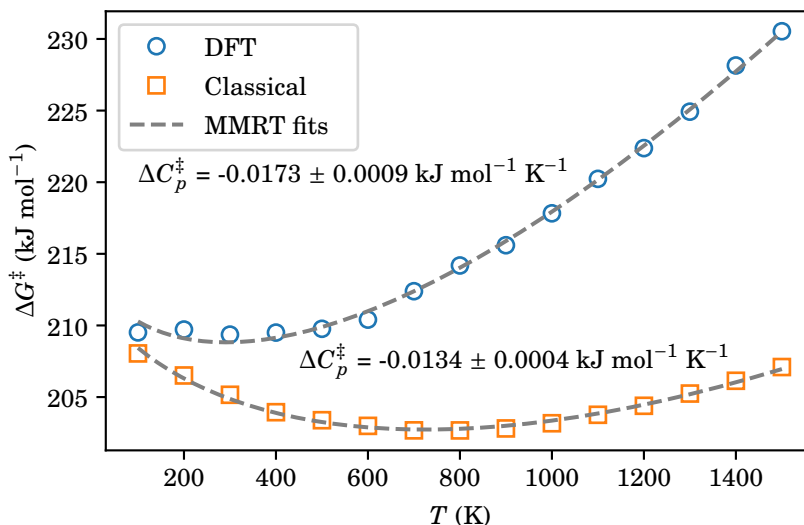


FIGURE 5.14. Temperature variation of ΔG^\ddagger of Mg^{2+} vacancy migration in MgO. The two marker styles represent the DFT and classical results, and the dashed lines are fits to equation (5.3).

state and ground state, as MgO is much more rigid than zeolite frameworks and enzymes. We compare ΔC_p^\ddagger obtained by the first derivatives of enthalpy using equation (5.6) in Figure 5.15 with those obtained by fitting ΔG^\ddagger to equation (5.3), as shown in Figure 5.14. The comparison of those ΔC_p^\ddagger values is shown in Figure 5.16. Interestingly, ΔC_p^\ddagger obtained from the first derivatives of entropy or enthalpy of activation using equation (5.6) is temperature-dependent. For both classical and DFT results, ΔC_p^\ddagger decreases rapidly in the low-temperature range of 100-300 K. However, except for ΔC_p^\ddagger at 1400 K from the DFT simulation, the ΔC_p^\ddagger changes only slightly as the temperature is elevated. At 100 K, ΔC_p^\ddagger obtained from the MMRT fitting is lower than those from equation (5.6), and the opposite trend is observed elsewhere. Overall, ΔC_p^\ddagger for the Mg^{2+} vacancy migration lies between -0.01 and -0.04 kJ mol $^{-1}$ K $^{-1}$ at temperatures higher than 200 K.

5.5.2 Ethene and Propene Diffusion through an LTA Zeolitic Micropore

Previously, Ghysels *et al.*³⁸⁵ have shown that the diffusion of small alkenes through micropores of various zeolitic materials is an activated process, which plays a vital role in the methanol-to-olefins (MTO) or methanol-to-hydrocarbons (MTH) conversion process in the petrochemical industry. The energy barrier of the diffusion depends on several factors,

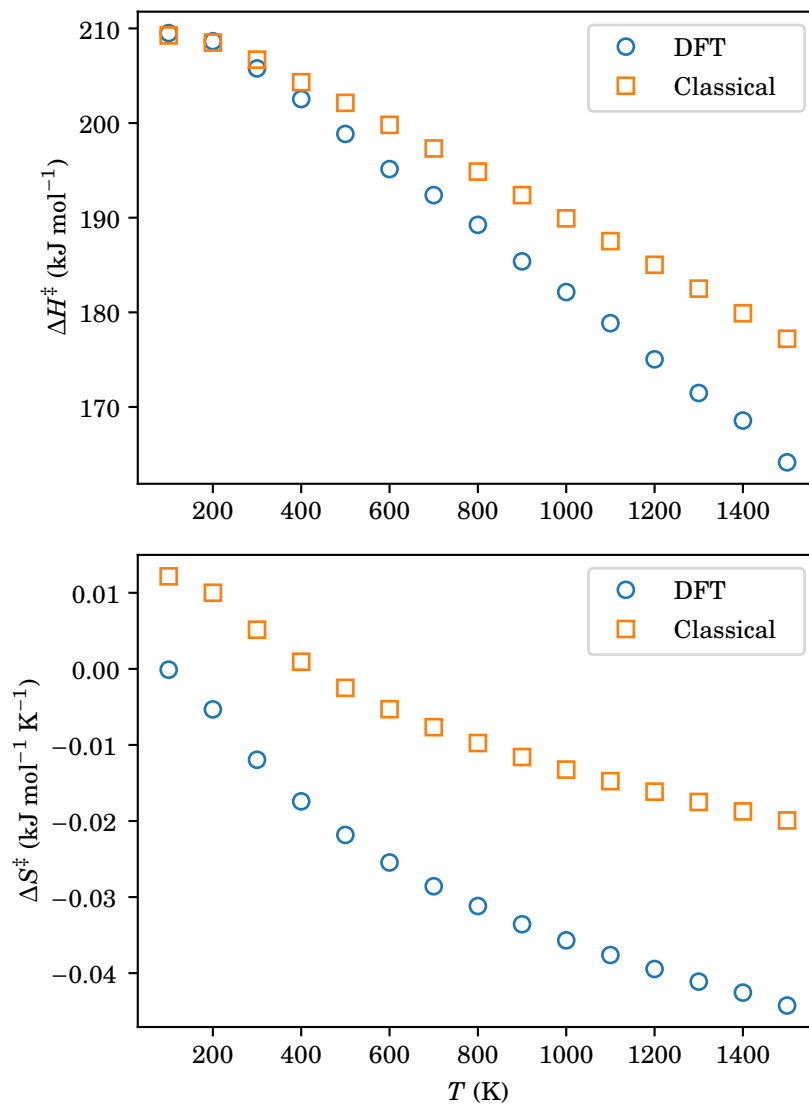


FIGURE 5.15. Temperature variation of (a) ΔH^\ddagger and (b) ΔS^\ddagger of Mg^{2+} vacancy migration in MgO . The two marker styles represent the DFT and classical results.

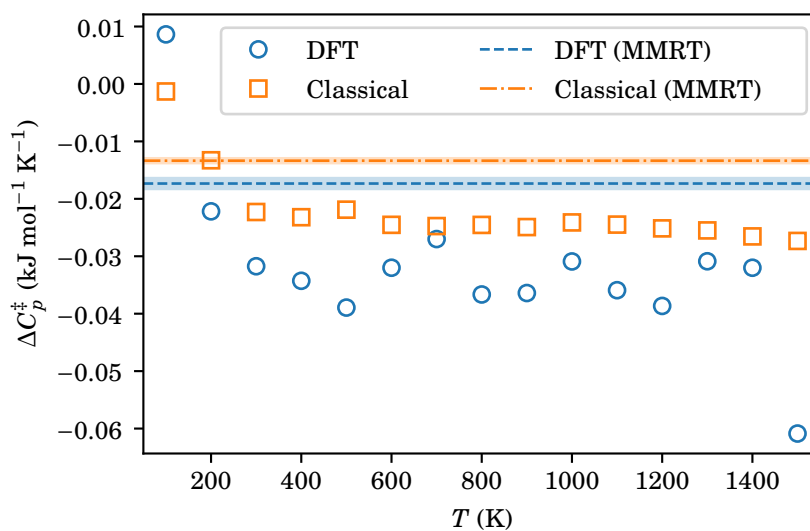


FIGURE 5.16. Temperature variation of ΔC_p^\ddagger of Mg^{2+} vacancy migration in MgO obtained from equation (5.6). The two marker styles represent the DFT and classical results. The horizontal lines represent the fitted ΔC_p^\ddagger from Figure 5.14. The ± 1 standard deviation error of each fitted ΔC_p^\ddagger is shown by the horizontal shaded band.

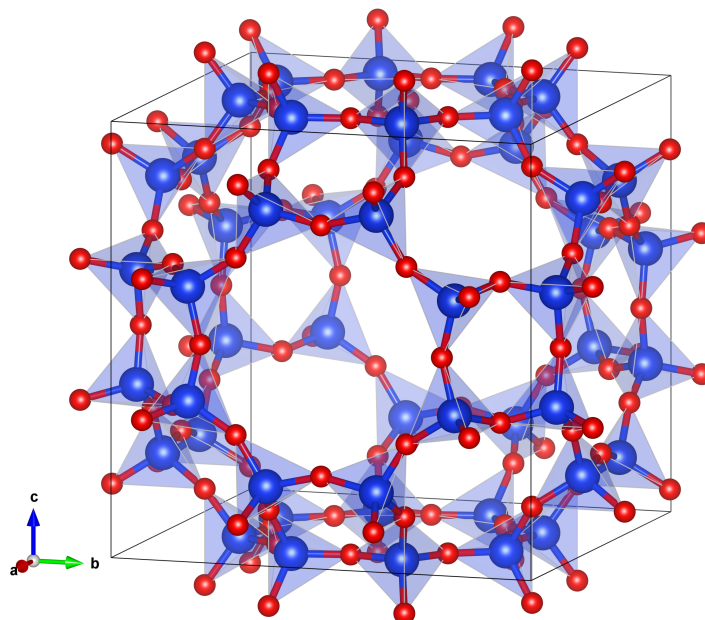


FIGURE 5.17. The crystal structure of the LTA zeolite.

TABLE 5.5. Buckingham potential parameters for pure-silica zeolitic frameworks.³⁸⁶

Interaction	Potential parameter			Atomic charge (<i>e</i>)
	<i>A</i> (eV)	ρ (Å)	<i>C</i> (eV Å ⁶)	
O–O	1338.7730	0.36232	175.0000	$q(\text{O}) = -1.2$
Si–O	18003.7572	0.20520	133.5381	$q(\text{Si}) = +2.4$

including the ring topology and composition and temperature. As previously discussed in Chapter 2 (in Subsection 2.1.5), one needs to perform advanced molecular dynamics simulations using enhanced-sampling techniques, *e.g.*, metadynamics or umbrella sampling, in order to accelerate and study the dynamics of rare events and activated processes such as chemical reactions and the diffusion processes of small guest molecules adsorbed in porous materials. Therefore, in this subsection, we perform metadynamics simulations based on classical force fields to study the temperature dependence of the free energy barriers of the ethene and propene diffusion through an eight-membered ring window of the pure-silica LTA zeolitic framework over 100-600 K. The crystal structure of the pure-silica LTA (Linde Type A) zeolitic framework is shown in Figure 5.17. Its conventional cubic unit cell comprises 72 atoms with a lattice parameter $a = 11.9190$ Å.³⁴⁸ The largest ring windows in the LTA structure consist of eight T-sites, *i.e.*, eight Si atoms. Smaller six-ring and four-ring windows are also present in the framework.

A $2 \times 2 \times 2$ supercell of the LTA framework was used for the metadynamics simulation. The BKS force-field parameters³⁸⁶ for the LTA framework are listed in Table 5.5. The CVFF bonded and non-bonded interaction parameters³⁸⁷ for ethene and propene generated by the DL_FIELD code¹³³ are listed in Table 5.6. The framework-guest non-bonded interactions were described by the Lennard-Jones parameters listed in Table 5.7. All the classical metadynamics calculations were performed using the DL_POLY4 package^{132,389} integrated with the PLUMED code.¹³⁵ The Nosé-Hoover thermostat and barostat^{390,391} with a coupling time constant of 1 ps were used for controlling the temperature and pressure in the *NVT* and *NPT* MD runs, respectively. A cutoff of 10.0 Å was used for the short-range and long-range interactions. In the DL_POLY4 package, the long-range interaction potentials are evaluated via the smoothed particle meshed Ewald method. The Velocity Verlet algorithm was used to integrate the equations of motion.⁹⁴ The pressure was set to zero in all MD runs.

NPT MD runs at different temperatures ranging from 100-600 K were first performed to account for the thermal expansion of the pure-silica LTA framework. In each *NPT*

TABLE 5.6. CVFF potential parameters for alkenes.³⁸⁷

Bonded interactions			
Bonds: $0.5k_r(r - r_0)^2$	k_r (eV Å ⁻²)	r_0 (Å)	Charge (e)
$C_{sp^2}-C_{sp^2}$	56.82	1.330	$q(C_{sp^2}) = -0.2$
$C_{sp^2}-C_{sp^3}$	28.00	1.500	$q(C_{sp^3}) = -0.2$
$C_{sp^2}-H$	31.36	1.090	$q(H) = +0.1$
$C_{sp^3}-H$	29.54	1.105	
Angles: $0.5k_\theta(\theta - \theta_0)^2$	θ_0 (eV rad ⁻²)	θ_0 (°)	
$C_{sp^2}-C_{sp^2}-C_{sp^3}$	3.13948	122.3	
$C_{sp^2}-C_{sp^2}-H$	3.25222	120.0	
$C_{sp^2}-C_{sp^3}-H$	3.85063	110.0	
$H-C_{sp^2}-H$	2.93134	121.2	
$H-C_{sp^3}-H$	3.42568	106.4	
Dihedral angles: $k_n(1 + \cos(n\omega - \xi))$	k_n (eV)	n	ξ (°)
$C_{sp^2}-C_{sp^2}-C_{sp^3}-H$	0.00915	3	0
$C_{sp^3}-C_{sp^2}-C_{sp^2}-H$	0.17671	2	180
$C_{sp^2}-C_{sp^2}-H-H$ (out-of-plane bending)	0.48133	2	180
Non-bonded interactions			
Lennard-Jones parameters	ϵ (10 ⁻³ eV)	σ (Å)	
$C_{sp^2}-C_{sp^2}$	6.417724	3.617049	
$C_{sp^2}-C_{sp^3}$	3.294446	3.744001	
$C_{sp^3}-C_{sp^3}$	1.691157	3.875409	
$C_{sp^2}-H$	3.251936	2.976855	
$C_{sp^3}-H$	1.669335	3.081338	
$H-H$	1.647794	2.449971	

 TABLE 5.7. Lennard-Jones potential parameters for host-guest interactions between alkenes and the zeolite framework.³⁸⁸

Interaction	ϵ (10 ⁻³ eV)	σ (Å)
$C_{sp^2}-O$	8.3642	2.9578
$C_{sp^3}-O$	7.0833	2.9225
$H-O$	4.9865	2.5568

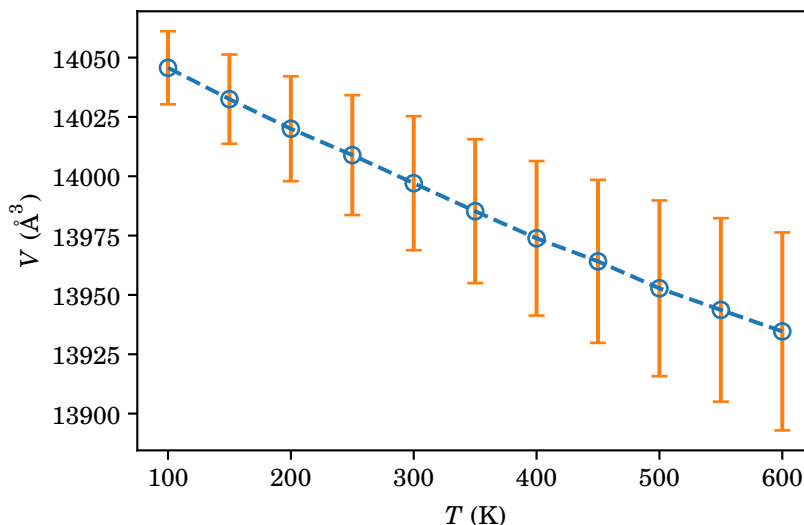


FIGURE 5.18. Temperature dependence of the crystal volume of the $2 \times 2 \times 2$ supercell of the LTA framework obtained using *NPT* MD simulation based on the BKS classical force field.³⁸⁶ Error bars indicate ± 1 standard deviations.

run, the total simulation time is 5.5 ns (5×10^5 equilibration and 5×10^6 integration steps of 1.0 fs). The trajectories were subsequently averaged out to obtain the initial configurations for the *NVT* metadynamics runs. The temperature dependence of the crystal volume of the LTA framework over 100-600 K is shown in Figure 5.18. The LTA framework exhibits negative thermal expansion since the crystal volume decreases slightly by $\sim 0.8\%$ as the temperature is elevated from 100 to 600 K. A larger fluctuation in crystal volume can be observed at a higher temperature, indicated by the error bars in Figure 5.18. The initial structure for the metadynamics simulation is generated by placing either a single ethene or propene molecule at the centre of an eight-membered ring window of the LTA framework.

To construct a free energy profile from a metadynamics calculation, a meaningful collective variable (CV) for distinguishing different steady and transition states must be defined. The collective variable dz for the metadynamics simulation is defined by the distance between the geometrical centre of the eight-membered ring window, GC_{ring} , and the centre of mass of the diffusing alkene molecule, COM_{alkene} , projected along the z -axis perpendicular to the ring plane: $dz = z(GC_{\text{ring}}) - z(COM_{\text{alkene}})$, as illustrated in Figure 5.19. A Gaussian hill with a height and width of 0.25 kJ mol^{-1} and 0.4 Å , respectively, was deposited every 5000 steps. Two potential walls with a harmonic spring constant of

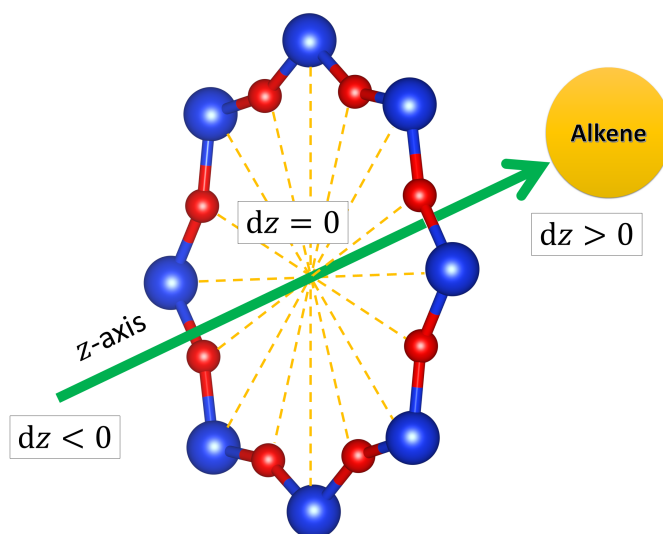


FIGURE 5.19. Schematic illustration of the collective variable for the metadynamics simulation of the alkene diffusion through an LTA zeolitic pore. dz is defined by the distance between the geometrical centre of the eight-membered ring window and the centre of mass of the diffusing alkene molecule projected along the z -axis perpendicular to the ring plane.

$2000 \text{ kJ mol}^{-1} \text{ \AA}^{-2}$ were placed at $\pm 8 \text{ \AA}$ along the collective variable axis to specify the diffusional region of our interest. An additional harmonic potential wall is introduced to limit the maximum distance of 5 \AA between $\text{COM}_{\text{alkene}}$ and the z -axis. At a given temperature, the free energy profile for the diffusion process was averaged out from ten independent metadynamics runs.

The free energy profiles and the temperature dependence of the energy barriers of the ethene and propene diffusion through an eight-membered ring window of the LTA zeolite are shown in Figures 5.20 and 5.21, respectively. As expected, the transition-state structures occur at $dz \approx 0$, *i.e.*, the centre of the window, in both cases. Over 100-600 K, the free energy barrier of the ethene and propene diffusion increases as the temperature is elevated. The free energy barrier of the ethene diffusion lies between *ca.* $5\text{-}20 \text{ kJ mol}^{-1}$ over the temperature range considered, whereas the energy barrier of the propene diffusion ranges from $15\text{-}35 \text{ kJ mol}^{-1}$. At a given temperature, the higher free energy barrier of the propene diffusion through an LTA zeolite pore reflects the larger size of the propene molecule than ethene.

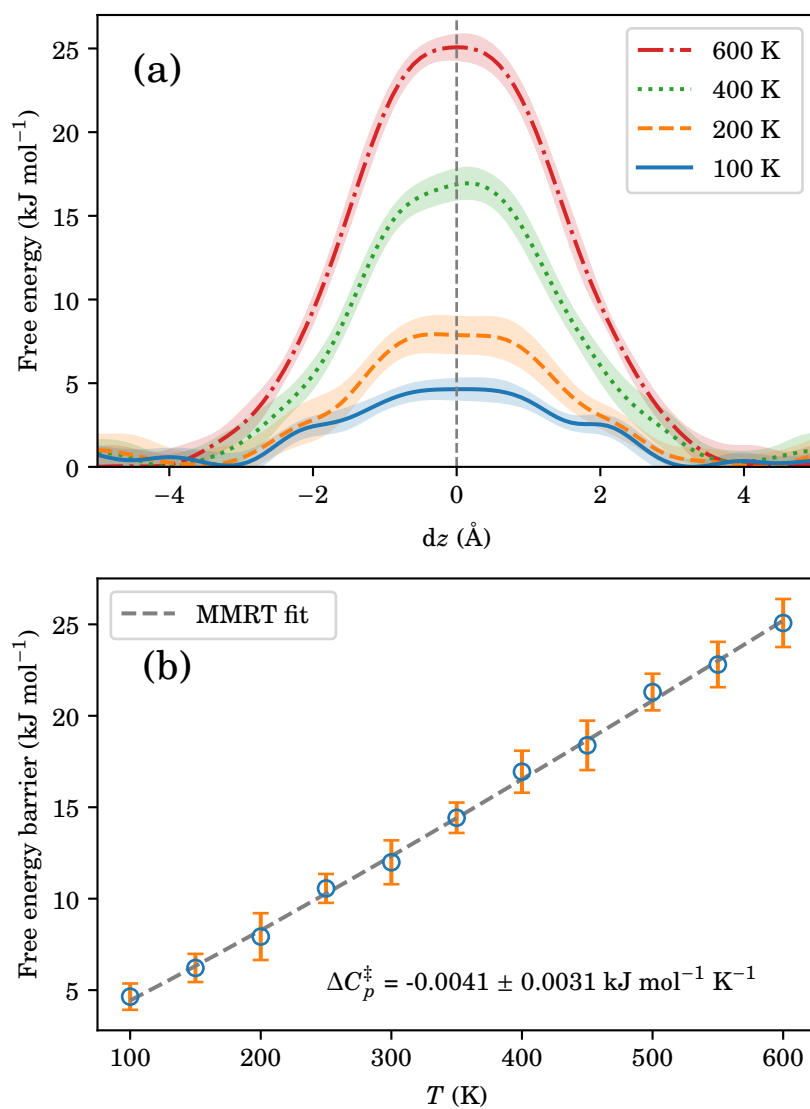


FIGURE 5.20. (a) Free energy profiles and (b) temperature variation of the energy barrier of the ethene diffusion through an eight-membered ring window of the LTA zeolite. Transparent bands in (a) and error bars in (b) indicate ± 1 standard deviations.

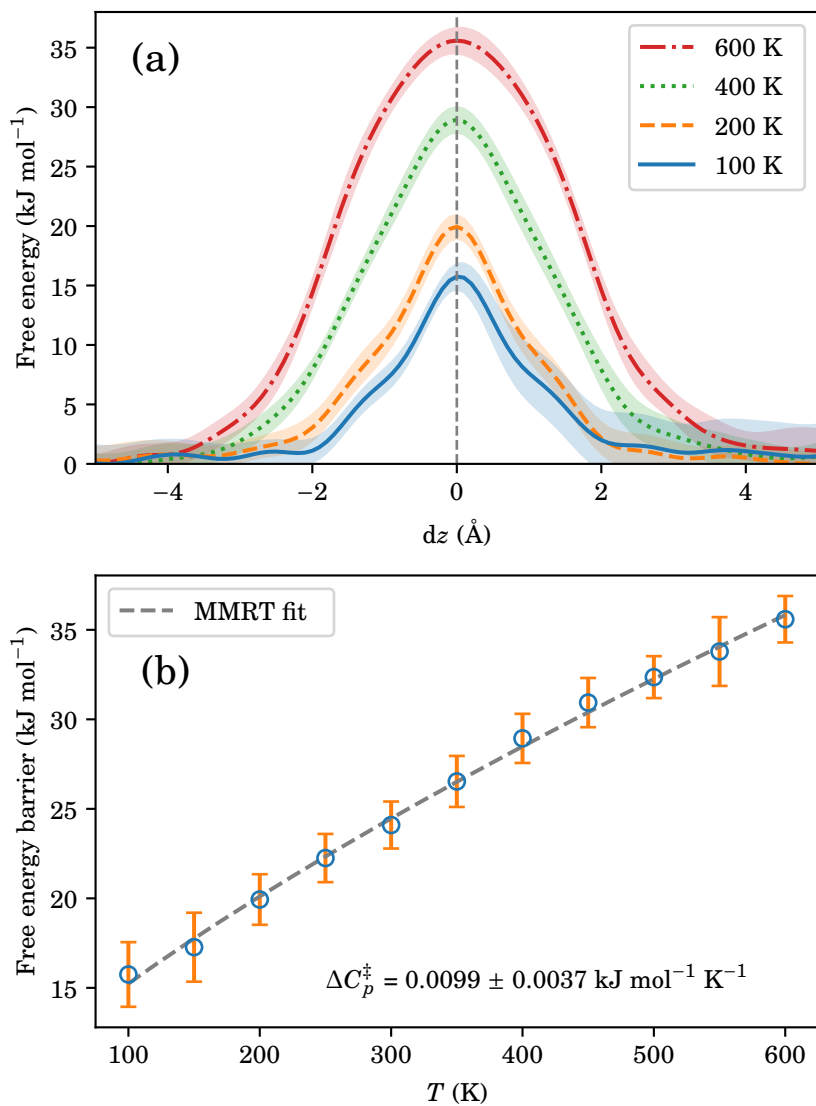


FIGURE 5.21. (a) Free energy profiles and (b) temperature variation of the energy barrier of the propene diffusion through an eight-membered ring window of the LTA zeolite. Transparent bands in (a) and error bars in (b) indicate ± 1 standard deviations.

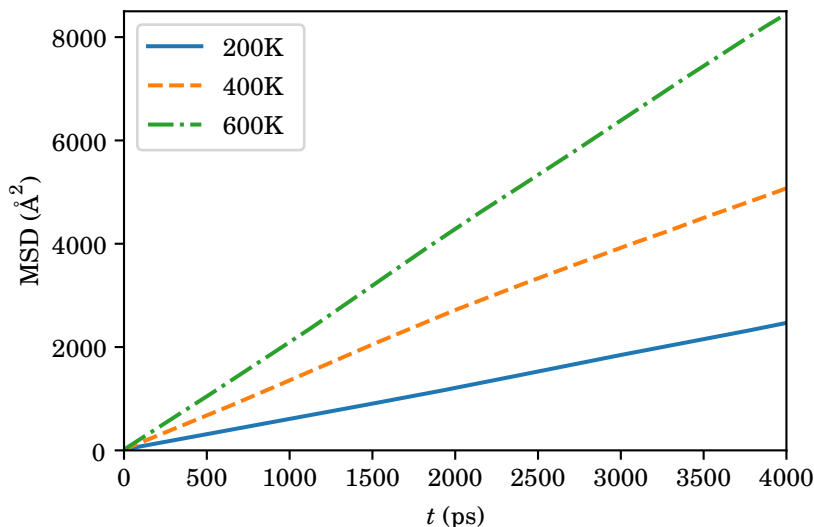


FIGURE 5.22. Mean-square displacement (MSD) plots of the centres of mass of 64 ethene molecules at 200, 400 and 600 K in a $2 \times 2 \times 2$ supercell of the LTA zeolitic framework.

Figures 5.20(b) and 5.21(b) show that the temperature variation of the two diffusion processes is largely linear. Hence, ΔC_p^\ddagger values of the ethene and propene diffusion obtained from the MMRT fitting are very small. ΔC_p^\ddagger for the ethene diffusion is $-0.0041 \pm 0.0031 \text{ kJ mol}^{-1} \text{ K}^{-1}$, while that of the propene diffusion is $0.0099 \pm 0.0037 \text{ kJ mol}^{-1} \text{ K}^{-1}$. A positive ΔC_p^\ddagger implies that the first derivative of ΔH^\ddagger with respect to temperature is positive and becomes larger at elevated temperatures. This might be the direct consequence of the more difficult diffusion of propene through the smaller zeolitic windows at higher temperatures due to the negative thermal expansion of the LTA framework itself, as shown in Figure 5.18. On the contrary, the value of ΔC_p^\ddagger for the ethene diffusion is small and negative, implying that ΔH^\ddagger decreases more slightly rapidly as the temperature is elevated. Therefore, the results suggest that the activation parameters for a diffusion process through a zeolitic micropore depend on the size of the guest molecule.

5.5.3 Diffusion Rates of Ethene and Propene in LTA Zeolite

In a given MD run, the time-dependent mean-square displacement (MSD) of diffusing atoms or molecules within the moving fragment, $\langle \Delta r^2 \rangle$, can be used directly to compute

their self-diffusivity or self-diffusion constant, D_s :

$$\langle \Delta r^2 \rangle = 6D_s t + b, \quad (5.11)$$

where Δr^2 is the atomic or molecular displacement from its initial position, b is a factor arising from atomic thermal vibrations, and t is the simulation time.^{93,94} Note that the brackets identify the averaged displacement of all the particles of interest. Using the classical MD simulation technique and the force-field parameters in the previous subsection, we calculated the MSD of diffusing 64 ethene molecules in a $2 \times 2 \times 2$ supercell of the LTA framework at various temperatures. The MSD plots of the centres of mass of the ethene molecules at 200, 400 and 600 K are shown in Figure 5.22. At each temperature, the total simulation time for the *NVT* run is 11 ns (2×10^6 equilibration and 2×10^7 integration steps of 0.5 fs). The trajectory analysis was performed using the DL_ANALYSER code.^{134,392} For each run, the MSD of the centre of mass of the 64 ethene molecules was estimated using multiple time origins. In these MD runs, we assume that the crystal volume of the LTA framework does not depend on the guest-molecule loading.

Using equation (5.11), the slope of each MSD plot Figure 5.22 defines the magnitude of the self-diffusion coefficient D_s . For instance, the slope of the MSD plot at 600 K is greater than that at 200 K, suggesting that the ethene molecule diffuses more rapidly in the LTA zeolite at 600 K than at 200 K. Therefore, the diffusion rate D_s is absolutely temperature-dependent. Analogously to the Arrhenius equation (5.1), the temperature variation of D_s is written as

$$D_s = D_0 \exp\left(-\frac{E_a}{RT}\right), \quad (5.12)$$

where D_0 is the high-temperature limit of D_s . Again, the activation energy E_a of self-diffusion is assumed to be temperature-independent.

In this subsection, we intend to probe the temperature dependence of the self-diffusivity of ethene and propene molecules in the LTA zeolite based on the MMRT approach, *i.e.*, by assuming that the thermodynamic activation parameters of the self-diffusion are temperature-dependent. We have performed ten independent MD runs at a given temperature to obtain the average ethene diffusion coefficient D_s . The Arrhenius plot of the ethene diffusion rate in the LTA zeolite is shown in Figure 5.23(a). The plot shows an obvious deviation from the classical Arrhenius law. After fitting the data to the MMRT equation (5.4), we obtain $\Delta C_p^\ddagger = -0.0282 \pm 0.065 \text{ kJ mol}^{-1} \text{ K}^{-1}$. Again, this negative value of ΔC_p^\ddagger implies a tighter binding mode in the transition state than in the ground state. It is important to note that the energy barriers of all activation processes

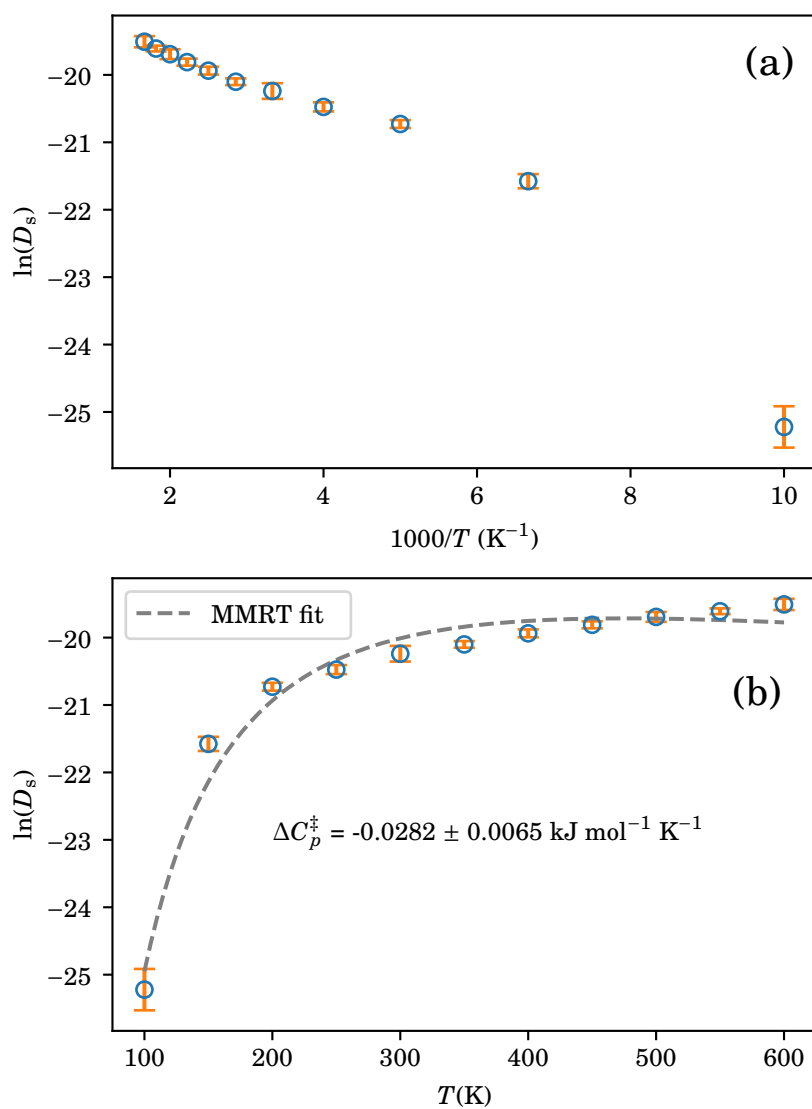


FIGURE 5.23. (a) Arrhenius plot and (b) MMRT fit of the ethene diffusion rate in the LTA zeolite over 100-600 K. Error bars indicate ± 1 standard deviations.

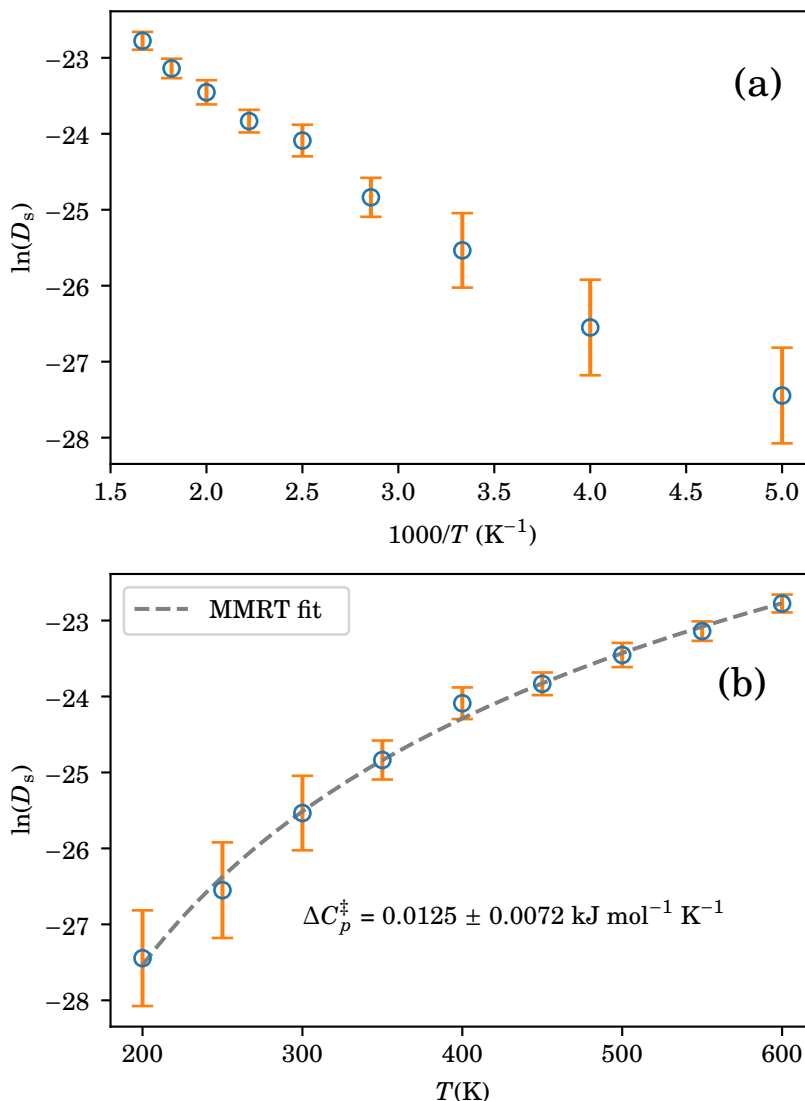


FIGURE 5.24. (a) Arrhenius plot and (b) MMRT fit of the propene diffusion rate in the LTA zeolite over 100-600 K. Error bars indicate ± 1 standard deviations.

during the simulation, *e.g.*, diffusion through pores, adsorption and desorption processes, contribute to the *overall* activation energy.

Analogous calculations have been performed to study the temperature dependence of the self-diffusivity of propene molecules in the LTA zeolitic framework. Figure 5.24 shows the Arrhenius plot and MMRT fit of the propene diffusion rate in the LTA zeolite over 100-600 K. At a given temperature, propene diffuses more slowly than ethene in the LTA framework due to its larger size. The Arrhenius plot for the propene diffusion

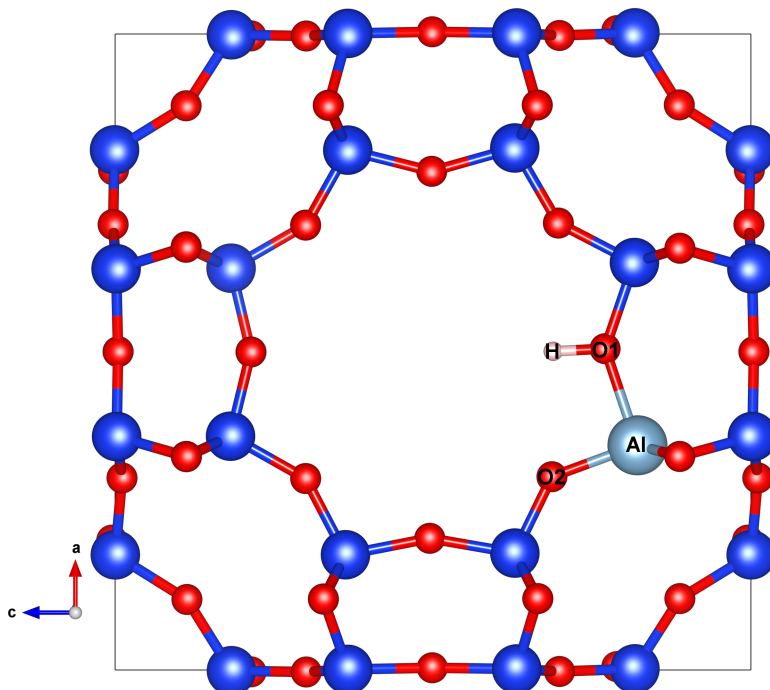


FIGURE 5.25. Structure of the H-LTA zeolite used for modelling the hydrogen hopping process.

in Figure 5.24(a) shows, again, a deviation from the Arrhenius law with a fitted ΔC_p^\ddagger of $0.0125 \pm 0.0072 \text{ kJ mol}^{-1} \text{ K}^{-1}$. Interestingly, the fitted ΔC_p^\ddagger for the propene self-diffusivity is close to that obtained from the free energy barriers of its diffusion through a zeolite pore in the previous subsection ($0.0099 \pm 0.0037 \text{ kJ mol}^{-1} \text{ K}^{-1}$).

5.5.4 Hydrogen Hopping in the H-LTA Zeolite

In this subsection, we investigate the temperature dependence of the free energy barrier for the hydrogen hopping or proton jump in the acidic H-LTA zeolite using *ab initio* MD and metadynamics simulation based on DFT. In an acidic zeolite framework, a proton Brønsted acid site is introduced by replacing one of the Si atoms with an Al atom. As a simple case study for modelling the proton hopping in the H-LTA zeolitic framework, we use the smallest 73-atom unit cell of the H-LTA structure with a Brønsted acid site located in an eight-membered ring, as shown in Figure 5.25. The CP2K code¹¹⁰ with a mixed Gaussian and plane-wave (GPW) basis set approach^{393–395} was used to perform all the DFT calculations. The revised version of GGA-PBE functional (revPBE)³⁹⁶ with Grimme DFT-D3 dispersion corrections³⁹⁷ were employed. The DZVP-GTH basis sets and

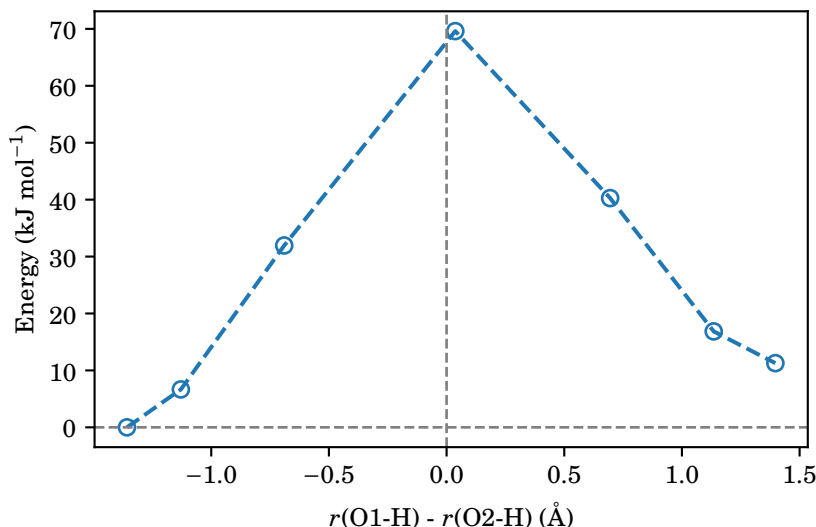


FIGURE 5.26. Climbing image nudged elastic band (CI-NEB) energy profile for hydrogen hopping in the H-LTA zeolite.

pseudopotentials were used for all the four atomic types.³⁹⁸ The Nosé-Hoover thermostat and barostat^{390,391,399} with a coupling time constant of 1 ps were used to control the temperature and pressure of the *NVT* and *NPT* MD simulations. Metadynamics free-energy calculations were carried out using the PLUMED software package.¹³⁵

The hopping of the proton between two different oxygen atoms in the $(\text{Si-O})_3\text{-Al(OH)}$ moiety, *i.e.*, labelled by O1 and O2 in Figure 5.25, is an activated process. The minimum energy path of the transition, obtained using a climbing image nudged elastic band method (CI-NEB)^{400,401} with seven replicas, is shown in Figure 5.26. Here, we plot the energies of the replicas as a function of the difference in interatomic distance between O1-H and O2-H, *i.e.*, $r(\text{O1-H}) - r(\text{O2-H})$. Note that the difference in distance $r(\text{O1-H}) - r(\text{O2-H})$ will later be used as the collective variable for the free energy profile construction in metadynamics runs. The NEB energy profile in Figure 5.26 demonstrates that the static-limit activation energy for the proton hopping in the H-LTA zeolite is *ca.* 70 kJ mol⁻¹. The replica with the highest energy is the approximate transition-state structure occurring at $r(\text{O1-H}) - r(\text{O2-H}) \approx 0$ Å. The energies of the two steady states (or reactant and product) are different as the two oxygen atoms, O1 and O2, are not equivalent. Next, we will study the temperature variation of the free energy barrier of the proton jump in the H-LTA framework through metadynamics simulations.

To account for the thermal expansion of the pure-silica LTA framework, we performed

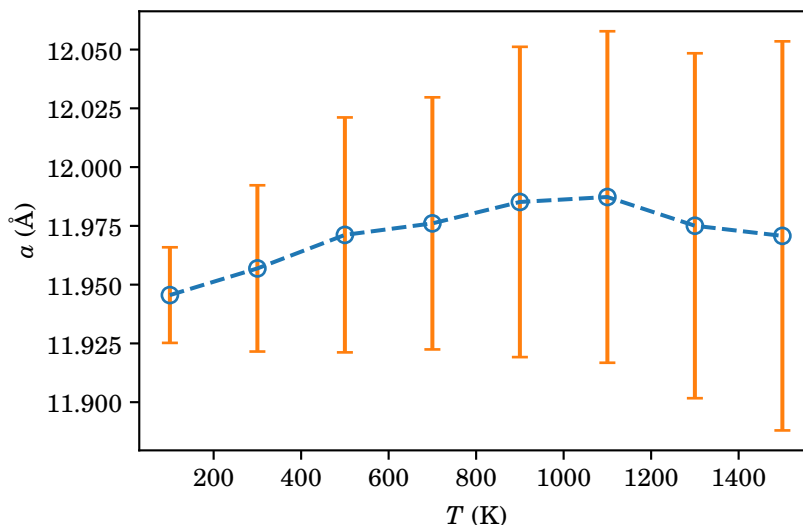


FIGURE 5.27. Temperature dependence of the lattice parameter a of the LTA zeolitic framework obtained using NPT molecular dynamics simulation based on DFT. Error bars indicate ± 1 standard deviations.

NPT MD runs at different temperatures ranging between 10 and 2050 K, and the pressure was set to zero. In each MD run, the total simulation time is 37.5 ps (5000 equilibration and 70000 integration steps of 0.5 fs). At each temperature, the average structure is obtained from the trajectory file, and this will then be used as the initial configuration for the metadynamics runs in the NVT ensemble. The temperature variation of the average lattice parameter a of the pure-silica LTA framework over 100-1500 K is shown in Figure 5.27. We have found that the temperature variation of the lattice parameter over the temperature range considered is roughly constant (around 11.950-11.975 Å). A larger fluctuation is observed at a higher temperature, as indicated by the error bars in Figure 5.27.

The initial structures of the H-LTA zeolite with a single Brønsted acid site (in Figure 5.25) for NVT metadynamics runs were constructed with the equilibrium volumes obtained from the previous NPT runs. Similar to the NEB calculation in Figure 5.26, we use $r(\text{O1-H})-r(\text{O2-H})$ as the collective variable to represent the reaction coordinates in the free energy profiles of the proton jump in the H-LTA zeolite. In each metadynamics run, the total simulation time is 67.5 ps (10^4 equilibration and 1.25×10^5 integration steps of 0.5 fs). A Gaussian hill with a height and width of 0.35 kJ mol^{-1} and 0.1 Å , respectively, was deposited every 25 MD steps. Twenty independent metadynamics runs have been performed at each temperature and subsequently averaged out to determine

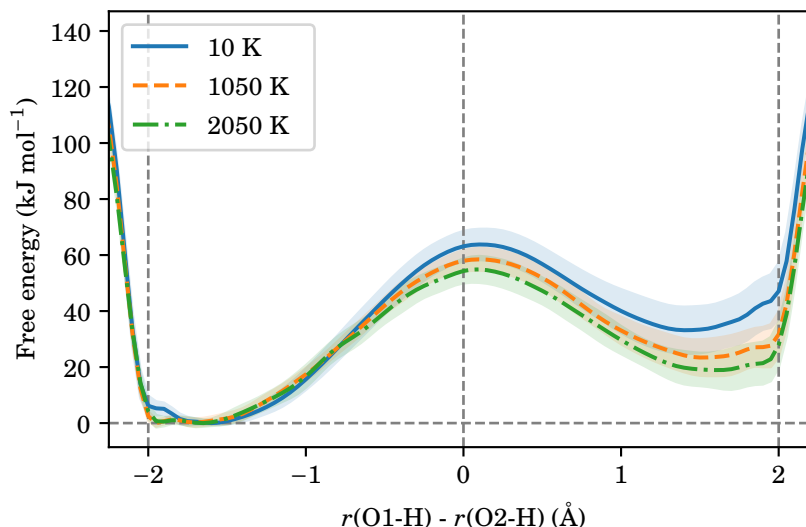


FIGURE 5.28. Free-energy profiles at 10, 1050 and 2050 K for hydrogen hopping in the H-LTA zeolite. Each profile has been averaged out from twenty independent metadynamics runs, and the transparent band indicates a ± 1 standard deviation error.

the sampling error. A few harmonic potential restraints with a spring constant of $2000 \text{ kJ mol}^{-1} \text{ \AA}^{-2}$ have been introduced to ensure that the hydrogen atom does not escape from the reaction proximity of interest. Two potential walls were placed at $\pm 2 \text{ \AA}$ along the collective variable axis. The maximum Al–H distance of 3.0 \AA was constrained by another harmonic wall. Additionally, the H–O1–Al–O2 torsion angle was also fixed at 0 rad by another potential wall.

The free energy profiles of the hydrogen hopping in the H-LTA framework at 10, 1050, and 2050 K averaged out from twenty independent metadynamics runs are shown in Figure 5.28. Similar to the NEB energy profile in Figure 5.26, the approximate transition state for the hydrogen hopping occurs at $r(\text{O1-H}) - r(\text{O2-H})$ close to zero. Unfortunately, the free energy barriers at the three temperatures are not significantly different, as indicated by the overlapping error bands. The temperature dependence of the free energy barrier for the hydrogen hopping in the H-LTA framework over 10-2050 K is shown in Figure 5.29. Over the temperature range considered, the free energy of activation for the proton hopping process lies between $55\text{--}65 \text{ kJ mol}^{-1}$, compared to the NEB static-limit value of $\sim 70 \text{ kJ mol}^{-1}$. The energy barrier tends to slightly decrease as the temperature is elevated. Again, the large error bars imply the insignificant difference of those energy barriers at various temperatures. Unfortunately, our calculated free energy barriers

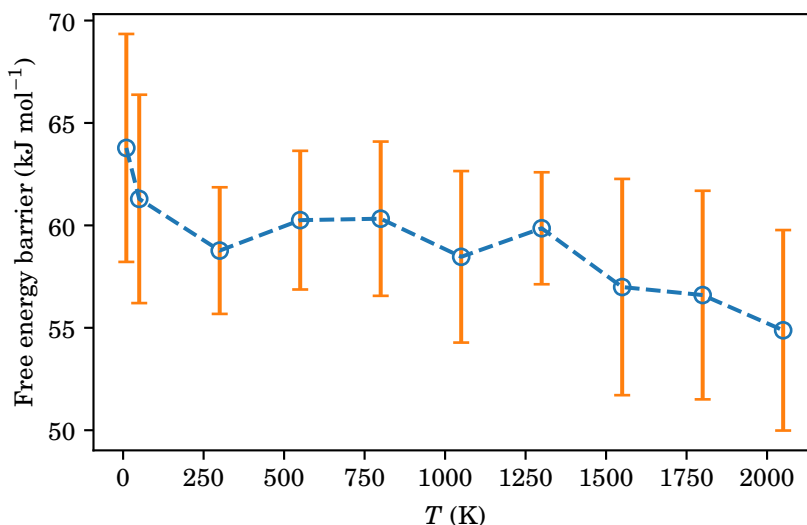


FIGURE 5.29. Temperature variation of the free energy barrier for hydrogen hopping in the H-LTA zeolite. Error bars represent ± 1 standard deviations.

cannot be fitted to the MMRT equation (5.6). However, we have shown that the computer simulation method based on *ab initio* metadynamics is very useful for calculating the free energy barrier of a given activated process in a solid-state material and investigating their temperature dependence.

5.5.5 *Ab initio* Simulation of Zeolitic Reactions

The experimental *apparent* activation energy of 103 kJ mol^{-1} for the methylation of ethene by methanol over the H-ZSM-5 zeolite at 350°C has been reported by Svelle *et al.*³⁴⁰ Van Speybroeck *et al.*⁴⁰² have performed first-principles calculations to study the kinetics of the ethene methylation by methanol over the H-ZSM-5 framework. Surprisingly, the computational results are in excellent agreement with those obtained from the experimental observations. Hence, the theoretical work of Van Speybroeck *et al.*⁴⁰² provides a crucial link between the experimental and theoretical kinetic studies of zeolite-catalysed methylation reactions.^{318,402} According to Svelle *et al.*,³⁴⁰ the reaction orders of the ethene methylation with methanol over the H-ZSM-5 zeolite are one and zero with respect to ethene and methanol, respectively. This means that methanol molecules cover all the catalytic sites fully, and these adsorbed sites undergo a bimolecular methylation reaction with ethene to form water and propene molecules. In this subsection, we will briefly present our periodic plane-wave DFT calculations of the methylation reaction of

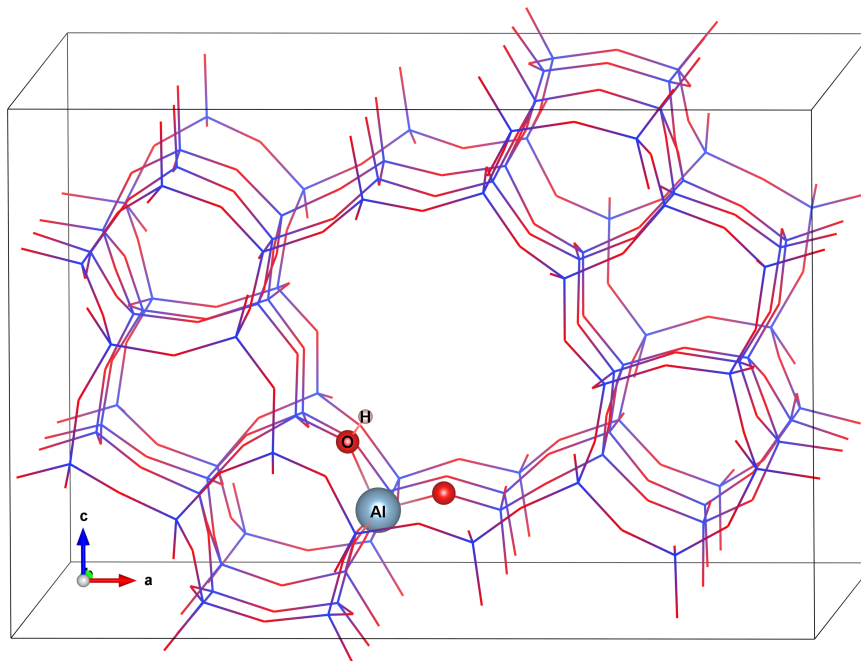


FIGURE 5.30. Structure of the H-ZSM-5 zeolite for modelling ethene methylation reaction by methanol. All other framework Si and O atoms have been omitted for clarity.

ethene by methanol over the H-ZSM-5 zeolite before discussing the potential application of *ab initio* metadynamics to investigate the temperature dependence of the free energy barrier of the zeolite-catalysed ethene methylation reaction.

The plane-wave DFT calculations in this subsection were performed using the Vienna *Ab initio* Simulation Package (VASP).^{105–107,403} The atomic wave functions were represented by the projected-augmented-wave (PAW) pseudopotentials.⁴⁰⁴ The GGA-PBE functional was chosen for evaluating the exchange-correlation contribution.¹¹⁴ The plane-wave cutoff of 400 eV and a $2 \times 2 \times 3$ **k**-mesh were used for all calculations. The transition-state search was performed using the dimer method implemented in the VASP program.^{405,406} The crystal structure of the pure-silica MFI parent zeolite framework, *i.e.*, the conventional unit cell consisting of 288 atoms, was taken from the IZA database.³⁴⁸

Figure 5.30 shows the optimised structure of the H-ZSM-5 zeolite with a single Brønsted acid site on its large ten-membered ring. To construct the energy profile for the methylation reaction, we create our model structures according to the bimolecular reaction mechanism proposed by Svelle *et al.*³⁴⁰ and Van Speybroeck and colleagues.⁴⁰² For instance, the transition-state geometry of the ethene methylation reaction by methanol

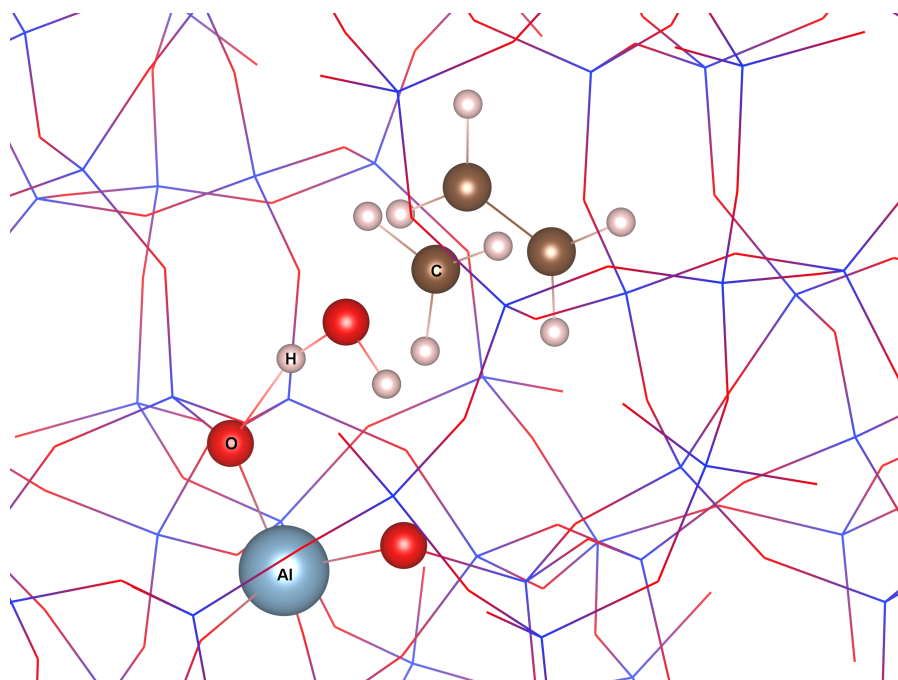


FIGURE 5.31. Transition-state geometry for the methylation reaction of ethene by methanol catalysed by the H-ZSM-5 zeolite. All other framework Si and O atoms have been omitted for clarity.

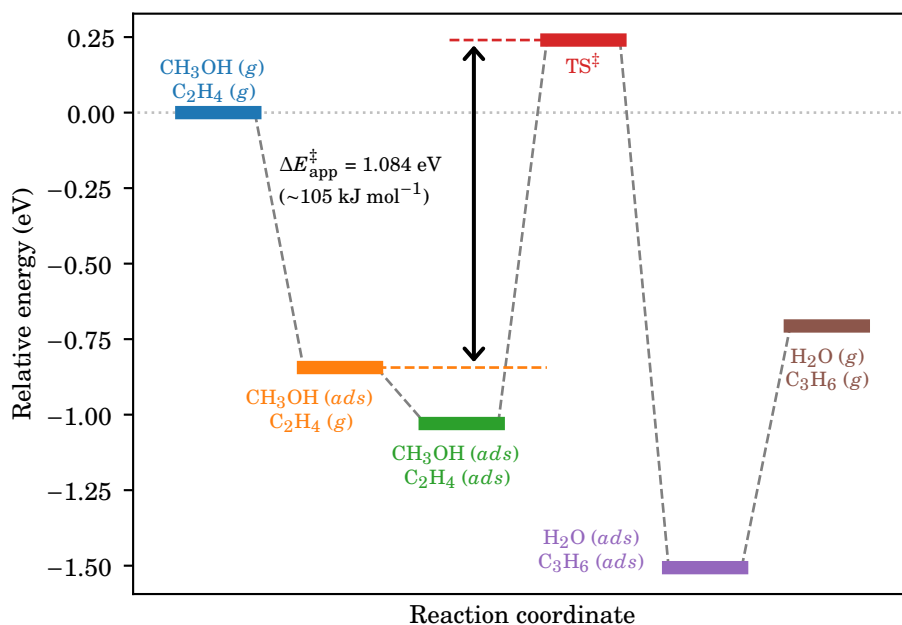


FIGURE 5.32. Energy diagram for the ethene methylation by methanol over H-ZSM-5 zeolite.

over the H-ZSM-5 is shown in Figure 5.31. Consequently, the energy diagram for the methylation reaction is shown in Figure 5.32. Note that the *apparent* activation energy is measured using the energy difference between the transition-state structure and the zeolite with adsorbed methanol and gas-phase ethene molecules, while the *intrinsic* activation energy refers to the energy difference between the transition-state complex and the complex with both adsorbed reactant molecules.^{318,340,402} Interestingly, our calculated apparent barrier of *ca.* 105 kJ mol⁻¹ is also in excellent agreement with the experimental value of 103 kJ mol⁻¹.³⁴⁰

Although the DFT method used in this subsection proves extremely useful for calculating the energy barrier of the methylation reaction, these plane-wave DFT calculations are tremendously expensive in terms of computational resources and computer time. At first, we intended to study the temperature variation of the free energy barrier of the ethene methylation reaction by methanol catalysed by the H-ZSM-5 based on the MMRT approach via *ab initio* molecular dynamics and metadynamics. However, those calculations are far beyond the capability of our computational resources, and the computer time for such calculations is too long. For these reasons, we currently cannot perform *ab initio* metadynamics to probe the temperature dependence of the free energy barriers of zeolite-catalysed reactions.

Recently, Bailleul *et al.*⁴⁰⁷ have performed advanced *ab initio* enhanced-sampling free-energy calculations, including metadynamics, variationally-enhanced sampling, umbrella sampling, and thermodynamic integration or umbrella integration, for the methylation reaction of ethene by methanol over the H-ZSM-5 zeolite. Bailleul *et al.*⁴⁰⁷ have only carried out the calculations at 623 K. The calculated energy barriers obtained from those sophisticated simulation techniques agree very well with the experimentally-observed values. Therefore, those advanced simulation methods have great potential to theoretically study the temperature variation of the free energy barriers of zeolite-catalysed reactions.

5.6 Conclusions

In this chapter, we have shown that many experimentally-observed zeolite-catalysed reaction rates, for instance, the methylation reactions of alkenes by methanol over the H-ZSM-5 zeolite and the oxidation-reduction reactions of nitrogen-containing gas molecules over copper-based zeolitic frameworks, are lower than expected as the temperature is increased based on the Arrhenius law. A negative value of the change in heat

capacity of activation is one possible reason for the negative curvature of the Arrhenius plots for those zeolitic reaction rates, as macromolecular rate theory (MMRT) explains. Consequently, the non-Arrhenius behaviour of those zeolite-catalysed reactions could be the direct consequence of the tighter binding mode in the transition state than in the ground state in the absence of the diffusional controls or changes in properties of catalytic centres in the high-temperature regime, as other possibilities previously suggested.^{55–57} However, we have observed that the magnitudes of the negative heat capacity of activation for zeolite-catalysed reactions obtained from the MMRT fits are significantly smaller than those for enzyme reactions and rationalised this in terms of the much more rigid frameworks of zeolites compared to enzyme structures. Furthermore, the MMRT kinetic parameters, *i.e.*, the heat capacity of activation and the optimum temperature, also depend on various factors, including the size of the reactant species and the topology and composition of the zeolitic framework. Hence, the MMRT concept offers the potential of designing and synthesising novel zeolitic materials with adjustable temperature-dependent catalytic properties of interest.

In the final part of the chapter, based on the MMRT approach, we have investigated the temperature dependence of the thermodynamic properties of activation and kinetic properties for various activated processes catalysed by zeolites theoretically via classical and first-principles computer simulation. First, we have performed classical and DFT calculations using quasi-harmonic lattice dynamics (QLD) to examine the temperature dependence of the free energy barrier of the Mg^{2+} vacancy migration in MgO . We have found that the entropy and enthalpy of activation for the Mg^{2+} vacancy migration are strongly temperature-dependent. The temperature variation of the free energy barrier can well be fitted to the MMRT equation, resulting in a small negative heat capacity of activation due to the rigid structure of the MgO crystal. The relatively small value of the heat capacity of activation for the defect migration process reflects the temperature-dependent behaviour close to that predicted by the Arrhenius law.

Next, we have carried out classical molecular dynamics (MD) and metadynamics to study the temperature-dependent free-energy barriers of the diffusion of ethene and propene through a pore of the LTA zeolite. Our MMRT fits show that the ethene diffusion through the LTA pore shows a small negative value of the heat capacity of activation. In contrast, the rates of the propene diffusion through the zeolite pore shows a positive heat capacity of activation. These results from the MMRT fittings are also consistent with those of their computed self-diffusion rates in the LTA zeolite obtained by classical MD simulations. The positive values of the heat capacity of activation for rates of the propene

diffusion in the LTA framework may be the direct consequence of the negative thermal expansion of the framework. Note again that the small values of the heat capacity of activation for these diffusion processes lead close to the classical Arrhenius behaviour.

Furthermore, we have performed static and metadynamics simulations based on DFT to compute the activation energy for the hydrogen hopping in an acidic H-LTA zeolite. The activation energy obtained from the static run is in reasonable agreement with the free-energy barriers obtained from the metadynamics calculations. However, the free-energy barriers for the hydrogen hopping in the H-LTA zeolite at different temperatures are not significantly different, and they cannot be fitted to the MMRT equation. Lastly, we have carried out static DFT calculations to evaluate the activation energy of the ethene methylation reaction over an acidic H-ZSM-5 zeolite. The calculated apparent activation energy for the ethene methylation is in excellent agreement with the experimental value. We commented that the temperature dependence of the free-energy barrier of the ethene methylation over the H-ZSM-5 zeolite could potentially be investigated using *ab initio* metadynamics.

CONCLUSIONS AND FUTURE WORK

All the results presented in this thesis have emphasised the importance of various atomistic modelling techniques to understand reactions and processes involving solid-state materials more thoroughly. The increasing power of highly-parallel supercomputers and advances in software engineering enable us to simulate highly complex chemical systems to gain microscopic insights into the chemical phenomena. Although numerous computational methods are available for simulating those complex systems, one must always consider the trade-off between computational cost and accuracy when contemplating the methods. This chapter summarises the results of all the thesis chapters individually and draws general conclusions from those results before discussing the future work.

6.1 Summaries

The results of our work have been presented in three independent chapters. In Chapter 3, we presented the computational study of the defect thermodynamics in crystalline solids and clusters. Next, we highlighted the application of the defect modelling discussed comprehensively in Chapter 3 in explaining the trace-element partitioning in minerals and melts in Chapter 4. Also, Chapter 4 discussed the computational investigation of the limitations of widely-used simple lattice strain models for describing trace-element partitioning. Lastly, in Chapter 5, we concentrated on exploring the non-Arrhenius behaviour of zeolite-catalysed reactions based on macromolecular rate theory (MMRT).

In general, we are particularly interested in studying the temperature dependence of reactions and processes in solid-state materials through the mean of computer simulation, *e.g.*, the temperature variation of the defect free-energies in solids and clusters in Chapter 3 and the temperature dependence of the zeolite-catalysed reactions in Chapter 5.

6.1.1 Defect Thermodynamics in Solids and Clusters

In Chapter 3, classical and first-principles density functional theory (DFT) calculations based on quasi-harmonic lattice dynamics (QLD) were performed to examine the temperature variation of defect properties in solids and clusters. We studied the substitutional defect formation in polar and metallic solids: (i) the substitution of a Mg^{2+} by a Ba^{2+} in MgO and (ii) the substitution of a Cu atom by a Ag atom in Cu metal. We emphasised that the temperature variation of those defect thermodynamics is significant and cannot be negligible as often assumed. We used the QLD technique to probe the effects of several factors on defect thermodynamics, including finite-size effects when using finite-size clusters of solids, system size and volume constraints in the periodic supercell approach, and defect clustering.

The calculated defect formation energies of larger finite-size clusters are closer to the bulk limit than those of the smaller clusters. The existence of the interfaces of finite-size clusters gives rise to the difference in degree of structural relaxation in the two simulation models. When performing calculations at constant-volume, the volume constraints also determine the calculated defect free energies, as they directly affect the interatomic force constants when evaluating the vibrational contributions via phonon calculations. The calculated defect volume and energy depend greatly on the concentration of defects in the crystal. The computed defect energies of the Ba^{2+} substitutional defect formation in MgO obtained from the classical simulations agree reasonably with those from DFT calculations.

6.1.2 Trace-Element Partitioning in Minerals and Melts

In Chapter 4, we use the computer simulation technique based on lattice statics to study the partitioning behaviour of trace elements between minerals and melts theoretically. The defect, relaxation and solution energies for the incorporation of homovalent (+2) and heterovalent (+1 and +3) trace elements in CaO and diopside minerals have been calculated via classical and DFT static calculations in the supercell approach.

The elastic lattice strain model of Blundy and Wood³³ uses the strain-energy expression of Brice³⁴ to explain trace-element partitioning. We assessed such models critically by comparing the predictions of the models with those from the simulations. Although the Blundy and Wood³³ model appears to explain the Onuma curve for an isovalent series, describing strains using the equation of Brice³⁴ is found to be inadequate and oversimplified. This is due to the poor description of lattice strains, which arises mainly from the simplifications made in the model formulation. The Brice³⁴ model assumes that the crystal medium is continuous and elastically isotropic; only one Young's modulus describes the lattice strains. However, our calculations show clearly that structural strains around the point defect are highly anisotropic. Additionally, the use of the fixed ionic radii is questionable as the radius of a given cation varies from crystal to crystal and lattice site to lattice site, depending greatly on the local environment. Describing the Onuma curve for a heterovalent series by a single Young's modulus is ambiguous as two heterovalent cations are simultaneously incorporated in the crystal. More importantly, the model of Blundy and Wood³³ does not take the role of the melt phases into account explicitly.

6.1.3 Non-Arrhenius Reaction Rates in Solids

In Chapter 5, we explored the non-Arrhenius zeolite-catalysed reaction rates based on macromolecular rate theory (MMRT). We found that many zeolite-catalysed reactions reported in the literature exhibit the non-Arrhenius behaviour in which the rate of reaction is lower than expected at higher temperatures. The changes in reaction mechanism, structural and dynamical changes of the catalytic centres and diffusional controls in different temperature ranges have previously been suggested as accounting for deviations from the classical Arrhenius equation. However, studies have shown that the non-Arrhenius behaviour of several zeolite-catalysed reactions does not relate to those phenomena as the reaction rates are reversible during temperature cycling.^{55–57} Consequently, a negative change in heat capacity of activation is one possible explanation of the negative curvature of the Arrhenius plots for those zeolitic reaction rates, as the MMRT approach suggests. The MMRT fits of the zeolite-catalysed reactions considered in this work yield smaller negative changes in heat capacity of activation than those of enzyme reactions. This has been rationalised in terms of the much more rigid frameworks of zeolites compared to enzyme structures. The fitted kinetic parameters depend on various factors, including the size of the reactant species, framework topology and composition. Hence, the MMRT approach offers the potential of designing and synthesising novel

zeolites with tunable temperature-dependent catalytic properties of interest.

We used various classical and *ab initio* simulation techniques, including QLD, molecular dynamics (MD) and metadynamics, to investigate the temperature dependence of the free energy barriers and kinetics of several diffusion processes in MgO and zeolitic frameworks. We found that the temperature variation of the calculated classical and DFT free energy barrier of the Mg^{2+} vacancy diffusion in MgO based on QLD can well be fitted to the MMRT equation. The MMRT fit of the calculated free-energy barrier of the ethene diffusion inside the framework and through a pore of the LTA zeolite from classical metadynamics simulations gives also a negative value of the heat capacity of activation. In contrast, the rates of the propene diffusion through the zeolite pore exhibits a positive heat capacity of activation. The MMRT fitted parameters for the ethene and propene diffusion through an LTA zeolite are also consistent with those from their self-diffusion rates in the LTA zeolite calculated by classical MD simulations. The negative thermal expansion of the framework is a possible cause of the positive values of the heat capacity of activation for the rates of the propene diffusion in the LTA zeolite.

We computed the activation energy for hydrogen hopping in an acidic H-LTA zeolite via DFT static and metadynamics simulations. The static-limit activation energy is in reasonable agreement with the metadynamics free-energy barriers. The temperature variation of the free-energy barriers of the hydrogen hopping in the H-LTA zeolite is insignificant. Lastly, we carried out static DFT calculations to calculate the activation energy of the ethene methylation reaction over an acidic H-ZSM-5 zeolite. The computed activation energy for the ethene methylation is in excellent agreement with the experimental value.

6.2 General Conclusions

In conclusion, we have shown that advanced atomistic computer simulation techniques based on classical force fields and first-principles methods play a crucial role in understanding the properties of inorganic and highly-porous solid-state materials, such as oxides, silicate minerals and zeolitic materials. Materials modelling provides insight into physical and chemical phenomena statically and dynamically at the microscopic level. In this thesis, in particular, we have emphasised the applications of state-of-the-art simulation methods, including lattice statics, quasi-harmonic lattice dynamics, advanced molecular dynamics and metadynamics simulations, in the fields of solid-state geochemistry and heterogeneous chemical catalysis.

Quasi-harmonic lattice dynamics simulations are useful for investigating the temperature dependence of the defect formation free-energies in oxide and metallic crystals and their finite-size clusters. Lattice statics calculations are helpful for studying the energetics and behaviour of the incorporated trace elements in oxides and silicates and investigating the critical limitations of the use of widely-used simple lattice strain models to explain the trace-element partitioning in minerals and melts. Molecular dynamics simulations are beneficial for examining the temperature variation of the self-diffusivity or self-diffusion rates of small guest molecules in porous zeolitic frameworks. Molecular dynamics can also be used to observe the negative thermal expansion of zeolites. Metadynamics simulations are useful for probing the temperature effects on the free-energy barrier of a specific process, for example, the diffusion of a small molecule through a narrow-ring window in a zeolite material and the proton hopping at a Brønsted acid site in an acidic zeolite. *Ab initio* metadynamics gives the promising potential of studying the temperature dependence of zeolite-catalysed chemical reactions. Based on macro-molecular rate theory (MMRT), the computational techniques used in this work are also helpful for understanding more fully the non-Arrhenius behaviour of activated processes catalysed by solid-state materials by taking the temperature dependence of the enthalpy and entropy of activation due to a negative activation heat capacity into account explicitly. As the concept of molecular rate theory proves useful for understanding the enzyme thermoadaptation and designing better enzymes with the desirable temperature-dependent properties, we hope that our theoretical findings will also help modern researchers gain a more insightful understanding of the properties of complex solid-state materials and design and synthesise novel materials for special purposes.

6.3 Future Work

Several challenging tasks remain for studying the defect thermodynamics in crystalline solids and clusters theoretically. Firstly, although we have shown that the temperature-dependent defect formation energies in solids and clusters are significantly different from the static-limit values, and one should not ignore the temperature effects on these defect properties when performing defect modelling, we have not yet investigated the effects of pressure on those defect energies. Both temperature and pressure effects are crucial in many geochemical processes under extreme conditions, such as at high pressures and temperatures of planetary cores.¹⁸⁰ Furthermore, the effects of temperature and pressure on the defect thermodynamics could be beneficial in making a more systematic

observation of the mineral-melt partitioning behaviour of trace elements under very different conditions computationally. Secondly, the dependence of the calculated quasi-harmonic vibrational entropies and heat capacities on small changes in the magnitude and number of low-frequency vibrational modes needs to be examined more thoroughly, *e.g.*, through the vibrational density of states analysis. Finally, apart from the structural and energetic properties of the defect formation in solids, other quantum mechanical properties, for instance, electronic structures and spectroscopic properties, must also be examined comprehensively.

The natural systems involving the partitioning process of trace elements between minerals and melts are far more complex than the computational models we have used to study the trace-element partitioning behaviour so far. Furthermore, existing simple models used to explain the trace-element partitioning behaviour, *e.g.*, the lattice strain model of Blundy and Wood,³³ are found to be inadequate and oversimplified due to many reasons, *e.g.*, the description of lattice strains is incomplete and the nature of the melt species is not taken into account explicitly. Therefore, further improvements to the underlying theoretical frameworks and computational models are needed. Firstly, we have studied only a few examples of many possible charge-compensating mechanisms for heterovalent substitutions in minerals. Other possibilities must also be explored. Several previous studies, *e.g.*, Purton *et al.*,³¹ used mainly classical simulation techniques to model heterovalent substitutions through various charge-compensating mechanisms. On the other hand, quantum mechanical simulations for the other compensation possibilities may reveal more insightful results since the lattice response to strains depends greatly on the local environment and local ordering (see, *e.g.*, van Westrenen *et al.*^{251,285}). Secondly, an explicit account of the variation of cation radii could improve the application of the Onuma diagrams and the lattice strain model of Blundy and Wood³³ in describing the trace-element partitioning in minerals and melts.¹⁸² Lastly, direct simulation techniques based on Monte Carlo (MC) methods outlined in, *e.g.*, Lavrentiev *et al.*²⁸⁷ and Allan and co-workers,⁴⁰⁸ could potentially be extended to model the heterovalent trace-element partitioning more realistically.

We also need to extend our work to explore the origins of the non-Arrhenius behaviour of the rates of activated processes catalysed by zeolitic materials and other solid-state catalysts computationally. For instance, metadynamics simulations can directly and straightforwardly be used to investigate the temperature variation of the free-energy barrier of the Mg^{2+} vacancy migration in MgO instead of running multiple series of calculations using the zero static internal stress approximation⁸⁵ and quasi-harmonic

lattice dynamics. For investigating the temperature dependence of the self-diffusion rates of small molecules in zeolites or free-energy of activation of the diffusion of a small molecule through a zeolite window, other various effects, such as the type of the zeolitic frameworks, the framework and ring composition, the number (or loading degree) of guest molecules, and so on, also need to be considered. Furthermore, as *ab initio* metadynamics are computationally expensive for calculating the temperature-dependent activation free energy of a zeolite-catalysed reaction, we must seek other computationally cheaper methods to perform such calculations. The computer simulation techniques based on the hybrid quantum mechanical/molecular mechanical (QM/MM) (see, *e.g.*, Metz *et al.*⁴⁰⁹) and density functional based tight-binding (DFTB) (see, *e.g.*, Spiegelman *et al.*⁴¹⁰) methods may offer access to comparably accurate results and the much faster computation compared to purely *ab initio* simulations. The concept of MMRT has been proved very useful for understanding enzyme thermoadaptation and designing better enzymes with the desirable temperature-dependent properties.^{43,44} As we have shown that zeolite frameworks share some common catalytic features of enzymes and they can be viewed as rigid variants of enzymes, we hope that a more insightful understanding of the non-Arrhenius behaviour of zeolite-catalysed reaction rates will help researchers design and synthesise novel zeolitic materials with tunable temperature-dependent properties for specific uses.

BIBLIOGRAPHY

- [1] S. M. Woodley and C. R. A. Catlow, *Nat. Mater.*, 2008, **7**, 937–946.
- [2] R. Dovesi, B. Civalleri, C. Roetti, V. R. Saunders and R. Orlando, *Rev. Comput. Chem.*, 2005, **21**, 1–125.
- [3] J. H. Harding, *Rep. Prog. Phys.*, 1990, **53**, 1403–1466.
- [4] T. Bredow, R. Dronskowski, H. Ebert and K. Jug, *Prog. Solid State Chem.*, 2009, **37**, 70–80.
- [5] H. Jónsson, *Proc. Natl. Acad. Sci.*, 2011, **108**, 944–949.
- [6] A. Rimola, D. Costa, M. Sodupe, J.-F. Lambert and P. Ugliengo, *Chem. Rev.*, 2013, **113**, 4216–4313.
- [7] A. J. O'Malley and C. R. A. Catlow, *Phys. Chem. Chem. Phys.*, 2015, **17**, 1943–1948.
- [8] A. Jentys, R. W. Grimes, J. D. Gale and C. R. A. Catlow, *J. Phys. Chem.*, 1993, **97**, 13535–13538.
- [9] S. T. Bromley, G. Sankar, C. R. A. Catlow, T. Maschmeyer, B. F. G. Johnson and J. M. Thomas, *Chem. Phys. Lett.*, 2001, **340**, 524–530.
- [10] N. L. Allan and W. C. Mackrodt, *Philos. Mag. B*, 1994, **69**, 871–878.
- [11] N. L. Allan, in *Chemical Thermodynamics of Materials: Macroscopic and Microscopic Aspects*, ed. S. Stølen and T. Grande, John Wiley & Sons, 2004, ch. 11, pp. 337–376.
- [12] R. J. D. Tilley, *Defects in Solids*, John Wiley & Sons, Inc., New Jersey, 2008, p. 529.
- [13] A. M. Stoneham, *Theory of Defects in Solids: Electronic Structure of Defects in Insulators and Semiconductors*, Clarendon Press, Oxford, 1975, p. 955.

- [14] *Theory of Defects in Semiconductors*, ed. D. A. Drabold and S. K. Estreicher, Springer-Verlag Berlin, Heidelberg, 2007, p. 286.
- [15] R. A. Evarestov, *Quantum Chemistry of Solids: LCAO Treatment of Crystals and Nanostructures*, Springer-Verlag Berlin, Heidelberg, 2nd edn., 2012, p. 734.
- [16] R. Rurali, M. Palummo and X. Cartoixa, in *Theoretical Aspects of Point Defects in Semiconductor Nanowires*, Springer Singapore, Singapore, 2021, pp. 349–367.
- [17] A. Alkauskas, P. Broqvist and A. Pasquarello, *Phys. Status Solidi B*, 2011, **248**, 775–789.
- [18] C. Freysoldt, B. Grabowski, T. Hickel, J. Neugebauer, G. Kresse, A. Janotti and C. G. Van De Walle, *Rev. Mod. Phys.*, 2014, **86**, 253–305.
- [19] A. Alkauskas, M. D. McCluskey and C. G. Van De Walle, *J. Appl. Phys.*, 2016, **119**, 181101.
- [20] C. E. Dreyer, A. Alkauskas, J. L. Lyons, A. Janotti and C. G. Van De Walle, *Annu. Rev. Mater. Res.*, 2018, **48**, 1–26.
- [21] F. Oba and Y. Kumagai, *Appl. Phys. Express*, 2018, **11**, 60101.
- [22] G. R. Schleder, A. C. M. Padilha, C. M. Acosta, M. Costa and A. Fazzio, *JPhys Mater.*, 2019, **2**, 032001.
- [23] J. C. M. Madrid and K. K. Ghuman, *Adv. Phys.: X*, 2021, **6**, 1848458.
- [24] A. Goyal, P. Gorai, H. Peng, S. Lany and V. Stevanović, *Comput. Mater. Sci.*, 2017, **130**, 1–9.
- [25] D. Broberg, B. Medasani, N. E. R. Zimmermann, G. Yu, A. Canning, M. Haranczyk, M. Asta and G. Hautier, *Comput. Phys. Commun.*, 2018, **226**, 165–179.
- [26] J.-P. Correa-Baena, K. Hippalgaonkar, J. van Duren, S. Jaffer, V. R. Chandrasekhar, V. Stevanovic, C. Wadia, S. Guha and T. Buonassisi, *Joule*, 2018, **2**, 1410–1420.
- [27] V. Wang, N. Xu, J.-C. Liu, G. Tang and W.-T. Geng, *Comput. Phys. Commun.*, 2021, **267**, 108033.
- [28] J. H. Harding, *Physica B+C*, 1985, **131**, 13–26.
- [29] J. D. Blundy and B. J. Wood, *Earth Planet. Sci. Lett.*, 2003, **210**, 383–397.

- [30] J. A. Purton, N. L. Allan, J. D. Blundy and E. A. Wasserman, *Geochim. Cosmochim. Acta*, 1996, **60**, 4977–4987.
- [31] J. A. Purton, N. L. Allan and J. D. Blundy, *Geochim. Cosmochim. Acta*, 1997, **61**, 3927–3936.
- [32] N. Onuma, H. Higuchi, H. Wakita and H. Nagasawa, *Earth Planet. Sci. Lett.*, 1968, **5**, 47–51.
- [33] J. D. Blundy and B. J. Wood, *Nature*, 1994, **372**, 452–454.
- [34] J. C. Brice, *J. Cryst. Growth*, 1975, **28**, 249–253.
- [35] G. Ertl, *Angew. Chem., Int. Ed.*, 2009, **48**, 6600–6606.
- [36] K. J. Laidler, *Chemical Kinetics*, Harper & Row, New York, 3rd edn., 1987, p. 531.
- [37] S. Arrhenius, *Z. Phys. Chem.*, 1889, **4U**, 226–248.
- [38] V. L. Arcus, E. J. Prentice, J. K. Hobbs, A. J. Mulholland, M. W. van der Kamp, C. R. Pudney, E. J. Parker and L. A. Schipper, *Biochemistry*, 2016, **55**, 1681–1688.
- [39] J. K. Hobbs, W. Jiao, A. D. Easter, E. J. Parker, L. A. Schipper and V. L. Arcus, *ACS Chem. Biol.*, 2013, **8**, 2388–2393.
- [40] M. W. van der Kamp, E. J. Prentice, K. L. Kraakman, M. Connolly, A. J. Mulholland and V. L. Arcus, *Nat. Commun.*, 2018, **9**, 1177.
- [41] H. B. L. Jones, R. M. Crean, C. Matthews, A. B. Troya, M. J. Danson, S. D. Bull, V. L. Arcus, M. W. van der Kamp and C. R. Pudney, *ACS Catal.*, 2018, **8**, 5340–5349.
- [42] S. D. Winter, H. B. L. Jones, D. M. Rășădean, R. M. Crean, M. J. Danson, G. D. Pantoș, G. Katona, E. Prentice, V. L. Arcus, M. W. van der Kamp and C. R. Pudney, *ACS Catal.*, 2021, **11**, 14854–14863.
- [43] H. A. Bunzel, H. Kries, L. Marchetti, C. Zeymer, P. R. E. Mittl, A. J. Mulholland and D. Hilvert, *J. Am. Chem. Soc.*, 2019, **141**, 11745–11748.
- [44] H. A. Bunzel, J. L. R. Anderson and A. J. Mulholland, *Curr. Opin. Struct. Biol.*, 2021, **67**, 212–218.

- [45] R. A. van Santen and C. Liu, in *Modelling and Simulation in the Science of Micro- and Meso-Porous Materials*, ed. C. R. A. Catlow, V. Van Speybroeck and R. A. van Santen, Elsevier, 2018, pp. 151–188.
- [46] E. Roduner, *Chem. Soc. Rev.*, 2014, **43**, 8226–8239.
- [47] R. Bermejo-Deval, R. S. Assary, E. Nikolla, M. Moliner, Y. Román-Leshkov, S.-J. Hwang, A. Palsdottir, D. Silverman, R. F. Lobo, L. A. Curtiss and M. E. Davis, *Proc. Natl. Acad. Sci.*, 2012, **109**, 9727–9732.
- [48] E. M. Gallego, C. Paris, A. Cantín, M. Moliner and A. Corma, *Chem. Sci.*, 2019, **10**, 8009–8015.
- [49] J. H. Yun and R. F. Lobo, *J. Catal.*, 2014, **312**, 263–270.
- [50] J. Kryca, P. J. Jodłowski, M. Iwaniszyn, B. Gil, M. Sitarz, A. Kołodziej, T. Łojewska and J. Łojewska, *Catal. Today*, 2016, **268**, 142–149.
- [51] H. Kubota, C. Liu, T. Toyao, Z. Maeno, M. Ogura, N. Nakazawa, S. Inagaki, Y. Kubota and K. Shimizu, *ACS Catal.*, 2020, **10**, 2334–2344.
- [52] F. Gao, J. H. Kwak, J. Szanyi and C. H. F. Peden, *Top. Catal.*, 2013, **56**, 1441–1459.
- [53] F. Gao, N. M. Washton, Y. Wang, M. Kollár, J. Szanyi and C. H. F. Peden, *J. Catal.*, 2015, **331**, 25–38.
- [54] S. Li, Y. Zheng, F. Gao, J. Szanyi and W. F. Schneider, *ACS Catal.*, 2017, **7**, 5087–5096.
- [55] B. Modén, P. Da Costa, B. Fonfé, D. K. Lee and E. Iglesia, *J. Catal.*, 2002, **209**, 75–86.
- [56] D. K. Lee, *Korean J. Chem. Eng.*, 2006, **23**, 547–554.
- [57] P. Xie, T. Pu, G. Aranovich, J. Guo, M. Donohue, A. Kulkarni and C. Wang, *Nat. Catal.*, 2021, **4**, 144–156.
- [58] A. M. Martin, J. K. Chen, V. T. John and D. B. Dadyburjor, *Ind. Eng. Chem. Res.*, 1989, **28**, 1613–1618.
- [59] F. Gao, E. D. Walter, M. Kollar, Y. Wang, J. Szanyi and C. H. F. Peden, *J. Catal.*, 2014, **319**, 1–14.

-
- [60] C. R. A. Catlow and W. C. Mackrodt, in *Theory of simulation methods for lattice and defect energy calculations in crystals*, Springer Berlin Heidelberg, Berlin, Heidelberg, 1982, pp. 1–20.
- [61] M. B. Taylor, G. D. Barrera, N. L. Allan, T. H. K. Barron and W. C. Mackrodt, *Faraday Discuss.*, 1997, **106**, 377–387.
- [62] C. R. A. Catlow, C. M. Freeman, B. Vessal, S. M. Tomlinson and M. Leslie, *J. Chem. Soc., Faraday Trans.*, 1991, **87**, 1947–1950.
- [63] H. Jobic and D. N. Theodorou, *Microporous Mesoporous Mater.*, 2007, **102**, 21–50.
- [64] A. J. O'Malley, V. García Sakai, I. P. Silverwood, N. Dimitratos, S. F. Parker and C. R. A. Catlow, *Phys. Chem. Chem. Phys.*, 2016, **18**, 17294–17302.
- [65] A. R. Leach, *Molecular Modelling: Principles and Applications*, Prentice Hall, 2001.
- [66] C. J. Cramer, *Essentials of Computational Chemistry: Theories and Models*, Wiley, 2005.
- [67] F. Jensen, *Introduction to Computational Chemistry*, Wiley, 2017.
- [68] J. Harvey, *Computational Chemistry*, Oxford University Press, 2018.
- [69] C. R. A. Catlow, *Computer Modeling in Inorganic Crystallography*, Elsevier Science, 1997.
- [70] *Computer Simulation of Materials at Atomic Level*, ed. P. Deák, T. Frauenheim and M. R. Pederson, Wiley-VCH, 2000.
- [71] R. Dronskowski and R. Hoffmann, *Computational Chemistry of Solid State Materials: A Guide for Materials Scientists, Chemists, Physicists and others*, Wiley, 2006.
- [72] A. P. Sutton, *Electronic Structure of Materials*, Clarendon Press, Oxford, 1993.
- [73] B. G. Dick and A. W. Overhauser, *Phys. Rev.*, 1958, **112**, 90.
- [74] G. V. Lewis and C. R. A. Catlow, *J. Phys. C: Solid State Phys.*, 1985, **18**, 1149.
- [75] T. S. Bush, J. D. Gale, C. R. A. Catlow and P. D. Battle, *J. Mater. Chem.*, 1994, **4**, 831–837.

- [76] H. B. Schlegel, *Wiley Interdiscip. Rev.: Comput. Mol. Sci.*, 2011, **1**, 790–809.
- [77] T. H. Barron, T. G. Gibbons and R. W. Munn, *J. Phys. C: Solid State Phys.*, 1971, **4**, 2805–2821.
- [78] T. G. Gibbons, *Phys. Rev. B*, 1973, **7**, 1410–1419.
- [79] D. C. Wallace, *Thermodynamics of Crystals*, John Wiley & Sons, New York, 1972, p. 484.
- [80] D. J. Chadi and M. L. Cohen, *Phys. Rev. B*, 1973, **8**, 5747–5753.
- [81] A. B. Pippard, *Elements of Classical Thermodynamics: For Advanced Students of Physics*, Cambridge University Press, Cambridge, 1957, p. 176.
- [82] C. R. A. Catlow, M. Dixon and W. C. Mackrodt, in *Interionic potentials in ionic solids*, Springer Berlin Heidelberg, Berlin, Heidelberg, 1982, pp. 130–161.
- [83] T. H. K. Barron and K. J. Rogers, *Mol. Simul.*, 1989, **4**, 27–35.
- [84] L. N. Kantorovich, *Phys. Rev. B*, 1995, **51**, 3520–3534.
- [85] N. L. Allan, T. H. K. Barren and J. A. O. Bruno, *J. Chem. Phys.*, 1996, **105**, 8300–8303.
- [86] G. W. Watson, P. Tschaufeser, A. Wall, R. A. Jackson and S. C. Parker, in *Computer Modeling in Inorganic Crystallography*, ed. C. R. A. Catlow, Academic Press, London, 1997, pp. 55–81.
- [87] N. L. Allan, M. Braithwaite, D. L. Cooper, W. C. Mackrodt and S. C. Wright, *J. Chem. Phys.*, 1991, **95**, 6792–6799.
- [88] N. L. Allan, M. Braithwaite, D. L. Cooper, B. Petch and W. C. MacKrodt, *J. Chem. Soc., Faraday Trans.*, 1993, **89**, 4369–4374.
- [89] G. D. Barrera, M. B. Taylor, N. L. Allan, T. H. K. Barron, L. N. Kantorovich and W. C. Mackrodt, *J. Chem. Phys.*, 1997, **107**, 4337–4344.
- [90] M. B. Taylor, G. D. Barrera, N. L. Allan, T. H. K. Barron and W. C. Mackrodt, *Comput. Phys. Commun.*, 1998, **109**, 135–143.
- [91] J. D. Gale and A. L. Rohl, *Mol. Simul.*, 2003, **29**, 291–341.

- [92] B. J. Alder and T. E. Wainwright, *J. Chem. Phys.*, 1959, **31**, 459–466.
- [93] D. Frenkel and B. Smit, *Understanding Molecular Simulation: From Algorithms to Applications*, Elsevier, 2001, vol. 1.
- [94] M. P. Allen and D. J. Tildesley, *Computer Simulation of Liquids*, Oxford University Press, 2017.
- [95] A. Laio and M. Parrinello, *Proc. Natl. Acad. Sci.*, 2002, **99**, 12562–12566.
- [96] A. Barducci, M. Bonomi and M. Parrinello, *Wiley Interdiscip. Rev.: Comput. Mol. Sci.*, 2011, **1**, 826–843.
- [97] G. Bussi and A. Laio, *Nat. Rev. Phys.*, 2020, **2**, 200–212.
- [98] L. Sutto, S. Marsili and F. L. Gervasio, *Wiley Interdiscip. Rev.: Comput. Mol. Sci.*, 2012, **2**, 771–779.
- [99] P. Tiwary and M. Parrinello, *Phys. Rev. Lett.*, 2013, **111**, 230602.
- [100] G. Bussi, A. Laio and P. Tiwary, in *Metadynamics: A Unified Framework for Accelerating Rare Events and Sampling Thermodynamics and Kinetics*, ed. W. Andreoni and S. Yip, Springer International Publishing, Cham, 2020, pp. 565–595.
- [101] P. Schwerdtfeger, *ChemPhysChem*, 2011, **12**, 3143–3155.
- [102] C. Kittel, *Introduction to Solid State Physics*, Wiley, 8th edn., 2004.
- [103] P. Giannozzi, S. Baroni, N. Bonini, M. Calandra, R. Car, C. Cavazzoni, D. Ceresoli, G. L. Chiarotti, M. Cococcioni, I. Dabo, A. Dal Corso, S. de Gironcoli, S. Fabris, G. Fratesi, R. Gebauer, U. Gerstmann, C. Gougoussis, A. Kokalj, M. Lazzeri, L. Martin-Samos, N. Marzari, F. Mauri, R. Mazzarello, S. Paolini, A. Pasquarello, L. Paulatto, C. Sbraccia, S. Scandolo, G. Sclauzero, A. P. Seitsonen, A. Smogunov, P. Umari and R. M. Wentzcovitch, *J. Phys.: Condens. Matter*, 2009, **21**, 395502.
- [104] P. Giannozzi, O. Andreussi, T. Brumme, O. Bunau, M. B. Nardelli, M. Calandra, R. Car, C. Cavazzoni, D. Ceresoli, M. Cococcioni, N. Colonna, I. Carnimeo, A. D. Corso, S. de Gironcoli, P. Delugas, R. A. DiStasio Jr, A. Ferretti, A. Floris, G. Fratesi, G. Fugallo, R. Gebauer, U. Gerstmann, F. Giustino, T. Gorni, J. Jia,

- M. Kawamura, H.-Y. Ko, A. Kokalj, E. Küçükbenli, M. Lazzeri, M. Marsili, N. Marzari, F. Mauri, N. L. Nguyen, H.-V. Nguyen, A. O. de-la Roza, L. Paulatto, S. Poncé, D. Rocca, R. Sabatini, B. Santra, M. Schlipf, A. P. Seitsonen, A. Smogunov, I. Timrov, T. Thonhauser, P. Umari, N. Vast, X. Wu and S. Baroni, *J. Phys.: Condens. Matter*, 2017, **29**, 465901.
- [105] G. Kresse and J. Hafner, *Phys. Rev. B*, 1993, **47**, 558.
- [106] G. Kresse and J. Furthmüller, *Comput. Mater. Sci.*, 1996, **6**, 15–50.
- [107] G. Kresse and J. Furthmüller, *Phys. Rev. B*, 1996, **54**, 11169.
- [108] R. Dovesi, V. R. Saunders, C. Roetti, R. Orlando, C. M. Zicovich-Wilson, F. Pascale, B. Civalleri, K. Doll, N. M. Harrison, I. J. Bush, P. D’Arco, M. Llunell, M. Causà, Y. Noël, L. Maschio, A. Erba, M. Rerat and S. Casassa, *CRYSTAL17 User’s Manual*, University of Torino, Torino, 2017, p. 461.
- [109] R. Dovesi, A. Erba, R. Orlando, C. M. Zicovich-Wilson, B. Civalleri, L. Maschio, M. Rerat, S. Casassa, J. Baima, S. Salustro and B. Kirtman, *Wiley Interdiscip. Rev.: Comput. Mol. Sci.*, 2018, **8**, e1360.
- [110] J. Hutter, M. Iannuzzi, F. Schiffmann and J. VandeVondele, *Wiley Interdiscip. Rev.: Comput. Mol. Sci.*, 2014, **4**, 15–25.
- [111] A. D. Becke, *J. Chem. Phys.*, 2014, **140**, 18A301.
- [112] P. Hohenberg and W. Kohn, *Phys. Rev.*, 1964, **136**, B864.
- [113] W. Kohn and L. J. Sham, *Phys. Rev.*, 1965, **140**, A1133.
- [114] J. P. Perdew, K. Burke and M. Ernzerhof, *Phys. Rev. Lett.*, 1996, **77**, 3865.
- [115] J. P. Perdew, A. Ruzsinszky, G. I. Csonka, O. A. Vydrov, G. E. Scuseria, L. A. Constantin, X. Zhou and K. Burke, *Phys. Rev. Lett.*, 2008, **100**, 136406.
- [116] G. I. Csonka, J. P. Perdew, A. Ruzsinszky, P. H. Philipsen, S. Lebègue, J. Paier, O. A. Vydrov and J. G. Ángyán, *Phys. Rev. B*, 2009, **79**, 155107.
- [117] C. Lee, W. Yang and R. G. Parr, *Phys. Rev. B*, 1988, **37**, 785–789.
- [118] A. D. Becke, *J. Chem. Phys.*, 1993, **98**, 1372–1377.

- [119] P. J. Hasnip, K. Refson, M. I. J. Probert, J. R. Yates, S. J. Clark and C. J. Pickard, *Philos. Trans. Royal Soc. A*, 2014, **372**, 20130270.
- [120] R. M. Martin, *Electronic Structure: Basic Theory and Practical Methods*, Cambridge University Press, 2020.
- [121] G. Prandini, A. Marrazzo, I. E. Castelli, N. Mounet and N. Marzari, *npj Comput. Mater.*, 2018, **4**, 1–13.
- [122] R. Car and M. Parrinello, *Phys. Rev. Lett.*, 1985, **55**, 2471–2474.
- [123] D. Sheppard, R. Terrell and G. Henkelman, *J. Chem. Phys.*, 2008, **128**, 134106.
- [124] J. D. Gale, *J. Phys. Chem. B*, 1998, **102**, 5423–5431.
- [125] N. F. Mott and M. J. Littleton, *Trans. Faraday Soc.*, 1938, **34**, 485–499.
- [126] K. Okhotnikov, T. Charpentier and S. Cadars, *J. Cheminform.*, 2016, **8**, 17.
- [127] N. L. Allan, J. D. Blundy, J. A. Purton, M. Y. Lavrentiev and B. J. Wood, in *Solid Solutions in Silicate and Oxide Systems*, Mineralogical Society of Great Britain and Ireland, 2001, ch. 11, pp. 251–302.
- [128] C. R. A. Catlow, J. Corish, P. W. M. Jacobs and A. B. Lidiard, *J. Phys. C: Solid State Phys.*, 1981, **14**, L121–L125.
- [129] J. Corish, C. R. A. Catlow and P. W. M. Jacobs, *J. Phys., Lett.*, 1981, **42**, 369–372.
- [130] M. J. Gillan, *Philos. Mag. A*, 1981, **43**, 301–312.
- [131] F. A. Kröger and H. J. Vink, in *Solid State Physics*, Elsevier, 1956, vol. 3, pp. 307–435.
- [132] I. T. Todorov, W. Smith, K. Trachenko and M. T. Dove, *J. Mater. Chem.*, 2006, **16**, 1911–1918.
- [133] C. W. Yong, *J. Chem. Inf. Model.*, 2016, **56**, 1405–1409.
- [134] C. W. Yong and I. T. Todorov, *Molecules*, 2017, **23**, 36.
- [135] G. A. Tribello, M. Bonomi, D. Branduardi, C. Camilloni and G. Bussi, *Comput. Phys. Commun.*, 2014, **185**, 604–613.

- [136] K. Momma and F. Izumi, *J. Appl. Crystallogr.*, 2008, **41**, 653–658.
- [137] M. D. Hanwell, D. E. Curtis, D. C. Lonie, T. Vandermeersch, E. Zurek and G. R. Hutchison, *J. Cheminf.*, 2012, **4**, 1–17.
- [138] W. Humphrey, A. Dalke and K. Schulten, *J. Mol. Graphics*, 1996, **14**, 33–38.
- [139] D. Fincham, W. C. MacKrodt and P. J. Mitchell, *J. Phys.: Condens. Matter*, 1994, **6**, 393–404.
- [140] R. M. Fracchia, G. D. Barrera, N. L. Allan, T. H. K. Barron and W. C. Mackrodt, *J. Phys. Chem. Solids*, 1998, **59**, 435–445.
- [141] M. T. Dove, *Introduction to Lattice Dynamics*, Cambridge University Press, 1993.
- [142] A. Stoneham and M. J. Sangster, *Philos. Mag. B*, 1985, **52**, 717–727.
- [143] C. G. Broyden, *IMA J. Appl. Math.*, 1970, **6**, 76–90.
- [144] R. Fletcher, *Comput. J.*, 1970, **13**, 317–322.
- [145] D. Goldfarb, *Math. Comput.*, 1970, **24**, 23–26.
- [146] D. F. Shanno, *Math. Comput.*, 1970, **24**, 647–656.
- [147] T. Kluyver, B. Ragan-Kelley, F. Pérez, B. Granger, M. Bussonnier, J. Frederic, K. Kelley, J. Hamrick, J. Grout, S. Corlay, P. Ivanov, D. Avila, S. Abdalla and C. Willing, *Positioning and Power in Academic Publishing: Players, Agents and Agendas*, 2016, pp. 87 – 90.
- [148] *Anaconda Software Distribution*, 2020, <https://docs.anaconda.com/>.
- [149] S. Zhen and G. J. Davies, *Phys. Status Solidi A*, 1983, **78**, 595–605.
- [150] M. Waldman and A. T. Hagler, *J. Comput. Chem.*, 1993, **14**, 1077–1084.
- [151] M. P. Habas, R. Dovesi and A. Lichanot, *J. Phys.: Condens. Matter*, 1998, **10**, 6897–6909.
- [152] M. I. McCarthy and N. M. Harrison, *Phys. Rev. B*, 1994, **49**, 8574–8582.
- [153] M. D. Towler, N. L. Allan, N. M. Harrison, V. R. Saunders, W. C. Mackrodt and E. Aprà, *Phys. Rev. B*, 1994, **50**, 5041–5054.

- [154] D. R. Gaskell and D. E. Laughlin, *Introduction to the Thermodynamics of Materials*, CRC Press/Taylor & Francis Group, Boca Raton, 2018.
- [155] M. D. Towler, R. I. Hines, N. L. Allan, M. Braithwaite and W. C. Mackrodt, *AIP Conf. Proc.*, 1994, **309**, 129–132.
- [156] J. D. Gale, *J. Chem. Soc., Faraday Trans.*, 1997, **93**, 629–637.
- [157] M. J. Frisch, G. W. Trucks, H. B. Schlegel, G. E. Scuseria, M. A. Robb, J. R. Cheeseman, G. Scalmani, V. Barone, G. A. Petersson, H. Nakatsuji, X. Li, M. Caricato, A. V. Marenich, J. Bloino, B. G. Janesko, R. Gomperts, B. Mennucci, H. P. Hratchian, J. V. Ortiz, A. F. Izmaylov, J. L. Sonnenberg, D. Williams-Young, F. Ding, F. Lipparini, F. Egidi, J. Goings, B. Peng, A. Petrone, T. Henderson, D. Ranasinghe, V. G. Zakrzewski, J. Gao, N. Rega, G. Zheng, W. Liang, M. Hada, M. Ehara, K. Toyota, R. Fukuda, J. Hasegawa, M. Ishida, T. Nakajima, Y. Honda, O. Kitao, H. Nakai, T. Vreven, K. Throssell, J. A. Montgomery, Jr., J. E. Peralta, F. Ogliaro, M. J. Bearpark, J. J. Heyd, E. N. Brothers, K. N. Kudin, V. N. Staroverov, T. A. Keith, R. Kobayashi, J. Normand, K. Raghavachari, A. P. Rendell, J. C. Burant, S. S. Iyengar, J. Tomasi, M. Cossi, J. M. Millam, M. Klene, C. Adamo, R. Cammi, J. W. Ochterski, R. L. Martin, K. Morokuma, O. Farkas, J. B. Foresman and D. J. Fox, *Gaussian 16 Revision C.01*, 2016.
- [158] F. Neese, F. Wennmohs, U. Becker and C. Riplinger, *J. Chem. Phys.*, 2020, **152**, 224108.
- [159] K. Hirata, K. Moriya and Y. Waseda, *J. Mater. Sci.*, 1977, **12**, 838–839.
- [160] R. B. Elo, S. P. Murarka and R. A. Swalin, *J. Phys. Chem. Solids*, 1973, **34**, 97–106.
- [161] P. Haas, F. Tran and P. Blaha, *Phys. Rev. B*, 2009, **79**, 085104.
- [162] G.-X. Zhang, A. M. Reilly, A. Tkatchenko and M. Scheffler, *New J. Phys.*, 2018, **20**, 063020.
- [163] D. Zagorac, K. Doll, J. C. Schön and M. Jansen, *Chem. - Eur. J.*, 2012, **18**, 10929–10936.
- [164] L. Valenzano, Y. Noël, R. Orlando, C. M. Zicovich-Wilson, M. Ferrero and R. Dovesi, *Theor. Chem. Acc.*, 2007, **117**, 991–1000.

- [165] L. Valenzano, F. J. Torres, K. Doll, F. Pascale, C. M. Zicovich-Wilson and R. Dovesi, *Z. Phys. Chem.*, 2006, **220**, 893–912.
- [166] G. Beata, G. Perego and B. Civalleri, *J. Comput. Chem.*, 2019, **40**, 2329–2338.
- [167] O. L. Anderson, D. Isaak and H. Oda, *Rev. Geophys.*, 1992, **30**, 57–90.
- [168] A. Erba, *J. Chem. Phys.*, 2014, **141**, 124115.
- [169] A. Erba, J. Maul, M. De La Pierre and R. Dovesi, *J. Chem. Phys.*, 2015, **142**, 204502.
- [170] A. Erba, J. Maul, R. Demichelis and R. Dovesi, *Phys. Chem. Chem. Phys.*, 2015, **17**, 11670–11677.
- [171] A. Erba, M. Shahrokhi, R. Moradian and R. Dovesi, *J. Chem. Phys.*, 2015, **142**, 044114.
- [172] O. L. Anderson, D. G. Isaak and T. J. Ahrens, *Mineral Physics and Crystallography: A Handbook of Physical Constants*, 1995, **2**, 64–97.
- [173] N. L. Allan, Z. Du, M. Y. Lavrentiev, J. D. Blundy, J. A. Purton and W. van Westrenen, *Phys. Earth Planet. Inter.*, 2003, **139**, 93–111.
- [174] A. De Vita, M. J. Gillan, J. S. Lin, M. C. Payne, I. Štich and L. J. Clarke, *Phys. Rev. B*, 1992, **46**, 12964.
- [175] A. v. Bondi, *J. Phys. Chem.*, 1964, **68**, 441–451.
- [176] R. D. Shannon, *Acta Crystallogr., Sect. A*, 1976, **32**, 751–767.
- [177] N. L. Allan, G. D. Barrera, J. A. Purton, C. E. Sims and M. B. Taylor, *Phys. Chem. Chem. Phys.*, 2000, **2**, 1099–1111.
- [178] R. M. Fracchia, G. D. Barrera, N. L. Allan, T. H. K. Barron and W. C. Mackrodt, *J. Phys. Chem. Solids*, 1998, **59**, 435–445.
- [179] M. B. Taylor, C. E. Sims, G. D. Barrera, N. L. Allan and W. C. Mackrodt, *Phys. Rev. B*, 1999, **59**, 6742–6751.
- [180] K. Valencia, A. De Moya, G. Morard, N. L. Allan and C. Pinilla, *Am. Mineral.*, 2022, **107**, 248–256.

- [181] Z. Du, N. L. Allan, J. D. Blundy, J. A. Purton and R. A. Brooker, *Geochim. Cosmochim. Acta*, 2008, **72**, 554–573.
- [182] B. Dubacq and A. Plunder, *J. Petrol.*, 2018, **59**, 233–256.
- [183] I. T. Todorov, N. L. Allan, M. Y. Lavrentiev, C. L. Freeman, C. E. Mohn and J. A. Purton, *J. Phys.: Condens. Matter*, 2004, **16**, S2751–S2770.
- [184] J. A. Purton, N. L. Allan, M. Y. Lavrentiev, I. T. Todorov and C. L. Freeman, *Chem. Geol.*, 2006, **225**, 176–188.
- [185] V. M. Goldschmidt, *J. Chem. Soc.*, 1937, **140**, 655–673.
- [186] G. Mallmann and H. S. C. O'Neill, *Geochim. Cosmochim. Acta*, 2007, **71**, 2837–2857.
- [187] G. Mallmann and H. S. C. O'Neill, *J. Petrol.*, 2009, **50**, 1765–1794.
- [188] J. A. Van Orman, T. L. Grove and N. Shimizu, *Earth Planet. Sci. Lett.*, 2002, **198**, 93–112.
- [189] C.-T. A. Lee, A. Harbert and W. P. Leeman, *Geochim. Cosmochim. Acta*, 2007, **71**, 481–496.
- [190] J. D. Blundy, T. J. Falloon, B. J. Wood and J. A. Dalton, *J. Geophys. Res.: Solid Earth*, 1995, **100**, 15501–15515.
- [191] J. D. Blundy, *Chem. Geol.*, 1997, **141**, 73–92.
- [192] B. J. Wood and J. D. Blundy, *Contrib. Mineral. Petrol.*, 1997, **129**, 166–181.
- [193] J. D. Blundy, J. A. C. Robinson and B. J. Wood, *Earth Planet. Sci. Lett.*, 1998, **160**, 493–504.
- [194] B. J. Wood, J. D. Blundy and J. A. C. Robinson, *Geochim. Cosmochim. Acta*, 1999, **63**, 1613–1620.
- [195] W. van Westrenen, J. D. Blundy and B. J. Wood, *Am. Mineral.*, 1999, **84**, 838–847.
- [196] J. D. Blundy and J. Dalton, *Contrib. Mineral. Petrol.*, 2000, **139**, 356–371.
- [197] K. M. Law, J. D. Blundy, B. J. Wood and K. V. Ragnarsdottir, *Mineral. Mag.*, 2000, **64**, 651–661.

- [198] E. Hill, B. J. Wood and J. D. Blundy, *Lithos*, 2000, **53**, 203–215.
- [199] T. H. Green, J. D. Blundy, J. Adam and G. M. Yaxley, *Lithos*, 2000, **53**, 165–187.
- [200] W. van Westrenen, J. D. Blundy and B. J. Wood, *Lithos*, 2000, **53**, 189–201.
- [201] B. J. Wood and R. Trigila, *Chem. Geol.*, 2001, **172**, 213–223.
- [202] D. Landwehr, J. D. Blundy, E. M. Chamorro-Perez, E. Hill and B. J. Wood, *Earth Planet. Sci. Lett.*, 2001, **188**, 329–348.
- [203] S. Klemme, J. D. Blundy and B. J. Wood, *Geochim. Cosmochim. Acta*, 2002, **66**, 3109–3123.
- [204] P. McDade, J. D. Blundy and B. J. Wood, *Am. Mineral.*, 2003, **88**, 1825–1831.
- [205] P. McDade, J. D. Blundy and B. J. Wood, *Phys. Earth Planet. Inter.*, 2003, **139**, 129–147.
- [206] S. L. Bennett, J. D. Blundy and T. Elliott, *Geochim. Cosmochim. Acta*, 2004, **68**, 2335–2347.
- [207] D. Frei, A. Liebscher, G. Franz, B. Wunder, S. Klemme and J. D. Blundy, *Contrib. Mineral. Petrol.*, 2009, **157**, 473–490.
- [208] E. Hill, J. D. Blundy and B. J. Wood, *Contrib. Mineral. Petrol.*, 2011, **161**, 423–438.
- [209] S. Mollo, J. D. Blundy, G. Iezzi, P. Scarlato and A. Langone, *Contrib. Mineral. Petrol.*, 2013, **166**, 1633–1654.
- [210] R. Dohmen and J. D. Blundy, *Am. J. Sci.*, 2014, **314**, 1319–1372.
- [211] P. Scarlato, S. Mollo, J. D. Blundy, G. Iezzi and M. Tiepolo, *Bull. Volcanol.*, 2014, **76**, 1–4.
- [212] S. Mollo, F. Forni, O. Bachmann, J. D. Blundy, G. De Astis and P. Scarlato, *Lithos*, 2016, **252**, 160–172.
- [213] S. Mollo, J. D. Blundy, P. Giacomoni, M. Nazzari, P. Scarlato, M. Coltorti, A. Langone and D. Andronico, *Lithos*, 2017, **284**, 447–461.
- [214] B. J. Wood and J. D. Blundy, *Geochim. Cosmochim. Acta*, 2002, **66**, 3647–3656.

- [215] J. D. Blundy and B. J. Wood, *Rev. Mineral. Geochem.*, 2003, **52**, 59–123.
- [216] B. J. Wood and J. D. Blundy, in *Treatise on Geochemistry*, ed. H. D. Holland and K. K. Turekian, Elsevier, Oxford, 2nd edn., 2014, pp. 421–448.
- [217] S. Mollo, J. D. Blundy, P. Scarlato, F. Vetere, F. Holtz, O. Bachmann and M. Gaeta, *Earth-Sci. Rev.*, 2020, **210**, 103351.
- [218] B. B. Jensen, *Geochim. Cosmochim. Acta*, 1973, **37**, 2227–2242.
- [219] E. H. Hauri, T. P. Wagner and T. L. Grove, *Chem. Geol.*, 1994, **117**, 149–166.
- [220] R. Rinaldi, G. Artioli, C. C. Wilson and G. McIntyre, *Phys. Chem. Miner.*, 2000, **27**, 623–629.
- [221] S. A. T. Redfern, G. Artioli, R. Rinaldi, C. M. B. Henderson, K. S. Knight and B. J. Wood, *Phys. Chem. Miner.*, 2000, **27**, 630–637.
- [222] P. Beattie, *Chem. Geol.*, 1994, **117**, 57–71.
- [223] J. D. Blundy, B. J. Wood and A. Davies, *Geochim. Cosmochim. Acta*, 1996, **60**, 359–364.
- [224] S. A. Morse, *Am. Mineral.*, 2015, **100**, 1021–1032.
- [225] J. A. Purton, J. D. Blundy and N. L. Allan, *Am. Mineral.*, 2000, **85**, 1087–1091.
- [226] P. Beattie, M. Drake, J. Jones, W. Leeman, J. Longhi, G. McKay, R. Nielsen, H. Palme, D. Shaw, E. Takahashi *et al.*, *Geochim. Cosmochim. Acta*, 1993, **57**, 1605–1606.
- [227] S. A. T. Redfern, C. M. B. Henderson, K. S. Knight and B. J. Wood, *Eur. J. Mineral.*, 1997, **9**, 287–300.
- [228] M. M. Hirschmann and M. S. Ghiorso, *Geochim. Cosmochim. Acta*, 1994, **58**, 4109–4126.
- [229] J. M. Brenan, H. F. Shaw, F. J. Ryerson and D. L. Phinney, *Earth Planet. Sci. Lett.*, 1995, **135**, 1–11.
- [230] T. LaTourrette, R. L. Hervig and J. R. Holloway, *Earth Planet. Sci. Lett.*, 1995, **135**, 13–30.

- [231] J. Adam and T. Green, *Eur. J. Mineral.*, 2003, **15**, 831–841.
- [232] J. Adam and T. Green, *Contrib. Mineral. Petrol.*, 2006, **152**, 1–17.
- [233] L. Fedele, A. Zanetti, V. Morra, M. Lustrino, L. Melluso and R. Vannucci, *Contrib. Mineral. Petrol.*, 2009, **158**, 337–356.
- [234] M. J. Severs, J. S. Beard, L. Fedele, J. M. Hanchar, S. R. Mutchler and R. J. Bodnar, *Geochim. Cosmochim. Acta*, 2009, **73**, 2123–2141.
- [235] Y. Liang, C. Sun and L. Yao, *Geochim. Cosmochim. Acta*, 2013, **102**, 246–260.
- [236] N. Dygert, Y. Liang, C. Sun and P. Hess, *Geochim. Cosmochim. Acta*, 2014, **132**, 170–186.
- [237] H. Nagasawa, *Science*, 1966, **152**, 767–769.
- [238] S. Ma and C. S. J. Shaw, *J. Petrol.*, 2021, **62**, 1–27.
- [239] C. Dalou, J. Boulon, K. T. Koga, R. Dalou and R. L. Dennen, *Comput. Geosci.*, 2018, **117**, 49–56.
- [240] C. Sun and Y. Liang, *Contrib. Mineral. Petrol.*, 2012, **163**, 807–823.
- [241] C. Sun and Y. Liang, *Chem. Geol.*, 2013, **358**, 23–36.
- [242] L. Levien, D. J. Weidner and C. T. Prewitt, *Phys. Chem. Miner.*, 1979, **4**, 105–113.
- [243] S.-i. Karato, *Am. Mineral.*, 2016, **101**, 2577–2593.
- [244] J. D. Eshelby, *Philos. Trans. R. Soc., A*, 1951, **244**, 87–112.
- [245] J. D. Eshelby, *J. Appl. Phys.*, 1954, **25**, 255–261.
- [246] J. D. Eshelby, in *Solid State Physics*, Elsevier, 1956, vol. 3, pp. 79–144.
- [247] M. A. Carpenter, R. E. A. McKnight, C. J. Howard, Q. Zhou, B. J. Kennedy and K. S. Knight, *Phys. Rev. B*, 2009, **80**, 214101.
- [248] R. M. Hazen and L. W. Finger, *J. Geophys. Res.: Solid Earth*, 1979, **84**, 6723–6728.
- [249] J. M. Hanchar and W. van Westrenen, *Elements*, 2007, **3**, 37–42.
- [250] W. van Westrenen, N. L. Allan, J. D. Blundy, J. A. Purton and B. J. Wood, *Geochim. Cosmochim. Acta*, 2000, **64**, 1629–1639.

- [251] W. van Westrenen, N. L. Allan, J. D. Blundy, M. Y. Lavrentiev, B. R. Lucas and J. A. Purton, *Phys. Chem. Miner.*, 2003, **30**, 217–229.
- [252] B. J. Wood and J. D. Blundy, *Earth Planet. Sci. Lett.*, 2001, **188**, 59–71.
- [253] A. Bosenick, M. T. Dove and C. A. Geiger, *Phys. Chem. Miner.*, 2000, **27**, 398–418.
- [254] A. Corgne, N. L. Allan and B. J. Wood, *Phys. Earth Planet. Inter.*, 2003, **139**, 113–127.
- [255] S. C. Kohn and P. F. Schofield, *Chem. Geol.*, 1994, **117**, 73–87.
- [256] W. L. Jaeger and M. J. Drake, *Geochim. Cosmochim. Acta*, 2000, **64**, 3887–3895.
- [257] H. S. O'Neill and S. M. Eggins, *Chem. Geol.*, 2002, **186**, 151–181.
- [258] B. O. Mysen and E. V. Dubinsky, *Geochim. Cosmochim. Acta*, 2004, **68**, 1617–1633.
- [259] S. Prowatke and S. Klemme, *Geochim. Cosmochim. Acta*, 2005, **69**, 695–709.
- [260] S. A. Miller, P. D. Asimow and D. S. Burnett, *Geochim. Cosmochim. Acta*, 2006, **70**, 4258–4274.
- [261] C. Beyer, J. Berndt, S. Tappe and S. Klemme, *Chem. Geol.*, 2013, **353**, 132–139.
- [262] A. D. Burnham and H. S. O'Neill, *Chem. Geol.*, 2016, **442**, 139–147.
- [263] N. L. Allan and W. C. Mackrodt, *Philos. Mag. A*, 1988, **58**, 555–569.
- [264] N. L. Allan and W. C. Mackrodt, *J. Chem. Soc., Faraday Trans. 2*, 1989, **85**, 385–405.
- [265] N. L. Allan and W. C. Mackrodt, *J. Am. Ceram. Soc.*, 1990, **73**, 3175–3184.
- [266] N. L. Allan and W. C. Mackrodt, in *Advances in Solid State Chemistry*, JAI (London), 1992, pp. 219–268.
- [267] K. Lejaeghere, G. Bihlmayer, T. Björkman, P. Blaha, S. Blügel, V. Blum, D. Caliste, I. E. Castelli, S. J. Clark, A. Dal Corso *et al.*, *Science*, 2016, **351**, aad3000.
- [268] A. Dal Corso, *thermo_pw version 1.6.0*, 2022, https://dalcorso.github.io/thermo_pw.
- [269] H. J. Monkhorst and J. D. Pack, *Phys. Rev. B*, 1976, **13**, 5188.

- [270] G. Fiquet, P. Richet and G. Montagnac, *Phys. Chem. Miner.*, 1999, **27**, 103–111.
- [271] M. Cameron, S. Sueno, C. T. Prewitt and J. J. Papike, *Am. Mineral.*, 1973, **58**, 594–618.
- [272] R. Hill, *Proc. Phys. Soc., London, Sect. A*, 1952, **65**, 349–354.
- [273] Z. P. Chang and E. K. Graham, *J. Phys. Chem. Solids*, 1977, **38**, 1355–1362.
- [274] H. E. Hite and R. J. Kearney, *J. Appl. Phys.*, 1967, **38**, 5424–5425.
- [275] K. S. Aleksandrov, T. V. Ryzhova and B. P. Belikov, *Crystallogr. Rep.*, 1963, **8**, 738–741.
- [276] L. Sang, C. B. Vanpeteghem, S. V. Sinogeikin and J. D. Bass, *Am. Mineral.*, 2011, **96**, 224–227.
- [277] R. D. T. Shannon and C. T. Prewitt, *Acta Crystallogr., Sect. B: Struct. Crystallogr. Cryst. Chem.*, 1969, **25**, 925–946.
- [278] L. E. Orgel, *An Introduction to Transition-metal Chemistry: Ligand-field Theory*, Methuen, 1960.
- [279] B. N. Figgis and M. A. Hitchman, *Ligand Field Theory and Its Applications*, Wiley, 2000.
- [280] L. Levien and C. T. Prewitt, *Am. Mineral.*, 1981, **66**, 315–323.
- [281] G. H. Aylward and T. J. V. Findlay, *Datensammlung Chemie in SI-Einheiten*, John Wiley & Sons, 2014.
- [282] A. B. Lidiard, *J. Chem. Soc., Faraday Trans. 2*, 1989, **85**, 341–349.
- [283] B. O. Mysen, *Chem. Geol.*, 2004, **213**, 1–16.
- [284] C. Pinilla, S. A. Davis, T. B. Scott, N. L. Allan and J. D. Blundy, *Earth Planet. Sci. Lett.*, 2012, **319**, 287–294.
- [285] W. van Westrenen, N. L. Allan, J. D. Blundy, M. Y. Lavrentiev, B. R. Lucas and J. A. Purton, *Chem. Commun.*, 2003, 786–787.
- [286] M. Kanzaki, in *Physics Meets Mineralogy: Condensed Matter Physics in the Geosciences*, ed. H. Aoki, Y. Syono and R. J. Hemley, Cambridge University Press, Cambridge, 2000, p. 381–390.

- [287] M. Y. Lavrentiev, N. L. Allan and J. A. Purton, *Phys. Chem. Chem. Phys.*, 2003, **5**, 2190–2196.
- [288] N. L. Allan, G. D. Barrera, M. Y. Lavrentiev, I. T. Todorov and J. A. Purton, *J. Mater. Chem.*, 2001, **11**, 63–68.
- [289] M. Y. Lavrentiev, N. L. Allan, G. D. Barrera and J. A. Purton, *J. Phys. Chem. B*, 2001, **105**, 3594–3599.
- [290] H. Eyring, *Chem. Rev.*, 1935, **17**, 65–77.
- [291] H. Eyring, *J. Chem. Phys.*, 1935, **3**, 107–115.
- [292] D. R. Glowacki, J. N. Harvey and A. J. Mulholland, *Nat. Chem.*, 2012, **4**, 169–176.
- [293] D. G. Truhlar and B. C. Garrett, *Annu. Rev. Phys. Chem.*, 1984, **35**, 159–189.
- [294] R. M. Daniel and M. J. Danson, *Trends Biochem. Sci.*, 2010, **35**, 584–591.
- [295] S. Roy, P. Schopf and A. Warshel, *J. Phys. Chem. B*, 2017, **121**, 6520–6526.
- [296] J. L. Kavanau, *J. Gen. Physiol.*, 1950, **34**, 193–209.
- [297] L. A. Schipper, J. K. Hobbs, S. Rutledge and V. L. Arcus, *Glob. Change Biol.*, 2014, **20**, 3578–3586.
- [298] V. L. Arcus and A. J. Mulholland, *Annu. Rev. Biophys.*, 2020, **49**, 163–180.
- [299] G. Feller and C. Gerday, *Nat. Rev. Microbiol.*, 2003, **1**, 200–208.
- [300] M. E. Peterson, R. Eisinger, M. J. Danson, A. Spence and R. M. Daniel, *J. Biol. Chem.*, 2004, **279**, 20717–20722.
- [301] M. E. Peterson, R. M. Daniel, M. J. Danson and R. Eisinger, *Biochem. J.*, 2007, **402**, 331–337.
- [302] A. Rohatgi, *Webplotdigitizer: Version 4.4*, 2020, <https://automeris.io/WebPlotDigitizer>.
- [303] G. I. Makhatadze, *Biophys. Chem.*, 1998, **71**, 133–156.
- [304] R. Wolfenden and M. J. Snider, *Acc. Chem. Res.*, 2001, **34**, 938–945.
- [305] R. E. Amaro and A. J. Mulholland, *Nat. Rev. Chem.*, 2018, **2**, 0148.

- [306] D. J. Huggins, P. C. Biggin, M. A. Dämgen, J. W. Essex, S. A. Harris, R. H. Henchman, S. Khalid, A. Kuzmanic, C. A. Laughton, J. Michel, A. J. Mulholland, E. Rosta, M. S. P. Sansom and M. W. van der Kamp, *Wiley Interdiscip. Rev.: Comput. Mol. Sci.*, 2019, **9**, e1393.
- [307] A. I. Iorgu, N. J. Baxter, M. J. Cliff, C. Levy, J. P. Waltho, S. Hay and N. S. Scrutton, *ACS Catal.*, 2018, **8**, 11589–11599.
- [308] S. Akanuma, M. Bessho, H. Kimura, R. Furukawa, S.-i. Yokobori and A. Yamagishi, *Sci. Rep.*, 2019, **9**, 9346.
- [309] J. Sočan, G. V. Isaksen, B. O. Brandsdal and J. Åqvist, *Sci. Rep.*, 2019, **9**, 19147.
- [310] R. Wolfenden, *J. Biol. Chem.*, 2014, **289**, 30198–30204.
- [311] J. Åqvist, G. V. Isaksen and B. O. Brandsdal, *Nat. Rev. Chem.*, 2017, **1**, 0051.
- [312] S. C. L. Kamerlin and A. Warshel, *Proteins: Struct., Funct., Bioinf.*, 2010, **78**, 1339–1375.
- [313] V. L. Arcus, M. W. van der Kamp, C. R. Pudney and A. J. Mulholland, *Curr. Opin. Struct. Biol.*, 2020, **65**, 96–101.
- [314] V. Vaissier Welborn and T. Head-Gordon, *Chem. Rev.*, 2019, **119**, 6613–6630.
- [315] R. M. Crean, J. M. Gardner and S. C. L. Kamerlin, *J. Am. Chem. Soc.*, 2020, **142**, 11324–11342.
- [316] G. Yang, C. M. Miton and N. Tokuriki, *Protein Sci.*, 2020, **29**, 1724–1747.
- [317] J. A. Moulijn, P. W. N. M. van Leeuwen and R. A. van Santen, in *Catalysis*, Elsevier, 1993, vol. 79 of Studies in Surface Science and Catalysis, pp. 69–86.
- [318] V. Van Speybroeck, K. De Wispelaere, J. Van der Mynsbrugge, M. Vandichel, K. Hemelsoet and M. Waroquier, *Chem. Soc. Rev.*, 2014, **43**, 7326–7357.
- [319] F.-X. Coudert, A. Boutin, M. Jeffroy, C. Mellot-Draznieks and A. H. Fuchs, *ChemPhysChem*, 2011, **12**, 247–258.
- [320] J. B. Parise and E. Prince, *Mater. Res. Bull.*, 1983, **18**, 841–852.
- [321] Y. Lee, J. A. Hriljac, T. Vogt, J. B. Parise, M. J. Edmondson, P. A. Anderson, D. R. Corbin and T. Nagai, *J. Am. Chem. Soc.*, 2001, **123**, 8418–8419.

- [322] Y. Lee, T. Vogt, J. A. Hriljac, J. B. Parise and G. Artioli, *J. Am. Chem. Soc.*, 2002, **124**, 5466–5475.
- [323] L. A. Villaescusa, P. Lightfoot, S. J. Teat and R. E. Morris, *J. Am. Chem. Soc.*, 2001, **123**, 5453–5459.
- [324] G. D. Barrera, J. A. O. Bruno, T. H. K. Barron and N. L. Allan, *J. Phys.: Condens. Matter*, 2005, **17**, R217–R252.
- [325] W. Miller, C. W. Smith, D. S. Mackenzie and K. E. Evans, *J. Mater. Sci.*, 2009, **44**, 5441–5451.
- [326] S. M. Auerbach, *Int. Rev. Phys. Chem.*, 2000, **19**, 155–198.
- [327] F. Leroy, B. Rousseau and A. H. Fuchs, *Phys. Chem. Chem. Phys.*, 2004, **6**, 775–783.
- [328] A. F. Combariza, G. Sastre and A. Corma, *J. Phys. Chem. C*, 2009, **113**, 11246–11253.
- [329] N. E. R. Zimmermann, S. Jakobtorweihen, E. Beerdsen, B. Smit and F. J. Keil, *J. Phys. Chem. C*, 2010, **114**, 15546–15546.
- [330] F. Jousse, D. P. Vercauteren and S. M. Auerbach, *J. Phys. Chem. B*, 2000, **104**, 8768–8778.
- [331] P. J. Bereciartua, A. Cantín, A. Corma, J. L. Jordá, M. Palomino, F. Rey, S. Valencia, E. W. Corcoran, P. Kortunov, P. I. Ravikovitch, A. Burton, C. Yoon, Y. Wang, C. Paur, J. Guzman, A. R. Bishop and G. L. Casty, *Science*, 2017, **358**, 1068–1071.
- [332] P. Demontis and G. B. Suffritti, *Microporous Mesoporous Mater.*, 2009, **125**, 160–168.
- [333] Y. Li, H. Cao and J. Yu, *ACS Nano*, 2018, **12**, 4096–4104.
- [334] M. Gao, H. Li, M. Yang, S. Gao, P. Wu, P. Tian, S. Xu, M. Ye and Z. Liu, *Commun. Chem.*, 2019, **2**, 1–10.
- [335] I. G. Clayson, D. Hewitt, M. Hutereau, T. Pope and B. Slater, *Adv. Mater.*, 2020, **32**, 2002780.
- [336] Y. Li and J. Yu, *Nat. Rev. Mater.*, 2021, **6**, 1156–1174.

- [337] K. Lu, Y. Fan, J. Huang, J. Wang, H. Xu, J. Jiang, Y. Ma and P. Wu, *J. Am. Chem. Soc.*, 2021, **143**, 20569–20573.
- [338] Z. Liu, A. Chokkalingam, S. Miyagi, M. Yoshioka, T. Ishikawa, H. Yamada, K. Ohara, N. Tsunoji, Y. Naraki, T. Sano *et al.*, *Phys. Chem. Chem. Phys.*, 2022, 4136–4146.
- [339] E. M. Gallego, M. T. Portilla, C. Paris, A. León-Escamilla, M. Boronat, M. Moliner and A. Corma, *Science*, 2017, **355**, 1051–1054.
- [340] S. Svelle, P. O. Rønning and S. Kolboe, *J. Catal.*, 2004, **224**, 115–123.
- [341] S. Svelle, P. O. Rønning, U. Olsbye and S. Kolboe, *J. Catal.*, 2005, **234**, 385–400.
- [342] I. M. Hill, S. A. Hashimi and A. Bhan, *J. Catal.*, 2012, **285**, 115–123.
- [343] E. G. Derouane, *J. Catal.*, 1986, **100**, 541–544.
- [344] E. G. Derouane, J. C. Védrine, R. R. Pinto, P. M. Borges, L. Costa, M. A. N. D. A. Lemos, F. Lemos and F. R. Ribeiro, *Catal. Rev.*, 2013, **55**, 454–515.
- [345] R. Gounder and E. Iglesia, *Chem. Commun.*, 2013, **49**, 3491–3509.
- [346] Y. Xiao, W. Chen, X. Yi, W. Peng, Z. Liu, H. Xia and A. Zheng, *J. Phys. Chem. C*, 2021, **125**, 11580–11590.
- [347] J. Bedard, H. Chiang and A. Bhan, *J. Catal.*, 2012, **290**, 210–219.
- [348] C. Baerlocher and L. B. McCusker, *Database of Zeolite Structures*, <http://www.iza-structure.org/databases/>, 2007, Accessed on 20 September 2021.
- [349] G. S. Lane, F. S. Modica and J. T. Miller, *J. Catal.*, 1991, **129**, 145–158.
- [350] Y. Li and W. K. Hall, *J. Catal.*, 1991, **129**, 202–215.
- [351] S. S. Arzumanov and A. G. Stepanov, *J. Phys. Chem. C*, 2018, **122**, 23432–23440.
- [352] R. G. Bell, in *Modelling and Simulation in the Science of Micro- and Meso-Porous Materials*, ed. C. R. A. Catlow, V. Van Speybroeck and R. A. van Santen, Elsevier, 2018, ch. 1, pp. 1–25.
- [353] Y. Li, G. Zhu, Y. Wang, Y. Chai and C. Liu, *Microporous Mesoporous Mater.*, 2021, **312**, 110790.

- [354] H. Liu, G. D. Lei and W. M. H. Sachtler, *Appl. Catal., A*, 1996, **137**, 167–177.
- [355] G. D. Lei, B. T. Carvill and W. M. H. Sachtler, *Appl. Catal., A*, 1996, **142**, 347–359.
- [356] D. S. Sabirov and I. S. Shepelevich, *Entropy*, 2021, **23**, 1240.
- [357] A. van de Runstraat, J. A. Kamp, P. J. Stobbelaar, J. van Grondelle, S. Krijnen and R. A. van Santen, *J. Catal.*, 1997, **171**, 77–84.
- [358] C. S. Triantafillidis and N. P. Evmiridis, *Ind. Eng. Chem. Res.*, 2000, **39**, 3233–3240.
- [359] S. Anis and Z. A. Zainal, *Bioresour. Technol.*, 2014, **151**, 183–190.
- [360] J. Shi, Y. Wang, W. Yang, Y. Tang and Z. Xie, *Chem. Soc. Rev.*, 2015, **44**, 8877–8903.
- [361] P. M. Yeletsy, R. G. Kukushkin, V. A. Yakovlev and B. H. Chen, *Fuel*, 2020, **278**, 118255.
- [362] R. Maghrebi, M. Buffi, P. Bondioli and D. Chiaramonti, *Renewable Sustainable Energy Rev.*, 2021, **149**, 111264.
- [363] S. Akbar and R. W. Joyner, *J. Chem. Soc., Faraday Trans. 1*, 1981, **77**, 803–809.
- [364] S. D. Yim, S. J. Kim, J. H. Baik, I. Nam, Y. S. Mok, J.-H. Lee, B. K. Cho and S. H. Oh, *Ind. Eng. Chem. Res.*, 2004, **43**, 4856–4863.
- [365] F. Lin, T. Andana, Y. Wu, J. Szanyi, Y. Wang and F. Gao, *J. Catal.*, 2021, **401**, 70–80.
- [366] P. Vanelderen, J. Vancauwenbergh, B. F. Sels and R. A. Schoonheydt, *Coord. Chem. Rev.*, 2013, **257**, 483–494.
- [367] S. Mohan, P. Dinesha and S. Kumar, *Chem. Eng. J.*, 2020, **384**, 123253.
- [368] M. A. Newton, A. J. Knorpp, V. L. Sushkevich, D. Palagin and J. A. Van Bokhoven, *Chem. Soc. Rev.*, 2020, **49**, 1449–1486.
- [369] C. Paolucci, J. R. Di Iorio, W. F. Schneider and R. Gounder, *Acc. Chem. Res.*, 2020, **53**, 1881–1892.
- [370] J. Xu, Y. Qin, H. Wang, F. Guo and J. Xie, *New J. Chem.*, 2020, **44**, 817–831.
- [371] H. Lei, V. Rizzotto, A. Guo, D. Ye, U. Simon and P. Chen, *Catalysts*, 2021, **11**, 52.

- [372] Y. Shan, J. Du, Y. Zhang, W. Shan, X. Shi, Y. Yu, R. Zhang, X. Meng, F.-S. Xiao and H. He, *Natl. Sci. Rev.*, 2021, **8**, nwab010.
- [373] R. Rudham and M. Sanders, *J. Catal.*, 1972, **27**, 287–292.
- [374] J. O. Petunchi and W. K. Hall, *J. Catal.*, 1982, **78**, 327–340.
- [375] J. Bandiera and C. Naccache, *Appl. Catal.*, 1991, **69**, 139–148.
- [376] A. Bellare, A. Raje and D. B. Dadyburjor, in *Catalyst Deactivation 1991*, ed. C. H. Bartholomew and J. B. Butt, Elsevier, 1991, vol. 68 of Studies in Surface Science and Catalysis, pp. 227–234.
- [377] M. Zahmakiran and S. Özkar, *Langmuir*, 2009, **25**, 2667–2678.
- [378] M. P. Wan, K. S. Hui, C. Y. H. Chao and C. W. Kwong, *Combust. Sci. Technol.*, 2010, **182**, 1429–1445.
- [379] C. Saux and L. B. Pierella, *Appl. Catal., A*, 2011, **400**, 117–121.
- [380] K. Y. Nandiwale, S. E. Patil and V. V. Bokade, *Energy Technol.*, 2014, **2**, 446–452.
- [381] C. Peng, Z. Liu, Y. Yonezawa, N. Linares, Y. Yanaba, C. A. Trujillo, T. Okubo, T. Matsumoto, J. García-Martínez and T. Wakihara, *J. Mater. Chem. A*, 2020, **8**, 735–742.
- [382] S. Mahmoud, P. Carrez, M. L. Dos Reis, N. Mousseau and P. Cordier, *Phys. Rev. Mater.*, 2021, **5**, 033609.
- [383] P. E. Blöchl, *Phys. Rev. B*, 1994, **50**, 17953.
- [384] A. Dal Corso, *Comput. Mater. Sci.*, 2014, **95**, 337–350.
- [385] A. Ghysels, S. L. C. Moors, K. Hemelsoet, K. De Wispelaere, M. Waroquier, G. Sastre and V. Van Speybroeck, *J. Phys. Chem. C*, 2015, **119**, 23721–23734.
- [386] B. W. H. Van Beest, G. J. Kramer and R. A. Van Santen, *Phys. Rev. Lett.*, 1990, **64**, 1955.
- [387] P. Dauber-Osguthorpe, V. A. Roberts, D. J. Osguthorpe, J. Wolff, M. Genest and A. T. Hagler, *Proteins: Struct., Funct., Bioinf.*, 1988, **4**, 31–47.
- [388] A. V. Kiselev, A. A. Lopatkin and A. A. Shulga, *Zeolites*, 1985, **5**, 261–267.

- [389] I. J. Bush, I. T. Todorov and W. Smith, *Comput. Phys. Commun.*, 2006, **175**, 323–329.
- [390] S. Nosé, *Mol. Phys.*, 1984, **52**, 255–268.
- [391] S. Nosé, *J. Chem. Phys.*, 1984, **81**, 511–519.
- [392] I. Rosbottom, C. W. Yong, D. L. Geatches, R. B. Hammond, I. T. Todorov and K. J. Roberts, *Mol. Simul.*, 2021, **47**, 257–272.
- [393] G. Lippert, J. Hutter and M. Parrinello, *Mol. Phys.*, 1997, **92**, 477–488.
- [394] G. Lippert, J. Hutter and M. Parrinello, *Theor. Chem. Acc.*, 1999, **103**, 124–140.
- [395] J. VandeVondele, M. Krack, F. Mohamed, M. Parrinello, T. Chassaing and J. Hutter, *Comput. Phys. Commun.*, 2005, **167**, 103–128.
- [396] Y. Zhang and W. Yang, *Phys. Rev. Lett.*, 1998, **80**, 890.
- [397] S. Grimme, J. Antony, S. Ehrlich and H. Krieg, *J. Chem. Phys.*, 2010, **132**, 154104.
- [398] S. Goedecker, M. Teter and J. Hutter, *Phys. Rev. B*, 1996, **54**, 1703.
- [399] G. J. Martyna, M. L. Klein and M. Tuckerman, *J. Chem. Phys.*, 1992, **97**, 2635–2643.
- [400] G. Henkelman, B. P. Uberuaga and H. Jónsson, *J. Chem. Phys.*, 2000, **113**, 9901–9904.
- [401] G. Henkelman and H. Jónsson, *J. Chem. Phys.*, 2000, **113**, 9978–9985.
- [402] V. Van Speybroeck, J. Van der Mynsbrugge, M. Vandichel, K. Hemelsoet, D. Lesthaeghe, A. Ghysels, G. B. Marin and M. Waroquier, *J. Am. Chem. Soc.*, 2011, **133**, 888–899.
- [403] G. Kresse and J. Hafner, *Phys. Rev. B*, 1994, **49**, 14251.
- [404] G. Kresse and D. Joubert, *Phys. Rev. B*, 1999, **59**, 1758.
- [405] G. Henkelman and H. Jónsson, *J. Chem. Phys.*, 1999, **111**, 7010–7022.
- [406] A. Heyden, A. T. Bell and F. J. Keil, *J. Chem. Phys.*, 2005, **123**, 224101.

- [407] S. Bailleul, K. Dedecker, P. Cnudde, L. Vanduyfhuys, M. Waroquier and V. Van Speybroeck, *J. Catal.*, 2020, **388**, 38–51.
- [408] N. L. Allan, G. D. Barrera, M. Y. Lavrentiev, C. L. Freeman, I. T. Todorov and J. A. Purton, *Comput. Mater. Sci.*, 2006, **36**, 42–48.
- [409] S. Metz, J. Kästner, A. A. Sokol, T. W. Keal and P. Sherwood, *Wiley Interdiscip. Rev.: Comput. Mol. Sci.*, 2014, **4**, 101–110.
- [410] F. Spiegelman, N. Tarrat, J. Cuny, L. Dontot, E. Posenitskiy, C. Martí, A. Simon and M. Rapacioli, *Adv. Phys.: X*, 2020, **5**, 1710252.